



THE HONG KONG  
POLYTECHNIC UNIVERSITY

香港理工大學

Pao Yue-kong Library

包玉剛圖書館

---

## Copyright Undertaking

This thesis is protected by copyright, with all rights reserved.

**By reading and using the thesis, the reader understands and agrees to the following terms:**

1. The reader will abide by the rules and legal ordinances governing copyright regarding the use of the thesis.
2. The reader will use the thesis for the purpose of research or private study only and not for distribution or further reproduction or any other purpose.
3. The reader agrees to indemnify and hold the University harmless from and against any loss, damage, cost, liability or expenses arising from copyright infringement or unauthorized usage.

If you have reasons to believe that any materials in this thesis are deemed not suitable to be distributed in this form, or a copyright owner having difficulty with the material being included in our database, please contact [lbsys@polyu.edu.hk](mailto:lbsys@polyu.edu.hk) providing details. The Library will look into your claim and consider taking remedial action upon receipt of the written requests.

# **“AlGa<sub>N</sub>/Ga<sub>N</sub> Based HEMT Structures and Applications”**

**Shrawan Kumar Jha**

**Doctor of Philosophy**

**The Hong Kong Polytechnic University**



**September, 2007**

# **CERTIFICATE OF ORIGINALITY**

I hereby declare that this thesis is my own work and that, to the best of my knowledge and belief, it reproduces no material previously published or written, nor material which has been accepted for the award of any other degree or diploma, except where due acknowledgement has been made in the text.

(Shrawan Kumar Jha)

Dated:

| ॐ |

माता श्रीमती रूकमिणी झा एवम पिता श्री मंगनू झा  
के प्रति सविनय समर्पित

Dedicated to the Uncountable Sacrifices  
of My Parents and Grandparents

ॐ पूर्णमदः पूर्णमिदं पूर्णात् पूर्णमुदच्यते ।  
पूर्णस्य पूर्णमादाय पूर्णमेवावशिष्यते ॥

The unmanifested source of the Nature is perfect, and the manifested nature is also perfect. Fullness proceeds from fullness. Taking fullness from fullness, all that remains is fullness.

-Isha Upanishad, 3000 BC.

# ABSTRACT

GaN based technologies are capable of addressing the emerging technological demands arising from the current needs of rapidly changing electronics markets. AlGaN/GaN heterostructures are promising candidates for a number of applications. Reliability and performance enhancement remains the biggest challenges in the commercialization of GaN based technologies. In this work, both of these issues were addressed in context of the devices incorporating, single and double AlGaN/GaN heterostructures. In addition, novel application of these heterostructures as HEMT based biosensor device was demonstrated.

Implementation of gate recess in field effect devices has been touted as an effective means for improving the transconductance of the transistors. Potential influence of this recess technology on the low-frequency noise characteristics of the HEMT devices was investigated. It was found that the magnitude of noise is strongly dependent on the recess depth. Degradation of excess noise, in unrecessed and recessed gate HEMTs, due to hot-electron stressing was also studied. It was observed that noise degradation can be identified to occur in two distinct phases. In the first phase, devices initially show fluctuations in the noise properties around a constant average value. This was shown to arise from the modulation of the percolation paths of the carriers in the two-dimensional electron gas. In the second phase, irreversible degradation of noise power was observed due to generation of interface states at the AlGaN/GaN heterointerface. The two phase degradation was observed for all the recessed and unrecessed devices, however, it was found that recessing significantly affects the device life time.

Low-frequency noise in MOCVD-grown AlGaIn/GaN/AlGaIn/GaN double channel HEMTs was investigated over a wide range of temperatures. Bias dependence of noise properties was studied. Generation-recombination noise was observed to be arising from the traps with activation energies 140 meV, 188 meV and 201 meV. Hooge parameter was estimated to be  $1.64 \times 10^{-3}$  at room temperature. Experimental results of the noise measurements on TLM structures reflected insignificant contribution of contact noise in studied structures.

A novel application of GaN based heterostructures for bio-sensing was demonstrated. Feasibility of using AlGaIn/GaN heterostructures for cell culture was studied. High density cell monolayers of human osteoblast-like cells could be achieved after surface functionalization. Effect of drug-H7, and trypsin was optically inspected. Large area gateless HEMT like devices were fabricated and cell monolayers were grown over the gate area. Effect of trypsin on these cells was electrically monitored with this device. Detection is based on current modulation in the device due to removal of the cells from the gate area. The time scale recorded from optical inspection and electrical inspection were found to be the same. This suggested the feasibility of using the proposed HEMT-based biosensor devices for a wide variety of biosensing applications.

## Publications Arising from the Thesis

1. S. Jha, C. Zhu, C. Surya, M. Pilkuhn, H. Schweizer: "Degradation of Low-frequency Noise in AlGaIn/GaN HEMTs under DC Bias Stress". *Fluctuations and Noise Letters* (accepted).
2. J. Yu, S. Jha, C. Surya, M. Yang: "AlGaIn/GaN HEMTs for Cell-culture Biosensor Devices". *Biosensors and Bioelectronics*, vol. 23, pp. 513-519, 2007.
3. S. Jha, C. Surya, K. Chen, K. Lau: "Low-frequency noise properties of Dual Channel AlGaIn/GaN High Electron Mobility Transistor". *Solid State Electronics*, (accepted).
4. S. Jha, C. Surya, K. Chen, K. Lau: "Generation Recombination Noise in Dual Channel AlGaIn/GaN High Electron Mobility Transistor". 36<sup>th</sup> European Solid-State Device Research Conference, Montreux, Switzerland. 19-21 September 2006. *Proceedings of the ESSDERC-2006*, pp. 105-8, 2006.
5. S. Jha, J. Gao, C. Zhu, E. Jelenkovic, K. Tong, M. Pilkuhn, C. Surya, H. Schweizer: "Low-frequency Noise Characterization of Hot-electron Degradation in GaN-based HEMTs". 18<sup>th</sup> International Conference on Noise and Fluctuations-ICNF 2005, 19-23 Sept. 2005, Salamanca, Spain; *AIP Conference Proceedings*, n 780, pp. 295-8, 2005.
6. S. Jha, C. Zhu, E. Jelenkovic, K. Tong, C. Surya, M. Pilkuhn, H. Schweizer: "Characterization of 1/f Noise in GaN-based HEMTs Under High dc Voltage Stress". *Noise in Devices and Circuits III*, May 24-26, 2005, Austin, TX, United States Sponsor: SPIE - The International Society for Optical Engineering; *Proceedings of SPIE - The International Society for Optical Engineering, Noise in Devices and Circuits III*, Vol. 5844, pp. 256-67, 2005. [INVITED PAPER]
7. S. Jha, B. Leung, C. Surya: "Studies of Hot-electron Degradation in GaN HEMTs with Varying Gate Recess Depths". Conference on Optoelectronic and Microelectronic Materials and Devices. 8-10 Dec. 2004, Brisbane, Qld., Australia. *Conference on Optoelectronic and Microelectronic Materials and Devices. Proceedings. (IEEE Cat. No. 04EX973)*, pp. 33-6, 2004.
8. S. Jha, B. Leung, C. Surya, H. Schweizer, M. Pilkuhn: "Low-Frequency Noise Characterization in AlGaIn/GaN HEMTs with Varying Gate Recess Depths". GaN, AlN, InN and Their Alloys. Symposium, 29 Nov.-3 Dec. 2004, Boston, MA, USA; *Materials Research Society Symposium Proceedings*, Vol. 831, pp. 465-70, 2005.

# Acknowledgements

It is unavoidable for me to recall my wonderful teachers, at my previous graduate schools, who strengthened my academic foundation. I take this opportunity to thank my previous supervisors Prof. S. Chandra, H.O.D, CARE and Dr. P. Srivastava, Asso. Prof., Department of Physics (both at IIT Delhi) and Prof. A. K. Jain, Department of Physics at IIT-Roorkee for everything they did for my academic and personal welfare. I gratefully remember the wisdom and warmth of my favorite teachers at both of those great institutions (IIT Delhi, and IIT Roorkee). Whatever success I have or whatever success I will achieve, a part of the credit will always go to my teachers who have contributed to shape my personality. It feels great to recall Prof. V. Vankar, Prof. O. Agnihotri, Prof. D. Pandya, Prof. B. Mehta, Prof. L. Malhotra and Prof. H. Sehgal (all at IIT-Delhi) and Associate Prof. S. Barthwal, Prof. G. Singh, Prof. R. Nath, Prof. Y. Singh, Prof. M. Srivastava, Prof. I. Tyagi, Prof. A. Tripathi, Prof. R. Srivastav and Prof. S. Auluck (all at Department of Physics, IIT-Roorkee).

I express my sincere gratitude to my Ph.D. supervisor, Prof. Charles Surya, for giving me wonderful opportunities. I am thankful for his invaluable guidance, support, encouragement and personal interest throughout this project which made this thesis possible.

I am indebted to the incredible support and encouragement I received from Dr. Jelencovic Emil, microelectronics group member and scientific officer, HKPU. His academic and personal support is instrumental for the success of this thesis.

I am thankful to Dr. Mo Yang, Asst. Prof., Department of Health Technologies, for allowing me to access his lab for a part of this work.

I am thankful to Prof. M. Pilkuhn and H. Schweizer (Stuttgart University, Germany) for a fruitful collaboration and inspiring discussions.

I am thankful to Prof. K. J. Chen and K. M. Lau (University of Science and Technology, Hong Kong) for a successful collaboration.

I am thankful to my friend and group mate C. P. Chan, for sharing instruments, thoughts, advice, breakfast and laughs at a number of occasions when I was in need.

I am also thankful to Mr. Terry, Department of Health Technologies, for his help and interest in my work, and for few restless nights he had to spend doing experiments with me.

I am thankful to my group mates Mr. C. W. Lip, Mr. B. H. Leung, Mr. H. Lui, Dr. W. K. Fong, and Dr C.F. Zhu for their help and advice. Special thanks go to Mr. Leung and Mr. Lip for their personal guidance, support and encouragement.

I am thankful to Dr G. Pang, (TEM Lab) and Mr. M. N. Yeung (Material Research Center) Department of Applied Physics and Miss Q. Tang, (AFM Lab) Department of Mechanical Engineering for their involvement.

Finally, I gratefully acknowledge the help I received from Dr. Khijvania (Asst. Prof., IIT Guwahati, India) and Dr. K. Nakeeran (University of Aberdeen, U.K.) to improve the thesis manuscript. Invaluable support of my friends Dr. S. K. Tyagi (Post Doctoral Fellow, BRE, PolyU), Dr. K. Senthilnathan (Research Associate, EIE, PolyU) and Mr. M. K. Sarkar (Ph.D. Student, Department of Textile Technology) is sincerely acknowledged. I also acknowledge the continuous support and timely help of the University and Departmental staff, especially to mention Ms. May Chu (RO) and Ms. Ann Wong, Ms. Cora Au and Ms. Suki Chu (all EIE office staff) for their kind help throughout my study.

(Shrawan Kumar Jha)

## List of Symbols

$A$	area of a device structure
$B$	frequency bandwidth of a system
$B_Z$	a magnetic field in the $z$ -direction
$c$	speed of light in vacuum
$d$	inter-planer spacing
$d_h$	effective thickness of the hetero-interface
$d_{hkl}$	inter-planer spacing between parallel planes with indices $h, k,$ and $l$
$d_l$	the conducting layer thickness
$d_r$	the depth of recess in the gate area of a device
$E$	Energy
$E_B$	the breakdown electric field
$E_F$	the Fermi energy level
$E_g$	the band gap energy
$E_p$	the activation energy at which Lorentzian is sharply peaked
$E_T$	the trap energy level
$E_x$	electric field in the direction of current conduction
$E_y$	the electric field in a direction perpendicular to the current conduction
$E_\tau$	Activation energy of a trap
$G_M$	the transconductance of a transistor
$G_{Mmax}$	the peak value of transconductance
$h$	the Plank's constant
$I$	Electric current in a sample
$I_{DS}$	drain to source current
$I_{DSS}$	the saturation drain current
$\Delta I_0$	the current fluctuation due to the capture of a single carrier
$k$	the Boltzmann constant
$L$	the length of a cross-bridge structure
$L_T$	the transfer length of a TLM structure
$l_i$	separation between two consecutive TLM pads

$m_0$	the rest mass of electron
$N$	number of the free carriers in the sample
$N_T$	the trap density
$n$	bulk carrier density
$n_s$	sheet carrier density
$q$	the fundamental electric charge
$R$	the device resistance
$R_c$	the contact resistance of a semiconductor
$R_H$	the Hall coefficient
$R_{Hs}$	the sheet Hall coefficient
$R_i$	Resistance between two consecutive TLM pads
$R_S$	the sheet resistance term in the van der pauw method
$R_{sh}$	Sheet resistance of the semiconductor material
$R_{SK}$	the sheet resistance of the material under the TLM pads
$R_s$	a series resistance
$S_N$	the power spectral density of $N$
$S_R$	the power spectral density of $R$
$S_V$	the power spectral density of $V$
$S_{Vmax}$	the maximum observed value of $S_V$
$S_{Vmin}$	the minimum observed value of $S_V$
$S_X(f)$	the power spectral density of a time variable $X$ as a function of $f$
$T$	the absolute temperature
$t$	time
$t_s$	the duration of applied electrical stress to a device
$V$	the bias voltage across a conducting sample
$V_{DS}$	drain to source voltage
$V_{GS}$	gate to source voltage
$V_h$	the Hall voltage
$V_r$	the resistance voltage
$V_{Th}$	the threshold voltage of a transistor
$v_x$	velocity of the charge carriers in the $x$ -direction

$W$	width of a device structure
$X$	the number of scanning points for AFM measurement
$X_{RMS}$	RMS value of the scanned area
$x$	an arbitrary signal variable
$x(t)$	random variations of $x$ in time
$\rho_c$	specific contact resistivity
$\alpha_H$	the Hooge parameter
$\beta$	the power exponent of bias voltage
$\chi$	Thermal Conductivity
$\varepsilon$	Relative Dielectric Constant
$\Phi_x(t)$	autocorrelation function
$\gamma$	the frequency exponent of a $1/f$ spectrum
$\lambda$	wavelength of the light source
$\mu$	the Hall mobility
$v_s$	Saturation Velocity of conduction electron
$\theta$	the angle between direction of the incident beam and the lattice plane
$\rho$	the bulk resistivity
$\rho_s$	the sheet resistivity
$\sigma$	the conductivity
$\tau$	the fluctuation time constant
$\tau_T$	the relaxation time constant associated with a trap
$\tau_0$	the inverse phonon frequency
$\omega$	angular frequency
$\Omega$	the total volume of a conducting sample

## List of Tables

Table-2.1: Basic material and electrical properties of GaN.	20
Table-2.2: Suitability of GaAs, Si, SiC, and GaN materials for high-power and high-frequency applications.	21
Table-2.3: Basic properties of selected semiconductor materials for high-power and high-frequency applications.	22
Table-3.1: Noise Classification.	90

## List of Figures

Fig. 2.1: Rapidly increasing publications in group III Nitride based research	13
Fig. 2.2: perspective views of wurtzite GaN along various directions.	18
Fig. 2.3: Ga (0001)A), and N (0001)B) polarities of wurtzite GaN.	19
Fig. 2.4: an eclipsed bond configuration in the wurtzite and a staggered configuration in the zinc blend as observed viewing along the $\langle 0001 \rangle$ axis.	20
Fig. 2.5: MESFET structures as reported in 1993 (left) and 2006 (right).	23
Fig. 2.6: (left) GaN MISFET as reported in 1994 (left) and in 2006 (right)	26
Fig. 2.7: Modulation doped heterostructure-a schematic representation	28
Fig. 2.8: A Basic HEMT structure and corresponding conduction band diagram showing formation of 2DEG in the vicinity of conduction band discontinuity.	30
Fig. 2.9: Plan and cross-sectional view of the 1st AlGaIn/GaN HEMT (right) and the epilayer structure (left).	31
Fig. 2.10: Cross-sectional structure of the RIE etched recessed gate HEMT grown on sapphire by MOCVD.	33
Fig. 2.11: Cross-sectional structures of the recessed and conventional device.	34
Fig. 2.12: Schematic of epilayer structure of a double channel HEMT.	35
Fig. 2.13: Schematic diagram of a basic AlGaIn/GaN heterostructure employed for sensor applications.	41
Fig. 3.1: A diagrammatic presentation of the experimental schedule	53
Fig. 3.2: a schematic illustration of AFM operation (left) and Force-distance relation at atomic scales (right).	62
Fig. 3.3: A typical AFM instrumentation.	64
Fig. 3.4: Schematic diagram showing Bragg's diffraction from a crystal plane.	66
Fig. 3.5 : Schematic diagram of a plane with Miller indices (1 1 1) in a cubic lattice (a); and a hexagonal lattice with lattice parameters a, and c (b).	67
Fig. 3.6: A four-index and a three index (miller) notation of various planes and directions in the hexagonal lattice.	68
Fig. 3.7: Schematic drawing of the Bruker D8 Discover X-ray optics consisting of the X-ray tube, hybrid monochromator, Euler cradle and the detector.	69

Fig. 3.8: Different types of HRXRD scan geometries (left); and Schematic diagram of the instrument geometry for $\theta$ - $2\theta$ scan (right).	70
Fig. 3.9: Schematic diagram of a four axes X-ray diffractometer instrument	69
Fig. 3.10: Schematic diagram of the instrument geometry for $\omega$ scan in case of poorly oriented grains (left); and the schematic representation of the influence of no strain (a), uniform (b) and non-uniform (c) microstrain on the XRD profile(right).	72
Fig. 3.11: Hall Effect measurements in a cross-bridge structure	74
Fig. 3.12: A schematic of a rectangular van der Pauw configuration	77
Fig. 3.13: Hall voltage measurement method in van der Pauw configuration	78
Fig. 3.14: A sample holder for the cryogenic Hall measurements	83
Fig. 3.15: Transmission line pattern on isolated semiconductor (top); and The TLM method for measuring the contact resistance.	85
Fig. 3.16: A Lorentzian Noise Spectra.	93
Fig. 3.17: $1/f$ spectra as superposition of Lorentzians.	98
Fig. 3.18 : Schematic diagram of a typical noise measurement setup.	102
Fig. 3.19: Circuit representation of a typical noise measurement setup.	102
Fig. 4.1: Schematic cross-sections of the recessed gate AlGaIn/GaN HEMTs.	115
Fig. 4.2: SEM image of a HEMT chip.	116
Fig. 4.3: SEM image of a recessed HEMT device.	116
Fig. 4.4: A chip containing HEMT devices bonded on a 24-pin DUI package.	117
Fig. 4.5: Background noise of the measurement system.	120
Fig. 4.6: Noise power spectra of devices with different $d_r$ .	121
Fig. 4.7: Dependence of $S_V$ on $d_r$ as observed at $f = 10$ Hz, for the maximum and minimum value of $S_V$ .	122
Fig. 4.8: Typical $I$ - $V$ characteristics (top) of a virgin Device A (for $V_{GS} = 0$ V to $V_{GS} = -4$ V with a step of $-0.5$ V, and Transfer characteristics (bottom) of the device at $V_{DS} = 5$ V.	125
Fig. 4.9: Experimental $S_V(f)$ recorded at $V_{DS} = 0.22$ V and $V_{GS} = -1.5$ V, plotted as a function of stress time, $t_S$ , for Device A ( $d_r = 6$ nm).	126

- Fig. 4.10: Experimental  $S_V(f)$  recorded at  $V_{DS} = 0.22$  V and  $V_{GS} = -1.5$  V, plotted as a function of stress time,  $t_S$ , for the devices A (solid spheres), B (solid triangles), and D (solid squares). Solid lines represent exponential fits to the original data points. 127
- Fig. 4.11: Calculated lateral electric field along the channel under the gate of an unrecessed HEMT device. 130
- Fig. 4.12: Computed  $N_T(E)$  before (open circles) and after (open triangles) the dc voltage stress. 131
- Fig. 4.13: Experimental  $I$ - $V$  characteristics (from  $V_{GS} = 0$  V to  $-2$  V, with a step of  $-0.5$  V) of a MOCVD-grown HEMT device; before (solid line), and after (dotted line) 1-minute voltage stress at  $V_{DS} = 10$  V and  $V_{GS} = -1.5$  V. Dashed line, represents the data measured after 20 minute baking at  $100$  °C. 133
- Fig. 4.14: Experimental  $S_V(f)$  observed under above mentioned conditions. 133
- Fig. 4.15: Experimental variations of  $S_V(f)$  vs  $V_{GS}$  for  $f = 173$  Hz measured at  $79$  K. Lines A and B are data measured consecutively, line C was measured after 10 minutes voltage stress at low-temperature and line D was measured after temperature cycling followed by voltage stress at room temperature. All the noise data were recorded at  $V_{DS} = 50$  mV. 135
- Fig. 4.16: Experimental  $S_V(f)$  of a MBE-grown HEMT device before (squares) and after (circles) 1-minute voltage stress at  $V_{DS} = 10$  V and  $V_{GS} = -1.5$  V. Experimental  $I$ - $V$  characteristics, before (solid line) and after (solid circles) stress are shown in the inset. 137
- Fig. 4.17: Schematic diagram of the epitaxial layer structure used for the fabrication of dual channel HEMT devices. 140
- Fig. 4.18: Optical-microscope image of a HEMT transistor. 141
- Fig. 4.19: An Illustration of current conduction through two channels controlled by the gate in different regimes of operation. A illustrates a normally on transistor and both channels are conducting. B illustrates the case when first threshold is reached and upper channel is cut off. Current conduction now takes place through the lower channel only. C illustrates the case when the gate voltage reaches a threshold value and second channel is also cut off. 143
- Fig. 4.20: SEM image of a linear TLM pattern on a double heterostructure film. 145

Fig. 4.21: Resistance vs. consecutive pad-separation observed from a TLM pattern.	145
Fig. 4.22: SEM image of a Hall bar.	146
Fig. 4.23: Optical microscope image of a large area Schottky contact on the chip.	147
Fig. 4.24: C-V profile of a Schottky contact having a diameter of 200 $\mu\text{m}$ .	148
Fig. 4.25: I-V characteristics of a dual channel device.	150
Fig. 4.26: Transfer characteristics of a dual channel device in saturation at $V_{DS} = 0.5 \text{ V}$ .	151
Fig. 4.27: $S_V(f)$ spectra observed at $V_{GS} = 0, -2, -5, \text{ and } -7 \text{ V}$ , for a range of drain bias voltages.	154
Fig. 4.28: Bias dependence of $S_V(f)$ at small $V_{DS}$ , as observed at $V_{GS} = 0 \text{ V}$ (solid squares) and at $V_{GS} = -4 \text{ V}$ (solid triangles). Solid lines represent linear fit to the experimental data.	155
Fig. 4.29: Variation of bias dependence slope ( $\beta$ ) with the gate bias voltage. (Data points are shown in solid squares. A dotted line is shown to help appreciate the double hump profile as also seen in the transfer characteristics.)	156
Fig. 4.30: Normalized noise power plotted against $V_{DS}$ for $V_{GS} = 0 \text{ V}$ , and $V_{GS} = -4 \text{ V}$ .	157
Fig. 4.31: $S_V(f)$ spectra at 81 K and 300K, acquired at $V_{GS} = 0 \text{ V}$ (top) and $V_{GS} = -5 \text{ V}$ (bottom).	159
Fig. 4.32: Temperature dependent variation of gamma at $V_{GS} = 0 \text{ V}$ .	160
Fig. 4.33: Temperature dependence of $S_V(f)$ at $V_{GS} = 0 \text{ V}$ (data points shown in square), and at $V_{GS} = -5 \text{ V}$ (data points shown in triangle) as observed at $f = 60 \text{ Hz}$ .	162
Fig. 4.34: Shift of the $S_V - T$ peaks at different observation frequencies.	163
Fig. 4.35: Selected $S_V$ (top) and $f * S_V$ (bottom) spectra at $V_{GS} = 0 \text{ V}$ , in the temperature range 177-190 K.	165
Fig. 4.36: Selected $S_V$ (top) and $f * S_V$ (bottom) spectra at $V_{GS} = -5 \text{ V}$ , in the temperature range 181-190 K.	166
Fig. 4.37: Selected $S_V$ (top) and $f * S_V$ (bottom) spectra at $V_{GS} = 0 \text{ V}$ , in the temperature range 196-216 K	167
Fig. 4.38: Arrhenius plots for the traps observed in the temperature range 81 K -300 K.	168

Fig. 4.39: Trap density derived from the noise data taken at $V_{GS} = 0$ V.	170
Fig. 4.40: Noise from TLM structure at different gate bias voltages.	172
Fig. 4.41: Normalized noise power observed across the TLM pads with separation $L_x$ , for different bias voltages.	172
Fig. 4.42: Epitaxial layer scheme of the AlGaIn/GaN heterostructures used for bio-sensing application.	181
Fig. 4.43: Cross-sectional SEM micrograph of a heterostructure sample.	182
Fig. 4.44: SEM image of the top surface of a heterostructure showing reasonably smooth surfaces.	182
Fig. 4.45: 2D AFM image of the top surface of a MBE grown AlGaIn/GaN heterostructure.	183
Fig. 4.46: $\theta$ -2 $\theta$ HRXRD scan of an AlGaIn/GaN heterostructure.	184
Fig. 4.47: Dependence of Hall mobility on temperature as observed for an AlGaIn/GaN heterostructure sample.	185
Fig. 4.48: Schematic diagram of a bare gate HEMT like detector device.	186
Fig. 4.49: $I$ - $V$ characteristics of a freshly fabricated device.	187
Fig. 4.50: Low frequency noise spectra of a virgin device at $V = 0.2$ V.	187
Fig. 4.51: Adherent cells on an untreated heterostructure surface.	190
Fig. 4.52: Cells cultured on untreated GaN surface in 24h.	191
Fig. 4.53: Cells cultured on FN modified AlGaIn surface in 24 h.	191
Fig. 4.54: Cultured cells as observed on a GaN surface, before (top) and after (bottom) introducing trypsin in the medium.	193
Fig. 4.55: Epifluorescence microscopy images of cultured cells as observed on a GaN surface, before (left) and after an hour of introducing H7 (right) in the medium.	194
Fig. 4.56: Epifluorescence microscopy images of cultured cells as observed on a GaN surface, 5 minutes after introducing trypsin in the medium.	195
Fig. 4.57: Growth profile of cell density with cell culture duration.	196
Fig. 4.58: Cell density as observed before (up) and 1 minute after (down) introducing trypsin.	197
Fig. 4.59 : Cell density as observed after 2 minute (up); and after 3 minute (down) of introducing trypsin.	198

Fig. 4.60: Cell density as observed after 4 minute of introducing trypsin	199
Fig. 4.61: Influence of trypsin on the device current observed at $V= 4$ V.	200

## ABBREVIATIONS

2DEG	Two Dimensional Electron Gas
AlGaN	Aluminum Gallium Nitride
AlN	Aluminum Nitride
CFOM	Combined Figure-Of-Merit
CMOS	Complementary Metal Oxide Semiconductor
DAC	Digital to Analog Converters
FET	Field Effect Transistors
FFT	Fast Fourier Transformation
GaAs	Gallium Arsenide
GaN	Gallium Nitride
G-R	Generation-Recombination
HBT	Heterostructure Bipolar Transistor
HCP	Hexagonal Closed Pack
HEMT	High Electron Mobility Transistors
HFET	Heterostructure FETs
HVPE	Hydride Vapor Phase Epitaxy
InN	Indium Nitride
ISFET	Ion Sensitive Field Effect Transistor
IT	Information Technology
LASER	Light Amplification by Stimulated Emission of Radiation
LD	Laser Diode
LED	Light Emitting Devices
LFN	Low-Frequency Noise
LNA	Low Noise Amplifier
MBE	Molecular Beam Epitaxy
MCM	Multi Chip Module
MESFET	Metal-Semiconductor Field Effect Transistors
MISFET	Metal-Insulator Field Effect Transistors
MOCVD	Metal Organic Chemical Vapor Deposition
MODFET	Modulation Doped FET
MOMBE	Metal Organic Molecular Beam Epitaxy
PAMBE	Plasma Assisted Molecular Beam Epitaxy
PAMBE	Plasma-Assisted Molecular Beam Epitaxy
PIMBE	Plasma Induced Molecular Beam Epitaxy
rf	Radio-Frequency
RTD	Resonant Tunneling Devices
SAG	Selective Area Growth Technique
SAG	Selective Area Growth Technique
SAW	Surface Acoustic Wave
SET	Single Electron Transistors
SIA	Semiconductor Industry Association
SiC	Silicon Carbide
SRAM	Static Random Access Memory
TLM	Transmission Line Method
UV	Ultra Violet
W-CDMA	Wideband Code Division Multiple Access
ZnSe	Zinc Selenide

# Table of Contents

CERTIFICATE OF ORIGINALITY	I
DEDICATION	II
ABSTRACT	III
PUBLICATIONS ARISING FROM THE THESIS	V
ACKNOWLEDGEMENTS	VI
LIST OF SYMBOLS	VII
LIST OF TABLES	X
LIST OF FIGURES	XI
ABBREVIATIONS	XVII
TABLE OF CONTENTS	XVIII

CHAPTER 1 THESIS INTRODUCTION	1
1.1 Worldwide Research Scenario	1
1.2 Motivation	2
1.3 Thesis Objective	4
1.4 Original Contribution	6
1.4 Thesis Orientation	7
Reference (CHAPTER 1)	9
CHAPTER 2 GaN BASED TECHNOLOGIES - A REVIEW OF THE STATE OF THE ART	10
2.1 The Drive for GaN Based Research Initiatives	10
2.1.1 Emerging Markets and Technologies	11
2.1.2 Potential of III Nitrides	12
2.2 The GaN Technology	15
2.2.1 Material Properties	17
2.2.1 GaN Based Transistor Technologies	21
2.3 Development of the GaN based HEMT Technology	26
2.3.1 Heterostructure and 2DEG	27
2.3.2 Basic HEMT Device	29
2.3.3 Recent Advances: Gate Recessed GaN HEMTs	32

2.3.4 Recent Advances: Double Heterostructure FETs	34
2.4 Challenges: Reliability and Performance Issues	36
2.4.1 General Understanding	36
2.4.2 Mechanisms	37
2.4.3 Noise Based Degradation Studies	38
2.5 Applications of Heterostructures Beyond HEMTs	40
Reference (CHAPTER 2)	44
CHAPTER 3 EXPERIMENTAL TECHNIQUES AND SETUPS	53
3.11 Plasma Assisted MBE Growth	54
3.12 MOCVD Growth	55
3.2 Material Characterization	59
3.2.1 Scanning Electron Microscopy	59
3.2.2 Atomic Force Microscopy	61
3.2.3 X-Ray Diffraction	65
3.3 Electrical Characterization	74
3.3.1 Hall Measurements	72
3.3.2 TLM Measurements	84
3.4 Low-frequency Noise Characterization	87
3.4.1 Noise: Relevance in Semiconductor Characterization	87
3.4.2 Statistical Definitions and Formulations	88
3.4.3 Classification of Noise	90
3.4.4 Thermal Noise	90
3.4.5 Shot Noise	91
3.4.6 Generation-Recombination Noise	91
3.4.7 Flicker (1/f) Noise	94
3.4.7.1 Mobility Fluctuation Models	94
3.4.7.2 Number Fluctuation Models	96
3.4.8 Difference between Tunneling and Thermal Activation Models	100
3.4.9 Experimental Setup for Noise Measurements	101
3.5 Epifluorescence Microscopy	104

3.6 Cell Culture	106
Reference (CHAPTER 3)	108

## CHAPTER 4 RESULTS AND DISCUSSIONS

### PART I - DEGRADATION MONITORING IN ALGAN/GAN HETEROSTRUCTURES

BASED RECESSED-GATE HEMTs	110
4.1.1 Investigation Objectives	111
4.1.2 Methodology	112
4.1.3 Device Fabrication	114
4.1.4 Experimental Setup and Characterization Process	118
4.1.5 Effect of Gate Recess on Noise Properties	120
4.1.6 Degradation Monitoring in a Recessed HEMT device	123
4.1.7 Degradation Dependence on Recess Depth	126
4.1.8 Degradation Mechanism	129
4.1.9 Fluctuations in Early Phases	132
4.1.10 Evidence of Percolation Mechanism	129

### PART II - NOISE PROPERTIES OF ALGAN/GAN/ALGAN/GAN DUAL

HETEROSTRUCTURE HEMTs	139
4.2.1 Epi-layer Scheme of Dual Channel HEMT Devices	140
4.2.2 Investigation Objectives and Methodology	141
4.2.3 TLM measurements	144
4.2.4 Hall Measurements	146
4.2.5 C-V Measurements	146
4.2.6 HEMT dc Characterization	152
4.2.7 Experimental Setup for Noise Characterization	147
4.2.8 Room Temperature Noise Properties	153
4.2.9 Noise Properties at Cryogenic Temperatures	158
4.2.10 Signatures of g-r Process	164
4.2.11 Traps and their Activation Energy	168
4.2.12 Contribution of Contact Noise	171

4.2.13 Estimation of Hooge parameter	173
PART III - APPLICATION OF ALGAN/GAN HETEROSTRUCTURES IN BIOSENSORS	176
4.3.1 Investigation Objectives	177
4.3.2 Technical Background	177
4.3.3 Significance of using GaN-based heterostructures	178
4.3.4 Detection Mechanism of the Proposed Devices	180
4.3.5 Investigation Plan	173
4.3.6 Heterostructure Growth and Characterization	181
4.3.7 Fabrication of Device structures	186
4.3.8 Electrical Characterization of Virgin Devices	188
4.3.9 Cell on Chip: from Survival to High Density	189
4.3.10 Effect of Trypsin on Cultured Cells	192
4.3.11 Effect of Drug H-7 on Cultured Cells	194
4.3.12 Estimation of Cell Density and Growth Rate	195
4.3.13 Estimation of Detection Time	196
4.3.14 Electrical Detection of the Influence of Trypsin	200
Reference (CHAPTER 4)	203
CHAPTER 5 CONCLUSIONS	207
5.1 Summary of the Findings	208
5.2 Suggested Future Work	211

# CHAPTER 1

## THESIS INTRODUCTION

---

### 1.1 Worldwide Research Scenario

In the past century human civilization has experienced tremendous scientific and technological development. To be able to continue this progress, we need to consider a few critical factors which influence the direction of *future technological development*<sup>1</sup>. One such factor is the increasing demand of energy. Need for efficient energy utilization is also a factor. Another factor is the increasing demand for high speed in different sectors. To be specific, the demand for fast *communication*<sup>2</sup> and hence, the need for *high speed communication devices*<sup>3</sup> is a crucial factor. Human health is another important factor and hence, biomedical research is also at the core of attention in the present century. Having identified these factors, key technologies concerned with the mentioned factors are being extensively researched. Such technologies include nuclear energy, information technology (IT), biotechnology, *medical diagnosis and health care*, nanotechnology, and next generation *electronics and optoelectronics* technologies.

Electronics have been playing a crucial role since last century and there has always been a huge, ever-expanding consumer electronics market worldwide. As a result of rapidly developing consumer markets, there has been a continued shift in the requirements of innovative products in the electronics industry. No wonder

electronics and optoelectronics have witnessed one of the highest growth rates in technological research and research related funding since the last decade. Gallium nitride (GaN) is an advanced electronic material which is intensively researched for optoelectronics as well as for power and communication applications. According to a recent report<sup>4</sup>, 232 companies were participating in GaN production worldwide as of early 2005. The worldwide device market for GaN based components reached US\$3.2 billion in 2004. The GaN production market will reach US\$7.6 billion by 2009. Over the next five years, it is expected that GaN-based power transistors will capture a sizable portion of the base station power transistor market.

## **1.2 Motivation**

GaN-based devices are routinely setting new records for the highest achievable power density and maximum cutoff frequency with solid-state Field Effect Transistors (FETs). The GaN technology exploits the advantage of the high critical breakdown fields offered by GaN, which are associated with its large bandgap. The technology has also benefited from high saturation velocity in GaN. GaN-based devices can be exploited for a wide area of applications including cell phone base stations, radar systems, microwave ovens, and circuits in harsh environments such as those close to automotive or other engines. The new technology will provide cheap and powerful circuits currently not available. With the potential advantages of GaN-based technology well demonstrated, significant efforts are currently under way to accelerate its development for system insertion.

By now, GaN technology has resulted in various successful applications including but not limited to, blue and green light-emitting devices (LEDs), blue

diodes, short wavelength lasers, UV-sensitive light detectors, High temperature power electronics, and high frequency electronics. Next-generation wireless devices that allow users to get stock quotes off the Internet, send e-mails, or check their online calendars will need plenty of high-frequency bandwidth to push data through. High temperature chemical and gas detection are also successful applications.

There has been substantial interest worldwide in the development of GaN-based low-noise circuit elements, particularly transistors with superior characteristics. Most of the GaN-based device applications incorporate one or more heterostructures. Heterostructure technology allows simultaneous improvement<sup>5</sup> in the carrier density and the carrier mobility. Two unique features of the heterostructure transistor technology are: (i) high electron mobility which allows high-frequency applications and (ii) high electron density which allows high current capabilities. A widely explored GaN-based heterostructure is the AlGaN/GaN heterostructure. One of the most important applications<sup>6</sup> of heterostructure technology is in the High Electron Mobility Transistors (HEMTs). However, the capabilities of GaN-based devices presently fall short of the requirements for a long lifetime, low defect density, and low and stable contact resistance. Hence, applying existing GaN-based technologies has proven problematic in terms of reliability. For GaN-based FET technology to become the main stream, some obstacles have to be overcome. The remaining challenges are technological hurdles rather than fundamental limitations. Significant research efforts are required to identify and solve the reliability problems. Reliability and performance related issues are often concerned with heterostructure properties. Studying different devices which

incorporate heterostructures can enhance the understanding of quality and performance related issues, thus help improve the current technology.

### 1.3 Thesis Objective

In this thesis, first, some of the reliability and performance issues have been addressed in the context of the AlGaIn/GaN heterostructure based devices which incorporate: (i) a *gate recessed HEMT structure*, and (ii) a *double channel HEMT structure*, and then their application in biosensors is demonstrated using a *HEMT structure*.

In a gate recessed HEMT, recessing is done by reactive ion etching technique. The dry etching process is destructive and it may introduce surface defects. This can affect the life time of the devices. There are other possible ways to create gate recess which introduce much less defect in the material, for example, wet chemical etching. Unfortunately, wet etching technique for GaN technology is in early stages and not yet successful in providing a controllable recess depth with high uniformity over a large area. Then it is important to understand the influences of gate recess of such technique on the defect sensitive GaN devices. Influence of recess depth on device degradation and life time can be non-destructively monitored using low-frequency noise (LFN) characterization. It is important to establish the detailed mechanism for the degradation of GaN-HEMTs and the effects on device reliability due to the recess formation. This will help understand the behavior and limitations of the device under high-power operations. These problems have not yet been addressed

and little study is available in the literature on the monitoring of device noise degradation in GaN HEMTs for prolonged stress durations.

To enhance the device performance, namely current density, double channel HEMT structures are used. A double channel structure incorporates two heterostructures. Current conduction in such a HEMT is through two parallel conduction channels. Both of the channels have different details of defect density and properties. Consequently, their noise response may provide the information about properties of the heterostructures. However, rare reports are available in the literature on the study of properties of dual channel AlGaN/GaN HEMT devices.

Though the GaN technology for core electronics applications is in early stage of development, there are other serious applications where even the state-of-the-art can prove its potential. For example, GaN heterostructures may find important application in bioelectronics. In order to fabricate biosensors with living cells attached on the gate area of a biosensor device, the material should fulfill a few basic requirements which include: non-toxicity of the gate surface, hydrophilic nature of the cell/semiconductor interface, and chemical stability to allow stable transistor operation. GaN not only fulfills all these requirements but also offers additional features. GaN is chemically robust and stable in a large number of biological environment, as well as it is non toxic. It is hydrophilic (with a native oxide over it, alternatively the surface can be oxidized for this purpose), and it can be prepared to be cell friendly. If a double side polished transparent sapphire substrate is used then it becomes even more useful. Because, then it allows simultaneous analysis of electrical activity as well as optical analysis of the cell area by a microscope.

Considering these qualities, heterostructure based biosensor devices could be a very promising application of GaN technology. Studies on the application of GaN heterostructures for bio-sensing are rarely reported and hence in this thesis application of GaN HEMT technology for biosensor application is explored.

## 1.4 Original Contribution

The major contributions of this research study are summarized below:

1. Potential of low-frequency noise characterization as a nondestructive tool for degradation monitoring in GaN-based HEMTs was demonstrated. Strong negative influence of gate-recess technology on device life time was established. A noise-mechanism for the degradation observations in the early phase was proposed.
2. Merits of the double-heterostructure HEMTs were evaluated. Thermal activation process as a dominant noise mechanism was identified. Negligible contribution of ohmic-contact noise in studied HEMTS was established.
3. Application of the state-of-art AlGaIn/GaN heterostructures for biosensors was demonstrated. Effect of *trypsin* on *human osteoblast like Saos-2* cells were electrically recorded with help of gate-less HEMT structures.

## 1.4 Thesis Orientation

A synopsis of the thesis is provided here:

In **CHAPTER 1** (*Thesis Introduction*), motivation behind the thesis is mentioned. Original contributions are introduced. Brief background of the research is introduced which is reviewed further in-depth in chapter 2.

In **CHAPTER 2** (*GaN-based Technologies: A review of State-of-the-Art*), state-of-the-art of GaN based research, as reported in literature, is reviewed. Topics relevant to this study are detailed. Context and need of the presented work is referred.

In **CHAPTER 3** (*Experimental Techniques*), experimental techniques used for this work are detailed. Theoretical concepts and related instrumentations are briefly described. General experimental setup and related conditions are specified. A brief introduction to the noise theories is provided that may help appreciate this study.

In **CHAPTER 4** (*Results and Discussions*), experiments and results are discussed in three parts. Each part is devoted to the experiments performed on devices incorporating a specific detail of AlGaIn/GaN heterostructure and for a specific purpose.

- In Part I, HEMT devices incorporating a single heterostructure are studied. Both recessed and non-recessed gate devices are investigated. The influence of gate recess on device life-time is studied by means of low-frequency noise monitoring. A physical mechanism is proposed that explains the results observed in the early phase of degradation.

- In Part II, HEMT devices incorporating a double heterostructure are studied. Room temperature and low temperature noise properties of the devices are investigated. Trap states and their possible affiliation to the channels are discussed. The influence of contact resistance and contact noise on Hooge parameter estimation is discussed.
- In Part III, the application of heterostructures to bio-sensing is investigated. The Preparation of heterostructures for this purpose is detailed. The fabrication of large-area gate-less HEMT-like devices using such heterostructures is described. High density monolayer of osteoblast cells cultured on heterostructure surface is demonstrated. Optical and electrical detection of the effect of trypsin and the drug H7 on the cell-monolayer cultured on a biosensor device is demonstrated.

In **CHAPTER 5** (*conclusions*), the research is summarized, conclusions are drawn, and possible future works are noted.

## REFERENCES (CHAPTER 1)

---

- <sup>1</sup> “Future and Emerging Technologies”, *Microelectronics Advanced Research Initiative MELARI NANO*. Editors: R. Compañó, L. Molenkamp, D.J. Paul. European Commission IST Program, 2005.
- <sup>2</sup> Kenneth A. LaBel, “NASA Roadmap for Microelectronic Needs”, *NASA/GSFC, MAPLD’99*.
- <sup>3</sup> Hiromichi Ohashi, “Power Electronics Innovation with Next Generation Advanced Power Devices”, *IEICEKEEE INTELEC’OJ*, Oct. 19-23, 2003.
- <sup>4</sup> *GaN Market Research*, ‘Strategies Unlimited’, 2006.
- <sup>5</sup> R. Dingle, H. L. Störmer, A. C. Gossard, and W. Wiegmann. *Appl. Phys. Lett.* Vol. 33, p 665, 1978.
- <sup>6</sup> M. A. Khan, J. N. Kuznia, J. M. Van Hove, N. Pan and J. Carter, *Appl. Phys. Lett.* Vol. 60, p 3027, 1992.

## **CHAPTER 2**

# **GaN BASED TECHNOLOGIES - A REVIEW OF THE STATE OF THE ART**

---

We have witnessed a great change in our lifestyle since the emergence of semiconductor electronics in the past century. This change was further revolutionized by the development of information technologies. Hybridization of very advanced communication technologies, internet, and the information technology added entirely new dimensions in our lives. For these sophisticated applications, most of the credit goes to the devices like transistors, lasers, light emitting diodes, and detectors. In this chapter, evolution of GaN based research, their importance, and their role in emerging technologies is reviewed.

### **2.1 The Drive for GaN Based Research Initiatives**

In the semiconductor industry, Silicon (Si) based technologies have been dominant. As per the Semiconductor Industry Association (SIA) roadmap<sup>1</sup>, complementary metal oxide semiconductor (CMOS) will have a dominant market position even after 2012. SIA, however, only deals with Si based technologies and does not cover other aspects. Telecommunications, III-V materials, analogue microelectronics, low-power portables, optoelectronics etc. are other critically researched areas. A few of these have successfully been commercialized and gaining momentum in the consumers market. An appropriate and timely example is the

lighting industry. This industry is being revolutionized after the commercial success of III-V materials based LED technology in past few years. Rapidly developing consumer electronics market has caused a restless shift in the requirement of innovative products. Consequently, new materials and applications have attracted research interest. Some of those are now successfully catching significant market segments around the globe.

### **2.1.1 Emerging Markets and Technologies**

It is projected that in the near future single electron transistors (SET), intramolecular nano-electronics, resonant tunneling devices (RTDs), and spin based devices will play key roles in fulfilling the emerging market demands<sup>2</sup>. In the context of information technology and communication driven products and applications, the requirements as suggested from the SIA roadmap may be relaxed *if new architectures and functions may be integrated* which allow similar functionality at reduced device numbers. Perhaps the most important driver for new technologies in the coming future is the ability to reduce the *cost per function* on a chip rather than *cost per unit device*. Hence, there is great scope for technologies which may be integrated on a CMOS chip and thus enhance the *functionality* of the CMOS chip. Several other alternative technologies can serve this purpose. For example, III-V materials are dominant in optoelectronics and also in radio frequency power electronics where CMOS cannot compete. Silicon is an indirect band-gap material and as such, Si optoelectronics is at a very immature stage when compared to III-V materials<sup>3</sup>. Poor Si emitter efficiencies can open opportunities for III-V materials to be used for optical communications in Si-integrated applications, for example in

multi chip modules (MCM). Si has limited applications in high-frequency and high-power electronics due to small breakdown fields. There are opportunities for alternative or complementary technologies to be integrated with the existing silicon technology. RTDs are one such alternative candidate that allows reduced transistor counts and either high speed or low power. An RTD circuit is attractive to implement high-speed dynamic logic families. Their characteristic features are reduced circuit complexity and great design flexibility. RTDs can be designed for much higher speeds than CMOS typically in the speed range 10 to 100 GHz. RTDs have demonstrated numerous applications and potential markets including, digital to analogue converters (DACs), clock quantisers, shift registers and ultra low power SRAM. RTDs are based mainly on III-V technology and resonant tunneling has proven fruitful application of III-V materials as a strong alternative of Si technology in the above areas. In near future, it is likely that several other non traditional technologies and products will dominate the market. Such applications include telecommunications, home entertainment, and portables. III-V materials could provide better alternatives in high-speed mobile communications.

### **2.1.2 Potential of III Nitrides**

Devices based on group-III nitrides are capable of operating at high temperatures and hostile environments<sup>4,5</sup>. They serve as key materials for emitters and detectors below green wavelengths. Existing Si and GaAs based technologies cannot tolerate greatly elevated temperatures or chemically hostile environments. SiC is also a competent material for high temperature electronics but it does not challenge the nitride based devices due to their other unique properties<sup>6</sup>. For emitter applications,

same is the case with ZnSe based II-VI compounds in the longer wavelength side<sup>7</sup>. The nitrides, AlN, GaN, and InN are most notable of all III nitrides. All three have direct band gap at room temperature in the wurtzite form while in cubic form AlN and GaN have direct band gap but InN has indirect band gap. One can tailor design the alloy of these nitrides for a desired band gap in much of the visible and ultraviolet energy range. This makes the nitride system attractive for optoelectronics device applications, such as LEDs, laser diodes (LDs), and detectors, which are active in the green, blue or UV wavelength<sup>8,9</sup>. Successful commercialization of these novel materials has already been shown in the growing demand for LEDs and LASERS in consumer electronics and in information technology products. By now, LEDs have proved to be reliable, and have applications, for example, in displays, lighting, indicator lights, advertisement, traffic signs and traffic signals, possibly light sources for accelerated photosynthesis, and medicine for diagnosis and treatment<sup>10,11</sup>. A rapidly increasing<sup>12</sup> number of publications in III-nitrides based research in the past decade have been observed, as shown in Fig. 2.1.

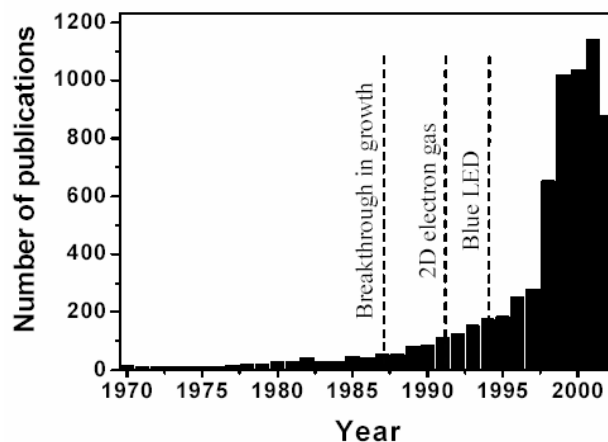


**Fig. 2.1: Rapidly increasing publications in group III Nitride based research<sup>12</sup>.**

In addition to the demonstrated potential of III nitrides in photoemission devices, they have been utilized for transistor and detector applications and further advancement is the subject of cutting edge research<sup>13,14</sup>. Heterostructure bipolar transistors<sup>15</sup>, field effect transistors<sup>16</sup>, and semiconductor-insulator-semiconductor based device structures<sup>17,18</sup> are other such areas of application. These devices are supposed to find important applications in high temperature high-power electronics. The materials like GaN and SiC possess wide band gaps and they become intrinsic at much higher temperatures than other common semiconductors such as Si, and Ge. This allows them to operate at higher temperatures<sup>19</sup> and requires less cooling. Consequently, the cost involved in cooling and the complex device design can be lowered. Further, as the critical breakdown electric field is roughly proportional to the square of the energy band gap, III nitrides can work at very high voltages as compared to other semiconductor materials. One of the most important features of III-V materials is that they can form heterostructures<sup>20,21</sup>. Compound III nitrides can be used to fabricate heterostructures that allow formation of high density two dimensional electron gas (2DEG) which can be used for sophisticated electronic applications. One such application is in HEMTs<sup>22</sup>. High mobility allows high speed transfer of electronic signals and hence high speed communications. Such properties together with specific property of a particular III nitride make them suitable for a range of applications in electronics. GaAs and GaN are the base materials for FET applications. GaAs is already an established technology which has developed to its theoretical limit while GaN is under the phase of rapid development.

## 2.2 The GaN Technology

Literature on the growth of nitrides based research dates back in early 60s. Since then, nitride technology has always lagged behind the easier to grow Si and GaAs based studies. The first systematic effort to grow InN, GaN and AlN by chemical vapour deposition or sputtering processes took place in the 1970s with the emphasis on characterization of structural and optical properties. The III nitride materials got serious attention in late 80s. In the early research, metalorganic precursors containing In or Al with electronic grade purity were not available, also the plasma sources for nitrogen radicals were not compatible with MBE systems. As a result substantial defect concentration and high n-type background was unavoidable in the growth of GaN films. A large concentration of free electrons was presumed to result from oxygen impurities and intrinsic defects. Films having relatively small background electron concentration or p-type doping could not be achieved even until recently. Also, substrate material with reasonably good thermal and lattice matches to the nitrides were not available. AlN was one of the options but the structural quality of the AlN films was not good enough for optical or electronic applications. All these problems resulted in late coming of technological spin-offs, only after some of these problems were addressed with reasonable success.

Large single crystal GaN substrate is not available commercially. This presents a key problem in the growth of homoepitaxial GaN films, making heteroepitaxy a necessity; consequently a suitable choice of substrate becomes crucial. Most often, the lattice constant mismatch has been the primary criterion for determining the suitability of a material as a substrate for GaN epitaxy however

other properties are also important, such as crystal structure, thermal expansion coefficient, chemical, and electrical properties, composition, reactivity, and surface finish. The substrate employed determines the crystal orientation, polarity, polytype, the surface morphology, strain, and the defect concentration of the GaN film, ultimately determining the optimal device performance. There are few techniques which can be employed to ameliorate some of the shortcomings of the substrate. Appropriate surface preparation such as nitridation, pendeoepitaxy<sup>23</sup>, epitaxial lateral overgrowth<sup>24</sup>, deposition of a low-temperature AlN or GaN buffer layer, multiple intervening low-temperature buffer layers<sup>25</sup>, and other techniques<sup>26</sup> have been employed for this purpose. Sapphire ( $\text{Al}_2\text{O}_3$ ) and SiC are the most popular substrate materials used currently, although, recently a few groups have reported using Si as a substrate material<sup>27-29</sup> for GaN film growth, in the drive to make it cheaper and Si compatible. The residual strain due to lattice misfit in GaN on sapphire is comparable to the strain due to misfit between 6H-SiC and GaN, as a result comparable dislocation densities have been observed. GaN layers with dislocation densities as low as  $10^7 \text{ cm}^{-2}$  have been produced but even lower defect densities are necessary for more sophisticated devices operating at more extreme conditions of temperature, voltages, and current densities. Thus far, the (0 0 0 1) sapphire are the most commonly used substrates for the growth of GaN, as this orientation is generally the most favorable for growing smooth films. However, interest in GaN epitaxial layers with other orientations is also increasing to eliminate the polarization effects as such effects can be deleterious for some optoelectronic applications, in which piezoelectric effects in quantum wells can cause a spatial separation of

electrons and holes, thereby decreasing the recombination efficiency<sup>30</sup>.

Many epitaxial thin film growth processes have been developed, including molecular beam epitaxy (MBE), hydride vapor phase epitaxy (HVPE), supersonic jet epitaxy<sup>31</sup>, and metalorganic chemical vapor deposition (MOCVD). Some combined and derivative techniques have also been tried to exploit the benefit of the individual technique. For example metalorganic molecular beam epitaxy (MOMBE), which combines the MOCVD and MBE technique in the same growth machine. Primarily, the development of MOCVD and plasma-induced molecular beam epitaxy (PIMBE) over the last eight years has led to a number of recent advances and important improvements in structural properties. As a result it could be possible to achieve few successful applications based on GaN. One such remarkable application is the achievement of super-bright blue LEDs which were fabricated by MOCVD method. High growth rates, high purity chemical sources, large scale manufacturing potential and the ability to grow abrupt junctions, and a high degree of composition control and uniformity, all these are characteristics of MOCVD that made it possible.

### **2.2.1 Material Properties**

Gallium nitride (as other III nitrides) is normally found in a wurtzite structure. Zinc blende and rock salt are the other possible structures. At room temperature the wurtzite is the thermodynamically stable structure not only for GaN, but for AlN and InN as well. The wurtzite structure has a hexagonal unit cell and hence two lattice constants  $a$ , and  $c$  with six atoms of each type per unit cell. The wurtzite structure consists of two interpenetrating hexagonal closed packed (HCP) sub-lattices, with each type of atom, offset along the  $c$ -axis by  $5/8$  of the cell height  $c$ . It consists of

alternating bi-atomic close-packed (0 0 0 1) planes of Ga and N pairs stacked in an ABABAB sequence. Atoms in the first and third layers are directly aligned with each other. The perspective views of wurtzite GaN along  $[0\ 0\ 0\ 1]$ ,  $[1\ 1\ \bar{2}\ 0]$  and  $[1\ 0\ \bar{1}\ 0]$  directions are shown in Fig. 2.2, where the large sphere represent gallium atoms and the small sphere represent nitrogen atoms. The group III nitrides lack an inversion plane perpendicular to the c-axis. So, the crystals surfaces have either a group III element (i.e. Al, Ga, or In) polarity (designated (0 0 0 1) or (0 0 0 1)A) or a N-polarity (designated (0 0 0  $\bar{1}$ ) or (0 0 0  $\bar{1}$ )B), as shown in Fig. 2.3.

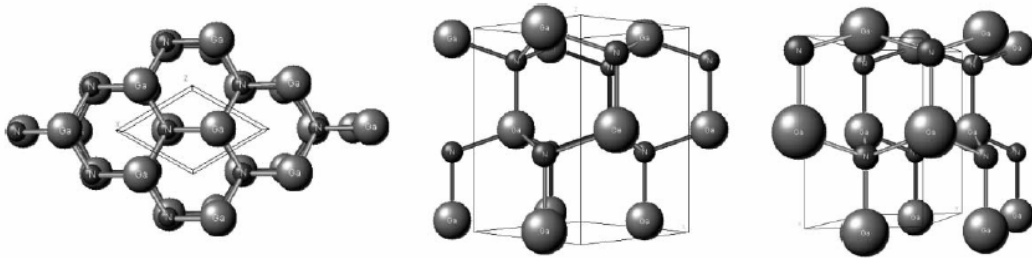


**Fig. 2.2: perspective views of wurtzite GaN along various directions: left  $[0\ 0\ 0\ 1]$ ; middle  $[1\ 1\ \bar{2}\ 0]$ ; right  $[1\ 0\ \bar{1}\ 0]$ <sup>32</sup>.**

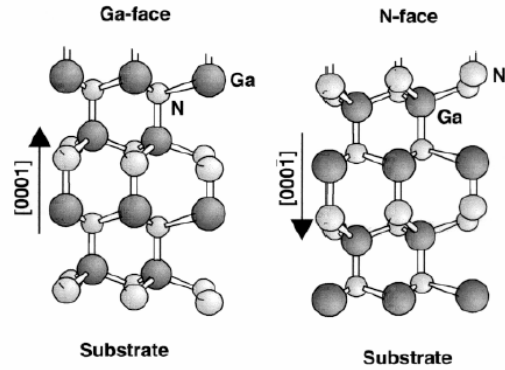


**Fig. 2.3: Ga (0001)A), and N (0001)B) polarities of wurtzite GaN<sup>33</sup>.**

In III-V alloys, a thermodynamically stable phase with wurtzite structure ( $\alpha$ -phase) as well as a meta-stable phase with zincblende structure ( $\beta$ -phase) exists. Because these phases of Group III-nitrides only differ in the stacking sequence of nitrogen and metal atoms (poly-types), the coexistence of hexagonal and cubic phases is possible in epitaxial layers, for example due to stacking faults. The wurtzite and zincblende structures are similar. All group III-Nitrogen bond lengths are equivalent in the zinc blende structures but there are slightly differing III-Nitrogen bond lengths in the wurtzite structures<sup>34</sup>. In either structure, each group III atom (Al, Ga, In) is coordinated by four nitrogen atoms. Conversely, each nitrogen atom is coordinated by four group III atoms. It is the stacking sequence of closest packed diatomic planes that makes difference between these two structures. The stacking sequence of (0001) planes is in  $\langle 0001 \rangle$  direction in wurtzite structure, while for zincblende the stacking sequence of (111) planes is in  $\langle 111 \rangle$  direction. The difference in both structures can be seen by viewing along a chemical bond in the  $\langle 111 \rangle$  or  $\langle 0001 \rangle$  (c-axis) direction as presented in Fig. 2.4. Some of the key

properties of wurtzite GaN material are listed in Table-2.1.

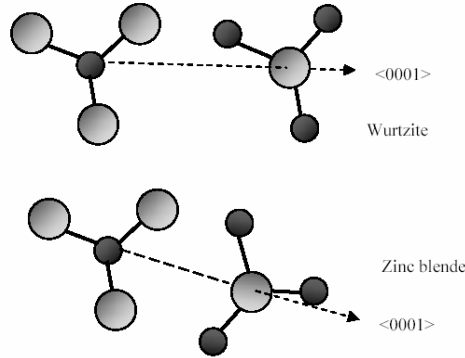


**Fig. 2.4:** an eclipsed bond configuration in the wurtzite and a staggered configuration in the zinc blend as observed viewing along the  $\langle 0001 \rangle$  axis<sup>25</sup>.

**Table-2.1: Basic material and electrical properties of GaN.**

Property	Value
Energy band gap (eV) (300 K)	3.44
Maximum electron mobility ( $\text{cm}^2/\text{V s}$ )	
300 K	1350
77 K	19200
Maximum hole mobility (300 K) ( $\text{cm}^2/\text{V s}$ )	13
Controlled doping range ( $\text{cm}^{-3}$ )	
n-type	$10^{16}$ to $4 \times 10^{20}$
p-type	$10^{16}$ to $6 \times 10^{18}$
Melting point (K)	>2573 (at 60 kbar)
Lattice constants (300 K)	
<i>a</i> (nm)	0.318843
<i>c</i> (nm)	0.518524
Percentage change in lattice constants (300–1400 K)	$\Delta a/a_0$ 0.5749, $\Delta c/c_0$ 0.5032
Thermal conductivity (300 K) (W/cm K)	2.1
Heat capacity (300 K) (J/mol K)	35.3
Modulus of elasticity (GPa)	$210 \pm 23$
Hardness (nanoindentation, 300 K) (GPa)	$15.5 \pm 0.9$
Hardness (Knoop, 300 K) (GPa)	10.8
Yield strength (1000 K) (MPa)	100

### 2.2.1 GaN Based Transistor Technologies

Like in Si technology, GaN based transistors also consist of two kinds, i.e. bipolar transistors and field effect transistors. GaN based high-power and heat tolerant hetero-junction bipolar transistors<sup>35</sup> can be important components of integrated systems designed for high-frequency and high speed applications, for example, in satellites and all electric aircraft. With our focus on HEMTs, which are field effect devices, in this section we will briefly review the progress made in the GaN based field effect transistor devices. GaN based FETs are projected to be highly useful for power amplification and switching in high temperature and high-power environment<sup>36</sup>, as can be understood from a comparison of suitability presented in Table-2.2 below. Some of the GaN properties are listed and compared with other prospective materials in Table-2.3. This table also presents the combined figure-of-merit (CFOM) factor. CFOM<sup>37</sup> is a figure-of-merit of a material for high-power and high-frequency applications.

**Table-2.2: Suitability of GaAs, Si, SiC, and GaN materials for high-power and high-frequency applications.**

Property	GaAs	Si	SiC	GaN
Suitability for high-power	Low	Medium	High	High
Suitability for high frequency	High	Low	Medium	High
low cost substrates	No	Yes	No	Yes
HEMT structure feasibility	Yes	No	No	Yes

**Table-2.3: Basic properties of selected semiconductor materials for high-power and high-frequency applications.**

<i>Characteristic Property</i>	<i>Unit</i>	<b><i>GaN</i></b>	<i>GaAs</i>	<i>SiC-H<sub>4</sub></i>	<i>Si</i>
<i>Relative Dielectric Constant (<math>\epsilon</math>)</i>	-	<b>9.0</b>	12.8	9.7	11.8
<i>Thermal Conductivity (<math>\chi</math>)</i>	W/cm·K	<b>1.3</b>	0.5	4.9	1.5
<i>Electron Mobility (<math>\mu</math>)</i>	cm <sup>2</sup> /V·s	<b>1300</b>	6000	800	1350
<i>Maximum Velocity (<math>v_s</math>)</i>	10 <sup>7</sup> cm/s	<b>3.0</b>	2.0	2.0	1.0
<i>Breakdown Field (<math>E_B</math>)</i>	MV/cm	<b>4.0</b>	0.4	3.0	0.25
<i>Band gap (<math>E_g</math>)</i>	eV	<b>3.40</b>	1.42	3.25	1.12
<i>Relative CFOM</i>	$\epsilon\chi\mu v_s E_B^2 /$ $(\epsilon\chi\mu v_s E_B^2)_{Si}$	<b>489</b>	8	458	1

Different types of GaN based FET structures have been investigated including metal-semiconductor field effect transistors (MESFETs), metal-insulator field effect transistors (MISFETs) and modulation-doped field effect transistors (MODFETs, also known as HEMTs). A brief introduction of the first report of these devices and their most advanced version would be useful to appreciate the efforts for advancement of these technologies. We start with MESFET structures, as they are the straightforward electronic device application of GaN material, and then we will look at MISFETs, while the HEMTs will be discussed in detail in the next few sections.

Khan et al.<sup>38</sup> were among the first few investigators to fabricate GaN MESFETs grown on sapphire using low-pressure MOCVD. A thin AlN buffer layer was used to enhance the quality of the GaN films. The gate length and width for the MESFETs were 4 and 100  $\mu\text{m}$ , respectively. The reverse leakage current density at a gate bias of - 5 V was measured to be  $\sim 1 \text{ mA/cm}^2$ . For such MESFET the transconductance was 23 mS/mm at a gate bias of - 1V. The measured carrier density and low-field mobility for a channel of thickness 0.6  $\mu\text{m}$  were  $10^{17} \text{ cm}^{-3}$  and  $350 \text{ cm}^2/\text{Vs}$ , respectively. The drift velocity of the carriers estimated from these values was  $5 \times 10^6 \text{ cm}^2/\text{s}$ . Since then, far better MESFETs have been achieved due to advancement of design and processing technologies. For example, very recently Hong et al.<sup>39</sup> have reported an improved MESFET using selective area growth technique (SAG). Schematic device design as proposed in these two investigations is shown in Fig. 2.5 below.

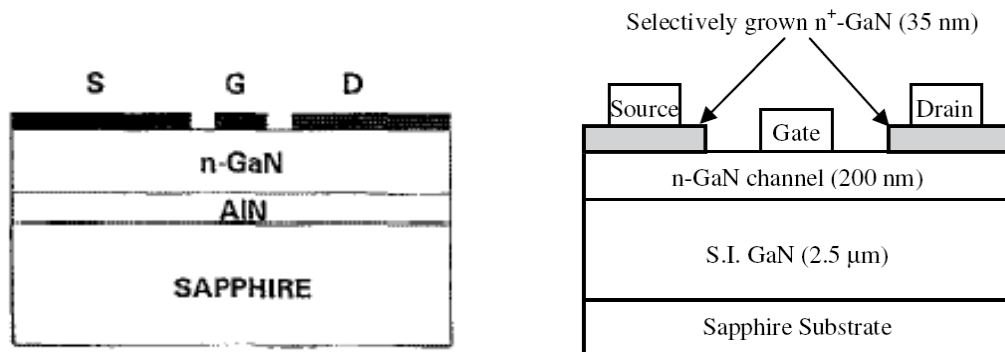


**Fig. 2.5: MESFET structures as reported in 1993 (left)<sup>38</sup>, and 2006 (right)<sup>39</sup>.**

Hong et al., used plasma-assisted molecular beam epitaxy (PAMBE), for the fabrication of a recessed-gate MESFETs. On patterned  $\text{SiO}_2$  samples, polycrystalline GaN and single crystal  $\text{n}^+$ -GaN were observed to grow in the masked and unmasked

regions, respectively. Ohmic contact formed on the  $n^+$ -GaN exhibited a vastly improved contact resistivity of  $1.8 \times 10^{-8} \Omega\text{cm}^2$ , giving rise to excellent device characteristics including a peak drain current of 360 mA/mm and a maximum transconductance of 46 mS/mm for a device with a gate length of 1  $\mu\text{m}$  and width of 100  $\mu\text{m}$ . When compared with the conventional unrecessed MESFET, the MESFET with a recessed-gate structure exhibited increased drain current, higher transconductance, and reduced surface leakage current. The Schottky diode current measured between the gate and the source under a reverse gate bias of 30 V was 51 mA/mm for the recessed-gate MESFET while that of the unrecessed MESFET was larger than 20 mA/mm.

In MESFETs, the Schottky type gates are formed directly on the GaN channel. The channel is highly doped with a tight profile as desired for a high transconductance ( $G_m$ ). While, formation of the Schottky junction often requires a lightly doped channel. As a good Schottky junction is mandatory, a compromise with the doping is done. This compromise leads to thicker and lightly doped GaN channel. As a result, the MESFETs show a low  $G_m$  (as reported in the mentioned studies<sup>38,39</sup>  $G_m = 23$ , and  $G_m = 46$  mS/mm). In addition, high series resistance is observed due to the low electron mobility in the bulk GaN channels that limit DC and RF performance of the MESFETs. The problem of low mobility can be solved by a HEMT structure which makes use of a high mobility two dimensional electron gas channel. In some applications an extremely low leakage current is desirable; however, as even base line HEMTs incorporates a similar Schottky junction, Schottky leakage is unavoidable. In that case, metal-insulator structures become the

choice of device design as applied in the MISFET structures. An added advantage of the MISFETs is the thermal stability of the gate characteristics at high temperature.

Binari et al<sup>16</sup> (1994) were among the first to report the GaN based metal-insulator-semiconductor field-effect transistors. A schematic structural cross-section of their MISFET design is shown in Fig. 2.6. For the design of these transistors, the GaN layers were grown on basal-plane sapphire substrates by MOVPE. An AlN layer, about 40 nm thick and grown at 450°C was used as buffer layer. The source-drain spacing for the MISFETs was 5  $\mu\text{m}$ . The total gate width was 150  $\mu\text{m}$  and gate lengths were 0.7 to 2.0  $\mu\text{m}$ . A PECVD grown 0.08  $\mu\text{m}$  thick SiN layer on GaN was used as gate insulator and a 0.3  $\mu\text{m}$  thick Al was deposited as gate metal. In order to minimize the substrate leakage current, 0.02  $\mu\text{m}$  thick GaN channel was confined by an AlN/GaN heterostructure. The MESFET measured gate leakage current of the device was less than 0.2  $\mu\text{A}$  over the entire range of gate and drain biases. The maximum extrinsic transconductance  $g_m$  of the MISFET was 16 mS/mm, the pinchoff voltage was - 50 V, and the maximum drain current density was 330 mA/mm. Interface traps were seen to be responsible for low values of the electrical parameters of these devices. In fact, the difficulty in obtaining high quality insulator in III-V semiconductors has prevented this device concept being implemented successfully<sup>40</sup>. Several groups have been working to improve the device design and to achieve the commercial standard MIS devices. As a result, advanced device concepts were introduced in the primary design and many successful devices have been reported in last few years. Recently (2006), a 140 W recessed gate AlGaN/GaN MISFET with field-modulating plate was reported by Nakayama<sup>41</sup> et al. The

reported device successfully incorporates an AlN layer as insulator and was fabricated using wet chemical etching technique with hot phosphoric acid. This technique improved ohmic-contact resistances for the source and drain, and provided a new and simple fabrication process for the MISFET with a 3  $\mu\text{m}$  gate length.

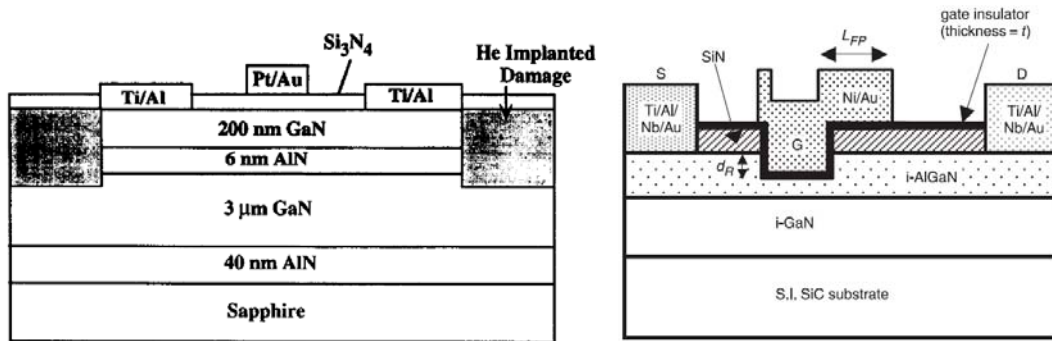


**Fig. 2.6:** (left) GaN MISFET as reported in 1994 (left)<sup>42</sup>, and in 2006 (right)<sup>43</sup>.

A maximum transconductance of 130 mS/mm and a maximum drain current of over 600 mA/mm were obtained. The recessed-gate structure with the field-modulating plate suppresses electric field concentration in the gate insulator and enables high voltage microwave power operation. At a reverse bias condition, gate Leakage current was  $10^{-9}$  A/mm and gate-drain breakdown voltage was over 200 V, which was four times higher than that of a conventional AlGaIn/GaN MISFET without a field plate.

### 2.3 Development of the GaN based HEMT Technology

In this section, a short description of the physics of HEMT device operation, and a brief review of the progress made in HEMT research is provided. As clear in the name of the device, the most important term related to HEMT is ‘mobility’ of electrons. A HEMT device is quite similar to the previously discussed GaN

transistors (MESFETs, MISFETs) in device operation, but quite different in device physics. This is because a HEMT consists of a carrier channel that is much thinner in dimension, much larger in electron density, and much faster due to high mobility of carriers. How this high mobility is achieved will be clear from the following description of 2DEG.

### **2.3.1 Heterostructure and 2DEG**

The semiconductor heterostructures are the material structures that consist of two or more semiconductor materials. The interface between such materials is called heterointerface. Heterostructures are interesting as they allow the achievement of low dimensional electronic systems which are considered extremely important because of the profound physical phenomenon involved in the properties of such low dimensional systems. Heterostructures have been employed in light emission, laser diodes, multi quantum well devices, and in high-speed transistors as well. AlGaAs/GaAs based heterostructure transistors and other similar structures like InGaAs/InP, AlGaN/GaN etc. are a few examples of such heterostructure material system among the III-V based heterostructures that have been successfully commercialized. Many important GaN based devices involve heterostructure as the primary means of achieving improved performance including the HEMT structures. For an in-depth understanding of the physical mechanisms underlying the operations of such devices, the properties of the heterostructure is needed to be extensively studied. In semiconductor heterostructures, it is the transition or interface between different semiconductors that plays an essential role in any device action, and many times the interface is the actual active device. So it is important to gain an in-depth

understanding on the electronic properties of heterostructures, especially how the carrier behaves at the heterointerface. In perspective of a device engineer's interest in heterostructures, it would be appropriate to mention the basic concept of modulation-doped heterostructures that allows very high carrier density confined in a nano scale dimension while at the same time allows high carrier mobility. In a common bulk semiconductor, one has to heavily dope the material to achieve a higher carrier concentration. However, heavier doping inevitably brings in more ionized impurity scattering and thus deteriorates the carrier mobility.

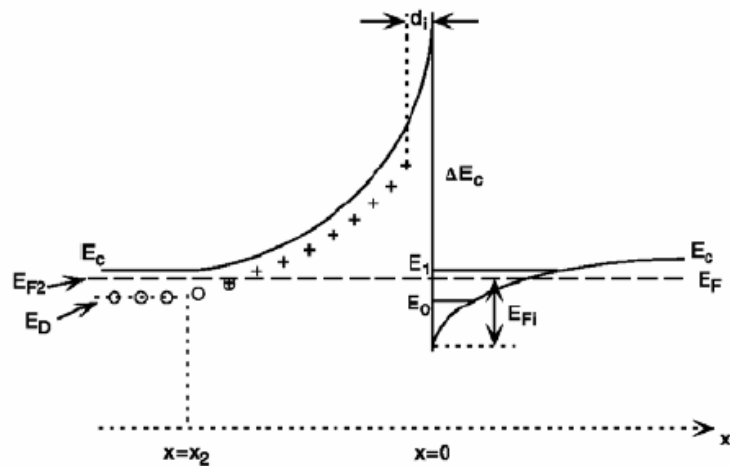


**Fig. 2.7: Modulation doped heterostructure-a schematic representation<sup>44</sup>.**

A schematic band diagram of a modulation doped heterostructure is shown in Fig. 2.7. It consists of a wide gap semiconductor and a semiconductor with narrower gap. At the interface a triangular quantum well is formed in the undoped narrow gap material. Electrons from the wider band gap material fall into this potential well and are confined within the well. Because of such quantum mechanical confinement in a very narrow dimension, they form a high density of electron gas in two dimensions.

Electrons can move freely within the plane of the heterointerface, while the motion in the direction perpendicular to the heterointerface is restricted to a well-defined space region by energy, momentum, and wave function quantization, thus forms the so-called 2DEG. As the narrow gap material is undoped and these electrons are away from the interface, the electron mobility can be simultaneously increased with high concentration of carriers. To further suppress the coulombic scattering from ionized donors, a spacer layer is sandwiched between the undoped channel layer and the doped barrier layer. This results in even higher carrier mobility.

Fruitful scientific achievements have been made, using heterostructures<sup>45</sup>. Dingle et al<sup>46</sup> proposed the n-type modulation doped semiconductor heterostructure in 1978, to simultaneously improve the carrier density and the mobility, and spatially isolate the carriers to the ionized scatters. Khan et al<sup>47</sup> reported an exciting development, formation of a 2DEG in the quantum wells at the interface of an AlGa<sub>0.09</sub>N and GaN heterostructure. Heterostructure was formed by depositing a 3000 Å thick unintentionally doped GaN on AlN buffer, capped by 500 Å undoped Al<sub>0.09</sub>Ga<sub>0.91</sub>N. The sheet carrier density in the quantum well was  $5 \times 10^{12} \text{ cm}^{-2}$ , and the carrier mobility was 620 cm<sup>2</sup>/Vs at 300 K, and 1600 cm<sup>2</sup>/Vs at 77 K.

### **2.3.2 Basic HEMT Device**

Channel formation from carrier's accumulated along a grossly asymmetric<sup>48</sup> heterojunction is a unique feature of the HEMT. Grossly asymmetric heterojunction means a junction between a heavily doped high bandgap and a lightly doped low bandgap region. Esaki<sup>49</sup> et al were the first to introduce the physics of carrier transport parallel to a heterojunction. Later, the enhanced mobility effect was

applied to demonstrate a HEMT<sup>50,51</sup> device. Electron mobility enhancement<sup>52</sup> at AlGa<sub>n</sub>/Ga<sub>n</sub> interface was first reported in 1991. This enhancement was attributed to the two-dimensional nature of the electron.

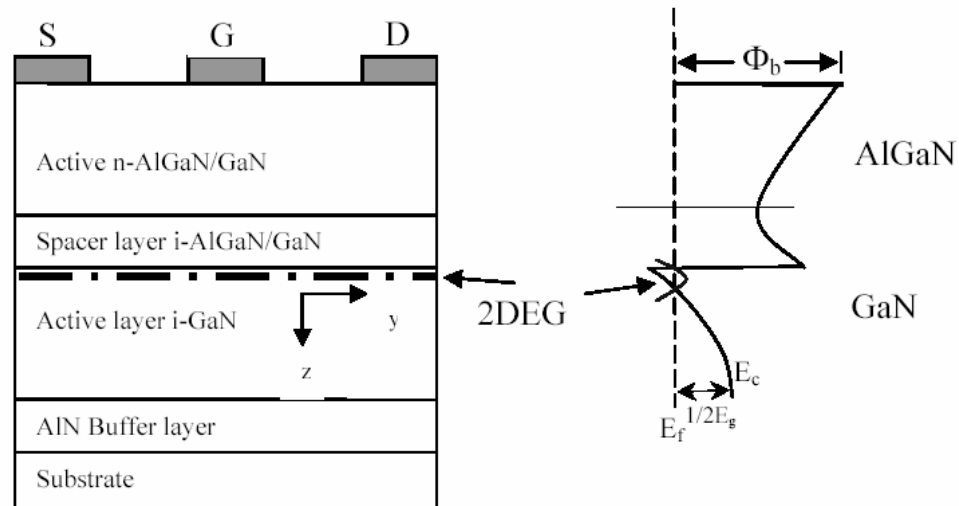


**Fig. 2.8: A Basic HEMT structure and corresponding conduction band diagram showing formation of 2DEG in the vicinity of conduction band discontinuity<sup>52</sup>.**

A typical GaN HEMT structure is shown in Fig. 2.8. This structure consists of an AlGa<sub>n</sub> barrier layer grown on Ga<sub>n</sub> channel layer. Sapphire or semi-insulating SiC substrates are the main substrates for growth of HEMT device structures. Both of these substrates are not lattice-matched to Ga<sub>n</sub>, with about 13% and 3.1% lattice mismatch respectively. To overcome this problem of lattice mismatch an AlN buffer layer is generally grown to isolate the channel layer from the substrate. With the thermal conductivity of SiC being about 10 times that of sapphire, it is evident that SiC is better suited for high-power and high-temperature applications, however sapphire being relatively cheap, remains the widely used substrate. The bandgap of

AlGaN layer is larger than that of GaN layer, so the electrons from the AlGaN diffuse into GaN and form a very thin 2DEG. The maximum electron concentration in the 2DEG layer depends on the bandgap energy difference between the barrier and the underlying buffer layer. Polarization doping effect<sup>53</sup> together with a very large bandgap offset enables the formation of a 2DEG layer even without any doping of the AlGaN barrier. In many designs, an intrinsic AlGaN spacer layer between doped AlGaN layer and intrinsic GaN layer is used to reduce the carrier scattering at the interface. Finally two different metallization are used for ohmic channel and schottky gate.

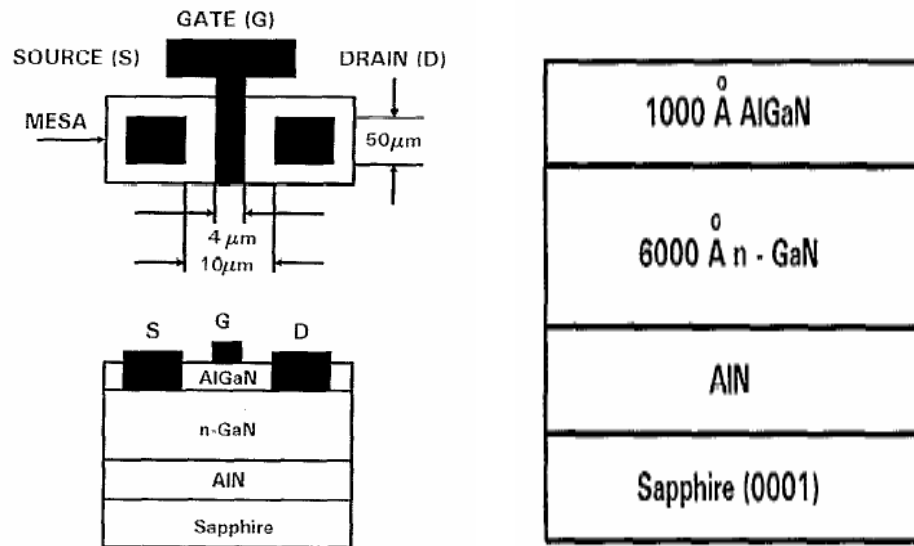


**Fig. 2.9: Plan and cross-sectional view of the 1st AlGaN/GaN HEMT (right) and the epilayer structure (left)** <sup>54</sup>.

Khan et al. were the first<sup>55</sup> to report the AlGaN/GaN HEMT in 1991. The

device design of this HEMT is shown in Fig. 2.9. For a device with a 10  $\mu\text{m}$  channel opening and a gate length and width of 4 and 50  $\mu\text{m}$  respectively, the sheet carrier density of the conduction channel of this device was  $1.15 \times 10^{13} \text{ cm}^{-2}$  at room temperature and the carrier mobility was  $563 \text{ cm}^2/\text{Vs}$ . A saturation drain current of 2 mA was observed at zero gate bias. Room-temperature transconductance of 28 mS/mm was measured at a gate voltage of 0.5 V. This increased to a value of 46 mS/mm at 77 K. Since the first demonstration of this device a continuously increasing research reports on the development of the AlGaIn/GaN HEMT technology and a number of issues involved have been reported. Present day's HEMTs are far advance than this device and the various dc and rf parameters have been much improved. In addition, several device designs as well as technology variations have been reported in literature and a few selected of them are mentioned in the following section.

### **2.3.3 Recent Advances: Gate Recessed GaN HEMTs**

Gate recessing is a technique to create recess in the vicinity of gate area. Recessing the gate area allows significant changes in device performance of GaN based HFETs<sup>56, 57</sup>. It provides an improvement in the transconductance in comparison to the conventional device<sup>58</sup>. A gate recess is also helpful to reduce source contact resistance<sup>59</sup> which is desirable for high-frequency applications. Fig. 2.10 shows a cross-sectional structure of a recessed gate HEMT device, as reported by Takashi et al<sup>60</sup> in 2003. In their device, a 2DEG mobility  $12000 \text{ cm}^2/\text{V-s}$  with a sheet carrier density of  $2.8 \times 10^{12} \text{ cm}^{-2}$  was observed at 8.9K. The recessed gate HEMT structure showed maximum extrinsic transconductance of 181 mS/mm and

drain-source current 1120 mA/mm for a gate length 1.5  $\mu\text{m}$  at 25 C with a recess depth of  $\sim 30$  nm and a recess width of  $\sim 6$  nm. The observed transconductance of this recessed device is much larger in comparison to basic HEMTs, as expected.

In a more recent study in 2005, Wang et al. have presented a study providing comparisons<sup>61</sup> between recessed and conventional AlGaN/GaN HEMTs. A schematic cross-section structure of the recessed and control devices is shown in Fig. 2.11. By using a n-GaN cap layer, the contact resistance and channel resistance was significantly reduced, increasing the RF and microwave power performance of the device. A lower knee voltage, a higher transconductance (223-mS/mm), a higher current density (1.104 A/mm), and a higher microwave output power (4-W/mm) was achieved in the recessed AlGaN-GaN HEMTs.

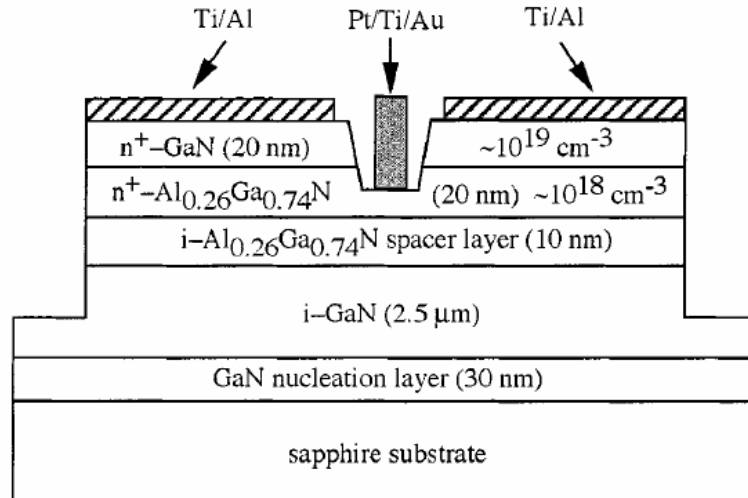


**Fig. 2.10: Cross-sectional structure<sup>62</sup> of the RIE etched recessed gate HEMT grown on sapphire by MOCVD.**

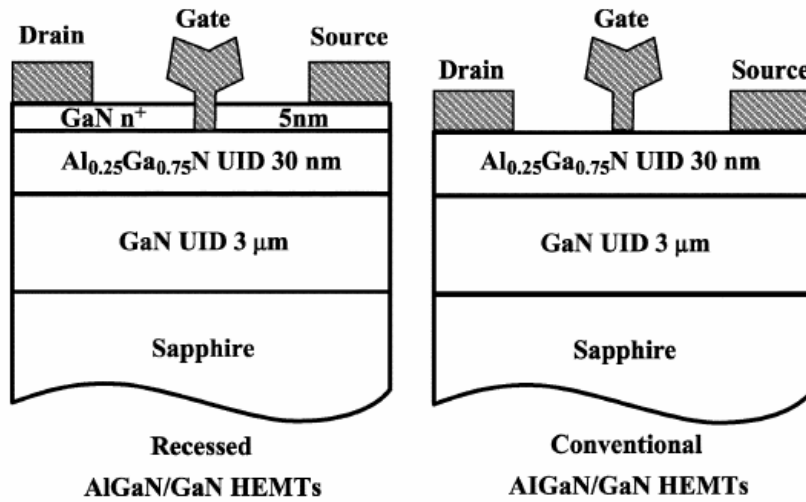
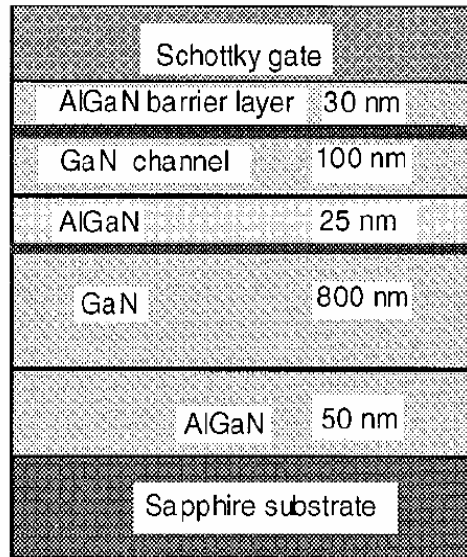


Fig. 2.11: Cross-sectional structures<sup>63</sup> of the recessed and conventional devices.

### 2.3.4 Recent Advances: Double Heterostructure FETs

Designing a device with double or multi heterostructure can, in principal, proportionally increase the device current and thus can enhance the total power output. Yoon et al. reported enhancement of carrier confinement and maximum saturation current in double<sup>64</sup> heterojunction InGaP/InGaAs HEMTs. The double heterostructure device enhanced the electron confinement in the channel by sandwiching the channel between two InGaP donor layers. The 0.35-µm DH-HEMT shows peak transconductance of 440 mS/mm, maximum current density of 500 mA/mm, and cut off frequency of 40 GHz. It was found that that DH-HEMT structures results in significant improvements in the dc characteristics when compared to the SH-HEMT, by more effective carrier confinement in the channel. In order to enhance the current drive in GaN based HEMTs, efforts were made by Gaska et al. to construct AlGaIn–GaN double-channel<sup>65</sup> HEMTs, though such efforts

have been very limited in number. A schematic diagram of their device is shown in Fig. 2.12.



**Fig. 2.12: Schematic of epilayer structure of a double channel HEMT<sup>65</sup>.**

Devices with a source-drain spacing of 5 mm a gate length of 2 mm, and a gate width of 50 mm were fabricated. Ti/Al/Ti/Au layers of thickness 25/170/50/100 nm, were used for ohmic contacts. A Pt/Au metal layer was used for the offset gate fabrication. The maximum source-drain current at zero gate bias was 0.6 A/mm, and maximum transconductance of 150 mS/mm was observed at a gate bias of 21.5 V. The maximum measured current was approximately the same as for the similar single channel devices with the same threshold voltage. The contribution to the current from the second channel was small but clearly distinguishable. The bottom channel appeared to have a large series resistance at low drain-source voltages, caused by the undoped 100 nm GaN layer and the presence of the second AlGaIn

barrier. At higher drain voltages, electron injection across the barrier drastically reduced this series resistance. It was suggested that the large series resistance for the bottom channel can be eliminated using ion implantation or selective epitaxial re-growth, and by optimizing the thickness of the various layers.

## **2.4 Challenges: Reliability and Performance Issues**

### **2.4.1 General Understanding**

GaN-based HEMTs manifest a number of deficiencies in their operation and the potential of nitride based HFETs has not been fully realized as yet. A very latest and one of the most accredited<sup>66</sup> developments is reported recently by Fujitsu Corporation. They have shown highly efficient push-pull amplifiers delivering 250 wideband code division multiple access (W-CDMA) signals based on these GaN HEMTs. Their devices are efficient and capable to produce high output powers, and can work at higher cut-off frequencies than other semiconductor materials. It is said that device degradation still remains the biggest obstacle to their commercialization. There are several general issues and challenges yet to be addressed in this field. Those challenges include current collapse, current and power degradation after RF stress, threshold voltage shift, reliability, necessary reproducibility, and the low cost. Although little has been reported on the reliability of AlGaN/GaN HEMTs, various related concerns such as the discrepancy between DC predicted and RF measured power have been discussed<sup>67,68</sup> in literature. Various solutions have been suggested to suppress these problems that include passivation, improved device design, barrier thickness control, gate dielectric, as well as field plate technology.

Most of the reliability and degradation problems affiliated to GaN HEMTs are often associated with the surface defects and hot electrons. Surface trapping-detrapping of electrons at surface states has been suggested as a possible mechanism responsible for some of the observed degradation effects. Trapping can compensate part of the surface component of spontaneous polarization and reduce the 2DEG electron concentration. The effects resemble those produced by a virtual gate<sup>69</sup> between the actual gate and the drain. One explanation of RF current slump is the reduction of compressive strain<sup>70</sup> of GaN under the gate and tensile strain of ungated AlGaIn upon negative bias application. Transconductance and output resistance dispersion are also providing means of evaluating the performance limitations.

#### **2.4.2 Mechanisms**

Earlier failure mechanisms<sup>71,72</sup> studies in AlGaAs/GaAs HEMTs shows evidences of gate sinking, ohmic contact degradation, and trapped charge formation near the 2DEG. Failure mechanisms of pseudomorphic HEMT's have been investigated by means of storage tests and hot-electron tests. Hot-electron effects can be related to trap-assisted phenomena that belong to two major categories: (1) modulation of the charge trapped under the gate either thermally-assisted or due to holes generated by impact-ionization leading to recoverable shifts of the threshold voltage. (2) generation of additional electrons traps in the AlGaAs layers under the gate, originating a permanent change in the output characteristics. It was observed that the drain resistance<sup>73</sup> increases faster than the source resistance due to hot carrier degradation. Surface passivation with SiN<sub>x</sub> has been reported to partly cure most of the surface state related problems<sup>74</sup>. Role of hot carriers<sup>75</sup> was held

responsible for the shift in the pinch-off voltage of AlGaN/GaN MODFETs. It was also suggested that keeping the Al mole-fraction to lower values<sup>76</sup> using a thicker barrier layer might be a remedy for this degradation. A long-term stability study conducted on sub-100nm gate-length metamorphic HEMTs revealed that the positive threshold voltage shift is caused by gate sinking. The source and a part of the drain resistance increase are caused by ohmic contact degradation<sup>77</sup>. In the long-term stability study of metamorphic HEMTs with gate lengths of 50 nm, main failure mechanisms<sup>78</sup> are caused by gate sinking, ohmic contact degradation and hot carrier induced degradation.

### **2.4.3 Noise Based Degradation Studies**

Accelerated aging tests are a traditional technique for the degradation study of electronic devices. Microwave and dc characterizations are normally employed ways to monitor changes in device performance. As the accelerated aging tests are performed at extreme temperature and stress conditions, test-results not necessarily represent the actual operational behavior of the device. Also, these tests usually enhance the failure mechanisms. A promising technique for monitoring the reliability characteristics is the evaluation of LFN of the device. It is a nondestructive and less-expensive measurement technique which is very sensitive and effective for materials and device characterization. LFN measurements are performed at normal operating conditions of electronic devices. LFN characterization gives more realistic information and has been extensively used as a diagnostic<sup>79,80</sup> tool for quality and reliability studies in semiconductor devices.

Several theories have been presented to explain the origin of  $1/f$  low-frequency noise in semiconductors. Most popular ones are based on mobility<sup>81</sup> fluctuation, and number<sup>82</sup> fluctuation of carriers. The number fluctuation theory<sup>83</sup>, relates the  $1/f$  noise behavior to trap density and band-tail states within the channel or in the barrier layer of the heterostructure. A correlation between the material quality and the  $1/f$ -noise characteristics allows evaluation of oxide trap density<sup>84</sup> in MOSFET devices and identification of the trap levels within the bandgap of semiconductor. Bias-dependent variations in the magnitude and frequency exponent of  $1/f$  noise characteristics allows to assess and understand the device characteristics such as: Schottky barrier height variations<sup>85,86</sup>, ohmic quality<sup>87</sup>, electromigration, and hot-carrier effects<sup>88</sup>.

A vast body of low-frequency noise studies on III-Nitride materials and devices is available in literature. In case of studies conducted with AlGaIn/GaN based FETs, there is considerable discrepancy between the reported noise levels<sup>89,90</sup>. Hooge parameter, which is considered to be a noise figure-of-merit, shows a large variation<sup>91,92</sup> in the range of  $10^{-5}$  to  $10^{-2}$ . Trapping of carriers and hot-electron effect were characterized by Sozza<sup>93</sup> et al. by means of low-frequency noise techniques. Degradation observed in AlGaIn/GaN HEMTs under on-state and off-state conditions includes decrease of the drain current and transconductance, and increase of the channel resistance. The on-state stress showed the most important degradation and ascribed to the effect of hot electrons. Valizadeh<sup>94</sup> et al. investigated the impact of surface passivation, barrier Al composition and heterointerface quality on the low-frequency noise characteristics of AlGaIn/GaN HFETs. It was found that the

drain noise current characteristics are independent of Al composition. The surface treatment of the devices with same heterointerface roughness was found to influence the noise characteristics. These observations suggested the possibility of conducting low-frequency noise studies for investigating the quality of the heterointerface. Pavlidis et al. found that a highly sensitive gate noise current is incapable to predict the gate failure under RF stress, and drain noise current values of the fresh devices in the linear operation regime for both passivated and unpassivated device categories demonstrate signatures<sup>95</sup> for degradation prediction. These properties make the degradation prediction possible independent of the requirement for those alternative methods that are expensive, destructive, and time consuming.

## **2.5 Applications of Heterostructures Beyond HEMTs**

GaN based heterostructures are most often referred in context of their application in high-power high-frequency communication. In addition to their analog transistor application, digital<sup>96,97</sup> applications have also been explored. Merits such as: (i) exceptional mechanical, chemical, and thermal stability, and (ii) excellent electronic properties, make the GaN eligible to be a prime candidate for a variety of applications. Application of heterostructures is not limited in HEMT transistors anymore and a number of other applications are being investigated. Solar blind UV detectors<sup>98,99</sup> have been reported exploiting the wide bandgap of GaN. The HEMT structures with catalytic gates have turned out to respond<sup>100</sup> to a large variety of gases. Their robust chemical properties have been utilized in high temperature gas sensors<sup>101</sup>. Passive surface acoustic wave (SAW) devices<sup>102</sup> have also been reported by authors. Chemical inertness of GaN surface and its ion sensitivity have been

utilized for ion sensing in ISFET structures<sup>103</sup>. Additional novel features like piezoelectricity and pyroelectricity<sup>104</sup> make them a unique candidate for multifunctional and versatile applications. Stress dependence of the Schottky barrier heights on *n*-GaN and *n*-AlGaN<sup>105, 106</sup>, and effect of pressure<sup>107</sup> on the dc characteristics of AlGaN/GaN HFET have been reported. Effect of hydrostatic pressure<sup>108</sup> has been demonstrated that can be exploited for liquid pressure sensing as well as in strain sensing applications. Most of such device concepts are based on *modulation of the carrier density in 2DEG*. The device designs essentially incorporate a basic HEMT structure with additional modifications. Most often, the modifications are introduced in the gate area. A number of device designs using heterostructures are possible. A typical design<sup>109</sup> is shown in Fig. 2.13. Most of the required designs can be derived from this basic structure, as per the specific requirement of a particular application.

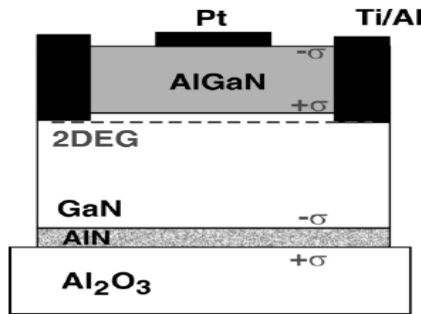


**Fig. 2.13: Schematic diagram of a basic AlGaN/GaN heterostructure employed for sensor applications<sup>110</sup>.**

The sensor function of such structures is determined by the complex response of the 2DEG to electrostatic boundary conditions of the free surface above

it. Any such device is designed to work in a specific environment that contains ions, polar liquids, gasses, or pressure etc. When it is exposed to such external environment, the electrostatic boundary condition at the surface is changed. This could be due to adsorbed ions, screening by polar liquids, decomposition of gases by catalytic Schottky contacts, or changes of polarization-induced interface charges by piezoelectric/pyroelectric coupling to elastic deformations. A change in the electrostatic boundary condition at the surface modulates the response of the 2DEG and results in the modulation of the device current. There is an attractive feature of employing a common device structure using the same material system. That is, several functions can be *integrated* with existing electronic or optoelectronic devices, micromechanical systems, or contact-less readout schemes on the same chip. Such integration facilitates complex applications at cheaper cost.

A particular application of GaN is in biosensors, which is rarely explored to date. Signal transfer in cells and tissue models have been analyzed with the help of semiconductor electronics coupled to bio-organic molecular assemblies. Hydrophilic SiO<sub>2</sub> surfaces, acting as gate material, with capacitive coupling to living cells have been reported<sup>111</sup>. But, the operation of Si based devices in aqueous solution suffers from various difficulties such as: chemical instability and degradation of gate insulator. Short term stability due to oxidation and subsequent hydratization limits the areas of application<sup>112</sup>. Alternatively, metal oxide gate layers make stable device operation possible and exhibit a significantly higher sensitivity<sup>113</sup> towards the detection; however, it also increases complexity in device fabrication. GaN based heterostructure can be a good solution to these problems, as they have already been

demonstrated to show good response in ISFET applications, as mentioned above. It has been expected that due to chemical stability, cell friendly surface, and high current density, GaN heterostructure could be a good candidate for biosensor applications<sup>114</sup>.

## REFERENCES (CHAPTER 2)

---

- <sup>1</sup> “SIA Roadmap,” 2006, [http://www.sia-online.org/iss\\_technology.cfm](http://www.sia-online.org/iss_technology.cfm).
- <sup>2</sup> “Technology Roadmap for Nanoelectronics” Editors: R. Compañó, L. Molenkamp, D.J. Paul. European Commission IST Program; ‘Future and Emerging Technologies’, *Microelectronics Advanced Research Initiative MELARI NANO*.
- <sup>3</sup> R. A. Soref, “Silicon based optoelectronics,” *Proc. IEEE*, Vol. 81, p. 1687, 1993.
- <sup>4</sup> *Transactions of the First International High Temperature Electronics Conference*. June 10-20, Albuquerque, New Mexico, U.S.A. 1991.
- <sup>5</sup> H. Morkoc, S. Ste, G. Gao, M. Lin, B. Sverdlov and M. Burns, *J. Appl. Phys. Rev.* Vol. 76, p. 1363, 1994.
- <sup>6</sup> D. Zook and B. Goldenberg. In *Proceedings of International Conference on Silicon Carbide and Related Materials*. Washineton. DC. U.S.A. 1993.
- <sup>7</sup> A. V. Nurmikko and R. L. Gunshor, *IEEE J. Quantum Electron.*, Vol. 30, p. 619, 1994.
- <sup>8</sup> S. Nakamura, *Technical Digest of the IEEE Electron Devices Meeting*, San Fransisco, CA, U.S.A. Vol. 14, p. 567, 1994.
- <sup>9</sup> D. Eason, Z. Yu, W. Hughes, W. Roland, C. Boney, J. Cook, J. Schetzina, G. Cantwell and W. Harsh, *Appl. Phys. Lett.*, Vol. 65, p. 115, 1995.
- <sup>10</sup> M. G. Crawford, *IEEE Circuits and Devices Mag.*, Vol. 8, p. 24, 1992.
- <sup>11</sup> H. Morkoc and S. N. Mohammad, *Science*, Vol. 267, p. 51, 1995
- <sup>12</sup> S. Rumyantsev, M. Shur and M. Levinshtein, “Material Properties of Nitrides”, *Int. Journ. of High Speed Electronics and systems*, Vol. 14, p. 1, 2004.
- <sup>13</sup> B. Goldenberg, J. Zook and R. Ulmer, “Fabrication and performance of GaN detectors,” *Topical Workshop on III-V Nitrides Proc.*, Nagoya, Japan, 1995.
- <sup>14</sup> S. Mohammad and H. Morkoc, *J. Appl. Phys.*, Vol. 78, p. 4200, 1995.
- <sup>15</sup> C. Mazier and M. Lundstrom, *IEEE Electron Devices Lett.*, Vol. 8, p. 90, 1987.

- 
- <sup>16</sup> S. Binari, L. Rowland, G. Kelner, W. Kruppa, H. Dietrich, K. Doverspike and D. K. Gaskill, *21<sup>st</sup> Int. Symp. Compound Semicond. Proc.*, 1994.
- <sup>17</sup> B. Maikusiak, *IEEE Trans. Electron Devices*, Vol. 37, p. 1087, 1990.
- <sup>18</sup> M. S. Shur, "GaAs Devices and Circuits," Plenum Press, New York, 1987, p. 521.
- <sup>19</sup> A. Khan, J. Meese, T. Stacy, E. Charlson, E. Charlson, G. Zhao, G. Popovici and M. Prelus, in "Diamond, SIC, and Nitride Wide Bandgap Semiconductors," Edt. C. H. Carter, G. Goldenblat, S. Nakamura and R. Nemanich, *Materials Research Soc.*, Pittsburgh, PA, 1994.
- <sup>20</sup> M. Khan, J. Kuznia, J. Van Hove, N. Pan and J. Carter, *Appl. Phys. Lett.*, Vol. 60, p. 3027, 1992.
- <sup>21</sup> S. Nakamura, T. Mukai, M. Seno and N. Isawa, *Jpn. J. Appl. Phys.* Vol. 30, p. 1708, 1991.
- <sup>22</sup> M. Khan, M. Shur, Q. Chen and J. Kuznia, *Electron. Lett.*, Vol. 30, p. 2175, 1994.
- <sup>23</sup> T. Zheleva, S. Smith, D. Thomson, K. Linthicum, P. Rajagopal, R. Davis, J. *Electron. Mater.*, Vol. 28, p. 5, 1999.
- <sup>24</sup> B. Beaumont, P. Vennegures, P. Gibart, *Phys. Stat. Sol. (b)*, Vol. 227, p. 1, 2001.
- <sup>25</sup> H. Amano, M. Iwaya, T. Kashima, M. Katsuragawa, I. Akasaki, J. Han, S. Hearne, J. Floro, E. Chason, J. Figiel, *Jpn. J. Appl. Phys.*, Vol. 37, p. 1540, 1998.
- <sup>26</sup> C. Ashby, C. Mitchell, J. Han, N. Missert, P. Provencio, D. Follstaedt, G. Peake, L. Griego, *Appl. Phys. Lett.*, Vol. 77, p. 3233, 2000.
- <sup>27</sup> T. Hisashi, I. Tomoyuki, M. Yuriko, K. Yoshihiro, K. Yoshinao, K. Akinori, "Growth of GaN directly on Si(111) substrate by controlling atomic configuration of Si surface by metalorganic vapor phase epitaxy," *Japanese Journal of Applied Physics, Part 2: Letters.*, Vol. 45, p. 478, 2006.
- <sup>28</sup> W. Yuen, Z. Li, L. Ming, L. Mao, "Epitaxial growth of high-quality GaN on appropriately nitridated Si substrate by metal organic chemical vapor deposition," *Journal of Crystal Growth.*, Vol. 280, p. 335, 2005.

- 
- <sup>29</sup> M. Yoshihiro, T Rie, K. Koichi, K. Akinori, "Influence of hydrogen coverage on Si(1 1 1) substrate on the growth of GaN buffer layer," *Journal of Crystal Growth*, Vol. 300, p. 66, 2007.
- <sup>30</sup> P. Waltereit, O. Brandt, M. Ramsteiner, A. Trampert, H. Grahn, J. Menniger, M. Reiche, R. Uecker, P. Reiche, K. Ploog, *Phys. Stat. Sol. (a)*, Vol. 180, p. 133, 2000.
- <sup>31</sup> B. Ferguson and C. Mullins, "Supersonic Jet Epitaxy of III-nitride semiconductors," *Journal of Crystal Growth*, Vol. 178, p. 134, 1997.
- <sup>32</sup> L. Liu and J.H. Edgar, "Substrates for gallium nitride epitaxy," *Materials Science and Engineering R*, Vol. 37, p. 61, 2002.
- <sup>33</sup> O Ambacher, "growth and application of group III nitrides," *J. Phys. D: Appl. Phys.*, Vol. 31, p. 2653, 1998.
- <sup>34</sup> J. Edgar, "Common crystal structure of group III Nitrides," *Inspec*, 1994, p. 3.
- <sup>35</sup> J. Pankove, S. Chang, H. Lee, R. Molnar, T. Moustakas, V. Zeghbroeck, *IEDM Tech. Dig.*, p. 389, 1994.
- <sup>36</sup> Ric Borges, "GaN Devices for High Power Wireless applications," *RF Semiconductors*, p. 72, 2001. <http://images.rfdesign.com/files/4/0901Borges72.pdf>.
- <sup>37</sup> J. Zolper, *Solid-State Electron.*, Vol. 42, p. 2153, 1998.
- <sup>38</sup> M. Khan, J. Kuznia, A. Bhattarai and D. Olson, *Appl. Phys. Lett.*, Vol. 62, p. 1786, 1993.
- <sup>39</sup> S. Hong, P. Chapman, P. Krein, and K. Kim, *phys. stat. sol. (a)*, Vol. 203, p. 1872, 2006.
- <sup>40</sup> Q. Chen, J. Yang, M. Blasingame, C. Faber, A. Ping and I. Adesida, "Microwave electronics device applications of AlGaIn/GaN heterostructures," *Materials Science and Engineering B*, Vol. 59, p. 395, 1999.
- <sup>41</sup> T Nakayama, Y. Ando, Y. Okamoto, T. Inoue, H. Miyamoto, "CW 140 W Recessed gate, AlGaIn/GaN MISFET with Field Modulating plate," *Electronics Letters*, Vol 42, p. 489, 2006.

- 
- <sup>42</sup> Q. Chen, J. Yang, M. Blasingame, C. Faber, A. Ping and I. Adesida, "Microwave electronics device applications of AlGa<sub>N</sub>/Ga<sub>N</sub> heterostructures," *Materials Science and Engineering B*, Vol. 59, p. 395, 1999.
- <sup>43</sup> T Nakayama, Y. Ando, Y. Okamoto, T. Inoue, H. Miyamoto, "CW 140 W Recessed gate, AlGa<sub>N</sub>/Ga<sub>N</sub> MISFET with Field Modulating plate," *Electronics Letters*, Vol 42, p. 489, 2006.
- <sup>44</sup> H. Morkoç, A. Carlo, and R. Cingolani, *Solid. State. Electron.*, Vol. 46, p. 157, 2002.
- <sup>45</sup> G. Bauer, F. Kuchar, and H. Heinrich, "Two-dimensional systems, Heterostructures, and Superlattices," Springer-Verlag, 1984.
- <sup>46</sup> R. Dingle, H. Störmer, A. Gossard, and W. Wiegmann, *Appl. Phys. Lett.*, Vol. 33, p. 665, 1978.
- <sup>47</sup> M. Khan, J. Kuznia, J. Hove, N. Pan, and J. Carter, *Appl. Phys. Lett.*, Vol. 60, p. 3027, 1992.
- <sup>48</sup> S. Karmalkar, *IEEE Trans. Electron Devices*, Vol. 45, p. 2187, 1998.
- <sup>49</sup> L. Esaki and R. Tsu, *IBM Research Note*, RC 2418, 1969.
- <sup>50</sup> T Mimura et al., *Jap. Appl Phys.*, Vol. 19, p. L225, 1980.
- <sup>51</sup> D Delagebeaudeuf et al., *Eelectron Lett.*, Vol. 16, p. 667, 1980.
- <sup>52</sup> M. A. Khan et al., *Appl. Phys. Lett.*, Vol. 58, p. 2408, 1991.
- <sup>53</sup> M. Khan, J. Yang, G. Simin, R. Gaska, M. Shur, A. Bykhovsky, "Piezoelectric Doping in AlInGa<sub>N</sub>/Ga<sub>N</sub> Heterostructures," *Appl. Phys. Lett.*, Vol. 75, p. 2806, 1999.
- <sup>54</sup> M. Khan, A. Bhattarai, J. Kuznia, and D. Olson, "High electron mobility transistor based on a Ga<sub>N</sub>-Al<sub>x</sub>Ga<sub>1-x</sub>N heterojunction ", *Applied Physics Letters*, Vol. 63, p. 1214, 1993.
- <sup>55</sup> M. Khan, A. Bhattarai, J. Kuznia, and D. Olson, "High electron mobility transistor based on a Ga<sub>N</sub>-Al<sub>x</sub>Ga<sub>1-x</sub>N heterojunction ", *Applied Physics Letters*, Vol. 63, p.

---

1214, 1993.

<sup>56</sup> T. Egawa, H. Ishikawa, M. Umeno and T. Jimbo, "Recessed gate AlGa<sub>N</sub>/Ga<sub>N</sub> MODFET on sapphire," *Appl. Phys. Lett.*, Vol. 76, p. 121, 1999.

<sup>57</sup> S. Binari, K. Doverspike, G. Kelner, H. Dietrich and A. Wickenden, *Solid State Electron.*, Vol. 41, p. 177, 1997.

<sup>58</sup> F. Stengel, S. Mohammad, and H. Morkoç, "Theoretical investigation of electrical characteristics of Ga<sub>N</sub>/AlGa<sub>N</sub> modulation doped field-effect transistors," *J. Appl. Phys.*, Vol. 80, p. 3031, 1996.

<sup>59</sup> T. Mizutani, Y. Ohno, M. Akita, S. Kishimoto and K. Maezawa. "Current collapse in AlGa<sub>N</sub>/Ga<sub>N</sub> HEMTs Investigated by Electrical and Optical Characterizations," *Phys. Stat. sol. (a)*, Vol. 194, p. 447, 2002.

<sup>60</sup> T. Egawa et al., "Characterizations of Recessed Gate AlGa<sub>N</sub>/Ga<sub>N</sub> HEMTs on Sapphire," *IEEE Trans. Electron Devices*, Vol. 48, p. 3, 2001.

<sup>61</sup> Wang et al., "Performance Enhancement by Using the n<sup>+</sup>-Ga<sub>N</sub> Cap Layer and Gate Recess Technology on the AlGa<sub>N</sub>-Ga<sub>N</sub> HEMT Fabrication," *IEEE Electron. Dev. Lett.*, Vol. 26, p5, 2005.

<sup>62</sup> T. Egawa et al., "Characterizations of Recessed Gate AlGa<sub>N</sub>/Ga<sub>N</sub> HEMTs on Sapphire," *IEEE Trans. Electron Devices*, Vol. 48, p. 3, 2001.

<sup>63</sup> Wang et al., "Performance Enhancement by Using the n<sup>+</sup>-Ga<sub>N</sub> Cap Layer and Gate Recess Technology on the AlGa<sub>N</sub>-Ga<sub>N</sub> HEMT Fabrication," *IEEE Electron. Dev. Lett.*, Vol. 26, p5, 2005.

<sup>64</sup> S. Yoon et al., "Fabrication of Strained and Double Heterojunction In Ga P/In Ga As High Electron Mobility Transistors Grown by Solid-Source Molecular Beam Epitaxy," *IEEE Trans. Electron Devices*, Vol. 47, p. 5, 2000.

<sup>65</sup> R. Gaska, M. S. Shur, T. A. Fjeldly, and A. D. Bykhovski, "Two-channel AlGa<sub>N</sub>-Ga<sub>N</sub> heterostructure field-effect transistors for high-power applications," *J. Appl. Phys.*, Vol. 85, p. 3009, 1999.

- 
- <sup>66</sup> T. Kikkawa, "Recent Progress of Highly Reliable GaN-HEMT for Mass Production," *CS MANTECH Conference*, April 24-27, Vancouver, British Columbia, Canada, 2006.
- <sup>67</sup> S. Hsu et al., "Impact of RF Stress on Dispersion and Power Characteristics of AlGaIn/GaN HEMTs" *IEEE GaAs IC Symposium*, Monterey, CA, USA, October 2002, p. 85.
- <sup>68</sup> K. S. Boutros et al., "A Study of Output Power Stability of GaN HEMTs on SiC Substrates", *Proc. IEEE Int. Reliability Physics Symp.*, Phoenix, AZ, 2004, p. 577.
- <sup>69</sup> R. Ventury et al., "The Impact of Surface States on the DC and RF Characterization of AlGaIn/GaN HFETs.," *IEEE Trans. on Elect. Dev.*, p. 560, 2001.
- <sup>70</sup> G. Simin et al., "Induced Strain Mechanism of Current Collapse in AlGaIn/GaN Heterostructure Field Effect Transistor", *Appl. Phys. Lett.*, Vol. 79, p. 2651, 2001.
- <sup>71</sup> K. Christianson et al., "Failure Mechanisms in AlGaAs/GaAs HEMTs," *Solid-Slate Electronics*, Vol. 38, p. 1623, 1995.
- <sup>72</sup> G. Meneghesso, "Failure Mechanisms of AlGaAs/InGaAs Pseudomorphic HEMT's: Effects Due to Hot Electrons and Modulation of Trapped Charge," *Microelectron. Reliab.*, Vol. 37, p. 1121, 1997.
- <sup>73</sup> Fukai, Y.K., et al., "Bias Acceleration Model of Drain Resistance Degradation in InP-based HEMTs," *IEEE Int. Reliability Physics Symp. Proc.*, 2003, p. 324.
- <sup>74</sup> R. Vetury, N. Zhang, S. Keller, and U. K. Mishra, "The impact of surface states on the dc and RF characterization of AlGaIn/GaN HFETS," *IEEE Trans. Electron Devices*, Vol. 48, p. 560, 2001.
- <sup>75</sup> P. Valizadeh et al., "Investigation of the Impact of Al Mole-Fraction on the Consequences of RF Stress on Al<sub>x</sub>Ga<sub>1-x</sub>/GaN MODFETs," *IEEE Trans. Electron Devices*, Vol. 52, p. 1933, 2005.
- <sup>76</sup> P. Valizadeh et al., "Effects of RF and DC Stress on AlGaIn/GaN MODFETs: A Low-frequency Noise Based Investigation," *IEEE Transactions on Device and Materials Reliability*, Vol. 5, p. 555, 2005.

- 
- <sup>77</sup> M. Dammann et al., "Reliability of 70 nm metamorphic HEMTs'," *Microelectron. Reliab.*, Vol. 44, p. 939, 2004.
- <sup>78</sup> M. Dammann et al., "Reliability of 50nm low-noise metamorphic HEMTs and LNAs," *Electronics Letters*, Vol. 41, p. 699, 2005.
- <sup>79</sup> L. Vandamme, "Noise as a diagnostic tool for quality and reliability of electronic devices," *IEEE Trans. Electron Devices.*, Vol. 41, p. 2176, 1994.
- <sup>80</sup> J. Peransin, P. Vignaud, D. Rigaud, L. Vandamme, "1/f noise in MODFET\_s at low drain biases," *IEEE Trans. Electron Devices*, Vol. 37, p. 2250, 1990.
- <sup>81</sup> F. Hooge and L. Vandamme, "On the origin of 1/f noise," *Inst. Phys. Conf. Ser.*, Vol. 43, p. 565, 1979.
- <sup>82</sup> A. McWhorter, "1/f noise and germanium surface properties," *Conf. Phys. Semicond. Surf.*, 1956, p. 207.
- <sup>83</sup> D Yakonova, M Levinshtein, and S Rumyantsev, "Nature of the bulk 1/f noise in GaAs and Si ," *Sov. Phys. Semicond.*, Vol. 25, p. 1241, 1991.
- <sup>84</sup> R. Jayaraman and C. Sodini, "A 1/f noise technique to extract the oxide trap density near the conduction band edge of silicon," *IEEE Trans. Electron Devices*, Vol. 36, p. 1773, 1989.
- <sup>85</sup> L. Vandamme, D. Rigaud, J. Peransin, R. Alabedra, and J. Dumas, "Gate current 1/f noise in GaAs MESFETs," *IEEE Trans. Electron Devices*, Vol. 35, p. 1071, 1988.
- <sup>86</sup> H. Meer, M. Valenza, K. van der Zanden, W. De Raedt, E. Simoen, D. Schreurs, and L. Kaufmann, "Effect of Schottky barrier alternation on the low-frequency noise of InP-based HEMT's," *IEEE Electron Device Lett.*, Vol. 19, p. 370, 1998.
- <sup>87</sup> D. Kuksenkov, H. Temkin, R. Gaska, and J. W. Yang, "Low-frequency noise in AlGaIn/GaN heterostructure field effect transistors," *IEEE Electron Device Lett.*, Vol. 19, p. 222, 1998.
- <sup>88</sup> O. Marinov, "The low-frequency noise in HFETs estimates the effect of electrical stress," *Microelectron. Reliab.*, Vol. 40, p. 1959, 2000.

- 
- <sup>89</sup> D. Yakonova, M. Levinshtein, S. Contreras, W. Knap, B. Beaumont, P. Gibart, “Low-frequency noise in n-GaN,” *Semiconductors*, Vol. 32, p. 257, 1998.
- <sup>90</sup> A. Vertiatchikh and L. Eastman, “Effects of the surface and barrier defects on AlGa<sub>N</sub>/Ga<sub>N</sub> HEMT low-frequency noise performance.” *IEEE Electron Dev Lett.*, Vol. 24, p. 535, 2003.
- <sup>91</sup> S. Rumyantsev, N. Pala, M. Shur, R. Gaska, M. Levinshte, M. Khan, “Low-frequency noise in Ga<sub>N</sub> metal semiconductor and metal oxide semiconductor field effect transistors,” *J. Appl. Phys.*, Vol. 90, p. 310, 2001.
- <sup>92</sup> A. Balandin, S. Cai, R Li, K. Wang, R. Ramgopal, C. Viswanathan, “Flicker noise in Ga<sub>N</sub>/Al<sub>0.15</sub>Ga<sub>0.85</sub>N doped channel heterostructure field effect transistors,” *IEEE Electron Dev. Lett.*, Vol. 19, p. 475, 1998.
- <sup>93</sup> A. Sozza et al., “Evidence of Traps Creation in Ga<sub>N</sub>/AlGa<sub>N</sub>/Ga<sub>N</sub> HEMTs After a 3000 Hour On-state and Off-state Hot-electron Stress,” *IEDM Technical Digest*, DOI:10.1109/IEDM.2005.1609416.
- <sup>94</sup> P. Valizadeh, “Low-frequency noise of AlGa<sub>N</sub>/Ga<sub>N</sub> MODFETs: A comparative study of surface, barrier and heterointerface effects,” *Solid-State Electronics*, Vol. 49, p. 1352, 2005.
- <sup>95</sup> D. Pavlidis et al., “AlGa<sub>N</sub>/Ga<sub>N</sub> HEMT reliability,” 13<sup>th</sup> GAAS Symposium, Paris 2005.
- <sup>96</sup> R. Gaska, J. Deng and M.S. Shur, “Low-threshold AlGa<sub>N</sub>-Ga<sub>N</sub> heterostructure field effect transistors for digital applications,” *Electronics Letters*, Vol. 34, p. 2367, 1998.
- <sup>97</sup> A Khan et al. “Enhancement and depletion mode Ga<sub>N</sub>/AlGa<sub>N</sub> heterostructure field effect transistors,” *Appl. Phys. Lett.*, Vol. 68, p. 514, 1996.
- <sup>98</sup> H. Looi, M. Whitfield, R. Jackman, *Appl. Phys. Lett.*, Vol. 74, p. 3332, 1999.
- <sup>99</sup> M. Razeghi, A. Rogalski, *J. Appl. Phys.*, Vol. 79, p. 7433, 1996.

- 
- <sup>100</sup> J. Schalwig, G. Muller, O. Ambacher, M. Stutzmann, *Phys. Stat. Sol. (a)*, Vol. 185 p. 39, 2001.
- <sup>101</sup> A. Lloyd-Spez, A. Baranzahi, P. Tobias, I. Lundstro'm, *Phys. Stat. Sol. (a)*, Vol. 162, p. 493, 1997.
- <sup>102</sup> C. Deger et al., *Appl. Phys. Lett.*, Vol. 72, p. 2400, 1998.
- <sup>103</sup> R. Neuberger, G. Mu'ller, O. Ambacher, M. Stutzmann, *phys. stat. sol. (a)*, Vol. 183, p R10, 2001.
- <sup>104</sup> M. Eickhoff et al., "Electronics and sensors based on pyroelectric AlGaIn/GaN heterostructures," *phys. stat. sol. (c)*, Vol. 0, p. 1908, 2003.
- <sup>105</sup> Y. Liu, M. Kauser, M. Nathan, P. Ruden, S. Dogan, H. Morkoç, S. Park, and K. Lee, *Appl. Phys. Lett.*, Vol. 84, p. 2112, 2004.
- <sup>106</sup> Y. Liu, M. Kauser, P. Ruden, Z. Hassan, Y. Lee, S. Ng, and F. Yam, *Appl. Phys. Lett.*, Vol. 88, p. 022109, 2006.
- <sup>107</sup> Y. Liu, P. Ruden, J. Xie, H. Morkoç, and K. Son, *Appl. Phys. Lett.*, Vol. 88, p. 013505, 2006.
- <sup>108</sup> Y Liu et al., "Effect of hydrostatic pressure on the current-voltage characteristics of GaN/AlGaIn/GaN heterostructure devices," *J. Appl. Phys.*, Vol. 99, p.113706, 2006.
- <sup>109</sup> M. Stutzmann et al., "GaN-based heterostructures for sensor applications, Diamonds and Related Materials," Vol. 11, p. 886, 2002.
- <sup>110</sup> M. Stutzmann et al., "GaN-based heterostructures for sensor applications, Diamonds and Related Materials," Vol. 11, p. 886, 2002.
- <sup>111</sup> L. Tam et al., *Biophys. J.*, Vol. 47, p. 105, 1985.
- <sup>112</sup> M. Madou et al. in "Chemical Sensing with Solid State Devices," Academic Press, New York, 1989.
- <sup>113</sup> L Bousse et al., *Sens. Actuators B*, Vol. 17, p. 157, 1994.
- <sup>114</sup> G Steinhoff et al., "AlGaIn a new material system for Biosensors", Vol. 13, p. 841, 2003.

# CHAPTER 3

## EXPERIMENTAL TECHNIQUES AND SETUPS

---

In this chapter, experimental methods and techniques are discussed. These techniques were used to characterize the heterostructure material and devices investigated in this thesis. A brief theoretical introduction is provided and general experimental conditions are mentioned. Some of the specific conditions for a particular technique or experiment are detailed at relevant places in Ch. 4. Before discussing the techniques in detail, an overview of the typical investigation process is precisely outlined in the following flowchart.

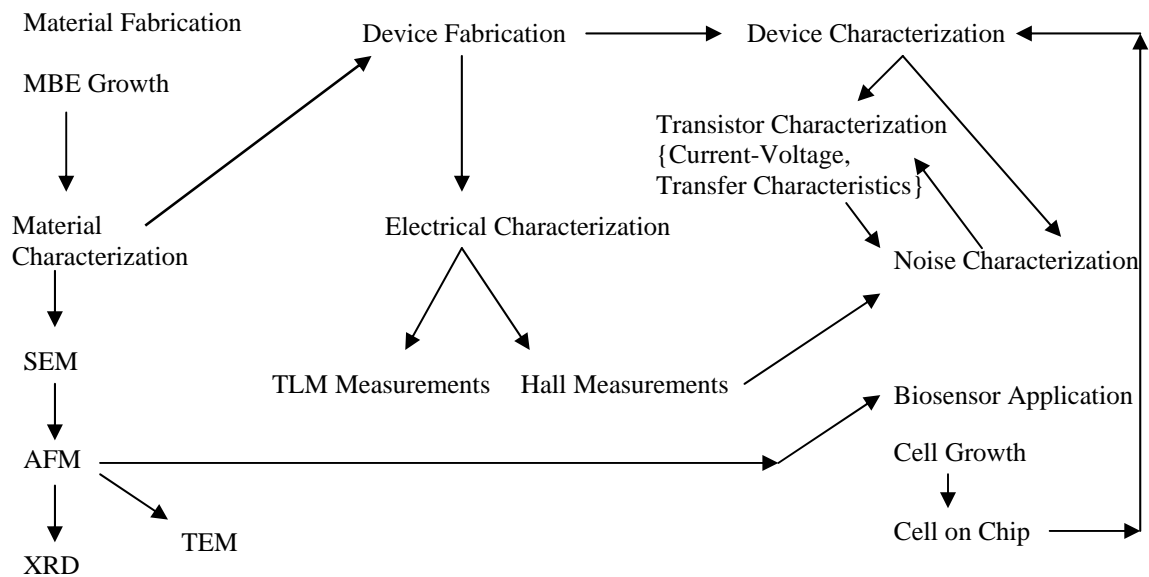


**Fig. 3.1:** A diagrammatic presentation of the experimental schedule

## 3.1 Techniques for Epitaxial Heterostructure Growth

### 3.11 Plasma Assisted MBE Growth

Molecular Beam Epitaxy (MBE)<sup>1,2</sup> and metalorganic chemical vapor deposition (MOCVD)<sup>3</sup> are the two main growth methods frequently used for the growth of III-nitrides. The heterostructures and devices studied in this work also rely on the MBE and MOCVD growth. MBE was developed in early 1970s for growing high-purity epitaxial layers of compound semiconductors<sup>4,5</sup>. It is a sophisticated and widely adopted crystal growth method. One of the advantages of MBE is the low temperature growth that minimizes diffusion and auto doping during the growth process. With MBE it is possible to produce high-quality layers with very abrupt interfaces with good control of thickness, doping, and composition. Such possibility of high degree of control makes it a valuable tool in the fabrication of sophisticated device structures.

To obtain high-purity layers, it is critical to use the extremely pure source material. In addition the entire process must be done in an ultra-high vacuum environment. In MBE growth processes the constituent elements of a semiconductor in the form of ‘molecular beams’ are deposited onto a heated crystalline substrate to form thin epitaxial layers. The growth rates are typically on the order of a few Å/s and the beams can be shuttered in a fraction of a second, allowing for nearly atomically abrupt transitions from one material to another. The ‘molecular beams’

are typically from thermally evaporated elemental sources. Other sources include gaseous group V hydride or organic precursors (gas-source MBE), metal-organic group III precursors (MOMBE), or a combination (chemical beam epitaxy or CBE) of these.

The MBE machine used to grow heterostructures for this work is designed for the growth of group III nitrides. The system consists of a load lock chamber and a main growth chamber. A UHV gate valve isolates these two chambers. Substrates are loaded through the load lock chamber and it is pumped with a Balzers TMU065 turbo molecular pump. The substrates are then transferred to the main chamber using a magnet coupled transfer rod. The main growth chamber is pumped with a cryopump, CTI Cryo Torr 8, and a base pressure of  $\sim 2 \times 10^{-10}$  Torr. A Hiden HAL201 residual gas analyzer (RGA) is used to detect the residual gasses. In-situ surface morphology and growth mode were monitored by a 10 keV RHEED system. The bottom flange of the growth chamber has eight ports for standard effusion cells. Substrate temperature, index of refraction and reflectance were monitored by a SVTA In-situ 4000 process monitor. EPI SUMO cells are used to evaporate high purity metallic Al, Ga, and Mg elements and Si is evaporated by a conventional Knudson effusion source. A careful tuning of Eurotherm 818 temperature controller allows a temperature stability of 0.1 °C. A flux monitor, equipped with a nude ionization gauge controlled by a Grandville Phillips 350 Ionization Gauge Controller, is used to monitor the incident flux of elements. This flux monitor is also used to measure the beam equivalent pressure, when extended to the growth position. A VLSI grade nitrogen gas was excited by an EPI UNI Bulb radio-frequency (rf)

plasma source. This plasma source consists of a one-piece PBN design, which promotes the efficient electron-nitrogen collision and maximizes the source efficiency. Nitrogen plasma is generated by a standard 13.56 MHz Advance Energy RFX-600 rf power supply at a power rating of 350 W. Power matching unit consists of two variable capacitors. This manual matching unit minimizes the reflected power to less than 1% of the input power. Flow of nitrogen to the EPI plasma source is controlled using a MKS 1179 mass flow controller.

The heterostructures were grown over commercially available MOCVD GaN templates on two-inch diameter sapphire substrates. The substrates are single side polished. The back side of the substrates was sputter coated with 5000 Å of Mo for improved effectiveness of heating. Before loading to the chamber, a brief degreasing process was applied that included ultrasonic treatment of samples in acetone and then in methanol. Surface damage due to polishing and contaminants were removed by an etching solution, which consists of a hot mixture of H<sub>2</sub>SO<sub>4</sub> and H<sub>3</sub>PO<sub>4</sub> in 3:1 ratio. Samples were dipped in this solution for 15 minutes at 150 °C. After etching, samples were rinsed in DI water for 5 minutes and then blown dry with filtered N<sub>2</sub> Gas. This step is important, as there are fair chances of contamination of the front surface during Mo deposition.

In order to mount the substrates to the Mo block, two Mo spring plates with fingers were used, so that the substrate is sandwiched by the two spring plates. Substrates were loaded through the load lock chamber and were heated to 850 °C and then out gassed for 30 minutes for thermal cleaning. After this, conventional

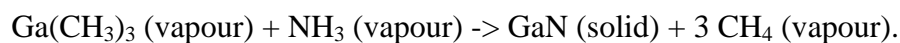
three step growth process<sup>6</sup> was used which includes, nitridation of sapphire surface; growth of low-temperature GaN Buffer layer; and the main epitaxial layer growth.

### **3.12 MOCVD Growth**

MOCVD has evolved as a leading technique, with the increasing innovations in nitride based opto-electronic technology and therefore increasing industrial demand, in past several years. In the early 1980s, it was argued whether MOCVD could ever compete with molecular beam epitaxy (MBE) with respect to the quality of grown epilayers such as thickness control, composition and composition uniformity, and the interface abruptness of the grown materials. MBE is problematic for growing Nitride- and Phosphide-based III-V semiconductors i.e. GaN, InP or InGaAsP. While MOCVD, has been renowned for its high production capability and its larger variety of source materials using metalorganic compounds. Large scale manufacturing potential of MOCVD is an important attribute of this technique. Hence, recently MOCVD has emerged as the preferred technique for GaN based commercial optoelectronic applications after invention of super bright LEDs and a number of following inventions thereafter.

MOCVD is a nonequilibrium growth technique that relies on vapour transport of the precursors and subsequent reactions of group-III alkyls and group-V hydrides in a heated zone. MOCVD utilizes gas mixtures containing the constituent molecules which are also called precursors to grow the epilayers. Nowadays the carrier gas is hydrogen due to its purity. The growth temperature is 550 °C ~ 700 °C due to the stable growth rates provided in this regime. Low pressure (50 ~ 150 torr)

operation is preferable for growing high-quality epitaxial layers. Within this temperature range, the driving force is thermodynamics and the reaction rates of surface kinetics are so high that diffusion is the rate-limiting step for the epitaxial process. In this regime, one can easily control the growth rate by adjusting the flow rate (partial pressure) of precursors with small variations of temperature and total reactor pressure. Composition and growth rates are controlled by precisely controlling mass flow rate and dilution of various components of the gas stream. Organometallic group-III sources are liquids (trimethylgallium, trimethylaluminum), or solids (trimethylindium). The Organometallic sources are stored in bubblers with the gas flows. The bubbler temperature is to precisely control over the vapour pressure of the source material. Carrier gas saturates with vapour from the source and transport vapour to the heated substrate. Group-V sources are most commonly gaseous hydrides and for nitride growth ammonia is used. For doping, metal organic precursors like cyclopenta-dienyl-magnesium (for Mg doping) are used. A typical deposition process for MOCVD growth of GaN can be expressed as:



The expression above is a very simplified one and ignores the specific reaction path and intermediate reaction species that are largely unknown and growth process is inadequately understood so far. The least developed and most difficult topic is the kinetics of process and growth mechanisms occurring at the solid/vapour interface during MOCVD growth. Optimization of MOCVD growth is typically done by empirical studies of external parameters such as growth temperature, V/III ratio, substrate tilt, and mass flow rates.

## 3.2 Material Characterization

### 3.2.1 Scanning Electron Microscopy

SEM is an established technique for surface analysis in various disciplines of science and technology<sup>7,8</sup>. In this study, Scanning Electron Microscopy was used for preliminary examination of the surface quality of films. In addition, it was also used to gather information of the top view geometry of the devices.

#### 3.2.1.1 Working Principle

The resolution of a microscope puts a restriction over the minimum observable size of an object. In an optical microscope, visible light is used as a medium to observe the tiny objects. The wavelength of light is too large to see the micron or sub micron size features. For this purpose, a medium with shorter wavelength is necessary. Because of the wave nature of electrons, they can be used for this purpose. The benefit of using electron as a medium is controllability over the electron energy and hence the wavelength and resolution. Including the relativistic correction, wavelength of an electron is written as,

$$\lambda = \frac{h}{\sqrt{2m_0eV\left(\frac{1+eV}{2m_0c^2}\right)}}, \quad 3.1$$

where  $\lambda$  is in nm,  $V$  is in volts,  $h$  is the plank constant,  $m_0$  is the electronic rest mass,  $e$  is the electronic charge, and  $c$  is the velocity of light. According to this

formula, electron wavelength at 10 kV, and 100 kV is 0.12 nm, and 0.0037 nm respectively. These resolutions are sufficient for a large variety of surface investigation and 10 kV is good enough for general surface studies.

### **3.2.1.2 Instrumentation and Operation**

In electron microscopy, magnetic and electrostatic lenses are used in a similar way as optical lenses in optical microscope. In an SEM, an electron gun at the top produces a beam of monochromatic electrons which is condensed by the first condenser lens, and is used to form the beam and limit the amount of current in the beam. It works in conjunction with the condenser aperture to eliminate the high-angle electrons from the beam. The second condenser lens forms the electrons into a thin, tight, coherent beam. A selectable objective aperture further eliminates high-angle electrons from the beam. A set of coils then "scan" or "sweep" the beam in a grid fashion, dwelling on points for a period of time determined by the scan speed, that is usually in the microsecond range. The objective lens focuses the scanning beam onto the part of the specimen desired. When the beam strikes the sample, interactions occur at the surface and secondary electrons are generated from the top few nanometers, while some electrons are backscattered. Before the beam moves to its next dwell point, these instruments count the secondary electrons and display a pixel on a CRT whose intensity is determined by this number. This process is repeated until the grid scan is finished and a complete picture is formed.

### **3.2.1.3 Experimental Setup**

In this study, a Leica Stereoscan 440 SEM was used which can, in principal, provide 300,000 times magnification and hence objects with the feature size above 50 nm can be conveniently studied with this machine. Samples were coated with a 10 nm gold film, to enhance the electron emission so that a sharper image is obtained.

### **3.2.2 Atomic Force Microscopy**

AFM has been extensively used in GaN research for a variety of purpose. It has been commonly used for typical surface examination to measure the surface quality, cracks, local variations, and surface roughness<sup>9</sup>. A very clear correlation of fabrication process with the surface quality has been shown with AFM surface images<sup>10</sup>. Surface relaxation<sup>11</sup> has been evidenced by AFM in GaN films grown on low quality substrates. In addition to its use for characterization, it has also been used as a tool for surface modification. One such application has been reported to result in reduction<sup>12</sup> of reverse leakage current in GaN Schottky devices. It is a recent, advanced, and very sophisticated surface characterization technique<sup>13,14</sup> used in microelectronics and other areas of research.

AFM is designed for qualitative and quantitative measurement of near surface characteristics of various objects with atomic resolution<sup>15,16</sup>. AFM images are much closer to the simple surface topology and it can image the non-conducting surfaces also. In addition it is a non destructive technique with a small instrument size which can be used immediately at any stage of fabrication to monitor the

surface quality.

### 3.2.2.1 Working Principle

AFM uses a probe moving across the sample's surface to identify its features as shown in Fig. 3.2 (left). The probe is a sharp tip, usually made of silicon, at the end of a cantilever that bends in response to the force between the tip and the sample being viewed. The force experienced by the tip is the inter-atomic force that acts at atomic scale distances and varies with the separation between the atomic scale objects, as shown in Fig. 3.2 (right). The variation in inter-atomic force between the apex of a tip and atoms of the surface is recorded by the measurement system, as the tip is scanned over the surface of the sample.

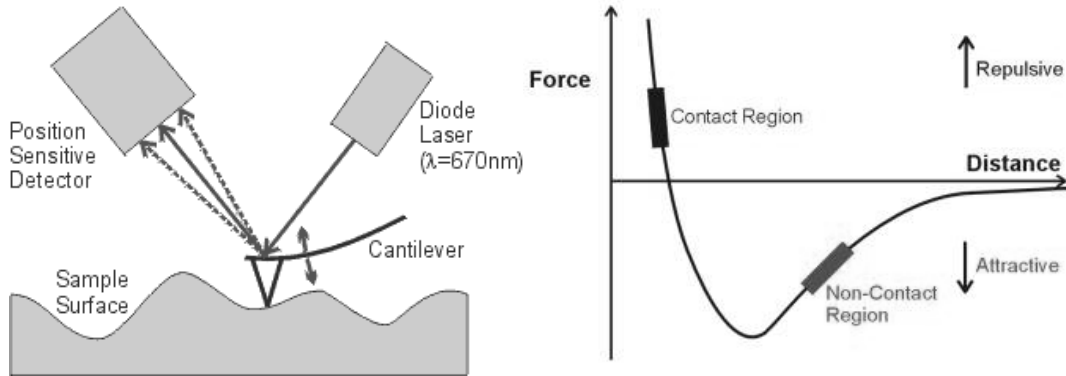


**Fig. 3.2:** a schematic illustration of AFM operation (left) and Force-distance relation at atomic scales<sup>17</sup> (right).

### 3.2.2.2 Instrumentation and Operation

As shown in Fig. 3.2, AFM utilizes a sharp probe moving over the surface of a sample in a raster scan. The sharp tip mounted on a cantilever is brought to a close

proximity of the surface, giving rise to the emergence of a force between the tip and the surface. First the force is attractive, but when the tip-to-sample distance gets very small, on the order of 0.3 nm, the force becomes repulsive and grows very steeply with decreasing distance. Typical force magnitude observed by the tip is in the range of micro Newton to nano Newton. This force acting on the tip will cause the cantilever to deflect. As the cantilever flexes, the light from the laser is reflected onto the split photo-diode. By measuring the difference signal (A-B), changes in the bending of the cantilever can be measured. For small displacements, cantilever obeys Hooke's law, and the interaction force between the tip and the sample can be found. The probe is moved by a piezoelectric unit and thus the tip-surface distance is gathered. Such scanners are designed to move precisely in any of the three perpendicular axes (x, y, and z). By following a raster pattern, the sensor data forms an image of the probe-surface interaction. Feedback from the sensor is used to maintain the probe at a constant force or distance. Accordingly there are two modes of AFM operation. A typical AFM instrumentation is shown in Fig. 3.3. An MDT Solver-P47 AFM measurement system was used for this study and its schematic diagram is also shown. When operated in normal ambient, the cantilever oscillates at its resonant frequency (typically in kilohertz or beyond), and is positioned above the surface. So, it only taps the surface for a very small fraction of its oscillation period. The cantilever is still in contact with the sample, but for a very short period of time, so that the lateral forces are dramatically reduced as the tip scans over the surface. This avoids the damage on the tip which could be caused by possible dragging of the tip over the surface. In constant force mode, the feedback loop adjusts so that the-

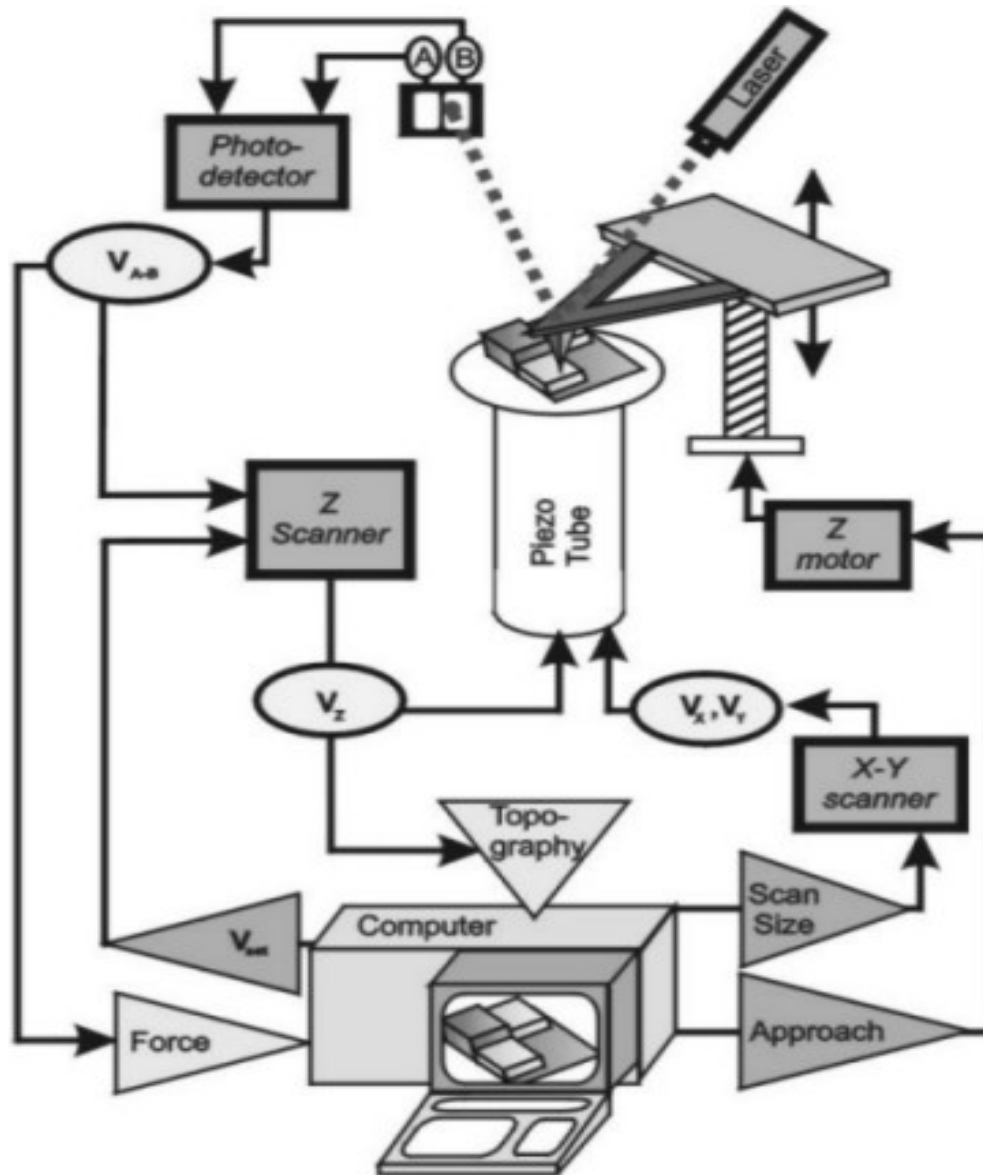


**Fig. 3.3: A typical AFM instrumentation.**

-amplitude of the cantilever oscillation remains nearly constant. An image can be formed from this amplitude signal, as there will be small variations in the oscillation amplitude due to the control circuit responding instantaneously to changes on the specimen surface. As the digital information is acquired from the experiment, a

software is used to process the information to calculate the root mean squared roughness of the scanned area as a standard parameter for the surface roughness.

### **3.2.2.3 Experimental Setup**

For this work, AFM Solver-P47 was operated in semi-contact operation mode at a tip resonance frequency of 350.043 KHz. Lateral scan velocity was chosen between 104000 and 441600 Å/s, depending on the scan area which was set between 1 μm × 1 μm, to 11 μ × 11 μ. For this machine, MAG signal (refers to magnitude) was set to 7.4 nA; S Point (a set point parameter) was set to 7; and FB Gain was set to 2.7 units. Lock-in (a parameter related to gain) gain was set to 2.7 and the L pass value was 3.0 units.

### **3.2.3 X-Ray Diffraction**

X-ray diffraction (XRD) is a non destructive technique that has been extensively used for characterization of imperfections, thickness, strain relaxation, and stoichiometric information of thin films and multilayers. In addition to structural characterization of epitaxial layers, composition in ternary compound and stress in hetero-epitaxial films can also be determined with this technique.

#### **3.2.3.1 Basic Diffraction Theory**

XRD analysis is based on Bragg's law according to which, when X-rays are scattered from a crystal lattice, peaks in the intensity of the scattered beam are observed which correspond to the following condition, known as the Bragg's Equation.

$$2d \sin \theta = n\lambda,$$

3.2

In the above expression,  $d$  is the inter-planer spacing,  $\theta$  is the incident angle between direction of the incident beam and the lattice plane,  $\lambda$  is the wave length of the X-ray beam, and  $n$  is an integer number. A schematic presentation of this Bragg diffraction condition is shown in Fig. 3.4 below.

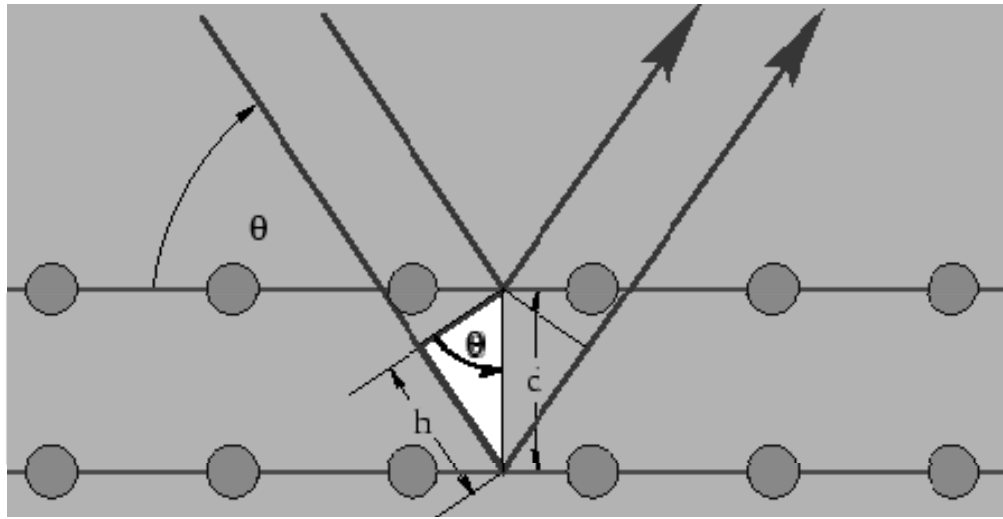


**Fig. 3.4: Schematic diagram showing Bragg's diffraction from a crystal plane.**

### Miller Indices

Miller indices of a crystal are given by three indices ( $h k l$ ) in a rectangular coordinate system indicated in Fig 3.5 (a). The interplaner spacing in case of a hexagonal lattice, as shown in Fig. 3.5 (b), for which  $a$  and  $c$  are the lattice parameters, is then given by,

$$\frac{1}{d^2_{hkl}} = \frac{4}{3} \left( \frac{h^2 + hk + k^2}{a^2} \right) + \frac{l^2}{c^2}. \quad 3.3$$

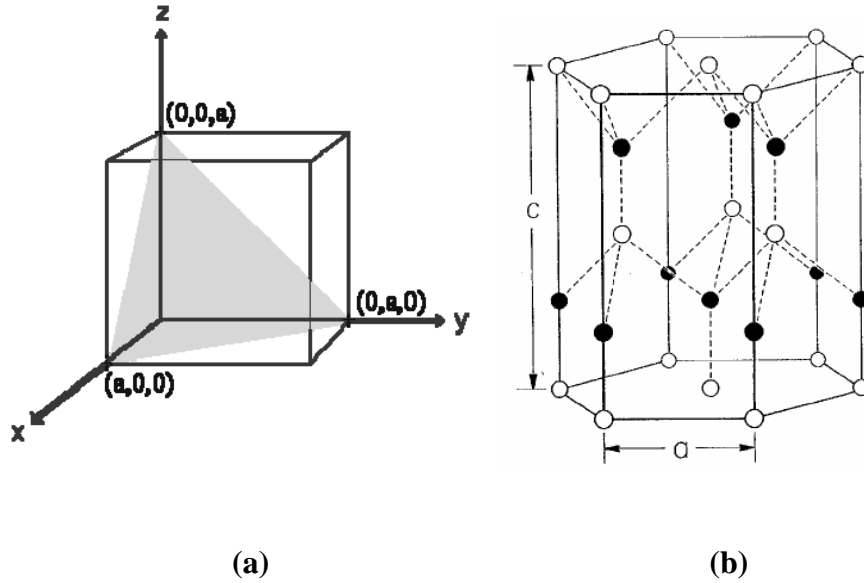


**Fig. 3.5 : Schematic diagram of a plane with Miller indices (1 1 1) in a cubic lattice (a); and a hexagonal lattice with lattice parameters a, and c (b).**

### 3.2.3.2 Four Index Notations for the Hexagonal Lattice

When analyzing a hexagonal lattice, it is convenient to adopt the four-index notation system rather than the three-index system commonly used for cubic lattices. This gives an advantage of presenting similar planes with similar indices for a hexagonal lattice. The directions in such a four-index system can be determined based on the vectors  $a_1$ ,  $a_2$ ,  $a_3$ , and  $c$  as shown in Fig. 3.6. If  $[h\ k\ l]$  are the indices of direction referred in three-index system, the corresponding four-index notation is given by  $[H\ K\ I\ L]$  so that,

$$h = H-I; k = K-I; l = L \text{ or} \tag{3.4}$$

$$H = (2h-k)/3; K = (2k-h)/3; I = -(H+K) = -(h+k)/3 \text{ and } L = l. \tag{3.5}$$

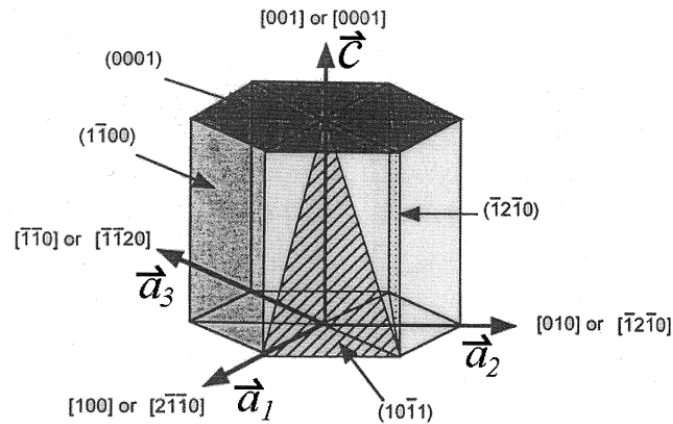


**Fig. 3.6: A four-index and a three index (miller) notation of various planes and directions in the hexagonal lattice.**

Accordingly, the  $[1\ 0\ 0]$  and  $[0\ 0\ 1]$  directions will be transformed to the new notations  $[2\bar{1}\bar{1}0]$  and  $[0\ 0\ 0\ 1]$  in the four-index notation.

### 3.2.3.3 High-resolution X-ray Diffraction (HRXRD)

Conventional high resolution X-ray diffraction is a powerful tool for nondestructive ex-situ investigation of the epitaxial layers and structures. In this technique, the information is obtained from diffraction patterns which carry the signature of composition and uniformity of the layers, layer thickness, built-in strain and strain relaxation, and the crystalline perfection related to dislocation density, domain miss orientation and distribution. All these can be investigated by recording  $\omega$ -rocking curves and  $\theta$ - $2\theta$  diffraction curves in a high resolution diffraction experiment.

### 3.2.3.4 HRXRD Instrumentation and the Measurement Geometries

A typical X-ray instrument for high resolution measurements is built by combining high performance components such as sources, optics, detectors, sample handling device etc. to meet the analytical requirements. A consequent modular design is the key to setup the best instrumentation. Bruker D8 Discover is one such HRXRD system that was used for this work. The instrument geometry with X-ray optics for this system is shown in Fig. 3.7. There are several reasons to use X-ray optics in an HRXRD experiment. Some of those include: (i) to increase the primary beam flux or the flux density; (ii) to improve the angular or energy resolution of a set up; (iii) improve the peak-to-background ratio etc. Several types of scans and scan geometries, as shown in Fig. 3.8, are used to obtain a variety of information. Corresponding instrumental arrangements are shown in Fig. 3.9. Next few paragraphs provide the details of these scan types.

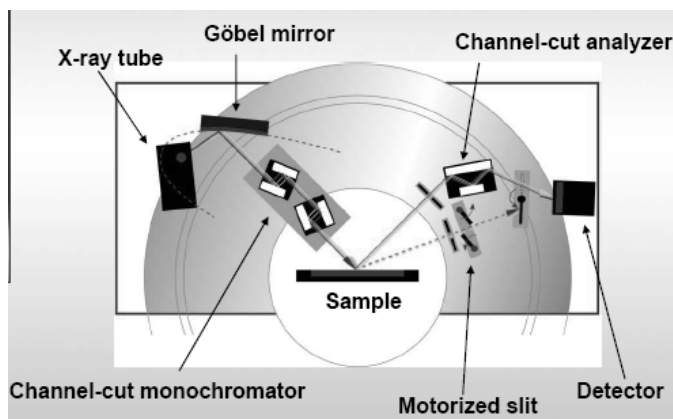


**Fig. 3.7: Schematic drawing of the Bruker D8 Discover X-ray optics consisting of the X-ray tube, hybrid monochromator, Euler cradle and the detector<sup>18</sup>.**

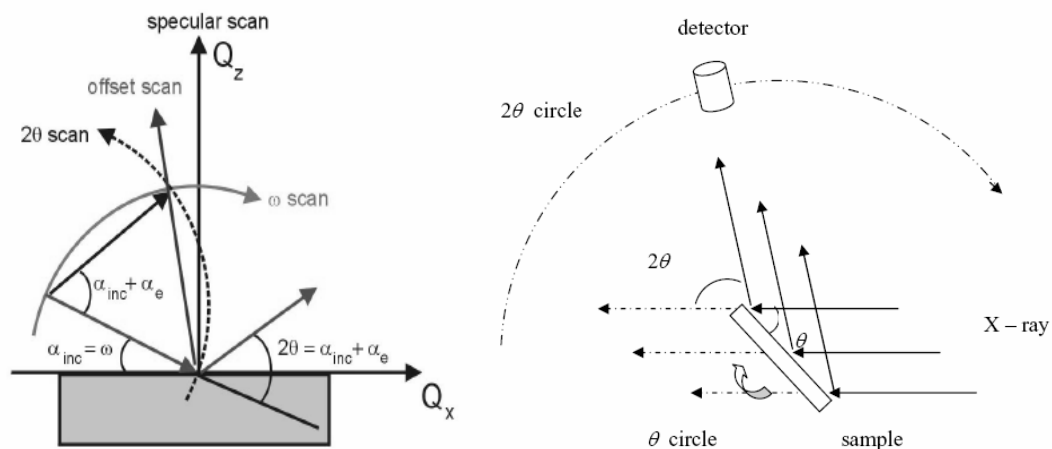


**Fig. 3.8: Different types of HRXRD scan geometries<sup>18</sup> (left); and Schematic diagram of the instrument geometry for  $\theta$ - $2\theta$  scan (right).**

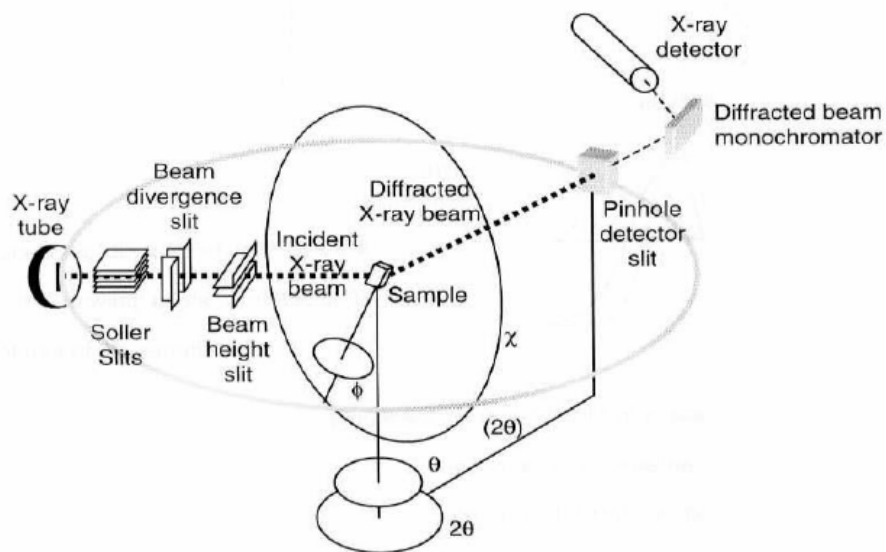


**Fig. 3.9: Schematic diagram of a four axes X-ray diffractometer instrument.**

An X-ray Diffractometer, as shown above, consists of an X-ray source, different kinds of slits, a monochromator, and a detector. There are four rotating axes;  $\theta$  ( $\omega$ ),  $2\theta$ ,  $\varphi$ , and  $\Phi$  for different scan modes. A brief description of the scan types is given below.

**( $\theta$ - $2\theta$ ) scan:** In this scan type, the position of the X-ray source is fixed, and the sample rotates a certain fixed difference of angle with respect to the X-ray incident beam axis, while the detector rotates at twice of this angle. This scan allows observing the lattice planes of the thin film grown in the direction parallel to the normal of the substrate surface. The diffraction profile reflects the crystal structure of the materials. We can determine the crystalline phases and orientations as well. If there are any crystals grown out of plane crystalline orientation of the film, corresponding information will be reflected in this scan. Fig. 3.8 shows the geometry of X-ray optics used for this kind of scan.

**$\omega$  scan:** For  $\omega$  scan,  $2\theta$  value for a selected peak is fixed and the angle  $\theta$  is scanned for a few degree around the corresponding original  $\theta$  value. A graph between the detected intensity and the varying  $\theta$  value is plotted after every scan. This intensity vs.  $\theta$  curve is referred to as rocking curves. This scan is performed to obtain the quantitative information of orientation. The degree of random orientation of the crystal grains with each other in the film is reflected by this scan. It also allows knowing, how good the film is oriented. Strong diffraction is observed when a particular plane of the grain is aligned at the angle that satisfies the Bragg's law. Hence, for poorly aligned grains or planes, a broader peak will be observed in a

rocking curve, while a sharp peak with a narrow width will reflect a high quality epitaxial film.

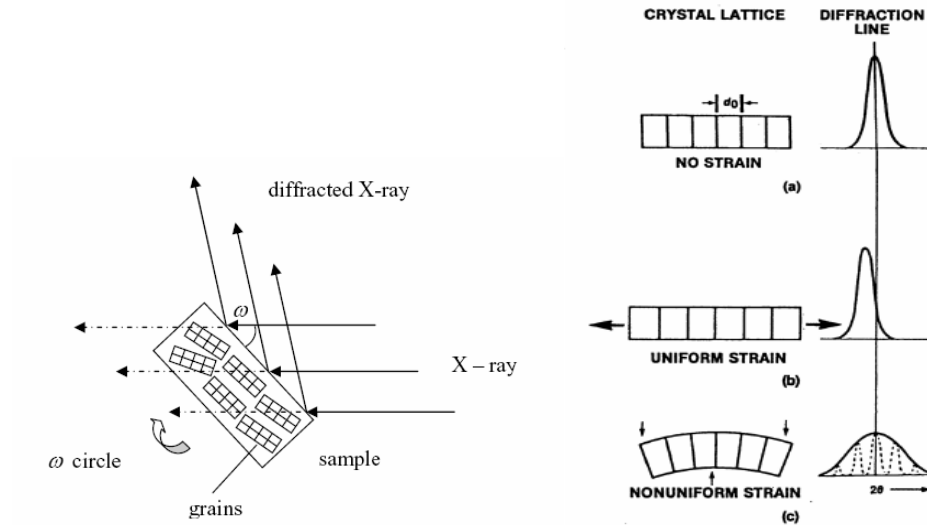


**Fig. 3.10: Schematic diagram of the instrument geometry for  $\omega$  scan in case of poorly oriented grains (left); and the schematic representation of the influence of no strain (a), uniform (b) and non-uniform (c) microstrain on the XRD profile(right) <sup>19</sup>.**

A film can be considered highly oriented or highly epitaxial if the FWHM of the rocking curve is less than around  $1^\circ$ . For comparison, FWHM of the rocking curves of commercial silicon substrates are  $0.2^\circ$ . In Fig. 3.10 (left), shown is the poorly aligned grains which will contribute in line broadening. At the same time, strain or stress can also result in line broadening as explained in the Fig. 3.10 (right). The effects are discussed on the following page.

**$\Phi$  scan:** When diffraction peaks from a single family of planes is observed in  $\theta$ - $2\theta$  scan, it is difficult to say if the films are epitaxially grown or just randomly oriented on the substrate. Hence, the above two scan types are insufficient to provide

information of crystal planes parallel to the surface and out of plane lattice spacing characteristics. A complete rotation along the  $\Phi$  axis can reflect this information precisely. For this scan,  $\theta$  and  $2\theta$  both values are kept fixed and the  $\Phi$  is rotated. For a film with simple cubic lattice structure, intensity vs.  $\Phi$  curve will show four peaks for a complete  $360^\circ$  rotation of the  $\Phi$ , reflecting the four fold symmetry. Similarly, a hexagonal lattice will show six peaks reflecting the six fold symmetry. If the peak position corresponding to the epitaxial film and the substrate align at the same angle, the film is with perfect match with the substrate.

### **3.2.3.4 Experimental Setup**

Bruker D8 Discover HRXRD machine was used for this work which provides a high intensity Cu  $K_\alpha$  (1.54060 Å) X-ray beam with a divergence of less than  $0.05^\circ$ . It consists of a four bounced Ge 220 monochromator for high resolution configuration. This Ge crystal removes the Cu  $K_{\alpha 2}$  component from the beam. The line focus combined with the hybrid monochromator gives a low beam divergence of only 47 arcsec with high intensity. The samples are mounted onto an Euler cradle, which allows an independent variation of the incident angle ( $\omega$ ), the diffraction angle ( $2\theta$ ), the angle around the surface normal ( $\varphi$ ) and the angle around an in-plane horizontal direction ( $\psi$ ). The divergence and receiving slit sizes are 0.25 and 0.1 mm. High resolution of 20 arc sec was achieved with a secondary Ge (220) crystal monochromator in front of the detector. Scan in  $\theta$ - $2\theta$  was performed to determine the film orientation and the rocking curves for the (0002) diffraction were performed to determine the crystalline quality.

## 3.3 Electrical Characterization

### 3.3.1 Hall Measurements

The basic physical principle underlying the Hall Effect is the Lorentz force acting on the charges in a current carrying sample placed in a magnetic field. When an electron moves along a direction perpendicular to an applied magnetic field, it experiences a force acting normal to both directions and moves in response to this force and the force affected by the internal electric field. To explain<sup>20,21,22</sup> the theory of Hall effect measurement, a cross-bridge structure is presented in Fig. 3.11. When an electron moves along a direction perpendicular to the applied magnetic field, it experiences a force acting perpendicular to both directions and moves in response to this force. Another force affected by the internal electric field is formed by the directional movement of carriers.

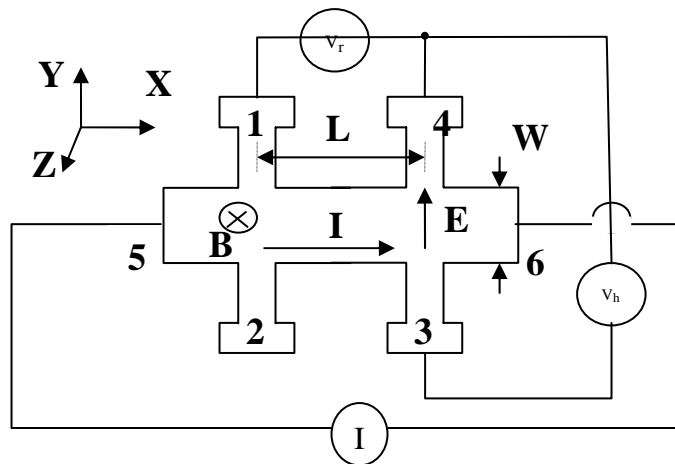


**Fig. 3.11: Hall Effect measurements in a cross-bridge structure**

For an  $n$ -type sample, assume that a magnetic field is applied to the sample in the negative  $z$ -direction, then the charge carriers will experience a Lorentz force perpendicular to their velocity, and they will drift parallel to the  $y$ -axis until they are stopped at the sides of the Hall bar. The charge at the sides of the sample will build up, establishing an electrical potential in the negative  $y$ -direction, which results in the Hall voltage  $V_h$ . And steady state will be reached when the force due to the intrinsic electric field just cancels the Lorentz force due to the magnetic field as

$$qE_y = qv_x B_z \quad 3.6$$

where  $q$  ( $1.602 \times 10^{-19}$  C) is the elementary electronic charge. The sign of the Hall voltage can be used to determine the doping type of the sample. In the above descriptive case, if  $V_h$  is positive (negative), the sample is  $n$ -type ( $p$ -type). When a current  $I$  flows from contact 5 to contact 6, the resistance voltage  $V_r$  is measured between contacts 1 and 4. From the definition of resistance and Ohm's Law, a sheet resistivity  $\rho_s$  is given by,

$$\rho_s = \frac{\rho}{H} = \frac{R \frac{A}{L}}{H} = \frac{V_r W}{I L} \quad 3.7$$

where  $W$  and  $L$  are the dimensions defined in Fig. 3.2.8 and  $H$  is the thickness of the active layer. The density of the charge carriers may be determined using a theoretical model for current and the definition of Hall coefficient  $R_H$ ,

$$I = qnHWv_x, \quad \text{and} \quad 3.8$$

$$R_H = \frac{1}{qn} \quad 3.9$$

where  $n$  is the carrier density. So by scalars, based on above Eq.s, it leads to a sheet Hall coefficient,

$$R_{Hs} = \frac{V_h}{IB_z} \quad 3.10$$

The sheet carrier density is calculated from  $R_{Hs}$ ,

$$n_s = \frac{IB_z}{qV_h} \quad 3.11$$

The calculation of Hall mobility  $\mu$ , depends on the values of  $\rho_s$  and  $R_H$ , which is given by

$$\mu = \frac{R_{Hs}}{\rho_s} = \frac{V_h L}{V_r W B_z} \quad 3.12$$

Since the Hall voltage may be quite small, the effects that have a vital influence on the value of the voltage should be considered. The more severe problem comes from the large offset voltage caused by non-symmetric contact placement and sometimes nonuniform temperature. The most common way to solve this problem is to acquire four sets of Hall measurements at both reverse current directions and two magnetic field directions. Therefore the actual resistance voltage and hall voltage can be expressed as:

$$V_r = \frac{|V_r(I) - V_r(-I)|}{2} \quad 3.13$$

$$V_h = \frac{\left| \frac{|V_h(I)(B) - V_h(-I)(B)|}{2} + \frac{|V_h(I)(-B) - V_h(-I)(-B)|}{2} \right|}{2} \quad 3.14$$

In theory, the value of  $V_r$  has no correlation with magnetic field direction.

### 3.3.1.1 The van der Pauw Method

For convenience the van der Pauw method is typically used for the measurement of the Hall voltage. As originally devised by van der Pauw, one uses an arbitrarily shaped (but simply connected, i.e., no holes or nonconducting islands or inclusions), thin-plate sample containing four very small ohmic contacts placed on the periphery (preferably in the corners) of the plate. A schematic of a rectangular van der Pauw configuration is shown in Fig. 3.12. Van der Pauw demonstrated that there are actually two characteristic resistances  $R_A$  and  $R_B$ , associated with the corresponding terminals shown in the picture.  $R_A$  and  $R_B$  are related to the sheet resistance  $R_S$  through the van der Pauw equation,

$$\exp(-\pi R_A/R_S) + \exp(-\pi R_B/R_S) = 1, \quad 3.15$$

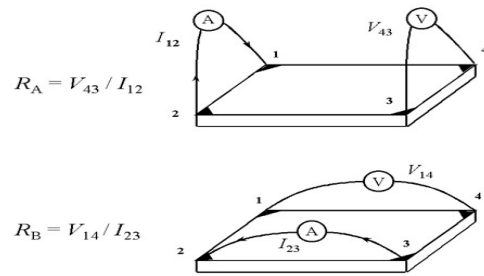


**Fig. 3.12: A schematic of a rectangular van der Pauw configuration**

The expression can be solved numerically for  $R_S$ . The bulk electrical resistivity  $\rho$  can be calculated as

$$\rho = R_S d \quad 3.16$$

To obtain the two characteristic resistances, one applies a dc current  $I$  into contact 1 and out of contact 2 and measures the voltage  $V_{43}$  from contact 4 to contact 3 as shown in Fig. 3.12. Next, one applies the current  $I$  into contact 2 and out of contact 3 while measuring the voltage  $V_{14}$  from contact 1 to contact 4.  $R_A$  and  $R_B$  are calculated by means of the following expressions:

$$R_A = V_{43}/I_{12} \text{ and } R_B = V_{14}/I_{23}. \quad 3.17$$

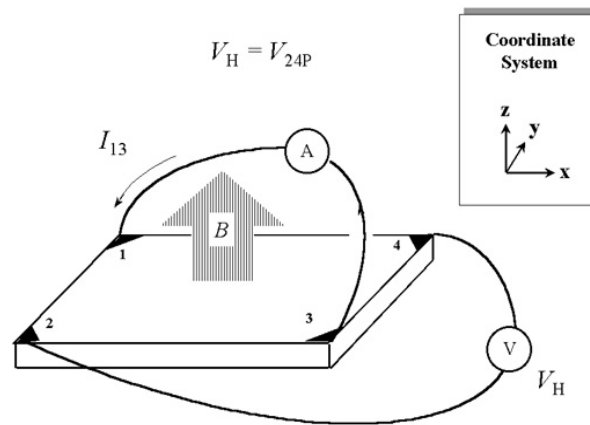


Figure 3

**Fig. 3.13: Hall voltage measurement method in van der Pauw configuration**

Sheet carrier density  $n_s$  can be determined by measuring the Hall voltage  $V_H$ . The Hall voltage measurement consists of a series of voltage measurements with a constant current  $I$  and a constant magnetic field  $B$  applied perpendicular to the plane of the sample. Conveniently, the same sample, shown again in Fig. 3.13, can also be used for the Hall measurement. To measure the Hall voltage  $V_H$ , a current  $I$  is forced through the opposing pair of contacts 1 and 3 and the Hall voltage  $V_H (= V_{24})$  is measured across the remaining pair of contacts 2 and 4. Once the Hall voltage  $V_H$  is

acquired, the sheet carrier density  $n_s$  can be calculated via  $n_s = IB/q|V_H|$  from the known values of  $I$ ,  $B$ , and  $q$ .

There are practical aspects which must be considered when carrying out Hall and resistivity measurements. Primary concerns are (1) ohmic contact quality and size, (2) sample uniformity and accurate thickness determination, (3) thermomagnetic effects due to nonuniform temperature, and (4) photoconductive and photovoltaic effects which can be minimized by measuring in a dark environment. Also, the sample lateral dimensions must be large compared to the size of the contacts and the sample thickness. Finally, one must accurately measure sample temperature, magnetic field intensity, electrical current, and voltage.

### **3.3.1.1.(A). Resistivity Measurements**

The data must be checked for internal consistency, for ohmic contact quality, and for sample uniformity.

1. Set up a dc current  $I$  such that when applied to the sample the power dissipation does not exceed 5 mW (preferably 1 mW). This limit can be specified before the automatic measurement sequence is started by measuring the resistance  $R$  between any two opposing leads (1 to 3 or 2 to 4) and setting  $I < (200R)^{-0.5}$
2. Apply the current  $I_{21}$  and measure voltage  $V_{34}$
3. Reverse the polarity of the current ( $I_{12}$ ) and measure  $V_{43}$
4. Repeat for the remaining six values ( $V_{41}$ ,  $V_{14}$ ,  $V_{12}$ ,  $V_{21}$ ,  $V_{23}$ ,  $V_{32}$ )

Eight measurements of voltage yield the following eight values of resistance, all of which must be positive:

$$\begin{aligned}
 R_{21,34} &= V_{34}/I_{21}, R_{12,43} = V_{43}/I_{12}, \\
 R_{32,41} &= V_{41}/I_{32}, R_{23,14} = V_{14}/I_{23} \\
 R_{43,12} &= V_{12}/I_{43}, R_{34,21} = V_{21}/I_{34}, \\
 R_{14,23} &= V_{23}/I_{14}, R_{41,32} = V_{32}/I_{41}.
 \end{aligned}
 \tag{3.18}$$

With this switching arrangement the voltmeter is reading only positive voltages, so the meter must be carefully zeroed. Because the second half of this sequence of measurements is redundant, it permits important consistency checks on measurement repeatability, ohmic contact quality, and sample uniformity. Measurement consistency following current reversal requires that:

$$\begin{aligned}
 R_{21,34} &= R_{12,43}, \text{ and } R_{43,12} = R_{34,21} \\
 R_{32,41} &= R_{23,14}, \text{ and } R_{14,23} = R_{41,32}
 \end{aligned}
 \tag{3.19}$$

And the reciprocity theorem requires that:

$$\begin{aligned}
 R_{21,34} + R_{12,43} &= R_{43,12} + R_{34,21}, \text{ and} \\
 R_{32,41} + R_{23,14} &= R_{14,23} + R_{41,32}.
 \end{aligned}
 \tag{3.20}$$

### 3.3.1.1.(B). Measurements Procedure

Hall measurement is performed in following sequence,

1. Apply a positive magnetic field  $B$
2. Apply a current  $I_{13}$  to leads 1 and 3 and measure  $V_{24P}$
3. Apply a current  $I_{31}$  to leads 3 and 1 and measure  $V_{42P}$   
Likewise, measure  $V_{13P}$  and  $V_{31P}$  with  $I_{42}$  and  $I_{24}$ , respectively
4. Reverse the magnetic field (negative  $B$ )
5. Likewise, measure  $V_{24N}$ ,  $V_{42N}$ ,  $V_{13N}$ , and  $V_{31N}$  with  $I_{13}$ ,  $I_{31}$ ,  $I_{42}$ , and  $I_{24}$ , respectively.

The above eight measurements of Hall voltages  $V_{24P}$ ,  $V_{42P}$ ,  $V_{13P}$ ,  $V_{31P}$ ,  $V_{24N}$ ,  $V_{42N}$ ,  $V_{13N}$ , and  $V_{31N}$  determine the sample type ( $n$  or  $p$ ) and the sheet carrier density  $n_s$ . The Hall mobility can be determined from the sheet carrier density  $n_s$  and the sheet resistance  $R_s$  obtained in the resistivity measurement. This sequence of measurements is redundant in that for a uniform sample the average Hall voltage from each of the two diagonal sets of contacts should be the same, as in case of a square size sample.

### 3.3.1.1.(C). Hall Calculations

Steps for the calculation of carrier density and Hall mobility are:

1. Calculate the following

$$V_C = V_{24P} - V_{24N}, V_D = V_{42P} - V_{42N},$$

$$V_E = V_{13P} - V_{13N}, \text{ and } V_F = V_{31P} - V_{31N}. \quad 3.21$$

The sample type is determined from the polarity of the voltage sum  $V_C + V_D + V_E + V_F$ . If this sum is positive (negative), the sample is  $p$ -type ( $n$ -type).

2. The sheet carrier density (in units of  $\text{cm}^{-2}$ ) is calculated from

$$p_s = 8 \times 10^{-8} IB/[q(V_C + V_D + V_E + V_F)] \quad 3.22$$

if the voltage sum is positive, or

$$n_s = |8 \times 10^{-8} IB/[q(V_C + V_D + V_E + V_F)]| \quad 3.23$$

if the voltage sum is negative, where  $B$  is the magnetic field in gauss (G) and  $I$  is the dc current in amperes (A).

3. The bulk carrier density (in units of  $\text{cm}^{-3}$ ) can be determined as follows if the conducting layer thickness  $d$  of the sample is known:

$$n = n_s/d ; \text{ or}$$

$$p = p_s/d \quad 3.24$$

4. The Hall mobility  $\mu = 1/qn_s R_S$  (in units of  $\text{cm}^2\text{V}^{-1}\text{s}^{-1}$ ) is calculated from the sheet carrier density  $n_s$  (or  $p_s$ ) and the sheet resistance  $R_S$ .

### **Experimental Setup**

Room temperature Hall measurements were performed using a Bio-Rad HL5500 Hall effect measurement system. For this system, thin film samples of size 5 mm  $\times$  5 mm were diced and ohmic contact were formed by soldering indium at the four corners of the squares. Low temperature Hall measurements were performed using a

custom-made setup which consists of a Keithley 220 programmable current source, a Keithley 182 sensitive digital voltmeter, a Neocera LTC-11 temperature controller, an ABBESS instruments DC electro-magnet, a Sorensen DCS 55-55 power supply for the magnet, and a Cryo Industries FGT cryostat. For this setup, both van der Pauw configuration as well as cross-bridge configuration were used. Ohmic contacts on the samples were formed by evaporating Ti/Al bilayers and then annealing at 650 °C for 40 seconds. A thin ceramic package, as shown in Fig. 3.14 with copper contacts was used which provides as an interface between the wire bonding of the ohmic contacts on the films as well as the soldered cryostat wiring. Above explained methods were followed at each temperature point to acquire the temperature dependence of resistivity and Hall data.

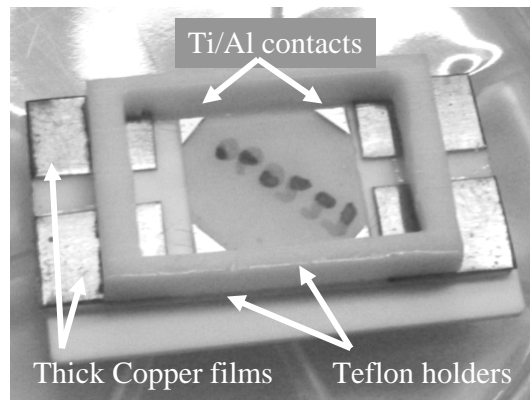


**Fig. 3.14: A sample holder for the cryogenic Hall measurements.**

### 3.3.2 TLM Measurements

Transmission Line Method test pattern are commonly used for accurate assessment of electrical quality of contact resistance<sup>23,24</sup> for planar ohmic contact. The TLM technique uses a test pattern composed of differently spaced ohmic contact pads as illustrated in Fig. 3.15. Ohmic contacts are formed on the semiconductor surface and separated by a distance  $l_i$ . The contact pads have a width,  $W$ , and a length,  $d$ , and the pattern is isolated to restrict the current to flow to the width  $W$ . The resistance between two such contacts,  $R_i$ , separated by  $l_i$  is:

$$R_i = \frac{2R_{sk}L_T}{W} + \frac{R_{sh}l_i}{W} \quad 3.25$$

where  $R_{sh}$  is the semiconductor sheet resistance ( $\Omega/\square$ ) and  $L_T$  is the transfer length,  $\rho_c$  is the specific contact resistivity at the metal-semiconductor interface. All voltage drops in the horizontal direction are attributed to the current flow in  $R_{sk}$  while the voltage drop in the vertical direction, perpendicular to the plane of the current, is due to  $\rho_c$ .

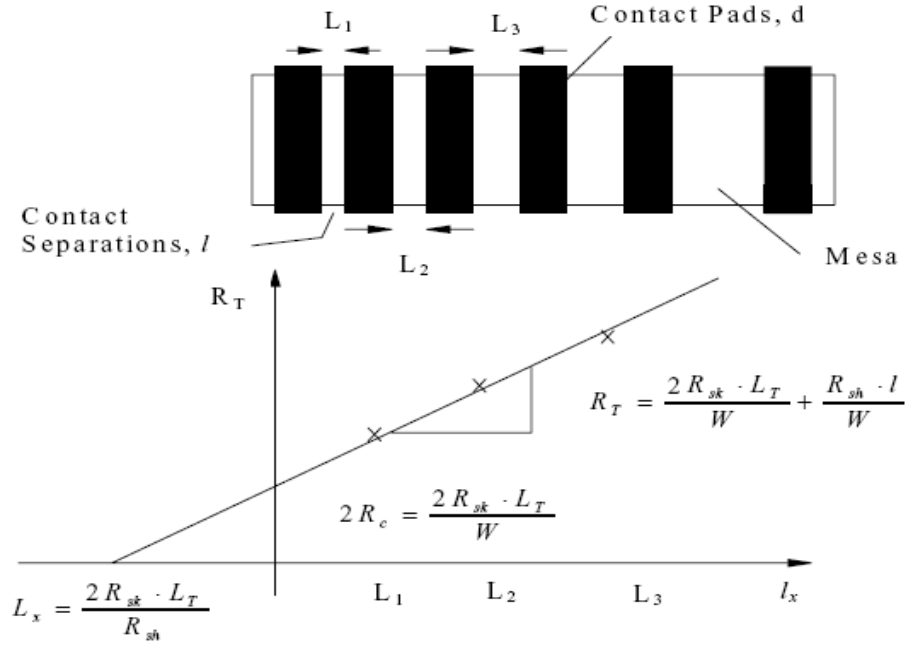


**Fig. 3.15: Transmission line pattern on isolated semiconductor (top); and the TLM method for measuring the contact resistance.**

$$R_i = 2R_c + R_{sh} \frac{l_i}{W} \quad 3.26$$

where  $R_c$  is the contact resistance of the semiconductor. A plot of  $R_i$  versus  $l_i$  will yield a straight line as shown in Fig. 3.6(b). The slope of this line gives the value of  $R_{sh}/W$  and the intercept with the  $R$ -axis gives the value of  $2R_c$ . The intercept with  $l$ -axis, called  $L_x$  is related to the transfer length  $L_T$  as:

$$L_x = \frac{2R_c W}{R_{sh}} = 2L_T \quad 3.27$$

If the contact length,  $d$  is much greater than the transfer length,  $L_T$ , ( $d \gg L_T$ ) the effective contact area is approximately  $WL_T$  instead of  $Wd$ . Thus, the specific contact resistivity, from the above expression becomes:

$$\rho_c = R_c WL_t = R_{sh} L_T^2 \approx \frac{(R_c W)^2}{R_{sh}} \quad 3.28$$

Since in practice  $\rho_c$  can be measured for semiconductors then the contact resistance can be calculated. It is to be noted that the value of  $R_c$  is independent of the contact length  $t$  only depends on its width i.e. only on the dimension *perpendicular* to the current flow.

### 3.3.2.1 Experimental Setup

For the TLM measurements, a probe station with optical microscope arrangement was used to place the samples and HP4140B measurement system was used to acquire the  $I$ - $V$  data.

## 3.4 Low-frequency Noise Characterization

In this thesis, a significant part deals with the low-frequency noise and its applications. Noise is not a very commonly used technique. In this section, this topic is introduced in brief and at a fundamental level.

### 3.4.1 Noise: Relevance in Semiconductor Characterization

In general, random fluctuations in any measurement are termed as noise. In an electronic device, a random spontaneous perturbation of a deterministic electrical signal, inherent to the physics of the device, is known as electrical noise. In context of this thesis, noise refers mainly to the *low-frequency electrical noise* associated with materials and device characterization. Hence, theories and models relevant to these *noise* features are briefly discussed.

For a long time, fluctuation phenomena in semiconductor materials and devices were considered only as a limitation to sensitivity and performance of devices. Therefore, all early investigations in this field were application-driven. They were directed towards understanding the origin of fluctuation to be able to reduce the noise level and increase sensitivity and stability of devices. From the initial studies, following important facts were discovered that attracted the interest in this topic:

1. Reduction of noise level increases the sensitivity or the performance of a device.
2. Noise generation process was found to be highly sensitive to particular physical features of a given device even if these features are not detectable by other means.

From the first observation, it was understood that origin of low-frequency noise is somehow related to few basic physical mechanisms governing device operation. Hence, noise investigations can provide valuable information about the different physical processes occurring in semiconductor materials and devices. In addition, from the second observation it became clear that noise study may serve as a very sensitive characterization tool of the material. In that capacity, it makes possible to obtain additional information about the semiconductor materials and structures that are not accessible by other physical characterization techniques. So the *noise* can actually be used as the *signal* to evaluate and get insight in the properties of a particular system<sup>25</sup>. As the noise is a random phenomenon, statistical analysis is required in order to extract any useful information. In the next section, the statistical foundation of noise is introduced.

### **3.4.2 Statistical Definitions and Formulations**

Noise refers to the fluctuations in an observed signal. Most generally it is the voltage or current in the device. Without sticking to the particulars of a signal, consider an arbitrary signal variable 'x', which shows random variations in time. Few key terms used in the noise formulation are then defined as follows.

#### **3.4.2.1 Autocorrelation Function**

In order to facilitate theoretical analysis of noise, memory of a stochastic process is reflected in the formulation of autocorrelation function defined as,

$$\Phi_x(t) \equiv \langle x(\tau)x(t+\tau) \rangle = \lim_{T \rightarrow \infty} \frac{1}{\Gamma} \int_{-\Gamma/2}^{\Gamma/2} x(\tau)x(t+\tau) d\tau, \quad 3.29$$

where, the brackets denote ensemble average. The ensemble formalises the notion an experimentalist repeating an experiment again and again under the same macroscopic conditions, but unable to control the microscopic details, may expect to observe a range of different outcomes. As far as the assumption of ergodicity holds (i.e. till a time average gives complete representation of the full ensemble), the ensemble average is replaced by time average.

### 3.4.2.2 Power Spectral Density

An important statistical function associated with such random variable is defined as the power spectral density,  $S_X(f)$ , that represent the average power per bandwidth for  $x_T$ , where  $x_T$  is the Fourier transform of the variable  $x(t)$ ,

$$x_T(t) = \begin{cases} x(t) \dots -\Gamma/2 \leq t \leq \Gamma/2, \\ 0 \dots \dots \dots \text{otherwise.} \end{cases} \quad 3.30$$

The power spectral density is then defined as,

$$S_x = \lim_{\Gamma \rightarrow \infty} \frac{2|X_T(f)|^2}{\Gamma}. \quad 3.31$$

### 3.4.2.3 Wiener-Kintchine theorem

The above two important terms used in noise theory, power spectral density and auto-correlation function, are related through the Wiener-Kintchine theorem, given as:

$$S_X(f) = 2 \int_{-\infty}^{\infty} \Phi_X(t) e^{i2\pi ft} dt . \quad 3.32$$

When restricting the frequency to positive values, the above expression becomes,

$$S_X(f) = 2 \int_{-\infty}^{\infty} \Phi_X(t) e^{i2\pi ft} dt = 4 \int_0^{\infty} \Phi_X(t) \cos(2\pi ft) dt . \quad 3.33$$

### 3.4.3 Classification of Noise

Based on the spectrum shape and origin noise can be broadly classified in four types as listed in Table-1 below. Brief information about the related theories is provided.

**Table-3.1: Noise Classification.**

<i>Name</i>	<i>Origin</i>	<i>Power Spectrum</i>
Thermal Noise	Thermal agitation of charge carriers	white
Shot Noise	Randomly generated charge carriers	white
G-R noise	Capture-emission of charge carriers	$f_c / (f_c^2 + f^2)$
Flicker Noise	Controversial	$1/f$

### 3.4.4 Thermal Noise

Atoms, in any object (and hence in a conducting device), vibrate at all non-zero temperatures and so does the lattice. Consider an ohmic device at a temperature  $T$ . Charge carriers inside the conductor collide with lattice vibrations called phonons, causing Brownian motion with a kinetic energy proportional to  $T$ . This yields open circuit voltage fluctuations with zero average value, but a nonzero rms value as

given by,

$$v_n = \sqrt{\frac{4hfBR}{e^{hf/kT} - 1}}, \quad 3.34$$

where  $v_n$  is the rms value in Volts,  $h$  is Planck's constant ( $6.63 \times 10^{-34}$ ) in Joule second,  $k$  is Boltzmann's constant ( $1.38 \times 10^{-23}$ ) in Joule/K,  $B$  is the bandwidth of the system in Hz,  $f$  is the center frequency of the band in Hz and  $R$  is the resistance in Ohms. At *low frequencies* using the Rayleigh-Jeans approximation, and considering only the first two terms of a series expansion of the exponential,  $e^{hf/kT} - 1 \approx hf/kT$ , and then converting to the voltage power spectral density,  $S_v$ , is given as,

$$S_v = v_n^2 / B = 4kTR. \quad 3.35$$

As clear from this equation, thermal noise has a white spectrum.

### 3.4.5 Shot Noise

The current flowing across a potential barrier, like in a pn-junction, is not continuous due to the discrete nature of the electronic charge. The current across a barrier is given by the number of carriers, each carrying the charge  $q$ , flowing through the barrier during a period of time. A shot noise current is generated when the electrons cross the barrier independently and at random. The current fluctuates with a PSD [99]

$$S = 2qI \quad 3.36$$

### 3.4.6 Generation-Recombination Noise

The generation-recombination (GR) noise arises due to the trapping-detrapping processes of carriers by localized states, mostly among energy states, mostly

between an energy band and a discrete energy level (trap) in the bandgap. A trapping-detrapping process results either in excess of carriers by 'generation' or in reduction of carriers by 'recombination'. This results in the fluctuation in the number of carriers from an equilibrium value. The process can be modeled as follows. Suppose there are  $N$  number of carriers at equilibrium in a semiconductor. If a GR process results in fluctuation  $\Delta N$  at any time  $t$ , the perturbation  $d\Delta N$  is given by,

$$\frac{d\Delta N}{dt} = -\frac{\Delta N}{\tau}, \quad 3.37$$

where  $\tau$  is the characteristic time of carrier recombination. In different physical systems and  $\tau$  is further modeled according to the fundamental details of that system.

Suppose there is a two-terminal resistive sample that is made of such a semiconductor. If the resistance of the sample is  $R$  and the bias voltage applied across the terminals is  $V$ , noise power arising from the GR process is given by,

$$\frac{S_R}{R^2} = \frac{S_V}{V^2} = \frac{S_N}{N^2} = \frac{\langle \Delta N^2 \rangle}{N^2} \frac{4\tau}{1 + (2\pi f\tau)^2}, \quad 3.38$$

where  $S_R$ ,  $S_V$ , and  $S_N$  are power spectrum density of resistance, voltage and number of carriers respectively and  $f$  is the observation frequency.

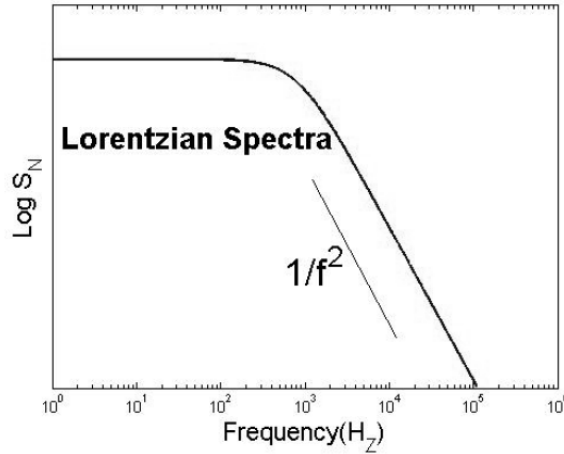


**Fig. 3.16: A Lorentzian Noise Spectra.**

When this concept is applied to a semiconductor sample having a two dimensional conduction channel in which the number fluctuation results in fluctuation in device resistance, the voltage noise power spectral density,  $S_V(f)$ , resulting from trapping and detrapping process of carriers by defect states is given by,

$$S_V(f) = 4I^2 (\Delta R)^2 \int_x \int_y \int_E N_T(x, y, E) \frac{\tau}{1 + 4\pi^2 f^2 \tau^2} dx dy dE, \quad 3.39$$

where  $I$  is the dc current bias applied to the device,  $\Delta R$  is the resistance fluctuation caused by the capture or emission of a single electron by a defect,  $N_T$  is the two-dimensional defect density per unit energy and  $\tau$  is the fluctuation time. The spectra resulting from the above expression is a Lorentzian<sup>26</sup> as shown in Fig. 3.16, if the traps are concentrated in one single energy level. A Lorentzian power spectrum shows almost a constant value before a corner frequency and rolls down as  $1/f^2$  after that.

### 3.4.7 Flicker (1/f) Noise

The  $1/f$  noise, also called flicker noise, refers to a spectrum that shows a power spectral density proportional to the  $1/f^\gamma$ . When  $\gamma = 1$ , it is called strictly  $1/f$  noise. It has been known as a fundamental<sup>27</sup> noise which is intrinsic to the different systems. It has been found in different kinds of materials and systems including semiconductor materials and devices, metals, biological systems, music etc. Interestingly, it has apparent lack of cutoff frequency. These peculiar aspects make it one of the most interesting physical phenomena. Origin of flicker noise has been highly debated in literature. One of the very few common agreements about the origin of the flicker noise is that it results from of the conductivity ( $\sigma$ ) fluctuation. As the  $\sigma$  depends on both the mobility ( $\mu$ ) and the number of carriers ( $N$ ), there are two school of thoughts regarding the origin of flicker noise. One of those is the *mobility fluctuation model*, and the other is the *number fluctuation model*. Both are briefed in the following sections.

#### 3.4.7.1 Mobility Fluctuation Models

##### 3.4.7.1.1 Hooge's Model

The basic concept behind the Hooge's empirical model is that carrier scattering by lattice vibrations cause fluctuations in mobility of the charge carriers. Such mobility fluctuations in turn result in conductance fluctuations and give rise to flicker noise<sup>28,29</sup>. As the carrier mobility in the bulk of the material is assumed to fluctuate and cause the observed conductivity fluctuations, hence it is a bulk effect. Hooge<sup>30</sup>

gave an empirical relation for  $1/f$  noise. The relation is based on homogenous samples of semiconductors or metals and given as,

$$\frac{S_V(f)}{V^2} = \frac{S_I(f)}{I^2} = \frac{\alpha_H}{fN}, \quad 3.40$$

where  $N$  is the total number of electrons in the sample and  $\alpha_H$  is a dimensionless constant, known as ‘Hooge parameter’.

Initially when the Hooge relation was proposed, the parameter  $\alpha_H$  was considered a universal constant with a value of  $2 \times 10^{-3}$ . Later, a number of studies resulted in following observations which made this relation questionable.

1.  $\alpha_H$  is not a universal constant, and A number of semiconductor samples reflect  $\alpha_H$  having a range of values<sup>31</sup>  $10^{-7} < \alpha_H < 10^{-2}$
2. Studies on devices such as MOSFETs gave extensive evidence for a surface effect, as opposed to bulk effect
3. Typical time scales of phonon scattering are of the order of picoseconds. The time scale is incompatible with the fact that flicker noise spectrum extends to frequencies as low as  $10^{-6}$  Hz.
4. Spectral slopes often deviates form -1 ( $-0.8 < \gamma < -1.4$ )

All these findings limited the validity of Hooge’s relation and the parameter. Later it was stressed that the above equation is an empirical relation and that the only theoretical idea behind it, is that whatever carriers do to produce  $1/f$  noise, they do it independently. Even though the relation has been questioned, it has been remaining in extensive use in literature. It turned out that the value of  $\alpha_H$  is very sensitive to

material quality and processing techniques, and hence it can be used as a measure of the quality and relative noise level of materials and devices.

#### **3.4.7.1.2 Handel's Model**

An attempt to give physical meaning to the Hooge parameter was the formulation of quantum mechanics based flicker noise theories. These theories are inline with the mobility fluctuation but consider different causes and mechanisms. One such mechanism<sup>32</sup> was proposed by Handel. He considered interaction of scattered charge with the electromagnetic field, which in turn modulates the scattering process. Unlike defect related noise, such interactions are fundamental in nature and can not be avoided with improvement in technology. The model predicts that inclusion of inter-valley scattering processes give rise to  $\alpha_H \sim 10^{-6}$ - $10^{-5}$ , otherwise  $\alpha_H \sim 10^{-9}$ - $10^{-8}$ . So, it fails to explain larger  $\alpha_H$  values. Hence, Handel further proposed a different quantum process<sup>33</sup>, which was 'coherent state quantum  $1/f$  fluctuations'. Calculations based on this model ( $\alpha_H \sim 4.65 \times 10^{-3}$ ) are quite close to the higher reported values. Handel's models are also limited to systems which exhibit strictly  $1/f$  spectrum.

#### **3.4.7.2 Number Fluctuation Models**

Several competing models based on carrier number fluctuation have been proposed to explain the flicker noise. Two widely used models are discussed here.

### 3.4.7.2.1 McWhorter's Model

McWhorter proposed<sup>34</sup> that, flicker noise in MOS systems originate from number fluctuations caused by carrier trapping by localized states in the oxide. Process of random capture and emission of carriers results in fluctuations in the charged state of an oxide trap. Such fluctuations modulate the local Fermi level at the semiconductor surface. Modulation of local Fermi level then causes fluctuations in the number of mobile carriers. Oxide traps are spatially separated from the carriers and the trapping-detrapping takes place via 'tunneling' mechanism. The power spectrum for fluctuations in the trap occupancy in an elemental volume  $\Delta\Omega = \Delta x\Delta y\Delta z$  is given by<sup>35</sup>,

$$S_{\Delta N}(f) = 4N_T(E, z)\Delta\Omega f_T(1-f_T) \frac{\tau}{1+4\pi^2 f^2 \tau^2}, \quad 3.41$$

where  $N_T(E, z)$  is the density of traps in  $\text{cm}^{-3}\text{eV}^{-1}$ , and

$$\tau = \tau_0 \exp(\lambda z_0) \quad 3.42$$

$z_0$  is the distance separation of localized state in oxide from the interface and  $\lambda$  is the WKB parameter. The Fermi factor  $f_T(1-f_T)$  as a function of trap energy  $E$  peaks sharply at  $E = E_F$ . Therefore, only traps with energies within a few  $kT$  from the Fermi level contribute to number fluctuation. Applying this model for a device with a finite resistance  $R$ , and having a total volume  $\Omega$ , which is voltage biased, following expression can be derived.

$$S_V(f) = 4N_T\Omega(\Delta I_0)^2 R^2 f_T(1-f_T) \frac{\tau}{1+4\pi^2 f^2 \tau^2}, \quad 3.43$$

$$= S_0 \frac{\tau}{1 + 4\pi^2 f^2 \tau^2}, \quad 3.44$$

where  $\Delta I_0$  is the current fluctuation due to the capture of a single carrier,  $f_T$  is the fraction of filled traps.

Though McWhorter's model was quite successful, Surya et. al. found that the model can not adequately explain the experimental data<sup>36</sup>, in particular the strong temperature dependence of the  $1/f$  slope i.e.  $\gamma$ . The data could be accounted for if the trap kinetics were governed by thermally activated processes, instead by tunneling processes. It is shown that the distribution of the trap density at  $z_0$  strongly affects the functional form of the noise power spectral density of the  $1/f^\gamma$  noise. If  $\partial N_T / \partial z|_{z=z_0} = 0$  then  $\gamma = 1$ , however, if  $\partial N_T / \partial z|_{z=z_0} < 0$  then  $\gamma > 1$  and if  $\partial N_T / \partial z|_{z=z_0} > 0$  then  $\gamma < 1$ .

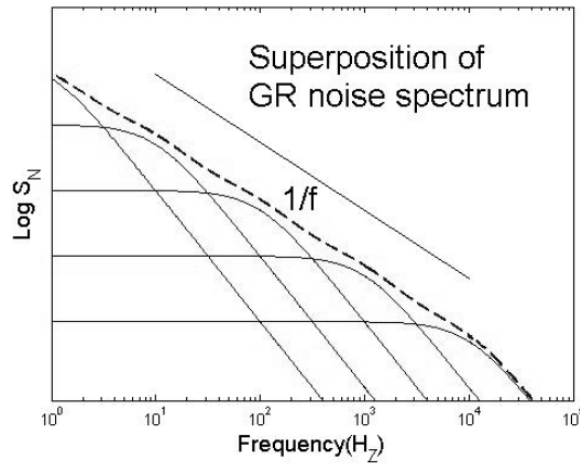


**Fig. 3.17:  $1/f$  spectra as superposition<sup>37</sup> of Lorentzians.**

### 3.4.7.2.2 Thermal Activation Model

Flicker noise has been shown to be resulting from the superposition of Lorentzian spectra of thermally activated processes<sup>38</sup>. As shown in Fig. 3.17, superposition of a number of Lorentzians characterized by different  $\tau$  will result in a  $1/f$  spectrum. The required distribution of  $\tau$  was shown to result from a distribution of  $E_\tau$ , i.e. a distribution of trap states with different activation energies.

Applying this model to a 2DEG conduction channel, the thermal activation model stipulates that the trapping and detrapping process is thermally activated in which  $\tau$  is given by

$$\tau = \tau_0 \exp\left(\frac{E_\tau}{kT}\right), \quad 3.45$$

where  $E_\tau$  is the activation energy for the capture and emission of the carriers,  $T$  is the absolute temperature and  $\tau_0$  is the inverse phonon frequency. In this case, the voltage noise power spectral density,  $S_V(f)$ , is given by<sup>36</sup>

$$S_V(f) = 4 \frac{V_{DS}^2}{N^2} \int_x \int_y \int_E N_T \frac{\tau}{1 + \omega^2 \tau^2} dx dy dE, \quad 3.46$$

where  $N$  is the total number of electrons in the two-dimensional electron gas (2DEG),  $V_{DS}$  is the dc voltage across the 2DEG channel,  $N_T$  is the two-dimensional defect density and  $\tau$  is the fluctuation time constant. The Lorentzian described by above equation is a sharply peaked function of the activation energy at

$$E_p = -kT \ln(\omega \tau_0). \quad 3.47$$

Thus,  $\gamma = 1$  for  $\partial N_T / \partial E |_{E=E_p} = 0$ ,  $\gamma > 1$  for  $\partial N_T / \partial E |_{E=E_p} < 0$  and  $\gamma < 1$  for  $\partial N_T / \partial E |_{E=E_p} > 0$ .

### 3.4.8 Difference between Tunneling and Thermal Activation Models

The main difference between the tunneling mechanism and the thermal activation mechanism lies in the temperature dependence of the noise. In contrast to the tunneling model, above equations governing thermal activation process indicate that traps at different energy levels are being activated as the device temperature is varied. This implies that there is a possibility of strong temperature dependence for  $\gamma$  if  $N_T(E)$  varies with energy  $E$ . On the other hand, the tunneling model, stipulates that as the temperature is varied essentially the same group of traps is responsible for the observed noise. This is because the WKB parameter is basically independent of the device temperature. Hence, if the noise is correctly described by the tunneling model then one would expect little change in the value of  $\gamma$  with temperature. Previous experiments performed on GaN-based devices clearly indicate systematic variation of  $\gamma$  with the device temperature. The results clearly show that a thermally activated trapping and detrapping process underlies the flicker noise in GaN devices. According to the thermal activation model, trap density can be estimated by<sup>36</sup>

$$N_T(E_p) = \frac{S_V(f) f N^2}{4V_{DS}^2 AkT} \cdot \quad 3.48$$

### **3.4.9 Experimental Setup for Noise Measurements**

Measurement of noise is a complex task as the signal to be measured is very weak (down to  $\sim 1$  pA). A DC bias current is usually present as well as disturbances from electronic equipments, which makes the task more complicated. The measurement setup must be designed carefully with appropriate shielding and preferably using batteries as power sources to avoid disturbances to be injected in the circuits. Schematic diagram of a typical low-frequency noise measurement setup used for the investigations is shown in Fig. 3.18. Circuit representation of the setup is shown in Fig. 3.19. In a noise measurement experiment, 'voltage fluctuations' across two terminals of a conducting channel are amplified by a low-noise preamplifier and fed to a signal analyzer. Signal analyzer presents those time domain input fluctuations in the form of 'noise power spectra'. In this thesis such power spectra of the open circuit voltage fluctuations were used for analysis.

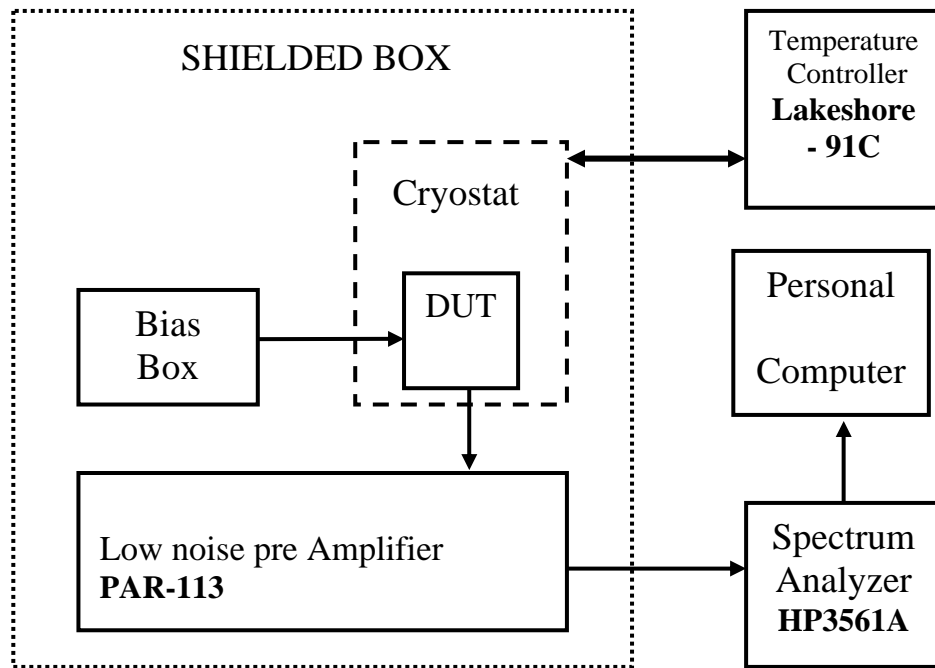


**Fig. 3.18 : Schematic diagram of a typical low-frequency noise measurement setup.**

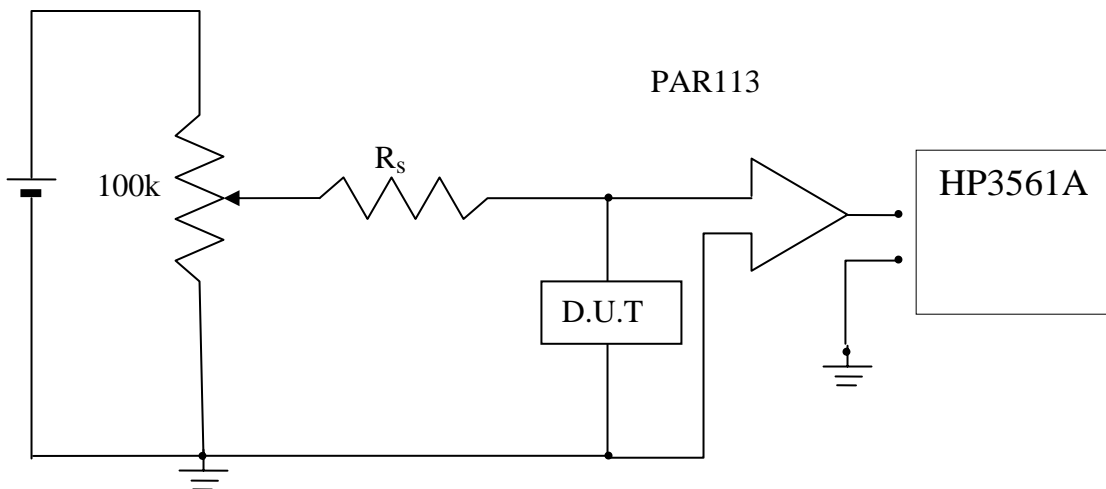


**Fig. 3.19: Circuit representation of a typical noise measurement setup.**

The complete noise measurement setup is configured in a noise shielded room. Such a shielded room helps in avoiding influence of the extraneous noise sources, such as electrical transmission lines. The experimental setup consists of following typical components:

1. ***Device Under Test (DUT)***- that is the test device itself.
2. ***A Bias Box***- contains a biasing circuitry designed to facilitate current bias for a particular test device. A series resistance is used that is at least 30 times larger in ohmic resistance than the test device. Standard lead-acid batteries are used to construct the voltage source. All noise-passive sources, like lead-acid cells, metal-film resistors were used to construct a noise free bias source.
3. ***Low Noise Preamplifier (LNA)***- is used to amplify the signals across the device terminals, typically with a gain factor of 10000. PAR-113 was used for this purpose.
4. ***Dynamic Signal Analyze***- is used to analyze the amplified signals from LNA. For this work, HP3561A was used. The basic operating principle of the analyzer is to collect the signal time data, digitize it and make a conversion to the frequency domain by discrete fast Fourier transformation (FFT). The analyzer presents (among other options) the power spectral density of the voltage noise at the analyzer input in  $V^2/Hz$ , averaged from at least 500 sweeps according to user settings.

The above constitutes the basic noise measurement setup, however, for low-temperature measurements two more components are required.

5. *Cryostat*- is used to facilitate a cryogenic environment to the test device, when the device is placed inside a cryostat. In our experiments an exchange gas cryostat or a continuous flow cryostat was used. Liquid Nitrogen was used as the cryogen.
6. *Temperature Controller*- is used to facilitate thermal equilibrium to the test device at a desired cryogenic temperature. Lakeshore 91C temperature controller was used for the experiments.

The measurements are usually performed in the frequency domain by measuring the power spectral density with a spectrum analyzer. The low-frequency noise in a device is sensitive to the device technology, especially the presence of traps, defects and crystal damage. Therefore, important information about reliability and sensitive areas for the current transport can be attained from noise studies. As per the need of a designed experiment, specific details are provided in the next chapter at appropriate places.

### **3.5 Epifluorescence Microscopy**

Epifluorescence microscopy was used for the optical inspection of human osteoblast cells which were used for the biosensor investigation. Basic information about this technique is provided in this section. In a normal bright field microscope, light passes through a thin specimen on a glass slide and is viewed through the eye piece. Fluorescence microscopy<sup>39</sup> differs from in that the visible light in the microscope eyepieces is not the original light emitted by the light source. The light seen is actually the light that has fluoresced from the fluorescing microscope specimen. A

high intensity light source is used. This light is passed through a dichroic filter cube containing a fluorescence bandpass excitation filter. Only specific wavelengths of light are allowed to pass and reach the fluorescence specimen. After the incident filtered light reaches the specimen, it is no longer used, and any amount reflecting back into the microscope objective to the dichroic filter is filtered out by the emission filter. The specimen fluoresces and it is this fluorescing light that passes back through the fluorescence emission filter and goes to the microscope eyepieces to provide a fluorescence image of the specimen. Confocal<sup>40</sup> microscope is a specific application of epifluorescence microscopy, widely used for fluorescence imaging of biological samples. A major application of confocal microscopy involves imaging either fixed or living cells and tissues that have usually been labeled with one or more fluorescent probes. Confocal microscopy offers several advantages over conventional optical microscopy, including shallow depth of field, elimination of out-of-focus glare, and the ability to collect serial optical sections from thick specimens. When fluorescent specimens are imaged using a conventional widefield optical microscope, secondary fluorescence emitted by the specimen that appears away from the region of interest often interferes with the resolution of those features that are in focus. This situation is especially problematic for specimens having a thickness greater than about two micrometers. The confocal imaging approach provides a marginal improvement in both axial and lateral resolution, but it is the ability of the instrument to exclude from the image the out-of focus flare that occurs in thick fluorescently labeled specimens. Resolution in the laser scanning confocal microscope is somewhat better than in the conventional widefield optical

microscope. The illumination is achieved by scanning one or more focused beams of light, usually from a laser, across the specimen. The images produced by scanning the specimen in this way are called optical sections. This terminology refers to the noninvasive method by which the instrument collects images, using focused light rather than physical means to section the specimen. In order to build an image using the confocal principle, the focused spot of light must be scanned across the specimen. Movement of the specimen can cause wobble and distortion, resulting in a loss of resolution in the image. The final resolution achieved by the instrument is governed by the wavelength of light, the objective lens, and the properties of the specimen itself. The dyes are used to add contrast to specimens. The image is serially built up from the output of a photomultiplier tube or captured using a digital camera incorporating a charge-coupled device, directly processed in a computer imaging system, displayed on a high-resolution video monitor. For the present work, propidium iodide dye that give red fluorescence, was used for color contrast and Nikon's Eclipse-TS100, and Eclipse-FN1 microscopes were used for the visual inspection of the cultured cells.

### **3.6 Cell Culture**

Cell culture is a process used for growing biological cells in controlled conditions. The controlled condition implies that cells are grown and maintained at a particular temperature and gas mixture (typically, 37 C and 5% carbon dioxide) in a cell incubator. Incubator is the instrument that facilitates a controlled environment to the

cells and maintains appropriate levels of humidity, gasses and temperature. Humidity is maintained above 95% and a significant amount of carbon dioxide helps keep a slightly acidic pH. In addition to growth environment, the most commonly varied factor in culture systems is the growth medium. Medium is a biochemical solution, in which cells are kept and this medium acts as a means to supply the nutrients to cell for their growth. It also provides protection against viruses. Cells generally continue to divide in process of culture. They divide and grow in number to fill the available area or volume. For this work, HERA Cell 150 incubator was used in which, a growth temperature of 37 C and 5% carbon dioxide was maintained. Human osteoblast-like cells from saos-2 cell line (ATCC, USA) were used for the experiments and standard McCoy's 5A medium was used as for the cell culture.

## REFERENCES (CHAPTER 3)

- 
- <sup>1</sup> Brandt et al., *Appl. Phys. Lett.*, Vol. 83, p 90, 2003.
- <sup>2</sup> Jas et al. in *MRS Internet J. Nitride Semicond. Res.*, 5S1, W3.81, 2000.
- <sup>3</sup> Nakamura et al., *Appl. Phys. Lett.*, Vol. 69, p. 4056, 1996.
- <sup>4</sup> A. Cho, "Film Deposition by Molecular Beam Techniques," *J. Vac. Sci. Tech.*, Vol. 8, p S31, 1971.
- <sup>5</sup> A. Cho, and J. Arthur, "Molecular Beam Epitaxy," *Prog. Solid-State Chem.*, Vol. 10, p. 157, 1975.
- <sup>6</sup> T. Moustakas and R. Molnar, "Growth and doping of GaN films by ECR assisted MBE," *Mat. Res. Symp. Proc.*, Vol. 281, p753, 1993.
- <sup>7</sup> D. Connor, B. Sexton, and C. Smart, "Surface Analysis Methods in Materials Science," *Springer, Physics and Astronomy*, 2003.
- <sup>8</sup> John C. Vickerman, "Surface Analysis-The Principal Techniques," *John Wiley & Sons*, 1997.
- <sup>9</sup> Schremer et al., "High electron mobility AlGaInGaN heterostructure on (111) Si," *Appl. Phys. Lett.*, Vol. 76, p. 736, 2000.
- <sup>10</sup> Lee et al., "Improvement of Electrical Properties of MOCVD Grown Al<sub>x</sub>Ga<sub>1-x</sub>N/GaN Heterostructure with Isoelectronic Al-Doped Channel," *phys. stat. sol. (c)* Vol. 1, p. 240, 2002.
- <sup>11</sup> Jeganathan et al., "Two-dimensional electron gases induced by polarization charges in AlInGaN heterostructure grown by plasma-assisted molecular-beam epitaxy," *Journal of Appl. Phys.*, Vol. 94, p. 3260, 2003.
- <sup>12</sup> Miller et al., "Reduction of reverse-bias leakage current in Schottky diodes on GaN grown by molecular-beam epitaxy using surface modification with an atomic force microscope," *Journal of Appl. Phys.*, Vol. 91, p. 9821, 2002.
- <sup>13</sup> Binning et al., "7X7 Reconstruction on Si (111) Resolved in Real Space", *Physical Rev. Lett.*, Vol. 50, p. 120, 1983.
- <sup>14</sup> Binning et al., "Atomic Force Microscopy," *Physical Rev. Lett.*, Vol. 56, p. 930, 1986.
- <sup>15</sup> Binning et al., "Atomic resolution with atomic force microscopy," *Europhys. Letters*, Vol. 3, p. 1281, 1987.
- <sup>16</sup> Martin et al., "Atomic Force Microscope mapping and profiling on a sub 100 Å scale," *Journal of Appl. Phys.*, Vol. 61, p. 4723, 1987.
- <sup>17</sup> University of Sheffield, <http://www.shef.ac.uk/>

- 
- <sup>18</sup> Bruker AXS homepage, [www.bruker-axs.com](http://www.bruker-axs.com).
- <sup>19</sup> R. Jenkins and L. Snyder, "Introduction to X-ray Powder Diffractometry," ed.: Winefordner, J.D.: *Chemical Analysis*, Vol. 138. New York, John Wiley, (1996).
- <sup>20</sup> HL5500PC Operator's Manual.
- <sup>21</sup> "Hall Measurement", a laboratory report, in Drexel University, U.S.
- <sup>22</sup> <http://www.eeel.nist.gov/812/intr.htm>
- <sup>23</sup> A. Chaddha et al., "Thermally stable, low specific resistance TiC Ohmic contacts to n-type 6H-SiC", *Appl. Phys. Lett.*, Vol. 66, p. 760, 1995.
- <sup>24</sup> J. Foresi and T. D. Moustakas, "Metal contacts to gallium nitride," *Appl. Phys. Lett.*, Vol. 62, p. 2859, 1993.
- <sup>25</sup> R. Landauer, "The noise is the signal," *Nature*, Vol. 392, p. 658, 1998.
- <sup>26</sup> B. Jones, "Low-frequency noise spectroscopy," *IEEE Trans. on Electron Devices*, Vol. 41, p. 2188, 1994.
- <sup>27</sup> A. van der Ziel, "Advanced Electronic Electron Physics," *Academic Press, New York*, 1987.
- <sup>28</sup> F. Hooge and L. Vandamme, "Lattice scattering causes 1-f noise," *Phys. Lett. A*, Vol. 66, p. 315, 1978.
- <sup>29</sup> F. Hooge, T. Kleinpenning and L. Vandamme, "Experimental studies on 1/f noise," *Reports on Progress in Physics*, Vol. 44, p. 479, 1981.
- <sup>30</sup> F. Hooge, "1/f noise is no surface effect," *Physics Letters A*, Vol. 29, p.139, 1969.
- <sup>31</sup> F. Hooge, "1/f noise sources," *IEEE Trans. on Electron Devices*, Vol. 41, p. 1926, 1994.
- <sup>32</sup> P. Handel, *Phys. Rev. Lett.*, Vol. 34, p. 1492, 1975.
- <sup>33</sup> P. Handel, in Proc. 7<sup>th</sup> Int. Conf. Noise in Physical Systems and 3<sup>rd</sup> Int Conf. on 1/f noise, ed. M Savelli, G. Lecoy, and J. P. Nougier, Montpellier, 1983, p. 97.
- <sup>34</sup> A. McWarter, Ph.D. Thesis, MIT, Lincoln Lab. Technical Report, Publ. 80, 1955.
- <sup>35</sup> A. van der ziel et al., "Noise in Solid State Devices," in *Advances in Electronics and Electron Physics*, ed. L. Marton: Academic Press, 1978, p. 225.
- <sup>36</sup> C. Surya and T.Y. Hsiang, "A thermal activation model for 1 / f noise in Si-MOSFETs," *Solid-state Electron.*, Pergamon, U.K., 1988, pp. 959 - 964.
- <sup>37</sup> M. Surdin, *J. Phys. Radium, Serie 10* (1939) 188.
- <sup>38</sup> P. Dutta et al., *Phys. Rev. Lett.*, Vol. 43, p. 646, 1979.
- <sup>39</sup> <http://epifluorescencemicroscopes.com/>
- <sup>40</sup> <http://www.microscopyu.com/articles/confocal/>

## CHAPTER 4

### RESULTS AND DISCUSSIONS

---

#### *Part I - Degradation Monitoring In AlGaIn/GaN Heterostructures Based Recessed-Gate HEMTs.*

To achieve better performance in GaN-based HEMTs, gate-recessing is used to provide improvements in the transconductance of the devices. The technique is also used to reduce source resistance, which is particularly beneficial for high frequency applications. Reactive ion etching is typically used for the formation of gate recesses. The process involves the use of energetic ions and may cause physical damages to the material in the recessed regions. This will strongly affect the integrity and the lifetimes of the devices. Influence of recess induced damage on the life time of devices can be studied using hot-electron stressing. Previous studies of hot-electron injection in Si-MOSFETs showed that the process leads to the degradation in the drain current ( $I_D$ ) and transconductance of the device. Low-frequency noise characterizations indicated that the degradations in the device characteristics originate from the generation of traps at the Si-SiO<sub>2</sub> interface. Experimental studies of hot-electron injection in GaN-based HEMTs exhibited a more complicated behavior. Results by Sahoo<sup>1</sup> *et al.* indicated significant degradations in the drain current,  $I_D$ , and the transconductance of GaN-HEMTs when the devices were subjected to high-voltage stress over short stress time ( $t_S$ ) of approximately 60 seconds. However, upon further stressing for a period up to about one hour, partial recovery in the device characteristics was observed. The physical mechanism

underlying this behavior is still a point of contention. It is important to establish the detailed mechanism for the degradation of GaN-HEMTs and the effects on device reliability due to the recess formation process, in order to fully understand the behavior and limitations of the device under high power operations<sup>2-3</sup>.

Prior to this work, no study has been reported to investigate the effects of gate recess formation on reliability of the GaN-based devices. In this part, detailed investigations were performed to examine the physical mechanisms underlying the low-frequency fluctuations. Degradation of noise properties caused by high dc voltage bias stress applied across the conduction channel was monitored with stress time  $t_S$ . Studies on the effects of gate-recess formation on the electronic properties of the HEMTs are also presented. An important aspect of the study is on the characterizations of the low-frequency excess noise. It is an important figure-of-merit of the device and is shown to be an effective tool<sup>4,5</sup> for monitoring the integrity of the semiconductor devices.

#### **4.1.1 Investigation Objectives**

To address the reliability concerns of GaN HEMTs, investigation objectives were broadly identified as follows:

- (i) Influence of recess on device noise performance
- (ii) influence of recess on device life time
- (iii) Influence of bias-stress on the stability of device properties
- (iv) Physical mechanism underlying the low-frequency noise in GaN HEMTs

## **4.1.2 Methodology**

An appropriate investigation methodology was adopted based on following considerations:

### **4.1.2.1 Variation in Device Type**

To compare the effect of recess, both recessed and unrecessed devices should be on the same AlGaIn/GaN heterostructure. Same epilayer scheme of heterostructures and processing them in one batch ensures the least influence of material and process induced variations. Two to three variations of recess depth ( $d_r$ ) would be fare to make better conclusions. HEMT devices with different recess depths and with no recess were fabricated on the same heterostructure films in the same batch process.

### **4.1.2.2 Characterization Method**

A consistent scheme of characterization is required to probe the differences in various HEMT structures. This characterization method must not influence the device properties during characterization at any point of time. Else, the results will appear which will be difficult to make strong conclusions. Usually, electrical characterization is used to study the reliability and degradation in the device community. However, it has repeatedly been observed that even the simplest characterization like  $I$ - $V$  'disturbs' the devices temporarily for prolonged durations. As the GaN-based structures are highly defect sensitive, the influence of effects produced by electrical characterization techniques could be strong enough to compete with the intrinsic effects which are characteristic of the material or structural changes under observation.

### 4.1.2.3 Stress Method

A unique means to *disturb* the devices from their *present physical details* is required. For simplicity one such measure could be bias stress to the device. If the bias stress is to be used for such purpose, it could be questionable to choose the *electrical characterization* to probe the intrinsic effects induced by the stress.

There are two types of bias stresses: stressing at constant current (current-bias) and stressing at constant voltage (voltage-bias). To keep consistency and simplicity of the overall characterization scheme, voltage bias is a better choice in case of the studied devices. This is explained further. If the constant current is chosen for stressing, different devices with different recess and with different current capabilities will actually be stressed unequally. Even the same device will be unequally stressed with aging, thus making it difficult to interpret the complete set of data. Alternatively, using a unique constant voltage stress for all devices will allow comparable electric fields with comparable distribution along the conduction channel. This is because the devices have same gate-length and width. They vary only in recess depth.

To choose an appropriate value of the voltage bias stress, a suitable criterion can be: a bias that is two times of the knee voltage at zero gate bias. As the knee voltage for all the devices are comparable and close enough, this criterion nicely fits with the above stated scheme. A moderately large bias will also ensure the degradation monitoring at a slower pace. This will help in recording those stress effects which occur in the early phases and disappears later.

Keeping the above discussion in mind use of bias-stress as a *disturbing-tool*, and *low-frequency noise* as a probing tool is adopted. As the noise experiments are performed at a very small bias, it is unlikely that devices will be affected electrically. As the noise is a characteristic quality of the device, influence of bias stress on material structure can be unambiguously detected and interpreted by noise investigations. In addition, as the noise properties are strongly influenced by the material quality, it is one of the best nondestructive tools to characterize the material related influences of recess and stressing of the devices. Thus, a characterization-stress-characterization cycle was used to monitor the long term degradation process.

### 4.1.3 Device Fabrication

GaN-based HEMTs were fabricated using MOCVD-grown AlGaIn/GaN heterostructures on sapphire substrates. A 1.5  $\mu\text{m}$  thick semi-insulating GaN layer was grown on top of a 50 nm thick low-temperature GaN buffer layer. This was followed by the growth of a 30 nm thick AlGaIn layer, consisting of a 15 nm Si-doped layer and a 15 nm thick spacer layer. A GaN cap layer of thickness around 2.5 nm was deposited on top of the AlGaIn layer. Schematic cross-sectional diagram of the epilayer design used for the device is shown in Fig. 4.1. The gate recess was created by reactive ion etching (RIE) process with a mixture of Argon and Freon at 100 V dc bias and 70 W HF power. Gate length of the devices was 2  $\mu\text{m}$ . Devices have a typical width of 100  $\mu\text{m}$ , as used for characterization, though some devices with different widths in the range 50  $\mu\text{m}$  – 300  $\mu\text{m}$  were also fabricated. Devices with different  $d_r$  were fabricated by reactive ion etching as listed here: Device A – 6 nm; Device B – 12 nm; Device C – 18 nm; and Device D – 0 nm (control device).

Ohmic contacts to the source and the drain regions were accomplished by deposition of Ti/Al/Au (20/120/200 nm) pads in an e-beam chamber, followed by annealing at 870°C for 45 seconds in a rapid thermal annealer. Schottky contacts in the gate regions were formed by deposition of Ni/Au (100/150 nm) double layer by e-beam evaporation at the base pressure of  $\sim 10^{-8}$  mbar. The fabrication process did not incorporate any surface passivation.

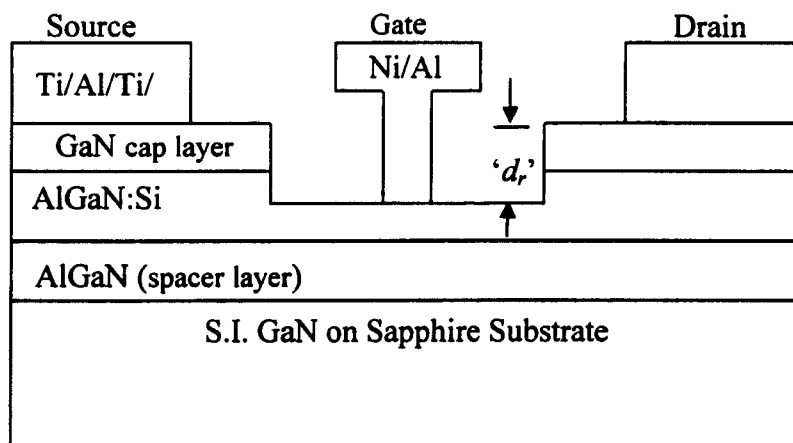


**Fig. 4.1: Schematic cross-sections of the recessed gate AlGaIn/GaN HEMTs.**

#### 4.1.3.2 Chip and Device lay-out

SEM image of the lay-out of a HEMT chip after complete fabrication process is shown in Fig. 4.2. HEMT devices with different gate width are visible. TLM patterns are seen in the region between two different groups of HEMTs. SEM image of a HEMT transistor is shown in Fig. 4.3. The HEMT device has a 'Π' gate geometry that is visible in the layout.

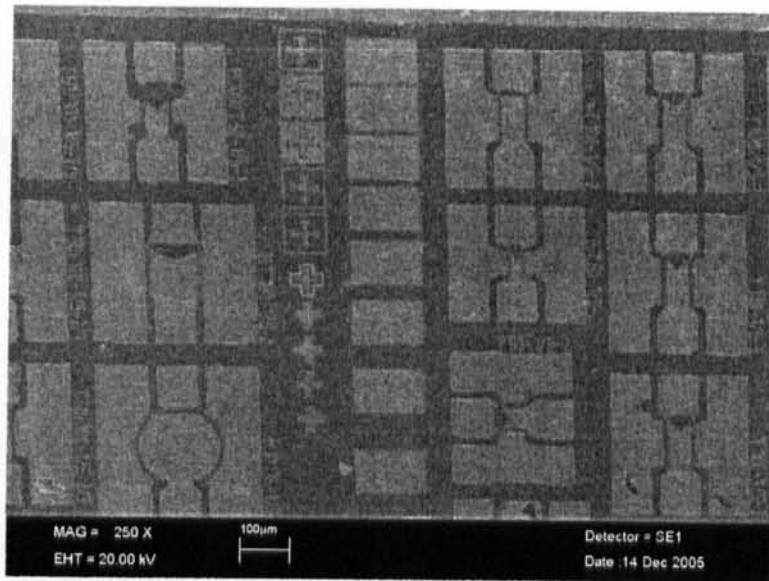


**Fig. 4.2: SEM image of a HEMT chip.**

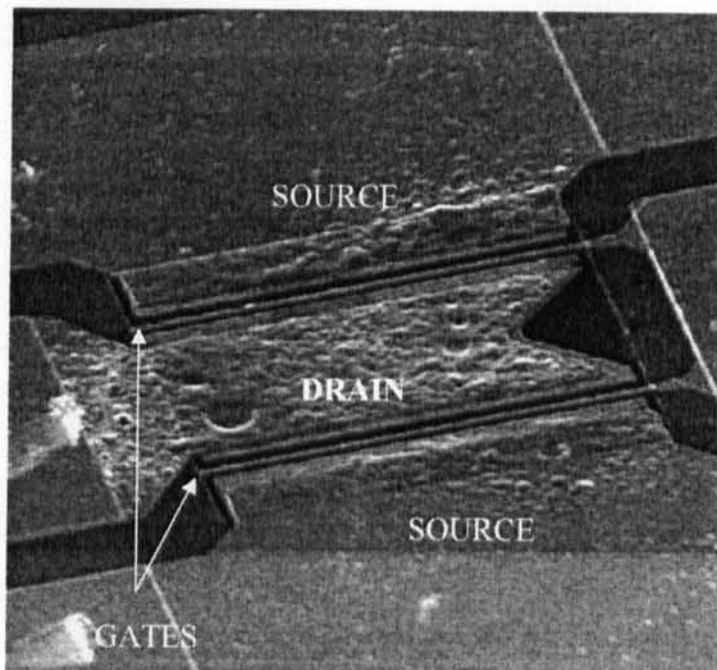


**Fig. 4.3: SEM image of a recessed HEMT device.**

#### 4.1.3.3 Electrical interface with Devices

A very limited interaction with the device is possible using contact probes. For the desired experiments devices are required to be subjected to different set of instruments, frequently. So, a reliable electrical interface with the device is required that lasts till the end of experiments. Such an interface method must not affect the noise measurements and should be easy to handle with reliable contact at room and cryogenic temperatures. Considering all these factors, it was decided to use the devices placed on ceramic packages. Electrical contacts of devices were ultrasonically wire bonded with a 1-mil Aluminium wire that connects them to the external contact pins on the package, as shown in Fig. 4.4.

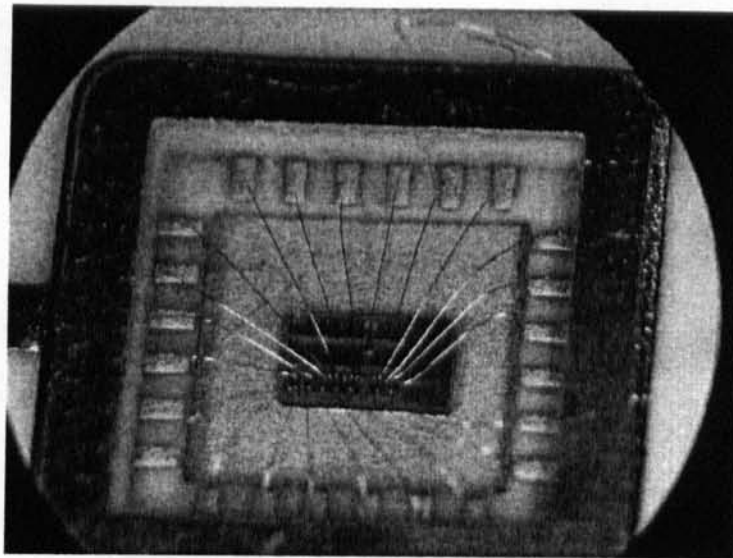


**Fig. 4.4: A chip containing HEMT devices bonded on a 24-pin DUI ceramic package.**

#### 4.1.4 Experimental Setup and Characterization Process

The transistor characteristics of the devices were measured with a Keithley Model-251 measurement system. All-passive sources were used for device biasing to minimize the system noise. For the noise experiments, the current source is constructed using a lead acid battery connected in series with a metal film resistor which is at least 30 times as large as the channel resistance. A large series resistance ensures a constant current through the device even in the presence of a small fluctuation in the device resistance. The fundamental trapping and detrapping process in the channel regions leads to the fluctuation in the conductance of the 2DEG. Hence, the application of a constant current through the 2DEG will produce a corresponding fluctuating voltage across the drain source region. These fluctuation signals were amplified using a PAR 113 low-noise preamplifier and  $S_V(f)$  was measured using an HP3561A dynamic signal analyser. For low-temperature measurements the devices were placed inside a continuous-flow cryostat using liquid nitrogen as the cryogen. The temperature variation of the device was kept within  $\pm 0.3$  K over the duration of the experiments using a Lakeshore 91C temperature controller equipped with a Si diode temperature sensor.

At first, initial dc and room temperature noise characteristics of all types of devices were recorded to study the general variation in noise characteristics with recess depth. Temperature dependence of noise in HEMT devices before (when it is virgin) and after the final stress experiments was recorded. As stated earlier, a characterize-stress-characterize cycle was used to induce and monitor the degradation. Bias stress was stopped when at least two orders of magnitude increase

in the noise power was observed after a number of stress cycles. Low-temperature noise characterization was then again performed. In addition, a different set of low-temperature noise experiments were performed only at liquid nitrogen temperature to investigate the percolation mechanism as detail further in a later section.

#### **4.1.4.1 Stress Bias condition**

The devices were subjected to dc voltage stressing at  $V_D = 10V$  and  $V_G = 0V$ .

#### **4.1.4.2 Noise Bias condition**

For the room-temperature noise measurements, the conduction channels were current biased at  $V_D = 0.22V$  with  $V_G = -1.5V$ . At this bias, devices are set to operate in the linear regime and current flow under such condition is small enough so the devices are essentially in thermal equilibrium. This condition enables a very stable and reliable acquisition of noise data without affecting the electrical or material condition of the device. The series resistance of the current source was set at about 30 times that of the channel resistances of the devices.

#### **4.1.4.3 Background Noise**

Before initiating the detailed room temperature and low-temperature noise investigation, background noise of the measurement system was recorded. Noise background was measured by replacing the device with a  $100 \Omega$  metal film resistor, and is shown in Fig. 4.5. From the figure, we find that background noise is essentially white noise with a power magnitude of  $\sim 10^{-16} V^2/Hz$ .

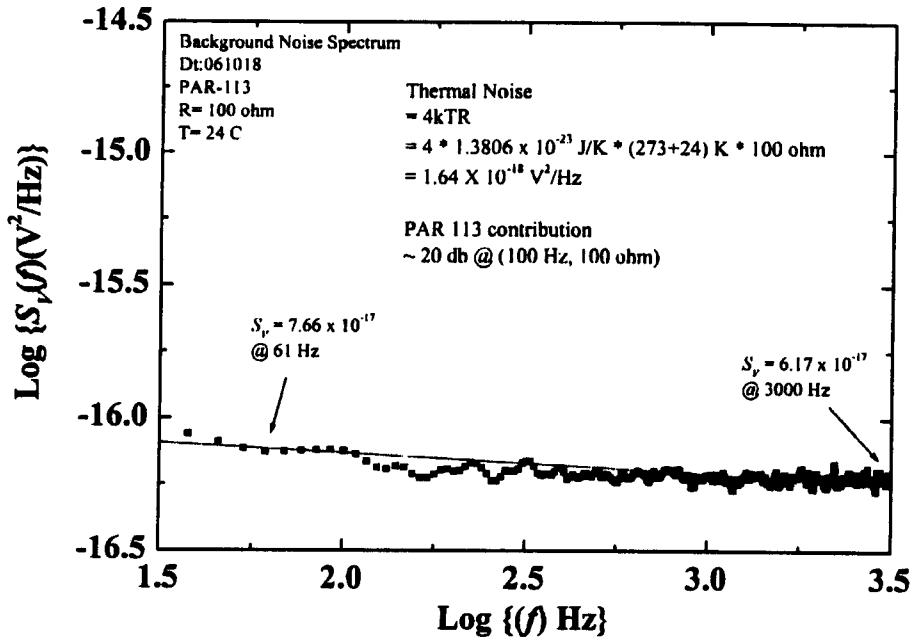
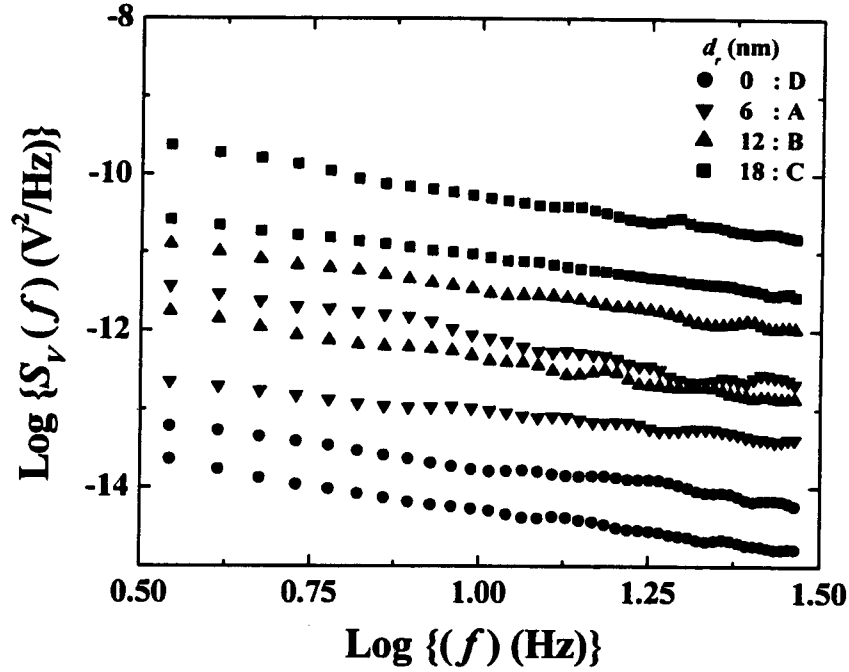


Fig. 4.5: Background noise of the measurement system.

#### 4.1.5 Effect of Gate Recess on Noise Properties

About 10 devices of each type were subjected to room-temperature noise characterization to see the influence of recess depth. It was found that the noise power magnitude observed for any particular device type show variations. Noise power spectra which refer to the maximum and minimum power magnitude for each device type are shown in Fig. 4.6.



**Fig. 4.6: Noise power spectra of devices with different  $d_r$ .**

A general observation from the above results is that all devices, irrespective of their recess depth, show almost  $1/f$  dependence for  $S_V(f)$ . It is evident that the control devices (device D) show the lowest noise levels while the device C, show highest value for  $S_V(f)$ . This is not unexpected, as the device C supposedly has the largest recess etching, resulting in highest defect density under the gate which will effectively influence the channel noise. A clearer observation of the influence of recess on  $S_V(f)$  is noticed when the noise power, at a fixed frequency, is plotted against  $d_r$ . Maximum ( $S_{V_{max}}$ ) and minimum ( $S_{V_{min}}$ ) magnitude of  $S_V$ , observed for a particular device type, are plotted against  $d_r$ , as shown in Fig. 4.7.

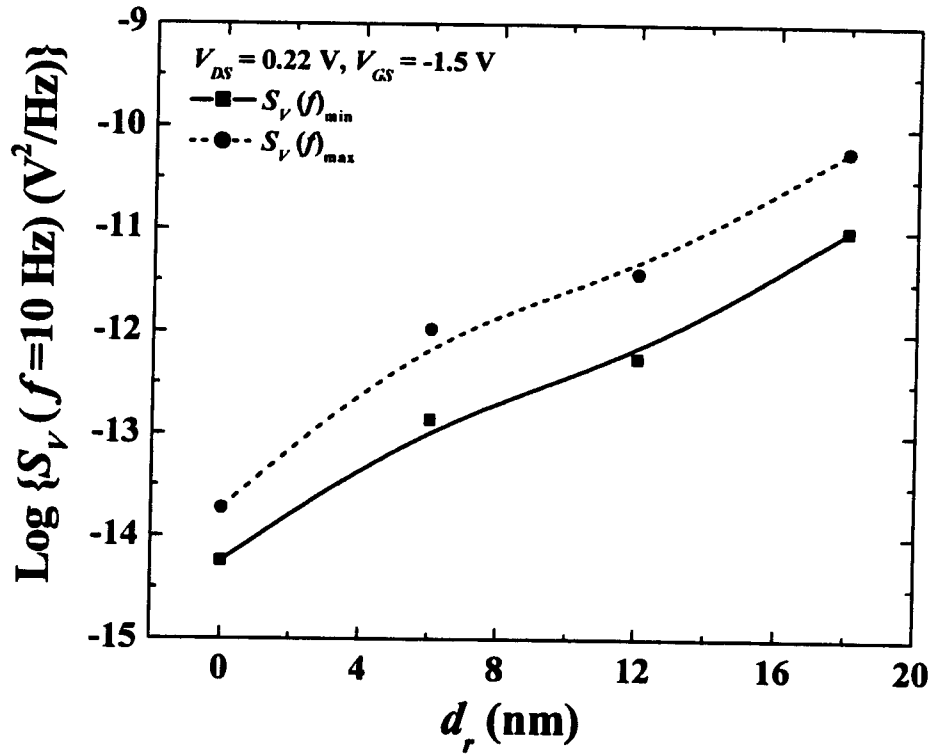


**Fig. 4.7: Dependence of  $S_V$  on  $d_r$  as observed at  $f = 10$  Hz, for the maximum and minimum value of  $S_V$ .**

From the graph, it is noted that:

- 1) There is about an order of magnitude variation in  $S_V$  for any particular device type
- 2) This variation is comparably smaller for device D
- 3) A large increase in  $S_V$  is seen with  $d_r$  when it undergoes transition from  $d_r = 0$  nm to  $d_r = 6$  nm

A variation in the noise spectral density for a particular device can be the result of intrinsic variation in material properties within the same chip area. Such a variation

would be statistically similar for any device type, as noted. Observations suggest that a large number of defects are created when a recess is formed as reflected in a rapid transition from non recess to recess structures. As the noise power is typically proportional to the defect density, it is suggested that defects induced by the etching process depends very strongly on the magnitude of etch depth. In first inspection, this has faster than exponential dependence. When the data points corresponding to recessed devices are extrapolated smoothly over the vertical axis, it is predicted that the noise level corresponding to a hypothetical zero recess will be more than half an order higher, in comparison to the experimental data for device D. A large difference in predicted and real magnitude of noise power for an unrecessed device indicates that even if a few monolayers are etched under the gate, considerable generation of defects will take place that will strongly influence the noise and electrical characteristics of the devices.

#### **4.1.6 Degradation Monitoring in a Recessed HEMT device**

After acquiring a general idea of the typical noise properties of the different devices, stress experiments were then performed to study the stress induced device degradation effects. In this section, degradation monitoring in Device-A is presented. Later, results on other devices shall also be discussed to build up on the knowledge gained in this process. To start the monitoring process, first, dc characterization was performed. Typical  $I$ - $V$  characteristics of a virgin HEMT device for  $V_{GS} = 0$  V to  $V_{GS} = -4$  V with a step of -0.5 V, and Transfer characteristics at  $V_{DS} = 5$  V, are shown in Fig. 4.8.

Saturation drain current,  $I_{DSS}$ , of this device is about 16 mA at  $V_{GS} = 0$  V. Transfer characteristics are presented for  $V_{DS} = 5$  V. The graph indicates that pinch off occurs at a threshold gate voltage,  $V_{Th}$ ,  $\sim -2.75$  V but the device does not show a hard pinch off and a considerable leakage current is seen. The maximum value of the transconductance measured at  $V_{GS} = 0$  V  $G_{Mmax}$  is about 130 ms/mm. After dc characterization, systematic characterizations of  $S_V(f)$  across the conduction channels were performed to monitor the degradation of the device properties with stress time. After every stress session, devices were relaxed for 10 minutes before they were subjected to characterization. The cycle was repeated until the observation of about two orders of magnitude increase in  $S_V(f)$ . In the first phase, fluctuations in the noise power spectra, about a relatively constant value, are observed. This phase lasts for about 175 hours. In the second phase, rapid degradation in the  $S_V(f)$  of the devices is observed. The degradation observed in this phase is irreversible and is accompanied by the general breakdown of the device characteristics.

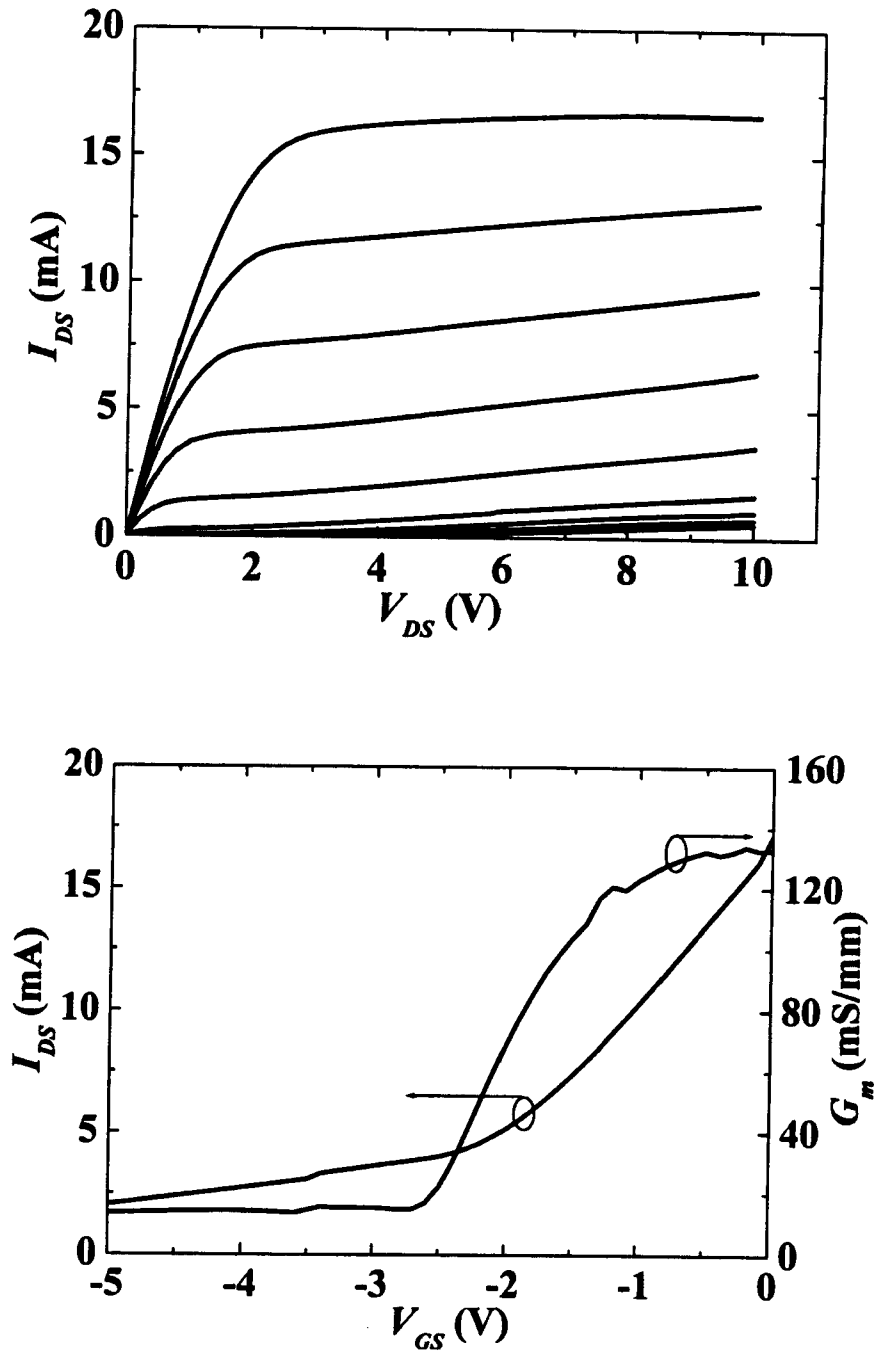


**Fig. 4.8:** Typical  $I$ - $V$  characteristics (top) of a virgin Device A (for  $V_{GS} = 0$  V to  $V_{GS} = -4$  V with a step of  $-0.5$  V, and Transfer characteristics (bottom) of the device at  $V_{DS} = 5$  V.

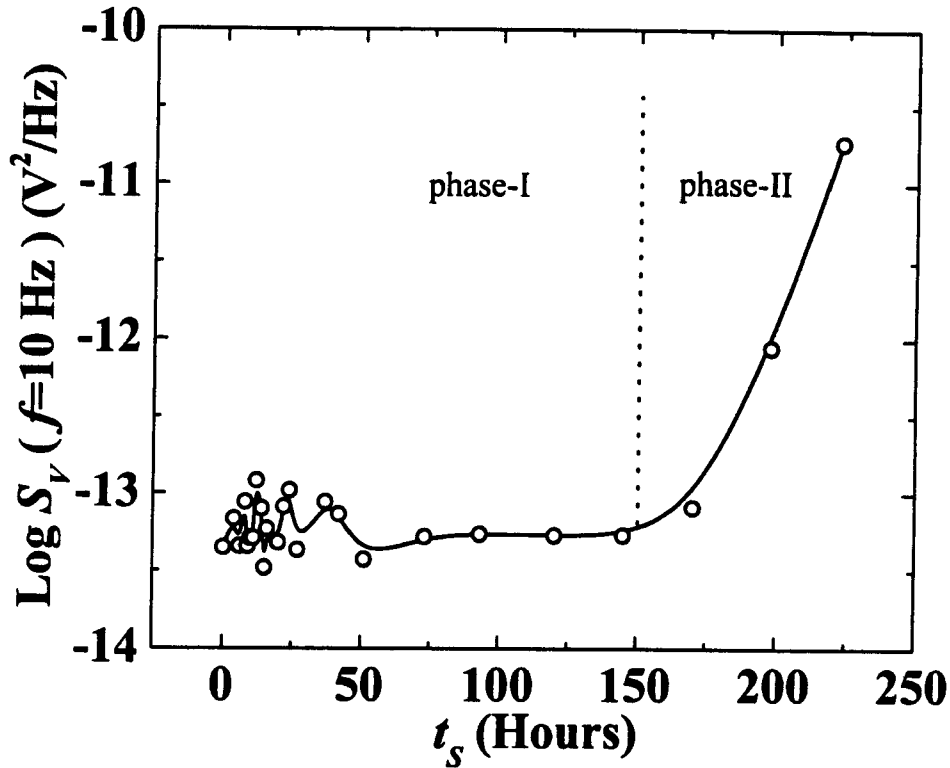


**Fig. 4.9:** Experimental  $S_v(f)$  recorded at  $V_{DS} = 0.22$  V and  $V_{GS} = -1.5$  V, plotted as a function of stress time,  $t_s$ , for Device A ( $d_r = 6$  nm).

#### 4.1.7 Degradation Dependence on Recess Depth

It was found that lifetime of an individual device with a particular  $d_r$ , vary substantially from one to another. They all reveal the same pattern in their low-frequency noise characteristics as a function of stress time, as shown in Fig. 4.10. It was observed that a very sharp increase in  $S_v(f)$  occurs in Device C ( $d_r = 18$  nm) even for a short stress duration of a few hours, after which it suffers breakdown.

This indicates a very short life time for Device C. Hence, it was not possible to get a long duration stress profile for these devices.

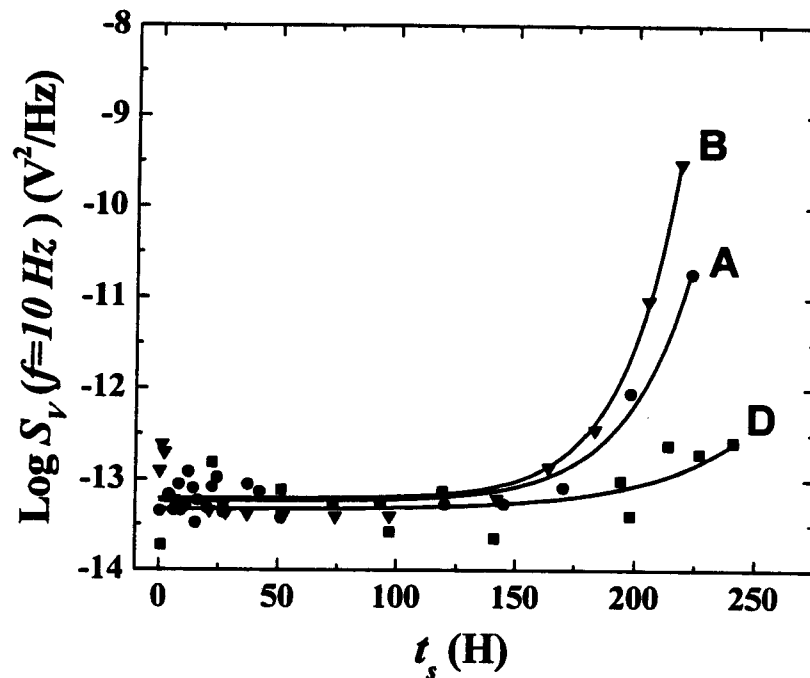


**Fig. 4.10: Experimental  $S_v(f)$  recorded at  $V_{DS} = 0.22$  V and  $V_{GS} = -1.5$  V, plotted as a function of stress time,  $t_s$ , for the devices A (solid spheres), B (solid triangles, and D (solid squares). Solid lines represent exponential fits to the original data points.**

A short life time of these devices may result from the damage created by a deep recess etching. In deeply etched devices remaining depth of AlGaIn layer can approach to a very narrow thickness due to uncontrollability of etching process over ultra thin material layers. Following points can be noted from Fig. 4.10:

- 1) In the initial part ( $0 < t_S < 25$ ) of phase-I, fluctuations in  $S_V(f)$  is evident for all devices, that lasts for about 25 hours. The fluctuation is of about an order in magnitude for any particular device;
- 2) For a particular device,  $S_V(f)$  settles down after this, and shows almost constant and very slow variation with  $t_S$  until near the start of phase-II;
- 3) All the devices, irrespective of the recess depth, show a fast increase in  $S_V(f)$  near the beginning of phase-II;
- 4) An aggressive increase is seen for the recessed devices (A, B) in comparison to the unrecessed device-D.

### 4.1.8 Degradation Mechanism

Degradation observed by the bias stress may be a result of hot-electron induced degradation. Based on a two-dimensional charge control model of HEMT, lateral electric field at the device surface is given by following equations<sup>6</sup>:

In the low-field region,

$$E(x) = \frac{I_{Dsat}}{\sqrt{\left(\frac{I_{Dsat}}{E_c} - \lambda V_{gt}\right)^2 - 2\lambda \left(\left(\lambda V_{gt} - \frac{I_{Dsat}}{E_c}\right) I_{Dsat} R_s - \frac{\lambda}{2} I_{Dsat}^2 R_s^2 + x I_{Dsat}\right)}}; 0 < x < L_1, \quad 4.1$$

where,  $\lambda = \frac{L_G \mu_0 \epsilon}{d_h}$ ;  $V_{gt} = V_{GS} - V_{th}$ ,

and in the high-field region,

$$E(x') = E_c \text{Cosh}\left(\frac{\pi}{2d_h}(x')\right); L_1 < x' < L_G. \quad 4.2$$

In the above equations,  $I_{Dsat}$  is the saturation drain current,  $E_c$  is the critical field,  $R_s$  is the dc source resistance,  $L_G$  is the gate-length,  $\mu_0$  is the low-field mobility,  $d_h$  is the effective thickness of the heterostructure interface, and  $\epsilon$  is the dielectric constant.  $L_1$  is the effective channel length, which represents the extent of the low-field region, given by:

$$L_1 = \frac{\lambda V_{gt}^2}{2I_{Dsat}} - \frac{V_{gt}}{E_c} + \left(\frac{\lambda R_s^2 E_c + 2R_s}{2E_c}\right) I_{Dsat} - \lambda V_{gt} R_s. \quad 4.3$$

Using this model, calculated field profile under the gate of an unrecessed device having a gate-length of 2  $\mu\text{m}$  when subjected to stress bias condition of  $V_{DS} = 10\text{V}$  and  $V_{GS} = 0\text{V}$  is plotted in Fig. 4.11. It is observed that near the drain end, lateral

electric field is  $\sim 100$  kV/cm and is confined in a very small dimension. Such a large field can support the hot-electron induced phenomenon. However, influence of the Joule-heating cannot be ignored.

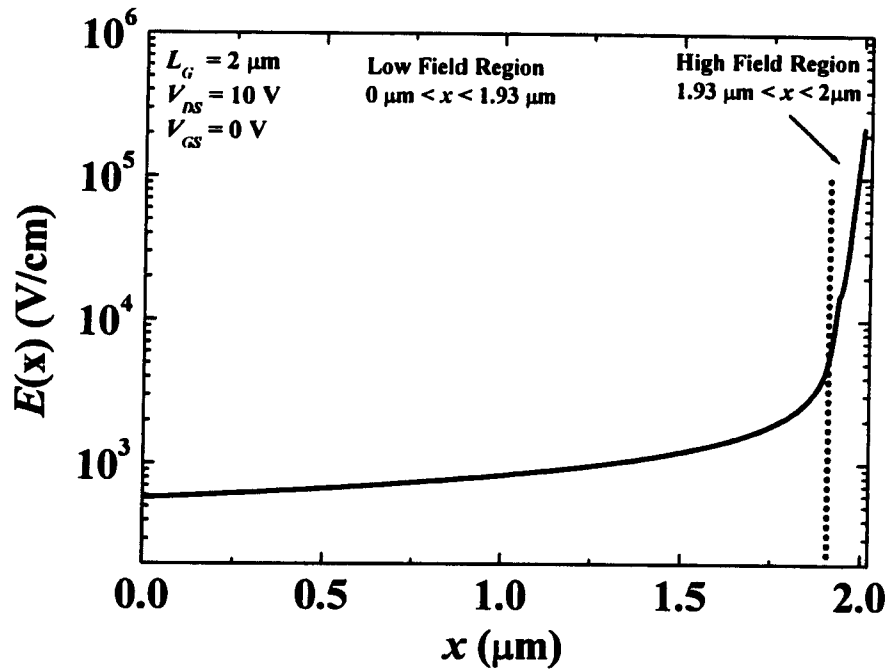


**Fig. 4.11: Calculated lateral electric field along the channel under the gate of an unrecessed HEMT device.**

## Estimation of Trap Density

As a result of the degradation process, a large number of traps are generated. The density of these traps can be estimated using the Eq. 3.48. Based on the low-temperature noise data taken before and after the stress experiments with Device A, trap density  $\{N_T(E)\}$  was calculated as shown in Fig. 4.12. It was found that stress induced permanent degradation of the AlGaIn/GaN interface results in several orders of magnitude increase in trap density.

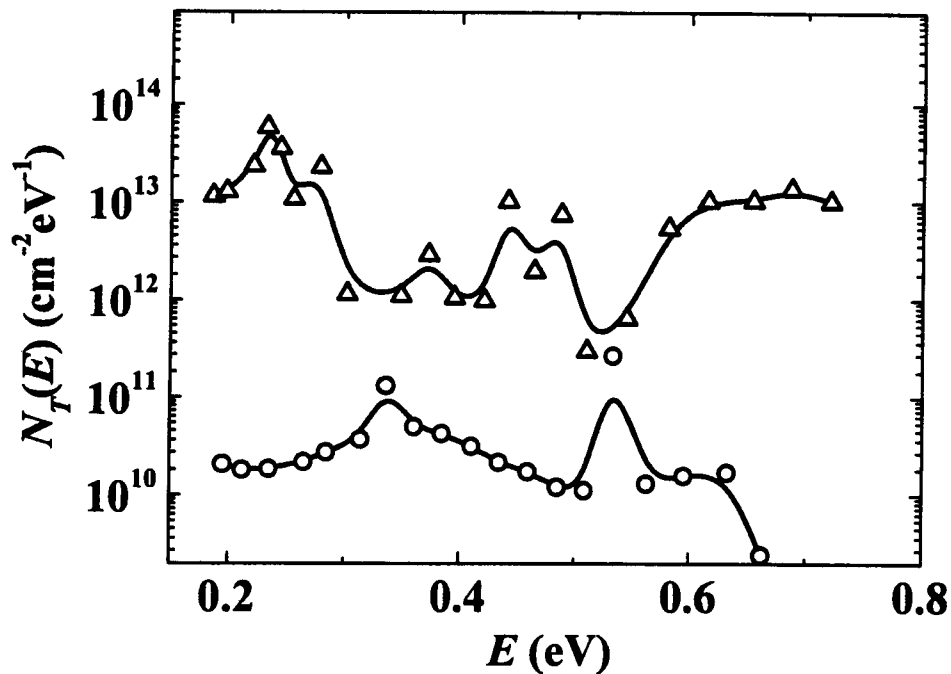
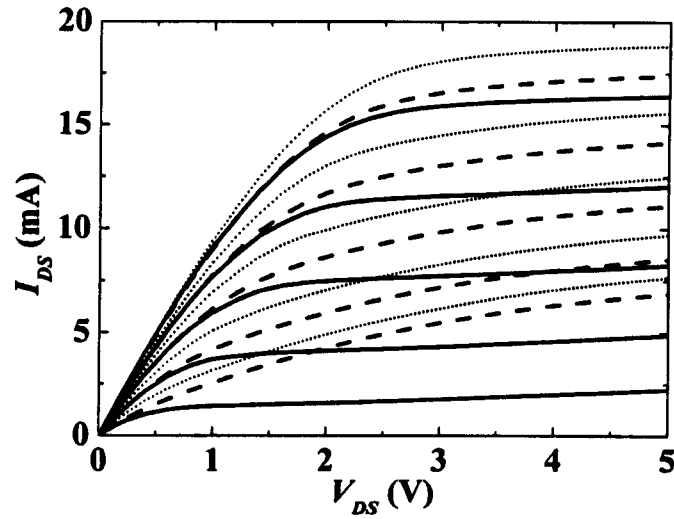


Fig. 4.12: Computed  $N_T(E)$  before (open circles) and after (open triangles) the dc voltage stress.

#### 4.1.9 Fluctuations in Early Phases

In order to understand the mechanism responsible for the observed fluctuations in the noise-magnitude in the first phase, several complementary experiments were done. In one such experiment, a device was subjected to bias stress for a very short duration of  $t_S = 1$  minute, and then was annealed for about 20 minutes in an electric furnace at  $100^\circ\text{C}$  in nitrogen ambient. Both the  $I$ - $V$  characteristics and the noise data were recorded prior to and after stress, and also after the low-temperature annealing. Experimental  $I$ - $V$  characteristics are shown in Fig. 4.13 for  $V_{GS} = 0$  V to  $V_{GS} = -2$  V with  $-0.5$  V steps. The data illustrate significant increase in  $I_{DS}$  at  $V_{DS} = 5$  V for different gate biases. It is interesting to note that the changes in  $I_{DS}$  can be partially reverted by annealing the device as shown in the figure. Similarly, substantial increase in the room temperature  $S_V(f)$  was observed in the device after stress, as shown in Fig. 4.14. The data also show that annealing results in significant reduction in  $S_V(f)$ . From the experimental data, one observes significant changes in the device characteristics and the low-frequency noise properties, even for such short stress duration. The increase in  $I_{DS}$  immediately after the short stress stipulates a significant increase in the number of positive charged centres in the AlGaIn layer. This can also result in the observed increase in  $S_V(f)$  as the localized states may serve as trapping centres leading to an increase in the trap-originated  $1/f$  noise. The trapping centres will be annealed during the baking process, causing a decrease in the magnitude of trap assisted tunnelling, and hence low-frequency noise magnitude will also decrease.



**Fig. 4.13:** Experimental  $I$ - $V$  characteristics (from  $V_{GS} = 0$  V to  $-2$  V, with a step of  $-0.5$  V) of a MOCVD-grown HEMT device; before (solid line), and after (dotted line) 1-minute voltage stress at  $V_{DS} = 10$  V and  $V_{GS} = -1.5$  V. Dashed line, represents the data measured after 20 minute baking at  $100$  °C.

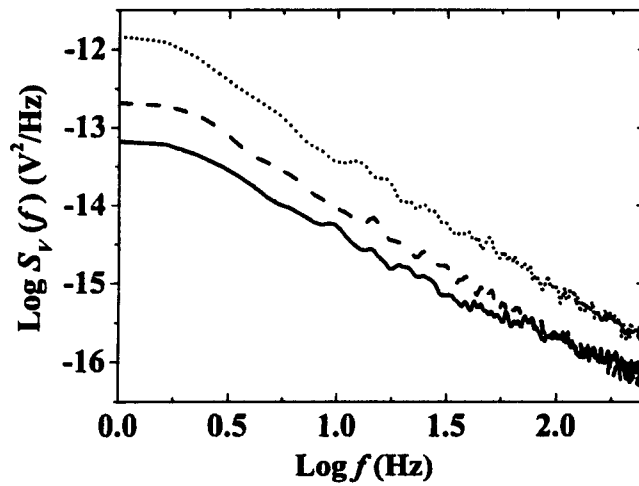


**Fig. 4.14:** Experimental  $S_V(f)$  observed under above mentioned conditions.

#### 4.1.10 Evidence of Percolation Mechanism

To investigate the mechanism responsible for the low-frequency noise, we note that the presence of a large quantity of positively charged centers at the AlGa<sub>N</sub>/Ga<sub>N</sub> interface will lead to the modulation of the local surface potential at the hetero-junction. This will result in a network of “valleys” in the free energy profile in the 2DEG. A similar system had been investigated by R.F. Voss who studied<sup>7</sup> Na<sup>+</sup> doped MOSFETs. It was shown that Na<sup>+</sup> ions incorporated at the Si-SiO<sub>2</sub> interface had led to similar random variations in the surface potential at the Si-SiO<sub>2</sub> interface resulting in the formation of various percolation paths at the interface. It was shown that when a strategically located Na<sup>+</sup> is neutralized through the capture of an electron or being displaced from its original position, the percolation path may be substantially altered leading to large changes in  $S_V(f)$ . It is conceivable in our case that the positive charge centers generated at the AlGa<sub>N</sub>/Ga<sub>N</sub> interface may also give rise to  $1/f$  fluctuations due to the percolation of carriers.

To confirm this, we first note that the percolation path of an electron is a strong function of the electron energy. Thus, the percolation model stipulates a strong dependence of  $S_V(f)$  on  $V_{GS}$  that reflects the characteristic energy distribution of the ions. In Fig. 4.15, we present the experimental results on  $S_V(f=173\text{Hz})$  as a function of  $V_{GS}$ , measured at 79 K with  $V_{DS} = 50$  mV. Lines 1 and 2 represent experimental data measured immediately one after the other on the same device without applying any voltage stress between the two measurements. Both sets of data illustrate similar  $V_{GS}$  dependence with peaks at around 350 mV and 550 mV as well as a valley at 450 mV.

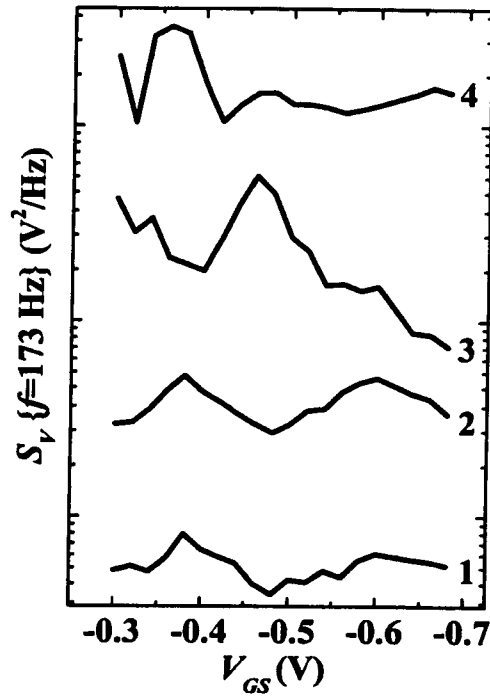


**Fig. 4.15: Experimental variations of  $S_v(f)$  vs.  $V_{GS}$  for  $f = 173$  Hz measured at 79 K. Lines A and B are data measured consecutively, line C was measured after 10 minutes voltage stress at low-temperature and line D was measured after temperature cycling followed by voltage stress at room temperature. All the noise data were recorded at  $V_{DS} = 50$  mV.**

It is noted that the data are repeatable as long as the device is kept at low-temperature, and no voltage stress applied to the device. However, if the temperature of the device is raised, or when a voltage stress is applied to the device, a totally different set of peaks and valleys are observed. Line 3 represents the data obtained after subjecting the device to voltage stress at  $V_{DS} = 10$  V for 10 minutes, keeping the device temperature unchanged. Experimental data represented by lines

1, 2, and 3 were obtained under continuous experimentation within a time span of no more than 16 hours. Line 4 represents noise data obtained after the device had been allowed to come to room temperature, stressed at  $V_{DS} = 10$  V and then brought back to 79 K for the noise measurements. The results clearly show that the peaks and valleys are the signature of the device reflecting the detailed position/networks of the positive ions. When subjected to voltage stress or temperature cycling, the arrangement of the ions will be changed resulting in the variations in the  $V_{GS}$  dependence of the noise. The experimental results provide strong evidence for percolation as the underlying mechanism for the observed noise.

The percolation mechanism can also be utilized to account for the observed peaks in  $S_V(f)$  for  $t_S < 50$  hours. With the application of a large  $V_{DS}$  across the device, the positive ions are caused to drift in the direction of the electric field towards the source region. This process will result in the random fluctuations in the magnitudes of  $S_V(f)$ . The physical origin of the positive ions induced at the AlGaIn/GaN interface is not clear. It is tempting to identify them as  $H^+$  for the following reasons:

- 1) large quantity of hydrogen is naturally incorporated during the MOCVD growth of the III-nitride layers<sup>8,9</sup> [20-23];

- 2) structure of the hydrogen network in semiconductor material can be easily rearranged using a relatively low annealing temperature as is often observed in hydrogenated amorphous hydrogen thin films and other semiconductor materials<sup>10-</sup>

12.

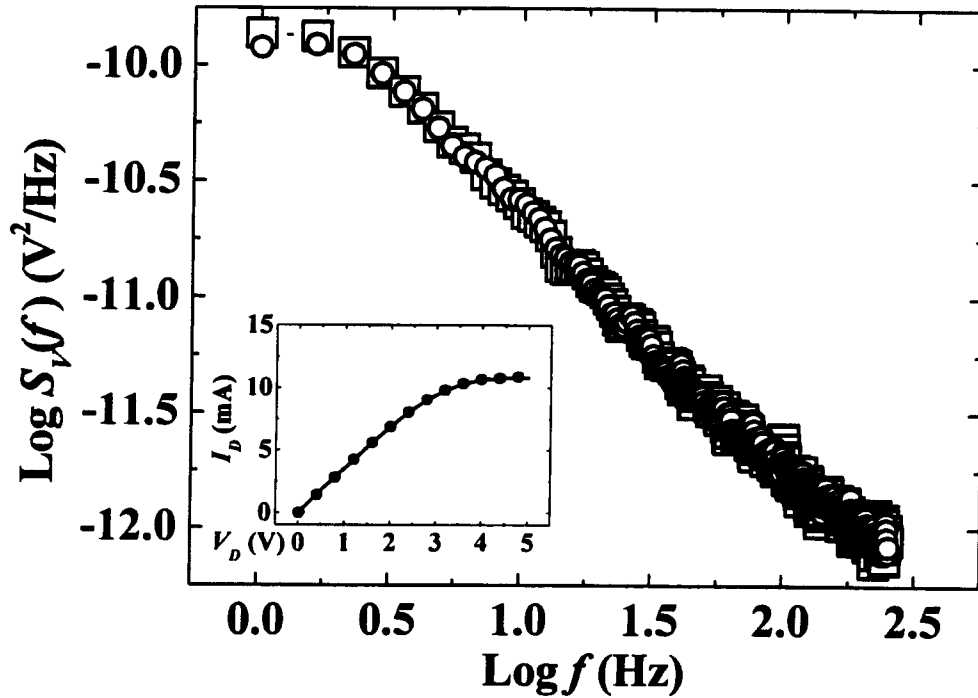


**Fig. 4.16: Experimental  $S_V(f)$  of a MBE-grown HEMT device before (squares) and after (circles) 1-minute voltage stress at  $V_{DS} = 10$  V and  $V_{GS} = -1.5$  V. Experimental  $I$ - $V$  characteristics, before (solid line) and after (solid circles) stress are shown in the inset.**

Furthermore, it was found that MBE-grown AlGaIn/GaN HEMTs do not show any significant change in either  $I$ - $V$ , or noise characteristics, when the devices were subjected to voltage stress for a short  $t_S = 1$  minute. The results are shown in Fig. 4.16. Although, there will still be some hydrogen incorporated in the MBE-grown devices due to the use of  $\text{NH}_3$ , its amount will be substantially less than in their MOCVD-grown counterparts. Work by Van de Walle and Neugebauer shows<sup>8</sup> that  $\text{H}^+$  is the stable species in n-GaN for  $E_f - E_V > 2.5$  eV. It is not clear whether  $\text{H}^+$  can

be formed in our case or not. So, based on low-frequency noise studies alone, it is not possible to specifically identify the physical nature of the positively charged ions, however, available details does point to  $H^+$  as a possible candidate responsible for the observed effects. In summary, experimental findings of this work can be listed as follows:

- Creating Recess by RIE drastically influences noise and dc properties,
- Deeper the recess noisier the device,
- Gate-recessed devices have much shorter life times,
- Deeper the recess smaller the life times,
- Mobile positively charged ions are responsible for the noise behavior observed in the early phase of bias stress effects in MOCVD HEMTs,
- Noise is shown to be used as a non destructive reliability evaluation tool in GaN technology.

In this part, HEMTs incorporating single heterostructures were studied. Stress induced degradation in recessed and unrecessed devices were investigated. In the next part, study on HEMTs incorporating double-heterostructure is presented.

## ***Part II - Noise Properties of AlGa<sub>N</sub>/Ga<sub>N</sub>/AlGa<sub>N</sub>/Ga<sub>N</sub> Dual Heterostructure HEMTs***

---

In a transistor, dual channel structure facilitates enhancement of drain current density and allows additional freedom of modulating gain linearity<sup>13</sup>. Hence, there had been lot of efforts to develop dual channel structures with GaAs<sup>14</sup> and InP<sup>15</sup> based materials. However, there is a common issue with these materials for dual channel application. HEMT fabrication with these materials usually requires intentional doping in the channel or in the barrier layer in order to form conduction channel. This leads to low electron mobility and large buffer leakage. This issue can be addressed if 2DEG channels are used. In an AlGa<sub>N</sub>/Ga<sub>N</sub> heterostructures, high density and high mobility 2DEG channel can be formed at the interface due to polarization induced charges, without any requirement for additional doping. This enables the design of dual and multi channel HEMT structures without sacrificing channel mobility and with hard pinch off properties. It becomes interesting to study the noise properties of dual channel HEMTs to determine if such HEMT structure offers similar or better noise properties in addition to their merits in electrical properties. If both, dc and noise characteristics are favorable, dual or multi-channel AlGa<sub>N</sub>/Ga<sub>N</sub> HEMTs can be a good candidate for high-power low phase noise applications.

In this chapter, dc and noise characterization results, performed on dual channel HEMT devices are presented. Before introducing the chapter objectives,

methodology, and experimental setup it would be better to first introduce the key information regarding epi-layer design and device structure.

#### 4.2.1 Epi-layer Scheme of Dual Channel HEMT Devices

The epi-layer for the devices consists of an AlGa<sub>x</sub>N/GaN double heterostructure, grown in an Aixtron 2000 HT metal-organic chemical vapor deposition reactor, on the sapphire substrate. The schematic cross-section of the material structure is shown in Fig. 4.17.

undoped AlGa <sub>x</sub> N (3nm)
Si doped AlGa <sub>x</sub> N (18nm)
undoped AlGa <sub>x</sub> N (3nm)
undoped GaN (14nm)
AlGa <sub>x</sub> N (21nm)
GaN (2.5 μm)
Sapphire substrate

**Fig. 4.17: Schematic diagram of the epitaxial layer structure used for the fabrication of dual channel HEMT devices.**

The structure consists of a 2.5 μm thick undoped GaN buffer layer, a 21 nm thick Al<sub>x</sub>Ga<sub>1-x</sub>N bottom barrier layer with the Al composition (x), graded from 3% at the lower interface to 6% at the upper interface, a 14 nm thick GaN upper channel layer, and a 21 nm thick Al<sub>0.3</sub>Ga<sub>0.7</sub>N top barrier layer, with a 3nm spacer layer. The top

heterostructure is modulation-doped with Si at a concentration of  $2 \times 10^{18} \text{ cm}^{-3}$ . This is to enhance the channel electron density and to facilitate good ohmic contacts. There are two conduction channels formed in this structure. One at the upper AlGaN/GaN interface (top channel) and the other at the lower AlGaN/GaN interface (bottom channel). Thus, upper and lower channels are formed at 24 nm and 59 nm below the top surface, respectively. An optical microscope image of a dual channel HEMT on chip is shown in Fig. 4. 18. The devices have a typical gate length of 1  $\mu\text{m}$  and a width of 100  $\mu\text{m}$ .

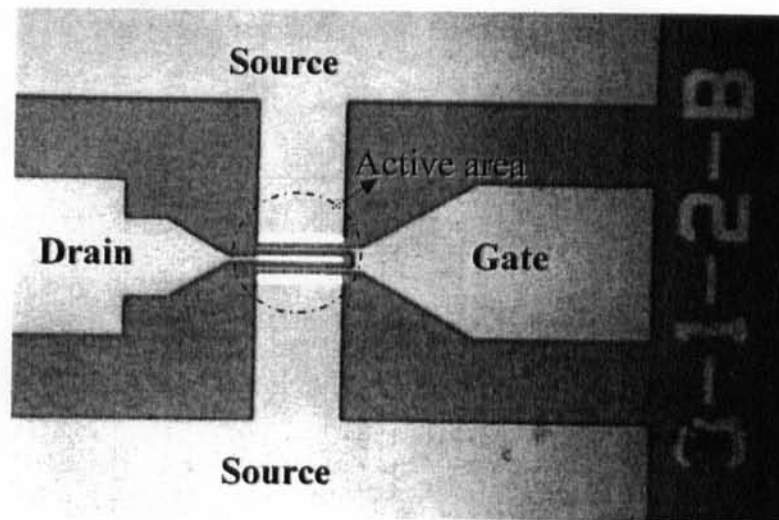


**Fig. 4. 18: Optical-microscope image of a HEMT transistor.**

#### **4.2.2 Investigation Objectives and Methodology**

Main investigation objective of this investigation is to present the details of the noise characteristics. The characteristics can reflect on the quality and merits of using a double heterostructure for HEMTs. In the framework of this investigation, first dc

characterization was performed, which suggested appropriate biasing conditions for the low-frequency noise investigation.

In Fig. 4.19, a pictorial illustration of current conduction in device for different gate voltage regimes is shown. In the illustration, it is shown that a double channel HEMT device has two conduction channels and those are controlled (switched on/off) by the gate. Part A illustrates the normally on operation condition when  $V_{GS} = 0V$ . Both channels are on and current conduction takes place through two parallel paths along the two (upper and lower) channels. In part B, When the gate-source bias reaches a significantly negative value ( $V_{th1} \sim -4.2V$ ) upper channel gets depleted in carrier and current conduction takes place through the lower channel. Later, when even larger negative gate bias ( $-4.2V < V_{GS} < V_{th2} = -8V$ ) is applied, the lower channel also starts depleting. Finally at  $V_{GS} = V_{th2} = -8V$ , second channel also completely depletes in carrier and the device is pinched off, as illustrated in part C. Any current observed in this condition is merely due to the leakage paths. Such behavior is clearly reflected in the *transfer characteristics*, as described later.

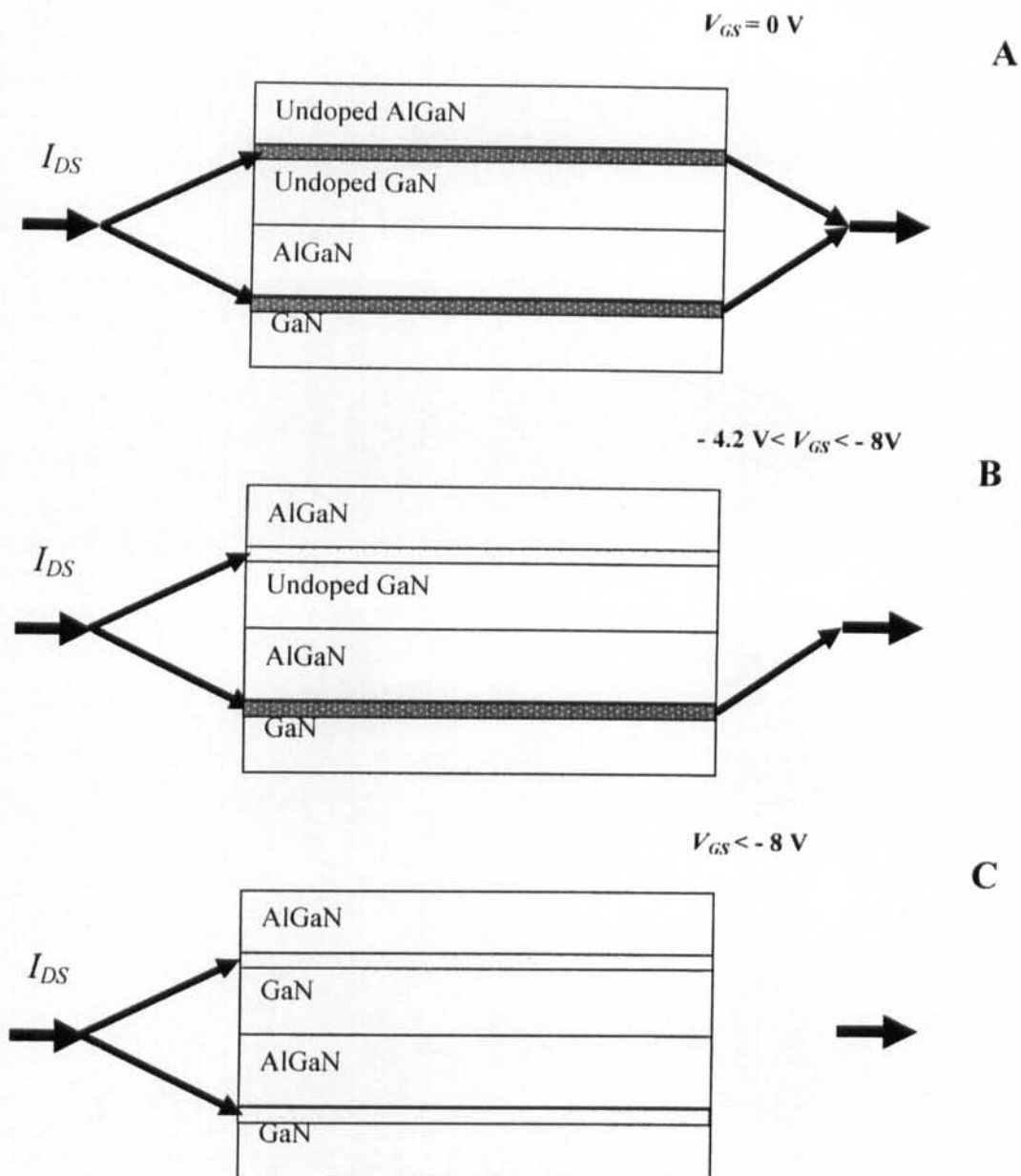


**Fig. 4.19: An Illustration of current conduction through two channels controlled by the gate in different regimes of operation. A illustrates a normally on transistor and both channels are conducting. B illustrates the case when first threshold is reached and upper channel is cut off. Current conduction now takes place through the lower channel only. C illustrates the case when the gate voltage reaches a threshold value and second channel is also cut off.**

As there are parallel conduction paths through the two channels, it is very difficult to make any conclusion regarding noise contribution from a *specific channel*. Though, collecting and analyzing noise data when the device is subjected to different biasing conditions might provide a basis to achieve useful information. It turns out that noise characteristics should be investigated at different gate biases. One of those should belong to the bias range in which both the channels are in operation while, the other should belong to the bias range in which lower channel is in operation and upper channel is off. So we choose two such gate voltages as  $V_{GS} = 0$  V (both channels on) and  $V_{GS} = -5$  V (lower channel is on).

After deciding the applied gate bias, next an appropriate drain-source bias is to be decided. This is important as a large  $V_{DS}$  will cause the device to operate at a large current and hence the temperature may rise during measurements. This is particularly important for GaN-based HEMTs fabricated on sapphire substrates which have low thermal conductivity. If a very small drain bias is chosen, the background noise may affect the measurements. A moderate value of  $V_{DS}$  will ensure that the measurement data reflect real contribution from the device being in thermal equilibrium. Hence a low drain bias of  $V_{DS} = 0.5$  V is chosen for the noise measurements.

### **4.2.3 TLM measurements**

In order to derive contact resistance and sheet resistivity TLM measurements were performed with the linear TLM pattern, as shown in Fig. 4.20, having contact pad dimensions of  $100 \mu\text{m} \times 100 \mu\text{m}$ , and pad separations of 2, 4, 8, 16, and 32  $\mu\text{m}$ .

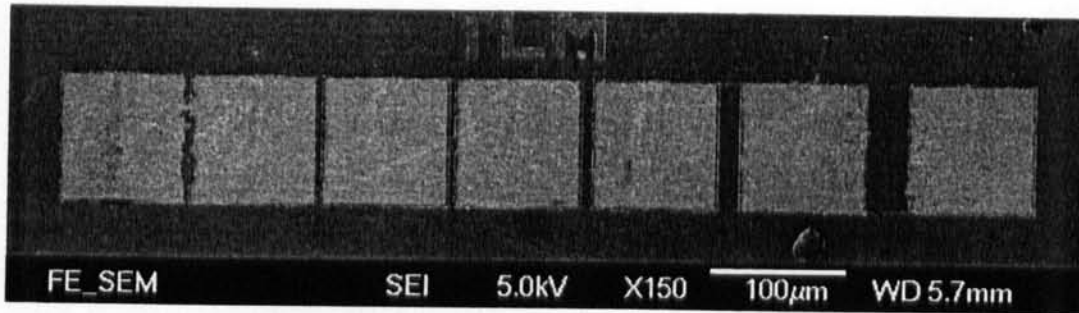


Fig. 4.20: SEM image of a linear TLM pattern on a double heterostructure film.

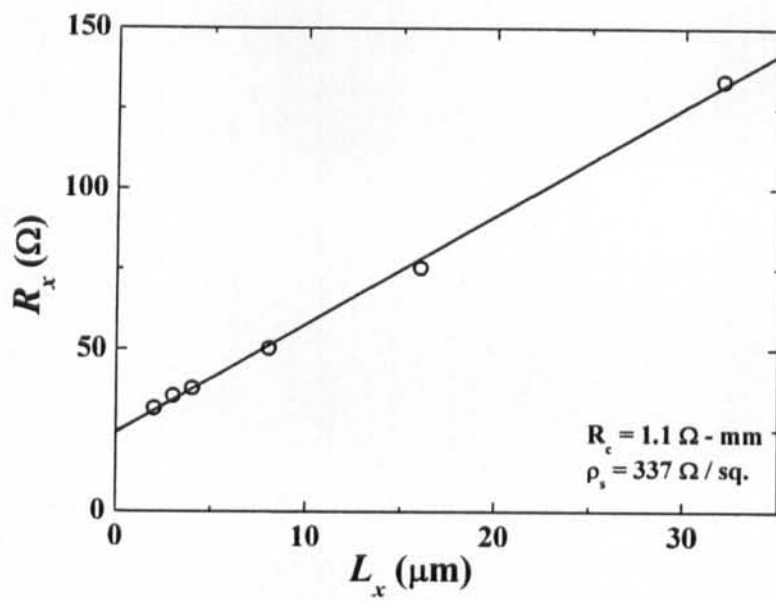
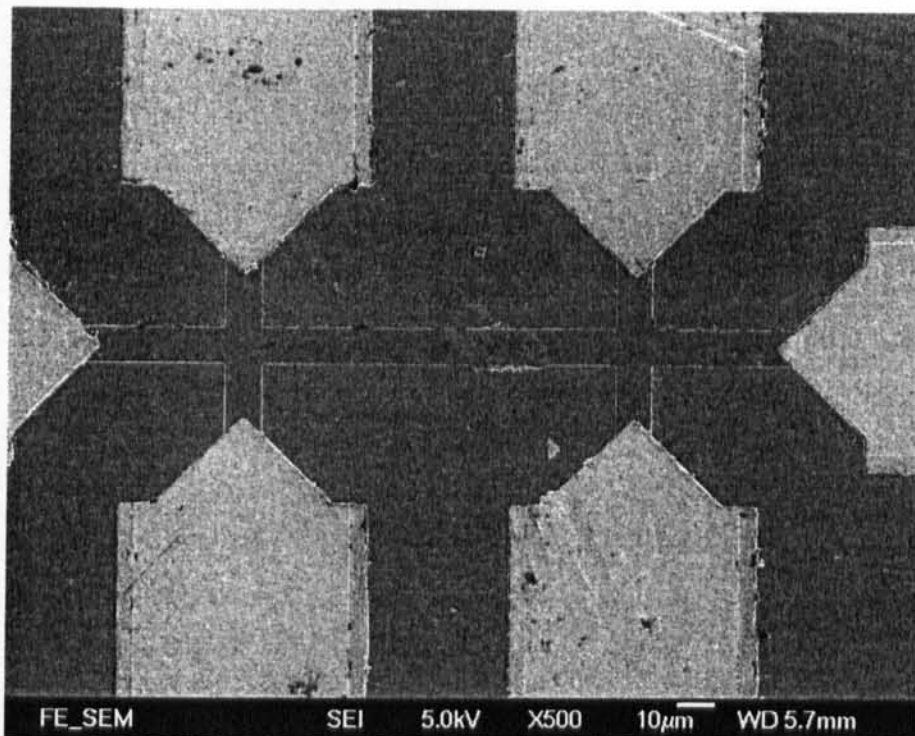


Fig. 4.21: Resistance vs. consecutive pad-separation observed from a TLM pattern.

From the results shown in Fig. 4.21, sheet contact resistance ( $1.1 \Omega\text{-mm}$ ), and sheet resistivity ( $336 \Omega/\square$ ) were derived.

#### 4.2.4 Hall Measurements

To obtain the Hall-mobility of heterostructure films, Hall measurements were performed on a bar type specimen, as shown in Fig. 4.22. From the measurements, room temperature Hall-mobility and sheet carrier concentration were derived to be  $1060 \text{ cm}^2/\text{V}\cdot\text{s}$  and  $1.6 \times 10^{13} \text{ cm}^{-2}$  respectively.



**Fig. 4.22: SEM image of a Hall bar.**

#### 4.2.5 C-V Measurements

One of the direct ways to probe the thin film electrical properties is C-V measurement. Particularly in the material structure under study, it plays a vital role. This is because the two conduction channels are created at two different positions in

the device. Hence, in order to be able to get a clear idea of such possibilities and also to precisely determine the charge density in a particular 2DEG layer,  $C$ - $V$  measurement is necessary. Optical microscope image of a large area Schottky contact lying on the chip with other HEMT devices is shown in Fig. 4.23.

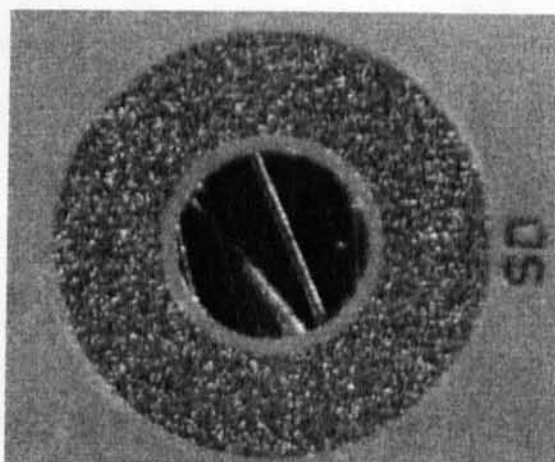


**Fig. 4.23: Optical microscope image of a large area Schottky contact on the chip.**

A large dimension Schottky contact forms a large area capacitor which is necessary for an error free capacitance measurement. Once the  $C$ - $V$  profile of a material structure under Schottky contact is known, the associated charge can be calculated by integrating the curve with respect to the applied voltage bias. The measured profile of one such structure scaled to its area with an internal diameter  $200\ \mu\text{m}$  is shown in Fig. 4.24. The measurements were performed with HP 4279  $C$ - $V$  meter at a frequency of 100 kHz with 50 mV ac signal.

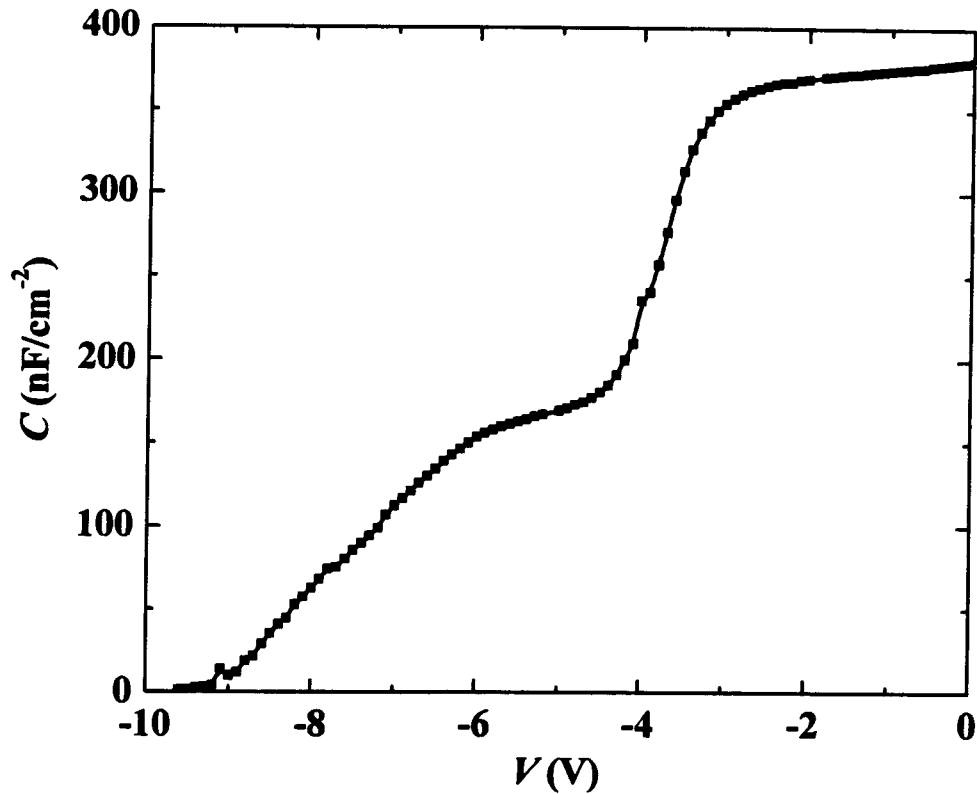


**Fig. 4.24:  $C$ - $V$  profile of a Schottky contact having a diameter of  $200\ \mu\text{m}$ .**

From the above figure, steps like profile are observed. This suggests that there are two high density charge carrying layers in the material and they are separated by a finite distance as suggested by the sharp decrease of capacitance around  $V = 3.5\text{V}$ . A flat profile in the  $0\text{V}$  to  $-4\text{V}$  range corresponds to the upper 2DEG layer while the lower one is reflected by the second flat profile. Threshold voltage of  $\sim -9\text{V}$  of an adjacent transistor can also be estimated from the figure. Though, about  $1\text{V}$  variation is possible, as the capacitance magnitude measured near the threshold would be of the order of instrument resolution, resulting in possible error in measurements. Variation may also arise as the material structure under a particular device may vary

within a same chip area. Charge density and hence the charge concentration per unit area was derived from the above plot and the total sheet charge density is found to be  $1.26 \times 10^{13} \text{ cm}^{-2}$ . This value is a little smaller than the one obtained from Hall measurements and reflects a slightly depleted layer under the Schottky contact. An estimation of the charge density in an individual channel can be made by approximating the area of the C-V curve in their characteristic gate voltage range. When this area is subtracted from the total area under the curve, resulting area will reflect the charge density in the other channel. Following this argument, a charge density of  $0.93 \times 10^{13} \text{ cm}^{-2}$  in the upper channel and  $0.33 \times 10^{13} \text{ cm}^{-2}$  in the lower channel was estimated. Values are quiet close to the one obtained by Poisson<sup>16</sup> simulations of this material structure.

## **4.2.6 HEMT dc Characterization**

### **4.2.6.1 *I-V Characteristics***

*I-V* characteristics of a 100  $\mu\text{m}$  wide dual channel HEMT with a gate length of 1  $\mu\text{m}$  are shown in Fig. 4.25. Efficient access to the lower channel is evident in the almost kink free *I-V* curves for all the gate bias values. The device showed a maximum drain current density of  $\sim 825 \text{ mA/mm}$  at  $V_{GS} = 0 \text{ V}$ . Negligible negative differential resistance was observed in the saturation region that arises from self-heating and poor thermal conductivity of the substrate.

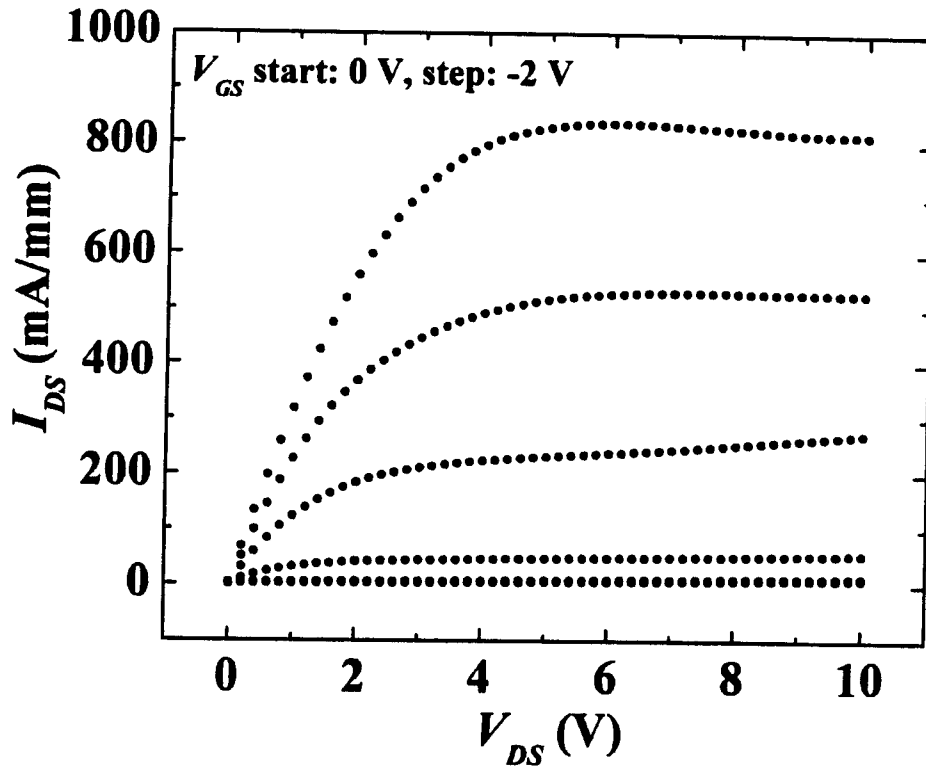
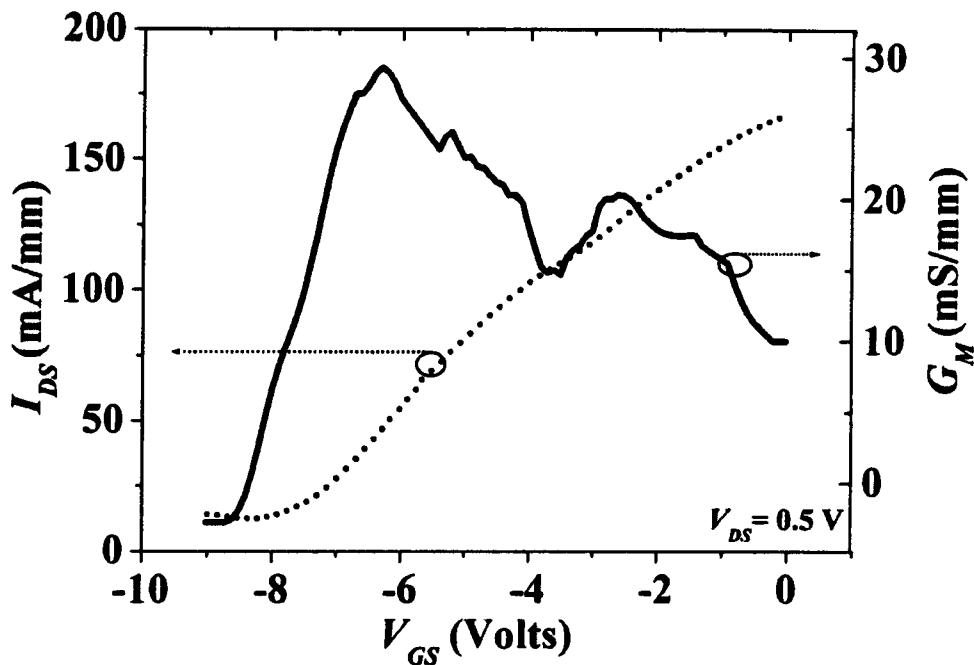


Fig. 4.25: I-V characteristics of a dual channel device.

#### 4.2.6.2 Transfer Characteristics

Transfer characteristics and transconductance curves of this device at  $V_{DS} = 0.5$  V is shown in Fig. 4.26. The peak transconductance of the device at  $V_{DS} = 5$  V, and  $V_{GS} = -6.3$  V was observed to be  $\sim 140$  mS/mm. A hard pinch-off characteristic is clearly seen in the figure which reflects good control over the gate so that both channels are effectively turned off below the threshold voltage. The transfer characteristics indicates fairly linear variation of drain current with gate bias above the threshold voltage ( $V_{Th}$ ), which was found to be  $\sim -8$  V. This was obtained by

extrapolating a tangent to this curve on the gate voltage axis. It would be appropriate to mention that these double channel devices generally show a clear change in the gradient of the  $I_{DS}$ - $V_{GS}$  curves at a gate voltage larger than the threshold and correspondingly a double hump structure in the  $G_M$ - $V_{GS}$  curve is observed. For the device under study, the  $G_M$ - $V_{GS}$  curve shows two transconductance peaks at  $V_{GS} \sim -6.3$  V and  $-2.6$  V respectively at  $V_{DS} = 0.5$  V.



**Fig. 4.26:** Transfer characteristics of a dual channel device in saturation at  $V_{DS} = 0.5$  V.

The double hump structure has also been reported earlier<sup>17,18</sup> which shows the unique feature signifying two parallel charge carrier conduction layers within the device. The presence of a second (lower) channel causes the change in the threshold voltage from  $V_{GS} \sim -4$  V to  $\sim -7$  V in the dual channel device. As the lower channel is at a larger distance from the gate, a much larger negative gate voltage would be

needed to deplete the carriers in the buried channel. The transconductance peak at a lower gate voltage (i.e. larger negative value) is the characteristics of the lower channel and the one observed at higher gate bias (i.e. smaller negative value) is the characteristics of the upper channel. As can be seen in Fig. 4.26, the peak transconductance value corresponding to the upper channel is a little smaller in comparison to the lower channel. This can be explained by different values of mobility in the two channels, as it is determined by heterointerface properties of the two individual channels. In the studied devices, the top heterostructure is modulation-doped with Si at a concentration of  $2 \times 10^{18} \text{ cm}^{-3}$ , while the buried heterostructure is undoped. This will result in a higher scattering rate for the carriers in the upper channel. In addition, electrons in the top channel will see the AlGaN both on top and below them, which also will account for the comparably larger scattering rate in the top channel. Consequently, carriers in the lower channel will have a relatively higher mobility resulting in a larger peak transconductance.

#### **4.2.7 Experimental Setup for Noise Characterization**

The details of the low-frequency noise experimental setup are described in Chapter-3. Biasing conditions are detailed here. Devices were current biased at  $V_{DS} = 0.5 \text{ V}$  in a common source configuration using an all-passive current source. Two different gate voltages,  $V_{GS} = 0 \text{ V}$  and  $-5 \text{ V}$ , were used for the noise measurements for the reasons stated above. Open circuit voltage fluctuations measured across the drain-source terminals were amplified using a PAR 113 low-noise preamplifier and were recorded by an HP 3561A dynamic signal analyzer in the frequency range of 1 Hz to

10 kHz. Low-temperature noise experiments were performed by placing the device in an exchange gas cryostat over a temperature range of 80 K to 300 K. The temperature of the device was monitored using a Lakeshore 91C temperature controller with a silicon diode temperature sensor. The device is allowed to stabilize for at least 1 minute at the set temperature before the commencement of data acquisition. Bias voltages and the drain current were measured using a Keithley-2000 multi-meter. Transistor characteristics of the devices were measured using a Keithley model-251 measurement system.

#### **4.2.8 Room Temperature Noise Properties**

In order to characterize the room temperature noise properties of the dual channel HEMT devices, bias dependence of the noise power at different drain and gate bias voltages was recorded. Noise spectra were recorded in the frequency range of 30 Hz–3 kHz, by first fixing the gate bias to a constant value and changing the drain bias voltage from a small value in linear regime to larger values in saturation regime. Then, gate bias was shifted to a larger negative bias voltage and the sequence was repeated. In this manner, noise spectra were acquired for a number of points following the  $I$ - $V$  characteristics of the device for the bias range  $V_{GS} = 0\text{V}$  to  $-7\text{ V}$  in steps of 1 V and  $V_{DS} = 0.25\text{ V}$  to 1 V in steps of 0.25 V and  $V_{DS} = 1\text{ V}$  to 5 V in steps of 1 V. Additional noise spectra were recorded for intermediate bias points in some cases. Noise spectra for  $V_{GS} = 0, -2, -5,$  and  $-7\text{ V}$  are shown in . Spectra were averaged 1000 times in order to acquire a fair line shape and are evidently clean and

free from 50 Hz spikes and its harmonics induced by the power transmission lines.

All the spectra essentially follow the  $1/f^\gamma$  power law with  $\gamma \sim 1$ .

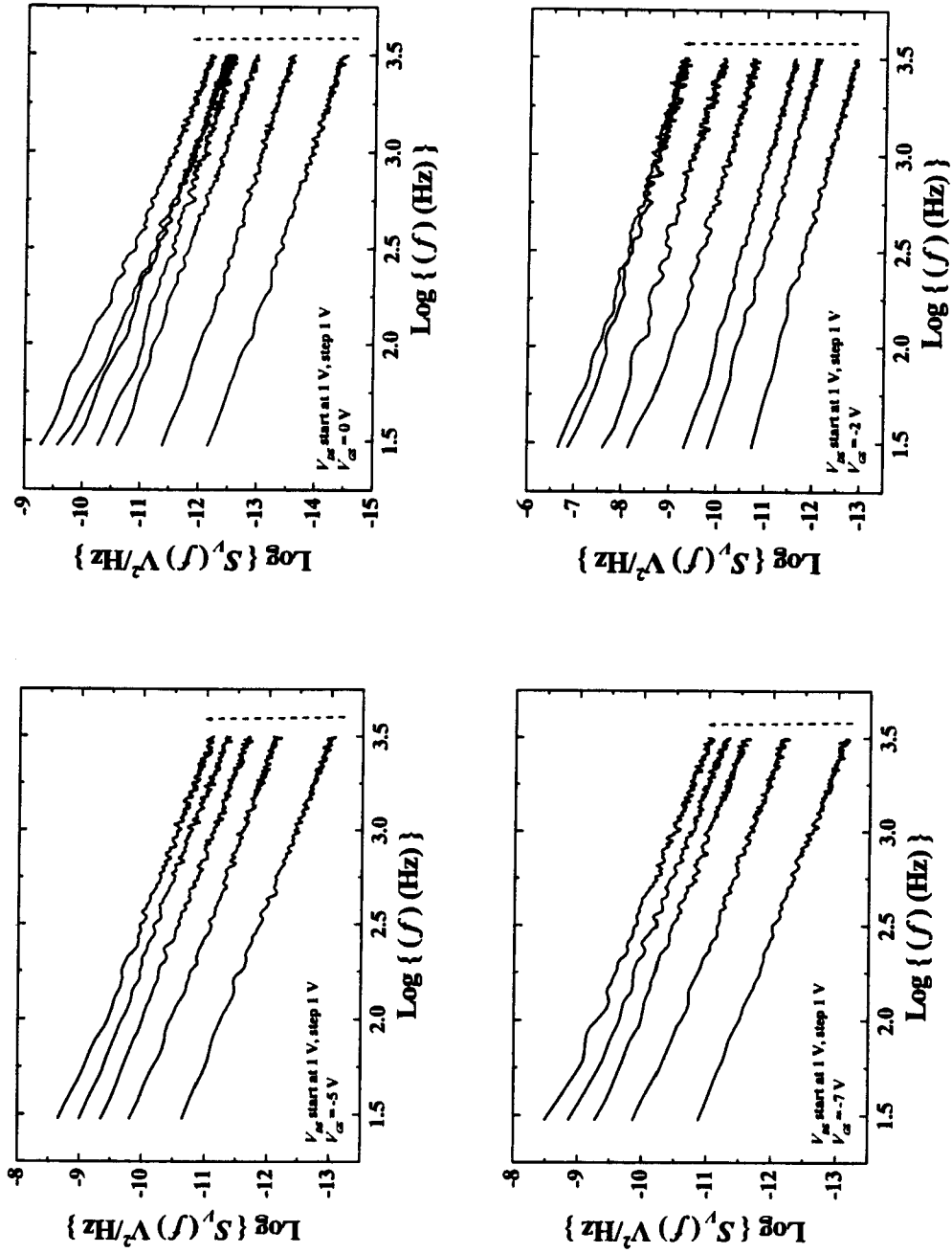
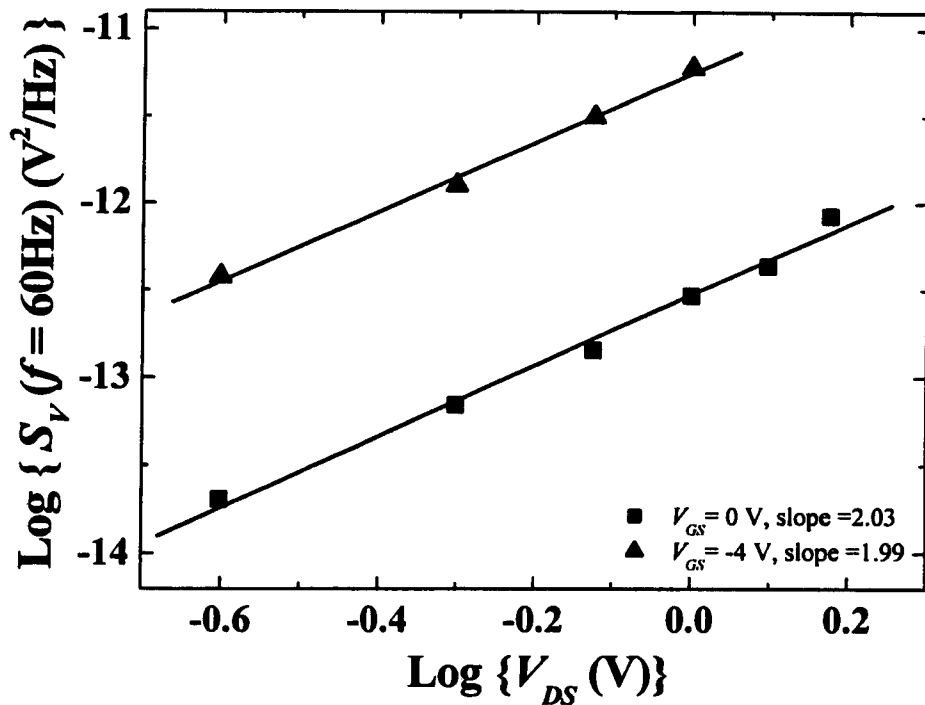


Fig. 4.27:  $S_V(f)$  spectra observed at  $V_{GS} = 0, -2, -5, \text{ and } -7 \text{ V}$ , for a range of drain bias voltages.

### 4.2.8.1 Gate Bias Dependence of $\beta$

Noise model for an ohmic channel predicts  $V_{DS}^\beta$  dependence of  $S_V$  at a fixed observation frequency where in ideal case  $\beta = 2$ . For small drain bias, mostly this has been observed to be true with  $\beta \sim 2$ . For two chosen gate bias voltages,  $V_{GS} = 0$  V and  $V_{GS} = -4$  V, drain bias dependence at small  $V_{DS}$  is shown in Fig. 4.28.



**Fig. 4.28: Bias dependence of  $S_V(f)$  at small  $V_{DS}$ , as observed at  $V_{GS} = 0$  V (solid squares) and at  $V_{GS} = -4$  V (solid triangles). Solid lines represent linear fit to the experimental data.**

As can be seen from the figure,  $S_V(f)$  has almost quadratic dependence ( $\beta \sim 2$ ) over  $V_{DS}$  for  $V_{GS} = 0$  V, and for  $V_{GS} = -4$  V. Even though, data taken at other gate bias

voltages present a different scenario. When  $\beta$  is plotted against  $V_{GS}$ , as shown in Fig. 4.29, it is observed that  $\beta$  seem to follow the transconductance curve shown in Fig. 4.26. The variation in  $\beta$  is  $\sim \pm 0.2$ , however, the fact that  $\beta$  seem to follow the transconductance curve, gives a hint that charge modulation by gate does play a vital role in dictating electrical as well as noise properties of the studied devices.

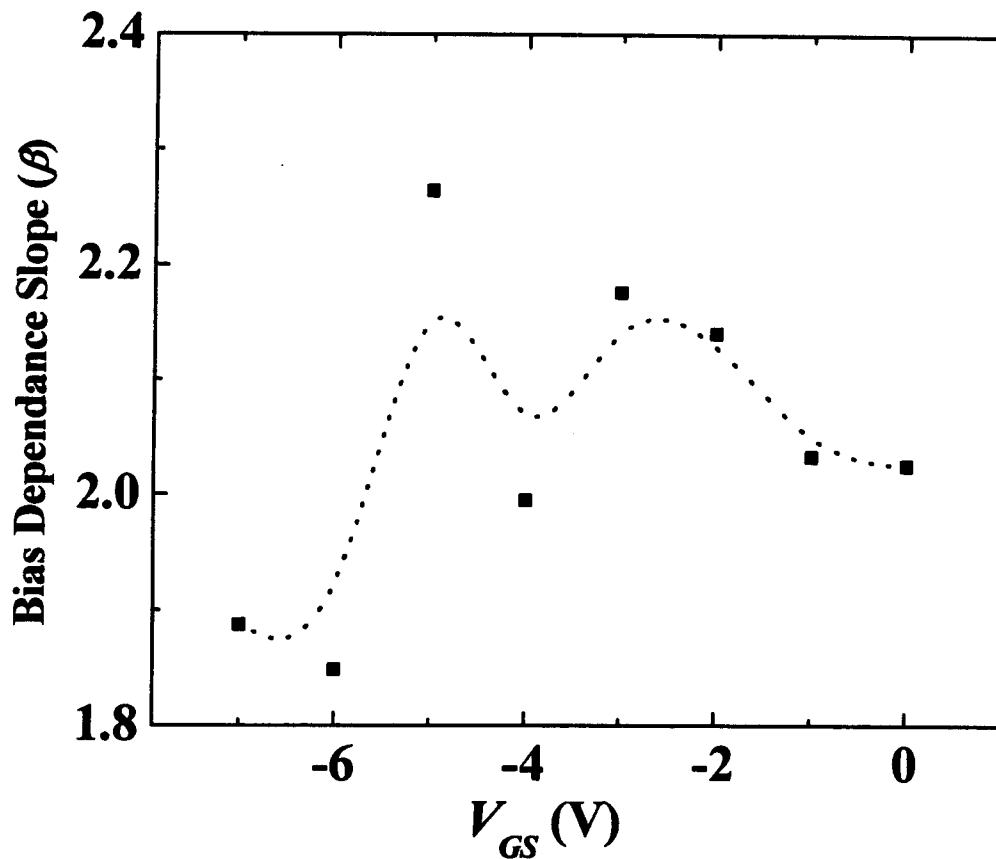


**Fig. 4.29: Variation of bias dependence slope ( $\beta$ ) with the gate bias voltage. (Data points are shown in solid squares. A dotted line is shown to help appreciate the double hump profile as also seen in the transfer characteristics.)**

#### 4.2.8.2 Bias Dependence in Linear and Saturation Region

It is important to look into the details of bias voltage dependence behavior of the drain-source voltage fluctuations. Consequently, a set of noise spectrum were taken at different  $V_{DS}$  and  $V_{GS}$  values following the  $I$ - $V$  curves from linear to saturation regime. In order to look into the details of the drain bias dependence of noise, normalized noise power data acquired at a fixed frequency of  $f = 60$  Hz is plotted against  $V_{DS}$  in Fig. 4.30.

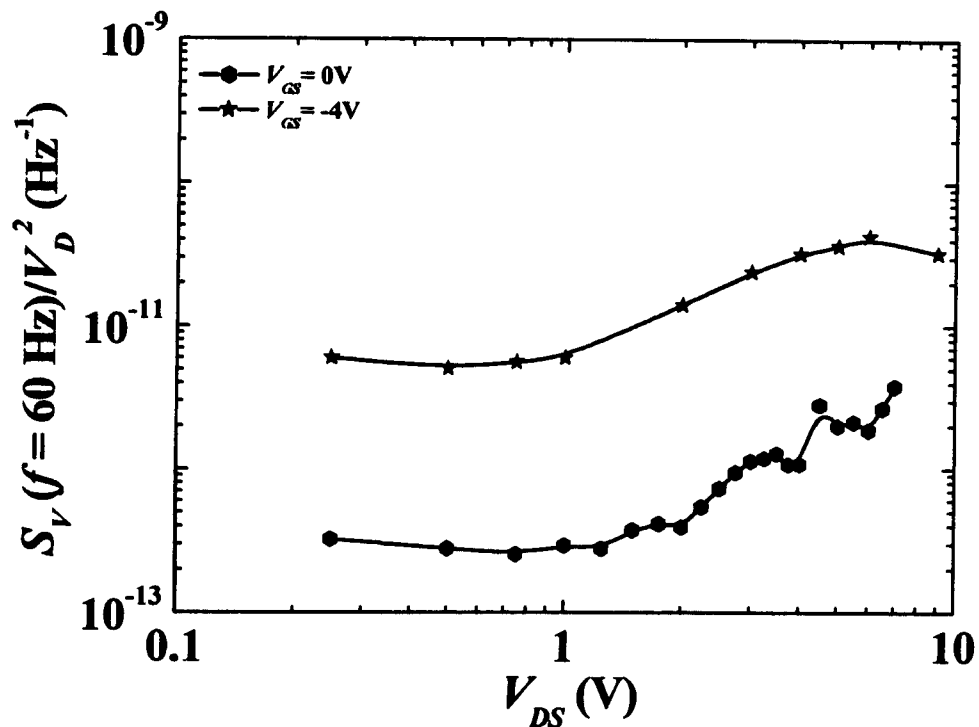


Fig. 4.30: Normalized noise power plotted against  $V_{DS}$  for  $V_{GS} = 0 \text{ V}$ , and  $V_{GS} = -4 \text{ V}$ .

From this figure, following points can be noted:

1. For  $V_{DS} < 1 \text{ V}$ , normalized noise power shows  $\beta \sim 2$  dependence on  $V_{DS}$  for

any  $V_{GS}$ , however; complete data set for any gate bias shows average  $\beta \sim 3$ . In fact, even  $\beta > 4$  are observed for a subset of data points at large  $V_{DS}$ .

2. The transition from  $\beta \sim 2$  to  $\beta > 2$  starts to occur when the drain current approaches near-saturation values in  $I$ - $V$  characteristics.

It is found that  $S_V/V_D^2$  is constant for the data corresponding to  $V_{DS} < 1$  V, as evident in a flat line profile for  $V_{DS} < 1$  V. This is a normally expected behavior for which Hooge relation holds. As a general trend in the figure, after  $V_{DS} > 1$  V and up to about  $V_{DS} = 3$  V,  $S_V/V_D^2$  is not a constant and shows almost linear dependence over  $V_{DS}$  for both curves with different slopes. These observations indicate that Hooge parameter is a constant only for small drain bias values when the channel is ohmic. Near and after saturation, it has large variation.

#### 4.2.9 Noise Properties at Cryogenic Temperatures

Low-temperature noise experiments were performed in the temperature range from 81 K to 300 K.  $S_V(f)$  spectra for  $V_{DS} = 0.5$  V at the lowest (81 K) and highest (300K) temperature as acquired at  $V_{GS} = 0$  V and  $V_{GS} = -5$  V are shown in Fig. 4.31. It is clear that the spectra are essentially  $1/f$  at these temperatures. The value of  $\gamma$  derived from the linear fit to the original data corresponding to  $V_{GS} = 0$  V is 0.99, and 1.00 at 81 K and 300 K respectively. While, for  $V_{GS} = -5$  V,  $\gamma$  values are 0.98 (81K), and 1.09 (300K). This implies significant variation in  $\gamma$  with temperature and hence is discussed in the next section.

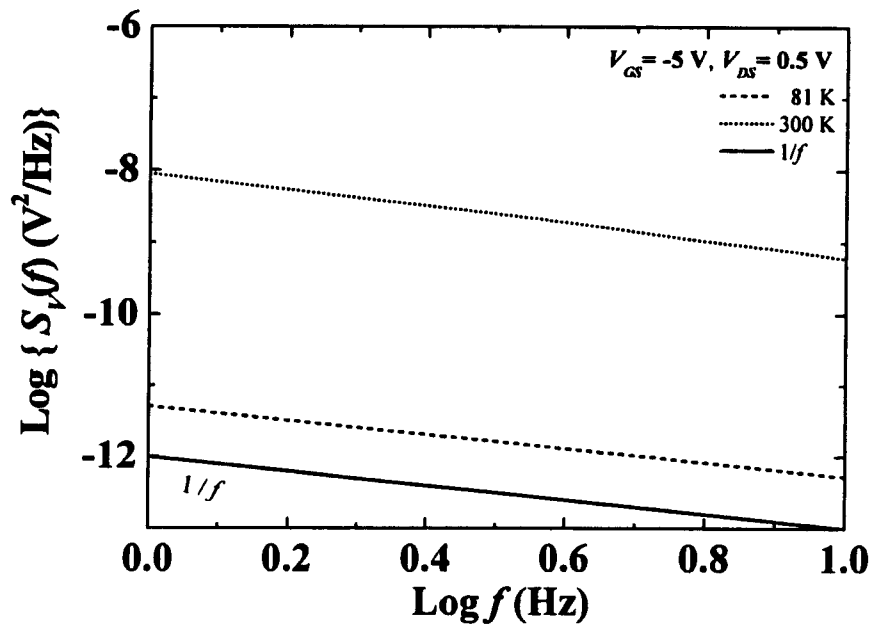
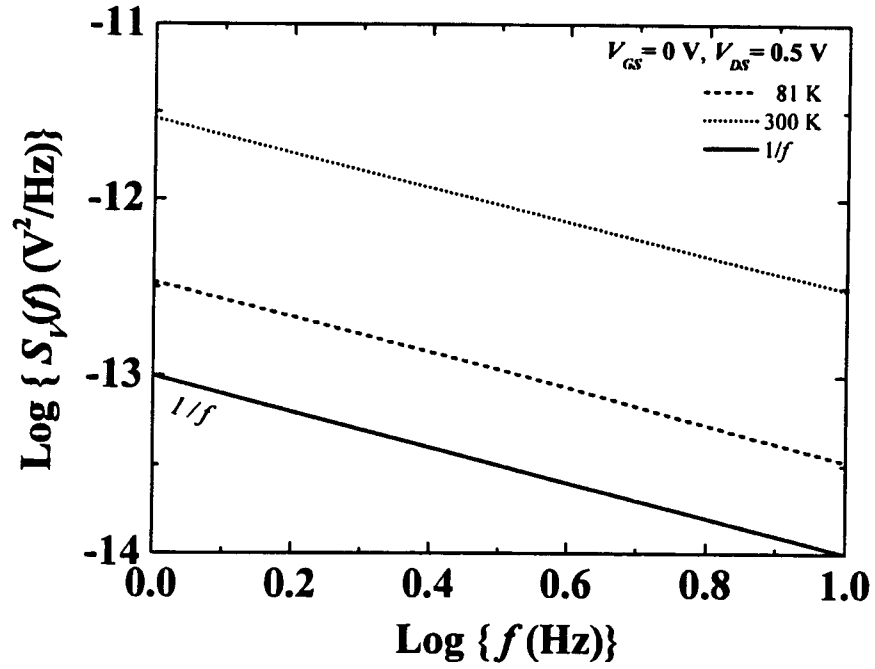


Fig. 4.31:  $S_V(f)$  spectra at 81 K and 300K, acquired at  $V_{GS} = 0 \text{ V}$  (top) and  $V_{GS} = -5 \text{ V}$  (bottom).

#### 4.2.9.1 Temperature Dependence of ' $\gamma$ '

It is found that, most of the spectra are strictly  $1/f$  over the observed temperature range. This is true for both gate biases. However, some of the spectra acquired at intermediate temperatures are distorted  $1/f$  type with Lorentzians superimposed. Such distorted  $1/f$  spectra worth separate attention and are discussed in the next section. A considerable variation in  $\gamma$  is seen when plotted against temperature, as shown in Fig. 4.32.

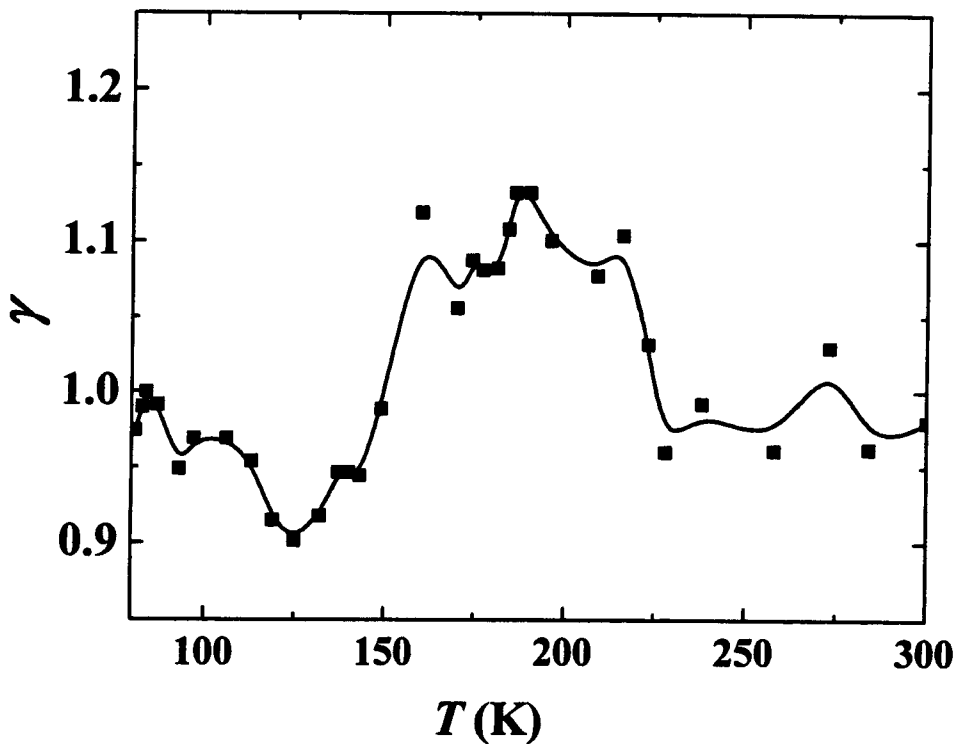


Fig. 4.32: Temperature dependent variation of gamma at  $V_{GS} = 0$  V.

A systematic variation in  $\gamma$  with temperature is evident. The variation is widely spread within the range  $0.9 < \gamma < 1.15$ . The variation can not be explained by the tunnelling mechanism based models. The main difference between the tunneling mechanism and the thermal activation mechanism lies in the temperature dependence of the noise. In contrast to the tunneling model, thermal activation model suggests that traps at different energy levels are activated as the device temperature is varied. This implies that there is a possibility of strong temperature dependence for  $\gamma$  if  $N_T(E)$  varies with energy  $E$ . Also, the tunneling model, with a fluctuation time constant given by  $\tau = \tau_0 \exp(\lambda z_0)$ , stipulates that as the temperature is varied essentially the same group of traps is responsible for the observed noise. This is because the WKB parameter is basically independent of the device temperature. Hence, if the noise is correctly described by the tunneling model then one would expect little change in the value of  $\gamma$  with temperature. Hence, the presented results clearly show that a thermally activated trapping and detrapping process underlies the flicker noise in the devices under study.

#### 4.2.9.2 Temperature Dependence of Noise Power Spectra

Temperature dependence of  $S_V(f)$  at  $V_{GS} = 0$  and  $-5$  V and at  $f = 60$  Hz is shown in Fig. 4.33. A pronounced maxima in the temperature range 150 K to 250 K is obvious from the figure. Such behaviour stipulates high concentration of defect states at the corresponding energy level.

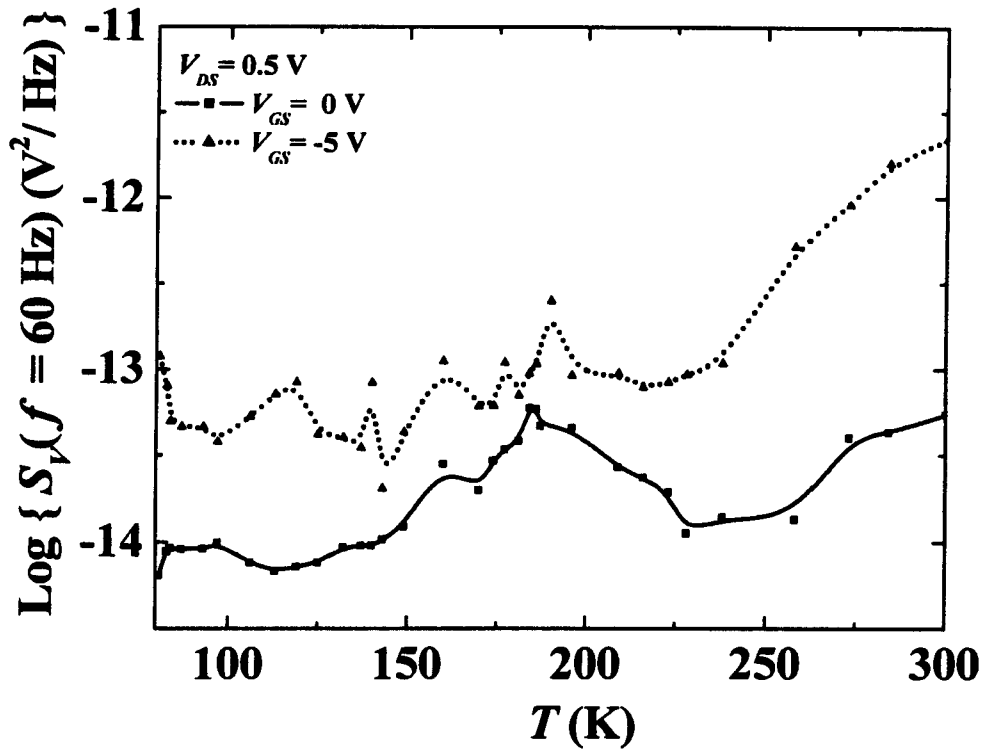
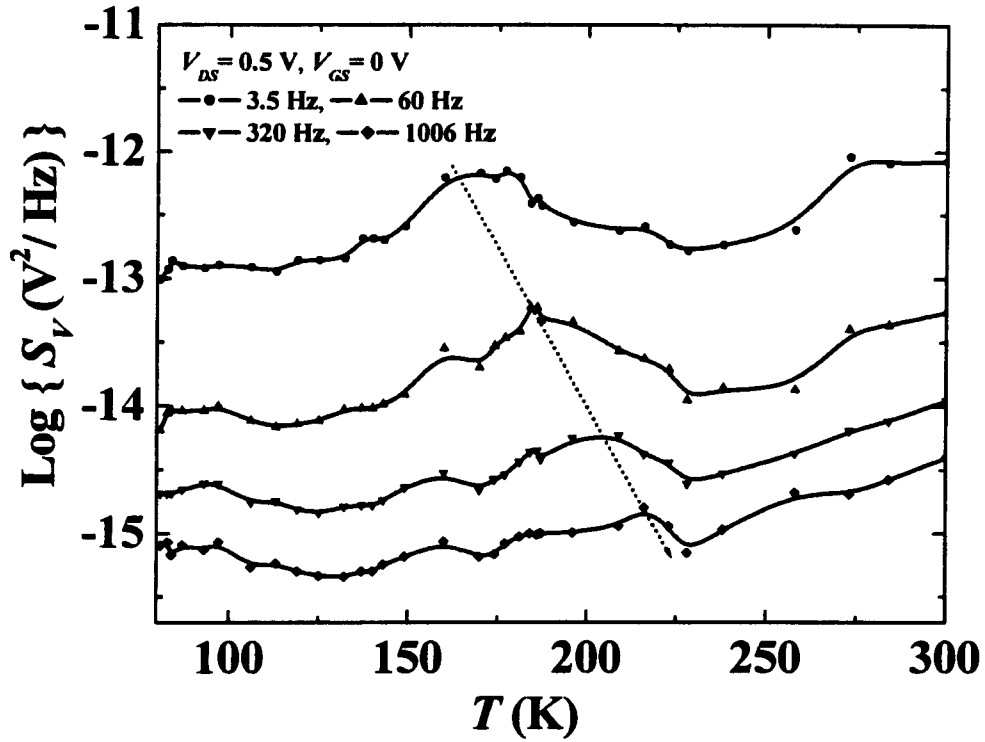


Fig. 4.33: Temperature dependence of  $S_V(f)$  at  $V_{GS} = 0$  V (data points shown in square), and at  $V_{GS} = -5$  V (data points shown in triangle) as observed at  $f = 60$  Hz.



**Fig. 4.34: Shift of the  $S_V$ - $T$  peaks at different observation frequencies.**

Temperature dependence of  $S_V$  observed at different frequencies is plotted in Fig. 4.34. It is found that the peak tends to shift towards higher temperature at a larger frequency. Such dependencies are typical for the noise originating from the local levels<sup>19,20</sup>. In order to gather more information on the nature of the traps, further analysis of the data is presented in the following section.

#### 4.2.10 Signatures of g-r Process

The low-temperature  $S_V(f)$  spectra exhibit g-r bumps superimposed over the  $1/f$  background at different temperatures. These bumps tend to shift towards higher frequency side at a higher temperature. The presence of these bumps and the behaviour of the shift indicate that these are the characteristic Lorentzians originating from the local traps. As the temperature is increased, the Lorentzian corner frequency tends to move at a higher value causing a shift in the location of the bump. The observation becomes clearer when  $f^*S_V(f)$  is plotted against  $f$ . In such plots, a perfectly  $1/f$  spectrum will appear as a flat line, and any deviation from  $1/f$  spectra will be clearly visual. Hence, a hardly distinguishable Lorentzian in power spectra can be easily identified as large bumps in  $f^*S_V(f)$  spectra.

In two temperature ranges, such corner frequency shifts were noticed. In temperature range 177 K - 190 K, peak shifts were observed at both gate biases, however in 196 K - 216 K range, frequency shift was observed only at  $V_{GS} = 0$  V. Corresponding power spectra and  $f^*S_V(f)$  spectra at a selected temperature points are shown in Fig. 4.35, Fig. 4.36, and Fig. 4.37. With the help of these plots, associated corner frequencies are known at different temperatures and trap activation energy is derived, as discussed in the next section.

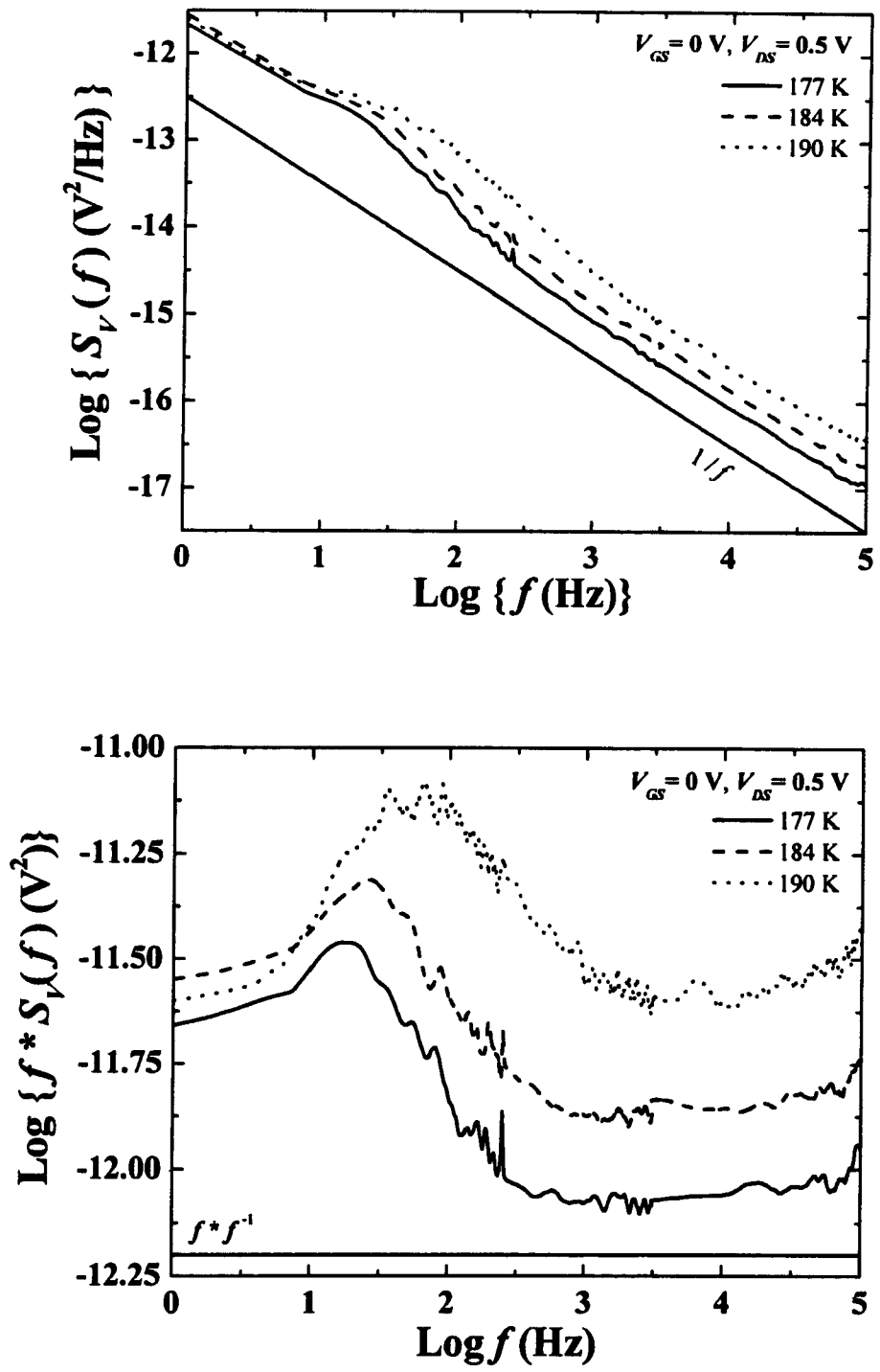


Fig. 4.35: Selected  $S_V$  (top) and  $f \cdot S_V$  (bottom) spectra at  $V_{GS} = 0 \text{ V}$ , in the temperature range 177-190 K.

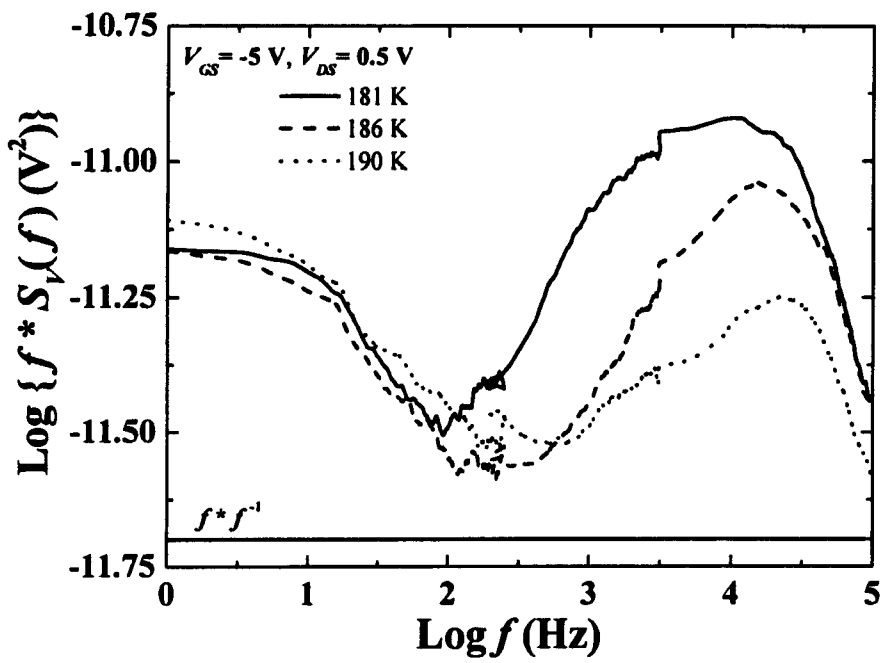
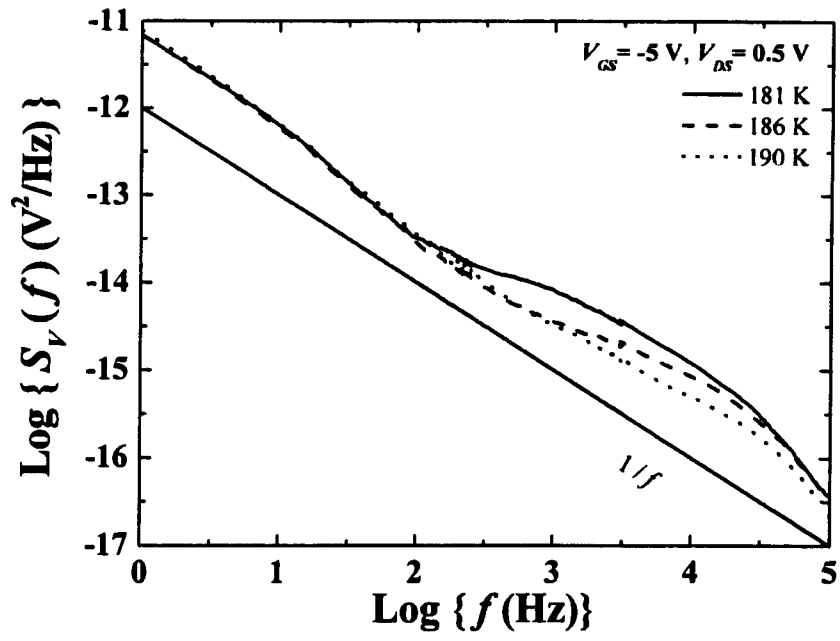


Fig. 4.36: Selected  $S_V$  (top) and  $f * S_V$  (bottom) spectra at  $V_{GS} = -5 \text{ V}$ , in the temperature range 181-190 K.

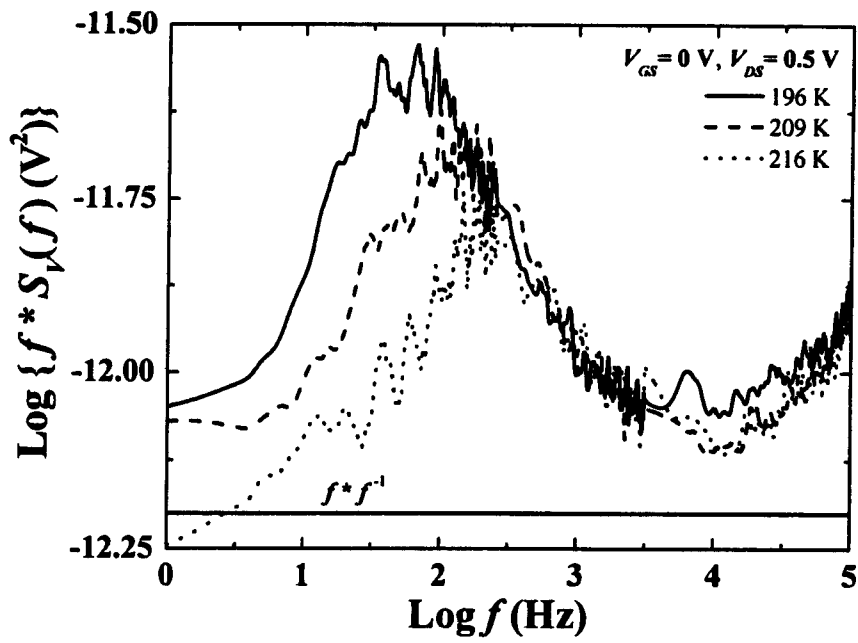
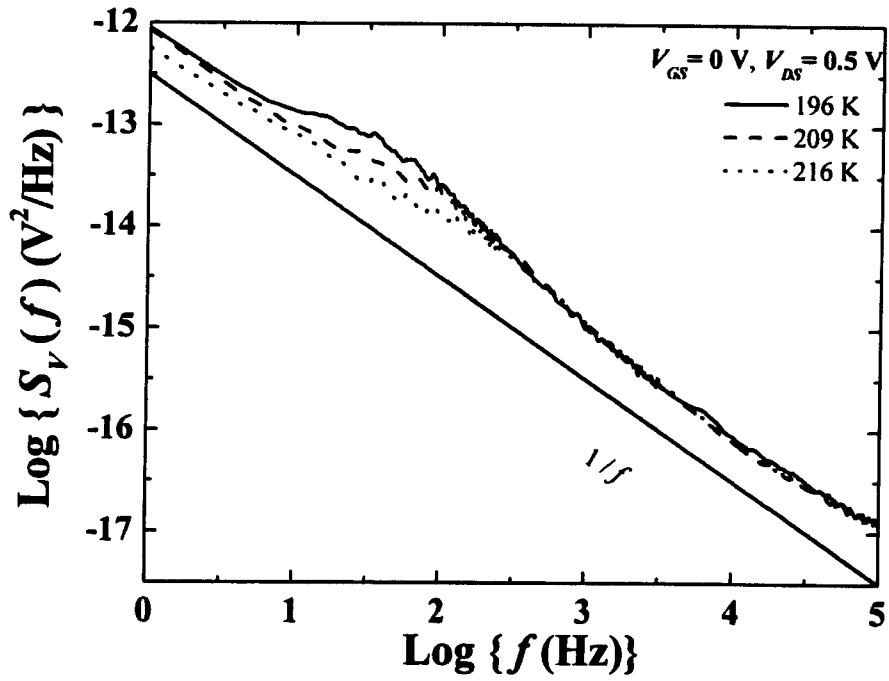
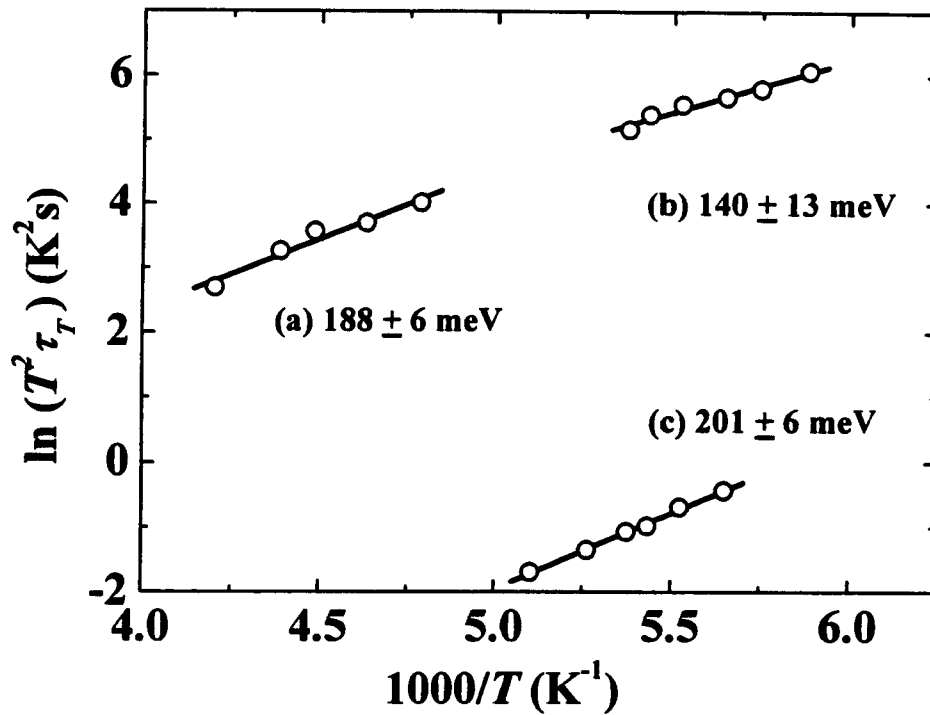


Fig. 4.37: Selected  $S_V$  (top) and  $f^*S_V$  (bottom) spectra at  $V_{GS} = 0 \text{ V}$ , in the temperature range 196-216 K.

### 4.2.11 Traps and their Activation Energy

The fluctuation time constant,  $\tau_T$ , associated with the g-r processes can be extracted from the cryogenic noise data. The activation energies of the traps are obtained from the Arrhenius plots shown in Fig. 4.38.



**Fig. 4.38:** Arrhenius plots for the traps observed in the temperature range 81 K -300 K.

From the noise data at  $V_{GS} = 0$  V, two g-r levels are identified, having activation energies of  $E_a=188$  meV and  $E_b=140$  meV as shown by lines (a) and (b) in Fig. 4.38 respectively. The noise data taken at  $V_{GS} = -5$  V indicates only one g-r level with the activation energy of  $E_c=201$  meV as shown by line (c) of Fig. 4.38. At this gate bias, the upper channel is depleted while the lower channel is still

conducting. Hence, the observed g-r noise at  $V_{GS} = -5$  V is likely to have originated from the lower channel. As can be noted, the activation energy for  $E_c$  (201 meV) is very close to the activation energy for  $E_a$  (188 meV). These values are estimated from the Arrhenius plots obtained by applying the least square linear fit to the data points. A standard error is associated with each fit, shown as an error in the estimation of the activation energy. Also, when the gate voltage is biased to a more negative value, the energy level of the trap will shift up leading to a slight increase in the measured activation energy. This may account for the observed difference in the activation energies between  $E_a$  and  $E_c$ . Hence, it seems possible that the observed g-r levels  $E_a$  ( $188 \pm 6$  meV) and  $E_c$  ( $201 \pm 6$  meV) are actually single physical species that exists either in the lower channel only or in both channels. Er implanted GaN has been reported<sup>21</sup> to have one of the levels with activation energy 0.188 eV. However, as the studied structure is not known to have intentional Er doping, this possibility is ruled out. Thin epitaxial GaN layers are also reported to have a trap with activation energy 0.18 eV. MOCVD grown GaN films, a level with activation energy 0.14 eV is also reported<sup>22</sup>. It has been suggested<sup>23</sup> that the 0.14 eV level may be related to carbon or hydrogen atoms that may be incorporated from the methyl radicals during growth of n type GaN by MOCVD. Native defect level  $V_{Ga}$ , and ionization energy of Mg (shallow acceptor) are also reported<sup>24</sup> to have 0.14 eV.

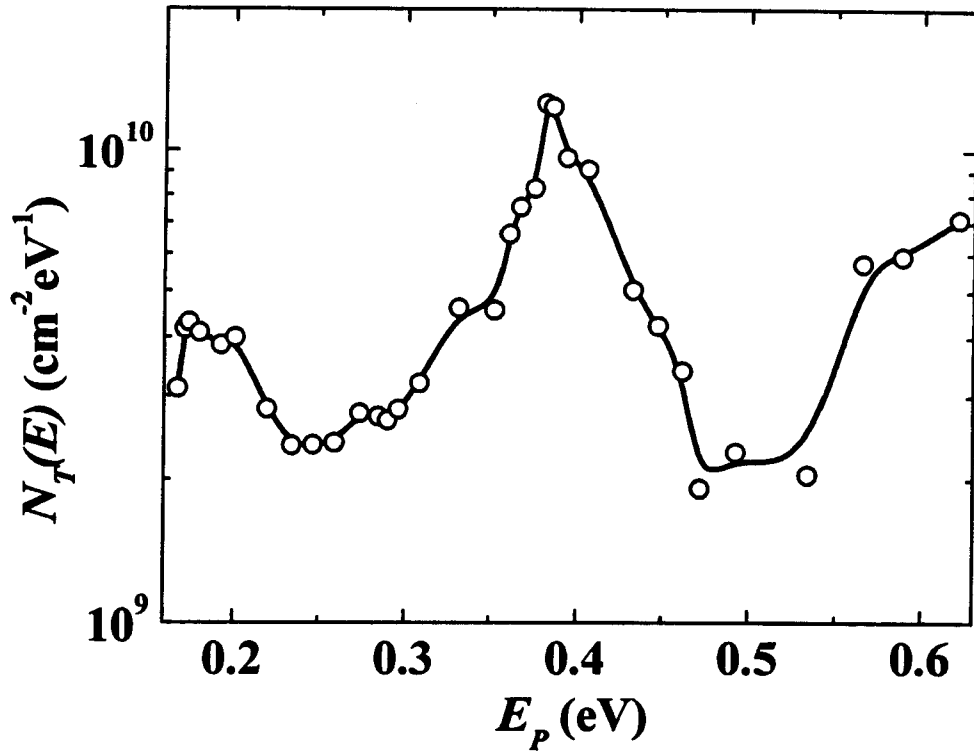


**Fig. 4.39:** Trap density derived from the noise data taken at  $V_{GS} = 0$  V.

Estimation of the trap density is helpful to examine the merits of the material and the device. Trap density was calculated with help of the formula  $E_p = -kT \ln(\omega\tau_0)$  and the results are shown in Fig. 4.39. The estimated value appears reasonable and is in agreement with the reported typical values of  $10^8$ - $10^{10}$   $\text{cm}^{-2}$ .

#### 4.2.12 Contribution of Contact Noise

Recalling the physical concept of TLM based contact resistance estimation, as described in Chapter 3, we observe that if the noise magnitude between two contact pads is proportional to the inverse square of the separation between them, then contribution of the ohmic contact is dominant. In case when the noise is dominantly contributed by the conduction medium i.e. the semiconductor channel between them, the noise magnitude will be proportional to the inverse of the separation length<sup>25</sup>. Noise spectra were taken at different bias voltage between 10 mV – 250 mV, and for different separation lengths between 3  $\mu\text{m}$  – 32  $\mu\text{m}$ . Results are plotted in Fig. 4.40. We find that the data points for all  $L_x$ , fit linearly with the  $V^2$ , which is an expected result for any ohmic channel in which conductance fluctuation is the dominant noise mechanism. Distinction of the result appears when the voltage normalized noise power i.e.  $S_V/V^2$  is plotted with the separation length, as shown in Fig. 4.41. A distinguished inverse  $L_x$  dependence is seen in the figure for the entire set of data points, confirming that contact noise is not a dominant mechanism in the presented devices.

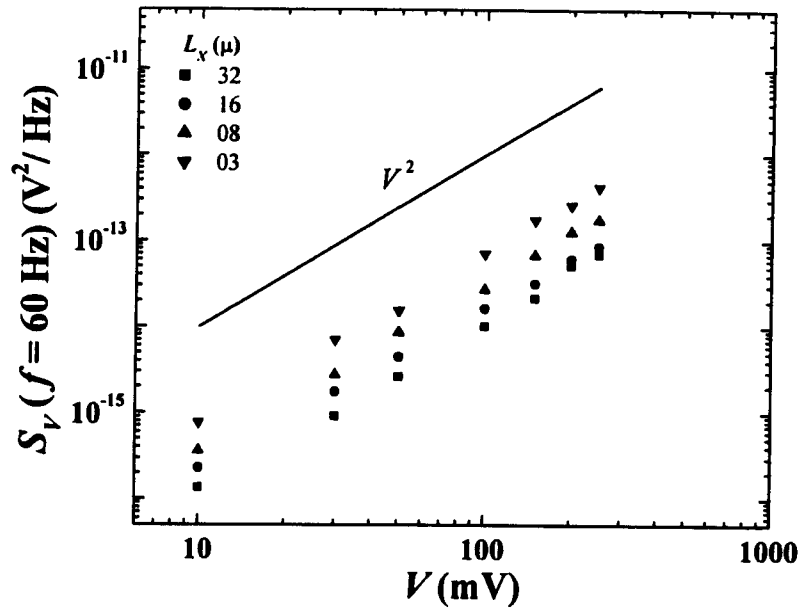


Fig. 4.40: Noise from TLM structure at different gate bias voltages.

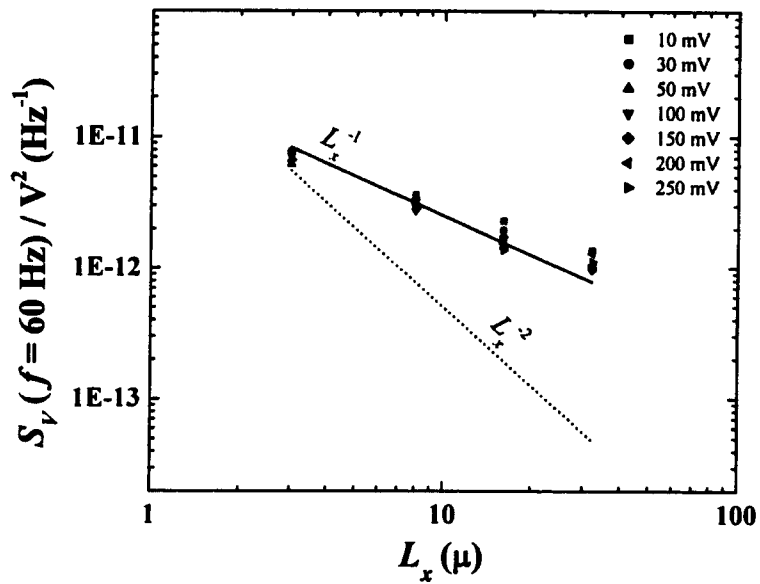


Fig. 4.41: Normalized noise power observed across the TLM pads with separation  $L_x$ , for different bias voltages.

### 4.2.13 Estimation of Hooge parameter

Hooge parameter,  $\alpha_H$ , has been used as a measure of the quality of the conducting films and devices<sup>26</sup>. It provides a suitable mean to compare the noise properties of the semiconductor devices fabricated by different technologies.

Recalling Hooge's equation,

$$\alpha_H = \frac{S_V(f)fN}{V_{DS}^2}. \quad 4.4$$

There are following considerations regarding estimation of  $\alpha_H$ :

1. Measured total noise of the device is the resultant noise of all possible contributions from different noise sources. Hence characteristic Hooge parameter for each source of origin shall be different. When it is not possible to resolve contribution of each kind of source, at least the contribution of dominant noise source should be identified.
2. It is important to estimate  $N$  carefully. Number of electrons under the gate can be calculated from  $C$ - $V$  measurements. Similarly, number of electrons in the source and drain regions can be calculated using the sheet resistivity obtained from TLM measurements and the known dimensions of the device.
3. The parameter is sensitive to the applied bias. Usually, for noise measurements in GaN-based FETs, a small value of  $V_{DS}$  are chosen to avoid ohmic heating. However, as the voltage drop across the source and drain ohmic contacts can be significant in the presented devices, an effective bias voltage should be considered for estimation.

Using the TLM results, and  $I$ - $V$  characteristics, estimated voltage drop across the contact resistance was found to be 0.19 V. As the resistivity of the channel under the gate and in the source/drain regions is comparable at zero gate bias, the noise contribution of the complete channel was considered for calculation of  $N$ . It is very hard to experimentally estimate the carrier density or mobility in the individual channels of a double heterostructure. A possible remedy to avoid estimation errors is to use the computational techniques like self-consistent Poisson-Schrodinger simulation of the structure. It allows determining the carrier concentration within the individual channels, which can directly be used to estimate  $N$ . However, that does not completely eliminate the problem, as the simulated values may vary largely from the actual values. This is because, during a material deposition process, typically the thickness of the individual layers may vary by as much as 20% from one run to another. In addition, it is also very difficult to accurately control the doping concentration in the AlGaIn layer. This makes it difficult to conclude anything precisely about the contribution from the individual channels. To experimentally obtain a reliable carrier concentration in the gate area,  $C$ - $V$  measurements was used. A total charge concentration of  $1.26 \times 10^{13} \text{ cm}^{-2}$  (obtained by calculating the area under the  $C$ - $V$  curve) was estimated. This accounts for a total of  $1.26 \times 10^7$  carrier under the gated area of  $100 \mu\text{m}^2$ . Similarly, the number of carriers in the source and drain regions were estimated to be  $3.18 \times 10^7$ . Finally, following the earlier discussed considerations, Hooge parameter was estimated to be  $1.64 \times 10^{-3}$ . This is comparable to the reported values<sup>27-30</sup> of Hooge parameter ( $10^{-3}$ - $10^{-4}$ ) for baseline HEMTs. In summary, following are the outcomes of the noise studies in dual channel devices:

- Dual Channel HEMTs offer good dc properties as evidenced by a high current density and a double hump in transconductance curve that can be controlled by appropriate design of the epitaxial layers to provide more control over gain linearity,
- Dual channel HEMTs offer comparable noise properties to base line HEMTs,
- Defect levels have strong contribution to device noise at low temperatures,
- At least two defect levels are present in the studied structures,
- Contact noise is not dominant in the studied HEMTs,

Noise characterization can be exploited as a good tool to probe individual material layers in a complex device structure.

## **Part III - Application of AlGaN/GaN heterostructures in Biosensors**

---

From the study presented in the previous parts, it is inferred that the state-of-the-art HEMTs are suitable for certain application beyond electronics. It is clear that typical life time of an unrecessed HEMT device is more than 200 hours even when operating in stressed conditions. Also, the noise properties of GaN HEMTs are at an acceptable level though there is still room for improvements. Hence, applications such as biosensors which do not require continuous operation at elevated current levels and require a large signal to noise ratio, can be a potential field of applications of the state-of-the-art GaN HEMTs beyond conventional electronics.

Also, it is customary to look for a wide variety of applications of any evolving technology so that market support can be attracted to fund its development. There could be manifold interests while looking for new prospective applications. Biosensors represent a rapidly expanding field, with a high annual growth rate that is backed by the health care industry. Research and development in this field is wide and multidisciplinary, spanning biochemistry, bioreactor science, physical chemistry, electrochemistry, electronics and software engineering. Clearly, a great deal of contribution is possible from a device engineer that could be drawn by academic or commercial interests while working for biosensor research. In this part, feasibility of using GaN-based heterostructures for biosensors is investigated as an initiative.

### **4.3.1 Investigation Objectives**

When initiating the work in such multidisciplinary area, it is good to focus first on the feasibility study. Following are the primary questions that reflect the objectives of the feasibility investigation of using AlGaN/GaN-based heterostructures for biosensor application.

- Is it possible to have a bio friendly cell-device interface?
- What possible way a heterostructure can be used for this investigation?

### **4.3.2 Technical Background**

Electron density in a heterostructure can be modulated by the action of charge over its surface. This will result in current modulation; hence the changes at the interface can be recorded as change in current through the conduction channel. So the physical entity which can interact with the heterostructure to produce detectable signals is the charge over the heterostructure surface or a potential applied on the heterostructure surface. Existence of electrical potential and charge in a biological species are well known phenomena. A common example is the 'nerve cells' that receive and send signal through a network of neurons which communicate through action potential<sup>31</sup>. The action potential is of the order of a few tens of millivolts. Electrical action in the biological species is a common phenomenon that has been extensively explored in biosensor technology. Biosensor technology is the driving force in the development of biochips for the detection of toxins<sup>32</sup>, environmental, biological and chemical pollutants<sup>33</sup>. Extracellular potential measurement from the cell membrane is considered to be a reliable indicator for the determination of the

presence of a specific agent in the cell's local environment<sup>34</sup>. In the present study, effect of Trypsin on saos-2 human osteoblast-like cells, cultured in high density on transparent AlGaIn/GaN-based large area HEMT like structures, is demonstrated by means of recording the change in the device current when subjected to Trypsin.

### **4.3.3 Significance of Using GaN-based heterostructures**

Extracellular potential measurement from the cell membrane is considered a reliable indicator for the determination of the presence of a specific agent in the cell's local environment. For extracellular signal recording from electrogenic cells in vitro, the use of microfabricated microelectrode arrays (MEAs) is one of the promising techniques although a large metal electrode must be used to obtain sufficient signals. Ability to create bio-semiconductor hybrid devices has gained much interest for cell activity analysis<sup>35</sup>. Electronic excitation of cells, cellular respiration and acidification, and ion channel activity<sup>36</sup> in cell adhesion has been achieved on the basis of Si ion sensitive field effect transistor (ISFET). There have been recent reports of the measurement of pH and oxygen partial pressure from cellular respiration and acidification with ISFET-based sensors<sup>37</sup>. Properties of Si ISFET, such as chemical instability and degradation of silicon oxide gate insulator in aqueous solutions as well as low signal to noise ratios, are insufficient to detect small changes of cell viability with large impedance. Recent progresses<sup>38</sup> using AlGaIn/GaN heterostructure based HEMTs is attractive to the biosensor applications due to the distinguished merits that include:

- Chemically inert surface (and hence bio-friendly),

- High chemical stability<sup>39</sup>,
- Large signal to noise ratio<sup>40</sup>,
- Transparent structure, allowing simultaneous optical and electrical monitoring of cell activity<sup>41</sup>.

All of the above mentioned points serve as motivation behind exploring the AlGaIn/GaN heterostructure for biosensing application. A major motivation also comes from the fact that a large transconductance is offered by HEMT based device structures. A large transconductance is favorable because it allows larger control over the device current. A large transconductance will result in a larger change in the measured drain current of a device when a fixed gate bias is applied. As every cell under investigation contain an extra cellular potential, a large number of such cells accumulated over a surface will result in buildup of an effective voltage in their close vicinity. In case, when these cells are accumulated over the gate area of a FET, it will serve as an applied bias over the gate area. Now, considering this voltage buildup as a fixed gate bias, a device offering large transconductance will offer larger change in drain current, when its gate area is exposed to accumulation of the cells. This in turn implies that a larger signal (drain current) will be detected for a fixed density of cells (gate voltage) if the transconductance is larger. Further, Transconductance<sup>42</sup> of a FET based device is proportional to electronic parameters of the device: (i) charge concentration and (ii) charge mobility. In addition, transconductance depends on the parameters which are externally controllable (i.e. drain and gate bias) and also on the device design parameters such as gate width and gate to drain spacing.

It is understood that a heterostructure based FET devices offer a very high carrier density together with high charge density. Hence, HEMTs can offer a large transconductance in comparison to other FET based devices when a similar set of bias voltages and device geometry is considered for comparison. This is important when very small changes in the electrical response are to be detected such as in biosensing applications. Therefore, application of heterostructure based devices is favorable for biosensors.

#### **4.3.4 Detection Mechanism of the Proposed Devices**

The fundamentals of the detection mechanism are rather simple for both biologists and device engineers. In the proposed AlGaN/GaN heterostructure based large area gateless HEMT structures; living cells are directly cultured on the bare gate area. Cell membrane and AlGaN surfaces are separated by a thin film of electrolyte that plays the role of a gate for the HEMT. The ion at the adherent cell membrane changes the extracellular voltage between cell and chip, which in turn modulates the drain-source current. Modulation of current is then recorded by a current meter.

#### **4.3.5 Investigation Plan**

The complete investigation process involved three major steps: 1) to develop good polarization doped heterostructures that are then used to fabricate devices; 2) to investigate the feasibility of cell-heterostructure interface; and 3) to achieve a high density cell-monolayer over the device surface and record the effect of the drug. Accordingly, the work is described further in following sections.

## 4.3.6 Heterostructure Growth and Characterization

### 4.3.6.1 Growth of AlGaN/GaN heterostructures

The material system consist of a 5 nm GaN cap layer, a 30 nm AlGaN barrier, and a 2  $\mu\text{m}$  thick GaN layer grown on sapphire substrates. Heterostructures were epitaxially grown by MBE. GaN cap layer was grown at the top of the AlGaN/GaN heterostructure to provide a stable and chemically inert surface. A cross-sectional diagram of the epilayer scheme is shown in Fig. 4.42.

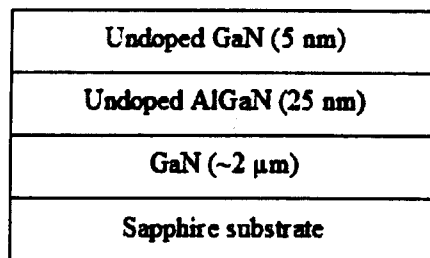


**Fig. 4.42: Epitaxial layer scheme of the AlGaN/GaN heterostructures used for bio-sensing application.**

Cross-sectional SEM image of such a heterostructure is shown in Fig. 4.43. GaN thickness (~2  $\mu\text{m}$ ) is properly estimated from this image. SEM image of the top surface of this heterostructure is shown in Fig. 4.44. Reasonable smoothness of the top layers can be observed.

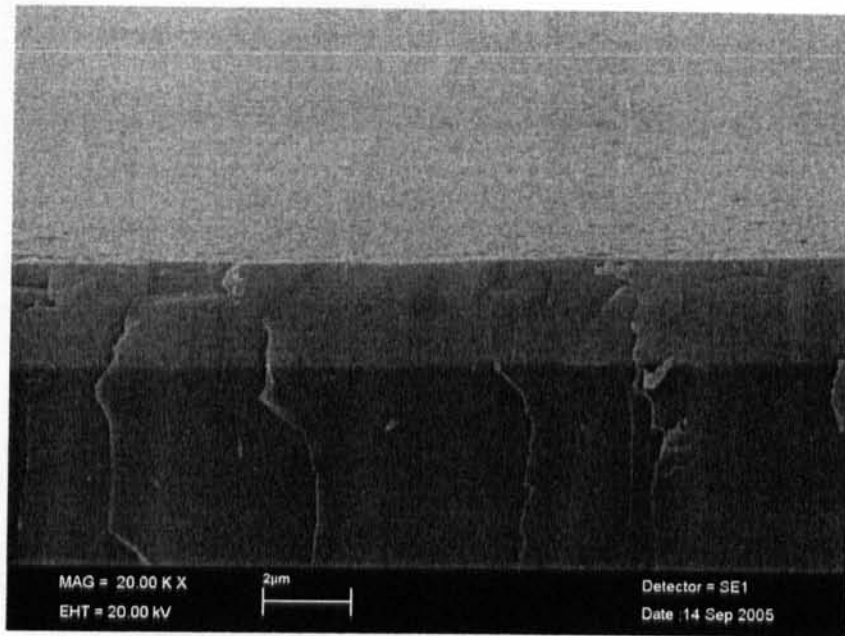


**Fig. 4.43: Cross-sectional SEM micrograph of a heterostructure sample.**

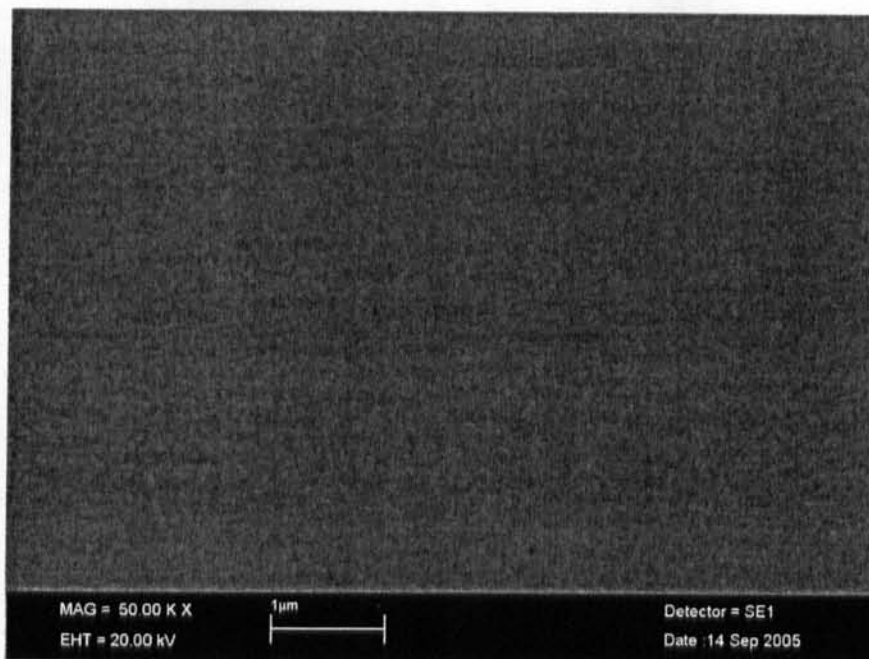


**Fig. 4.44: SEM image of the top surface of a heterostructure showing reasonably smooth surfaces.**

### 4.3.6.2 AFM Results

To further investigate the surface quality of the grown multilayers, AFM image was acquired, as shown in Fig. 4.45. The grown heterostructures possess a mean surface roughness of 80 nm and a rms roughness of 16 nm, as observed for a  $3.5 \mu\text{m} \times 3.5 \mu\text{m}$  scan area.

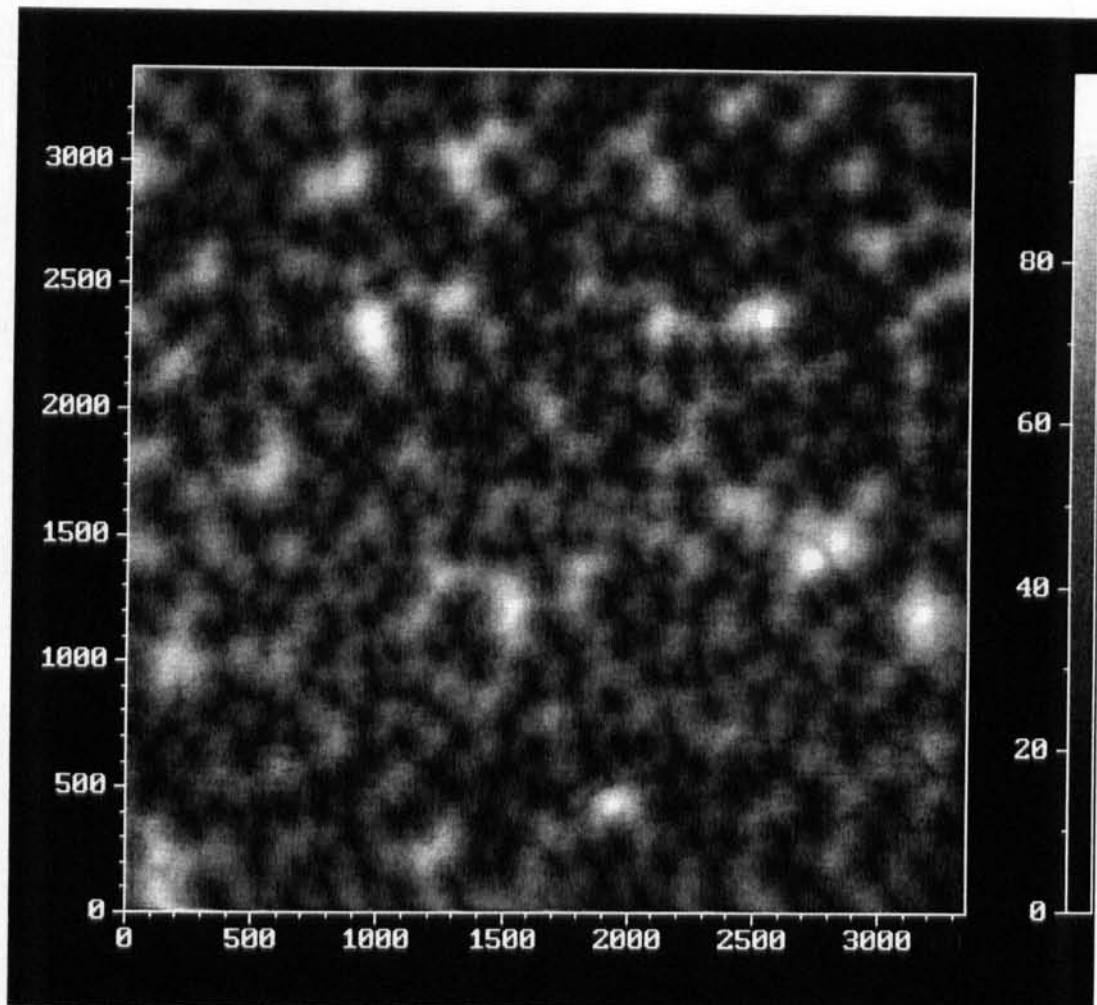


**Fig. 4.45: 2D AFM image of the top surface of a MBE grown AlGaIn/GaN heterostructure.**

### 4.3.6.3 HRXRD Results

To estimate the Al content in the grown heterostructures,  $\theta$ - $2\theta$  HRXRD scan was performed on a test heterostructure with a thick AlGa<sub>x</sub>N layer, that was also used to estimate the growth rate of the AlGa<sub>x</sub>N layer. The  $\theta$ - $2\theta$  profile is shown in Fig. 4.46. From the XRD data, Aluminum content ( $x$ ) of the Al <sub>$x$</sub> Ga<sub>(1- $x$ )</sub>N layers in the heterostructures was estimated to be  $x \sim 27\%$ .

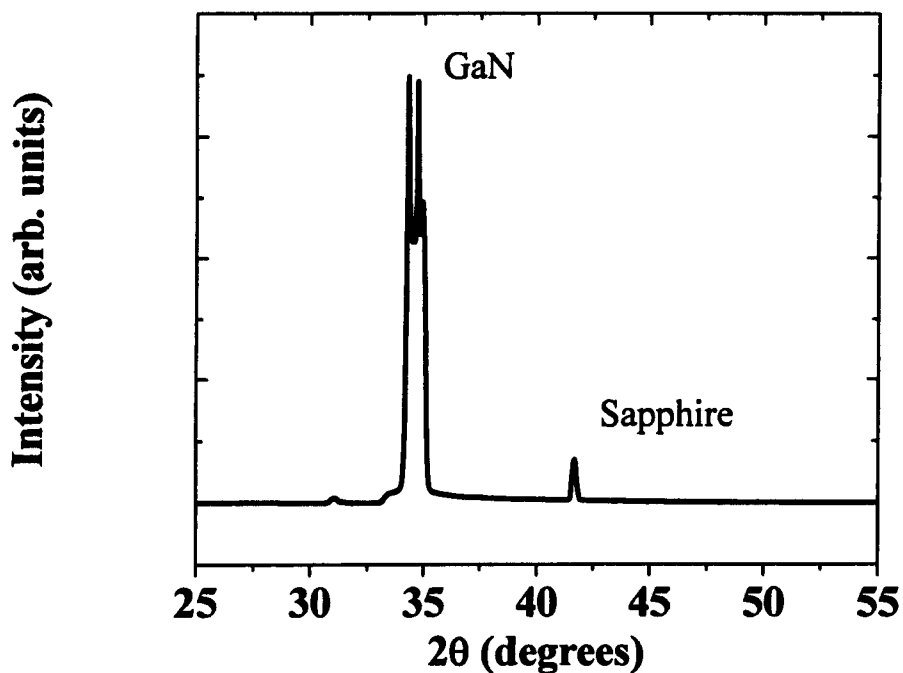
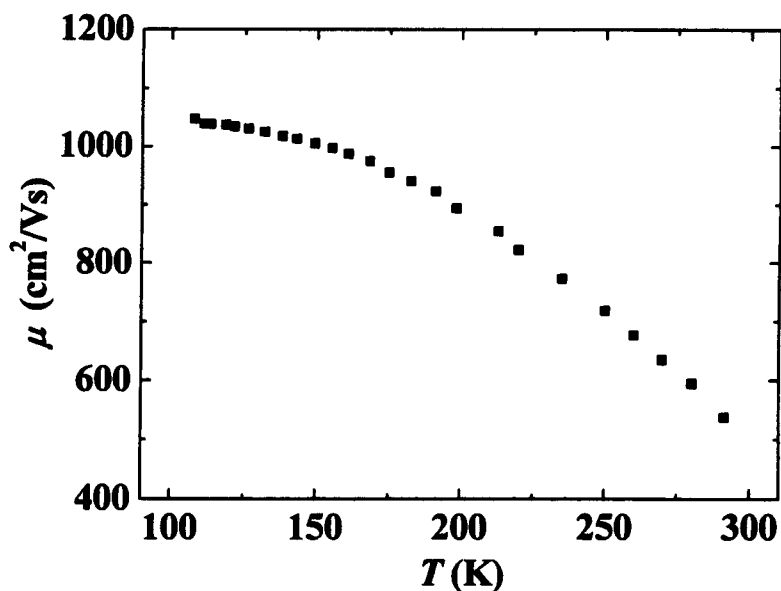


Fig. 4.46:  $\theta$ - $2\theta$  HRXRD scan of [0002] reflections from an AlGa <sub>$x$</sub> N/GaN heterostructure.

#### 4.3.6.4 Mobility Measurements

Hall measurements on a heterostructure sample of 6 mm × 6 mm dimension, in the van-der-pau configuration, were performed in the temperature range of 107 K to 300 K. From this experimental data, mobility vs. temperature profile is plotted in Fig. 4.47. A room temperature Hall mobility of 540 cm<sup>2</sup>/Vs was recorded. It was found that the mobility increases with the inverse of temperature showing a highest achievable value of 1050 cm<sup>2</sup>/Vs at 107 K, in the observed temperature range. Carrier concentrations at 300 K and 107 K were found to be 8.13 × 10<sup>12</sup> cm<sup>-2</sup> and 6.84 × 10<sup>12</sup> cm<sup>-2</sup> respectively. A high concentration and large mobility will allow a large current density in the channel, resulting in an increased sensitivity of the detector.



**Fig. 4.47: Dependence of Hall mobility on temperature as observed for an AlGaIn/GaN heterostructure sample.**

### 4.3.7 Fabrication of Device structures

Heterostructure were used for fabricating large area (3mm × 5 mm) HEMT like structures without any gate metal deposition. Two ohmic contacts were formed using electron beam deposition of Ti (20 nm) followed by Al (60 nm). The separation between the ohmic contacts represents length of the channel which was 3 mm. Deposition was followed by rapid thermal annealing (RTA) at 800 °C for 20 seconds. Such individual devices were placed on ceramic packages and were then wire bonded with an ultrasonic aluminum wire bonder. After wire bonding the device, all area except the active device area was covered with SU-8 photoresist to provide biocompatible electrical insulation when the device is exposed to the cells or solutions. A schematic diagram of the device is shown in Fig. 4.48.

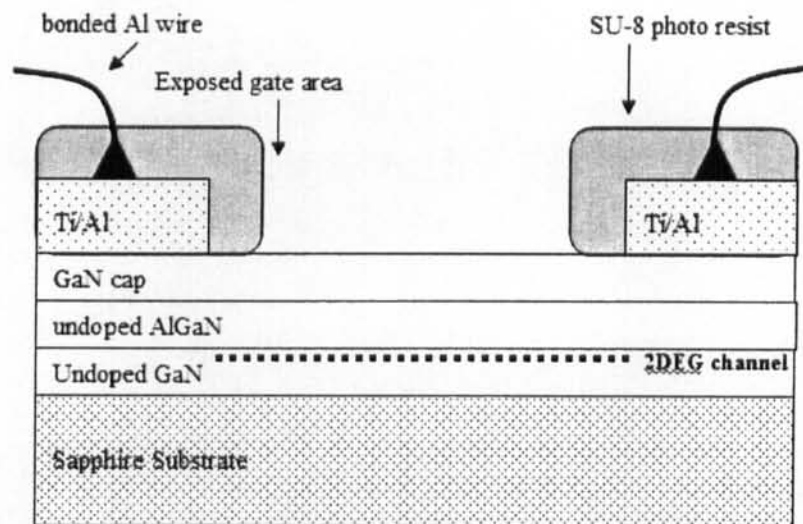


**Fig. 4.48: Schematic diagram of a bare gate HEMT like detector device.**

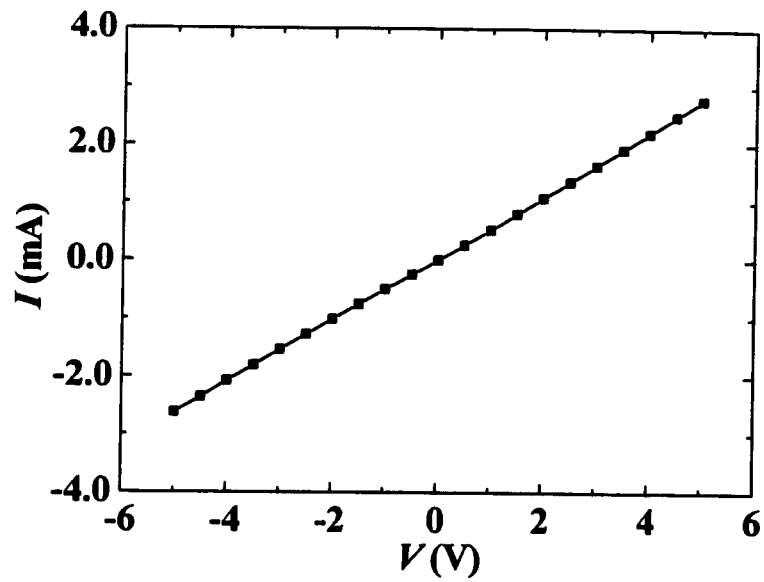


Fig. 4.49:  $I$ - $V$  characteristics of a freshly fabricated device.

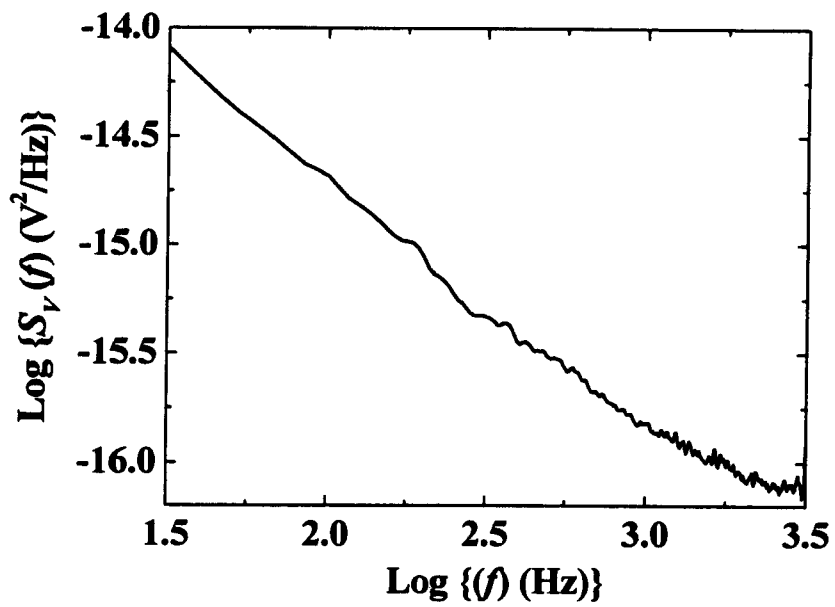


Fig. 4.50: Low frequency noise spectra of a virgin device at  $V = 0.2$  V.

### 4.3.8 Electrical Characterization of Virgin Devices

A virgin test device was subjected to  $I$ - $V$  and noise characterization after completing the fabrication and packaging steps.  $I$ - $V$  characteristic of a device is shown in Fig. 4.49, and a noise spectrum is shown in Fig. 4.50. The device shows a reasonable dc resistance of the order of a few  $k\Omega$ , allowing a channel current of the order of few milli amperes through the device. The noise spectrum indicates a low magnitude of intrinsic device noise. It allows a very small magnitude of change in voltage and hence current across the device to be easily sensed. For example, at bias voltage of 0.2 V and at operation frequency of 100 Hz, the recorded voltage fluctuation across the device terminals is of the order of  $\sim 50$  nV. When measured at 4 V bias, fluctuation becomes  $\sim 20$   $\mu$ V. As the magnitude of change in voltage induced by the experiments are orders of magnitude larger than this value, an excellent signal to noise ratio is offered by the presented devices.

After completing the fabrication and initial characterization of the packaged sensor devices, they were subjected to cell culture following the standard procedures that are discussed in the next section.

### **4.3.9 Cell on Chip: from Survival to High Density**

Once the initial goal of fabricating a complete device structure is completed, next comes the crucial part of achieving a successful cell-semiconductor junction. For this, a series of experiments were necessary and are described in this section.

#### **4.3.9.1 Cell Culture Protocol**

The following cell culture protocol was used for the investigations. Experiments were performed on human osteoblast-like cells from Saos-2 cell line (ATCC, USA). Cells were cultured in McCoy's 5A Medium Modified filtered by 0.22m filter paper supplemented with 2.2g/ml sodium bicarbonate, 50U/ml penicillin, 50g/ml streptomycin and 10% fetal bovine serum (FBS) (Invitrogen Corporation). Cells were cultured on gate area with 5ml medium and maintained in a humidified 95% air, 5% CO<sub>2</sub> atmosphere at 37°C. The density and morphology of cells on substrate surface were investigated with a phase contrast microscope (Nikon, TE 2000).

#### **4.3.9.2 Survival of cells on the GaN surface**

The basic requirement for cell-based FET biosensor is the survival of living cells on the GaN HEMT surface. Saos-2 cells on GaN surface at the density of  $4 \times 10^5$ /ml were deposited. An optical micrograph of the cells cultured on GaN surface after 24 h is shown in Fig. 4.51. The cells show good shapes and spreading after 24h culture indicating the good viability.

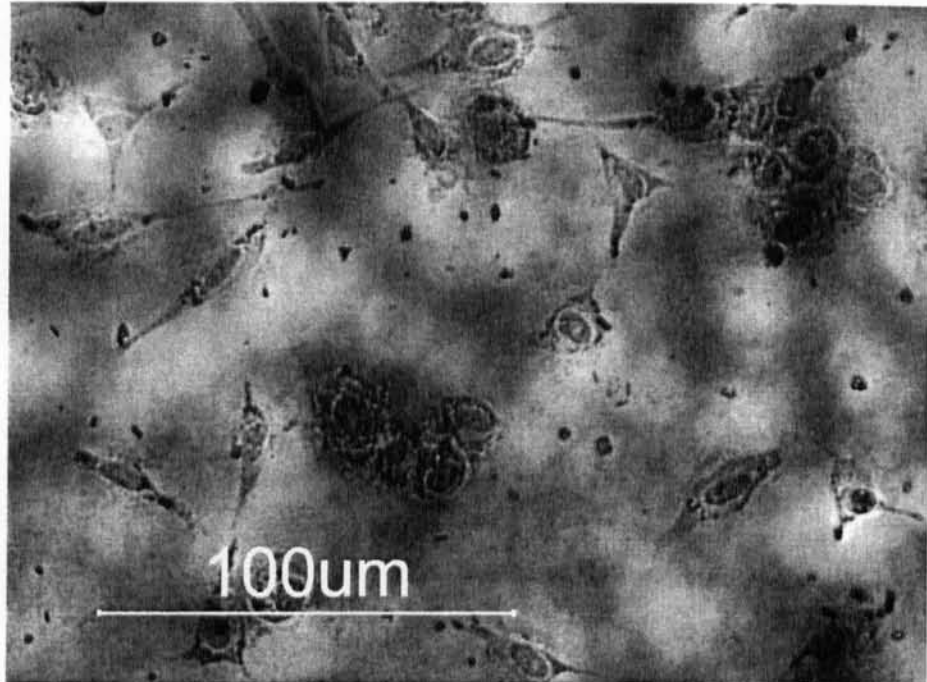


**Fig. 4.51: Adherent cells on an untreated heterostructure surface.**

#### **4.3.9.3 Surface Functionalization**

To increase the sensitivity of cell-based FET, one possible way is to increase the cell adhesion which will put the target cells as close as to the HEMT gate. Here, we examined the cell adhesion on two types of GaN: one was a GaN surface modified by fibronectin (FN), and the other was a non-treated surface. A small amount of FN was added to cover the whole GaN surface for the modification case. Optical images of saos-2 cells on both bare and modified GaN surfaces after one-day culture is shown in Fig. 4.52 and Fig. 4.53, respectively.

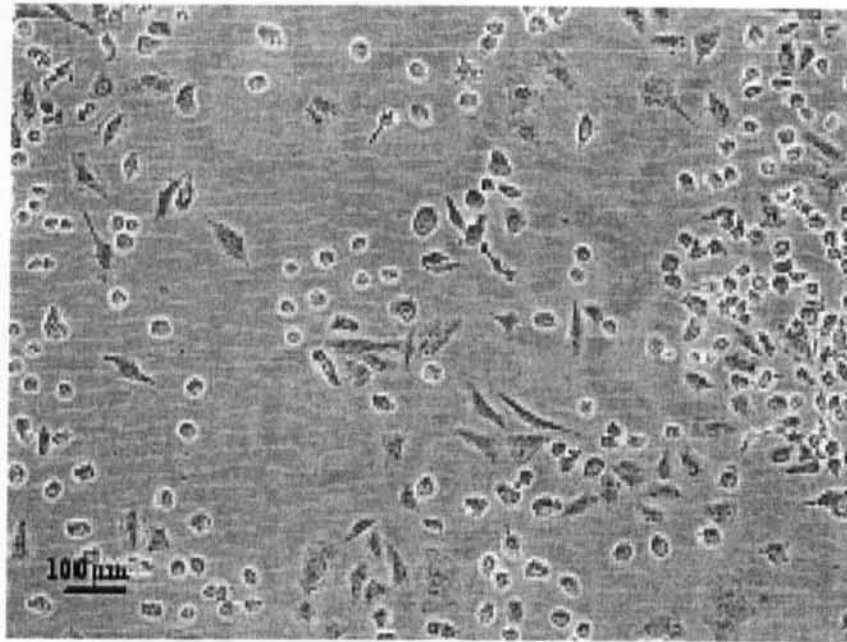


**Fig. 4.52: Cells cultured on untreated GaN surface in 24 h.**

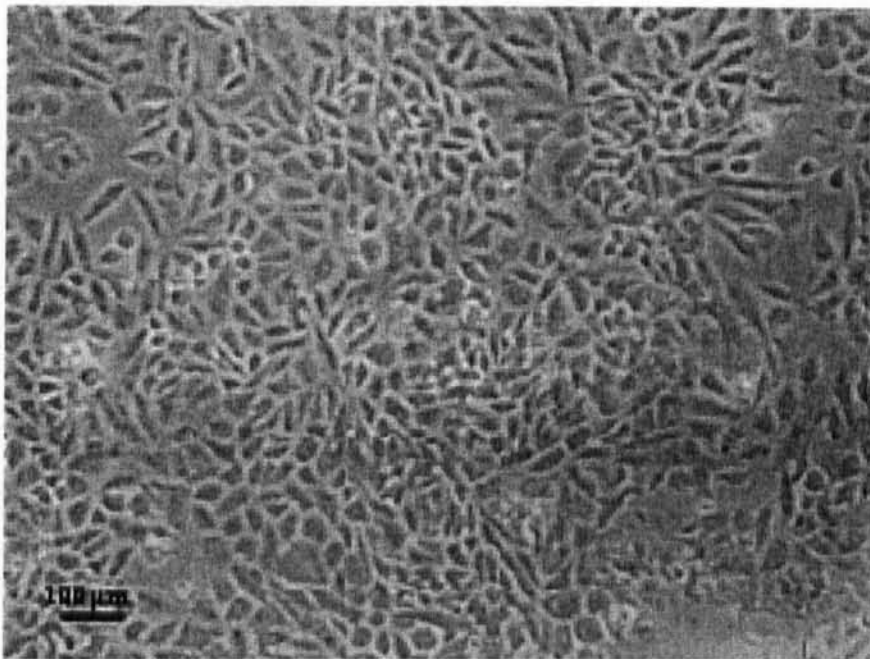


**Fig. 4.53: Cells cultured on FN modified GaN surface in 24 h.**

It is clear that the cells adhere very well to the FN modified AlGaIn surface. The cell density was  $2.6 \times 10^4$  cells/cm<sup>2</sup> on the non-treated surface, whereas it was  $5.4 \times 10^4$

cells/cm<sup>2</sup> on the FN-modified surface. The result shows that the surface modification by FN improves the cell adhesion to AlGaIn surface. This suggests the possibility of functionalizing the device surface for better performance as biosensors, which could increase the cell adhesion to the gate surface.

#### **4.3.10 Effect of Trypsin on Cultured Cells**

Trypsin is a proteolytic enzyme which can be used to detach adherent cells from the surface of a cell culture vessel. The procedure is called trypsinization and performed whenever the cells need to be harvested or to be subcultured. Protein kinase inhibitor, 1-(5-iso-quinolinyisulfonyl)-2-methylpiperazine (H-7), was obtained from Sigma Chemical Co. (St Louis, MO). H-7 was added to the growth medium to achieve a concentration equal to 120 nM. H-7 treatment reduces the abundance of large fibers in the cell cytoskeletal organization. To reverse the effects of H-7, the medium containing H-7 was replaced with fresh medium lacking H-7.

Effect of trypsin on the cell-semiconductor adhesion is shown in Fig. 4.54. Fig. 4.57 (top) shows five adherent living cells well attached to the underlying GaN surface; and the Fig. 4.57 (bottom) shows that the cells are detached and have become round. The microscope focus is shifted a little above the GaN surface to be able to view them.

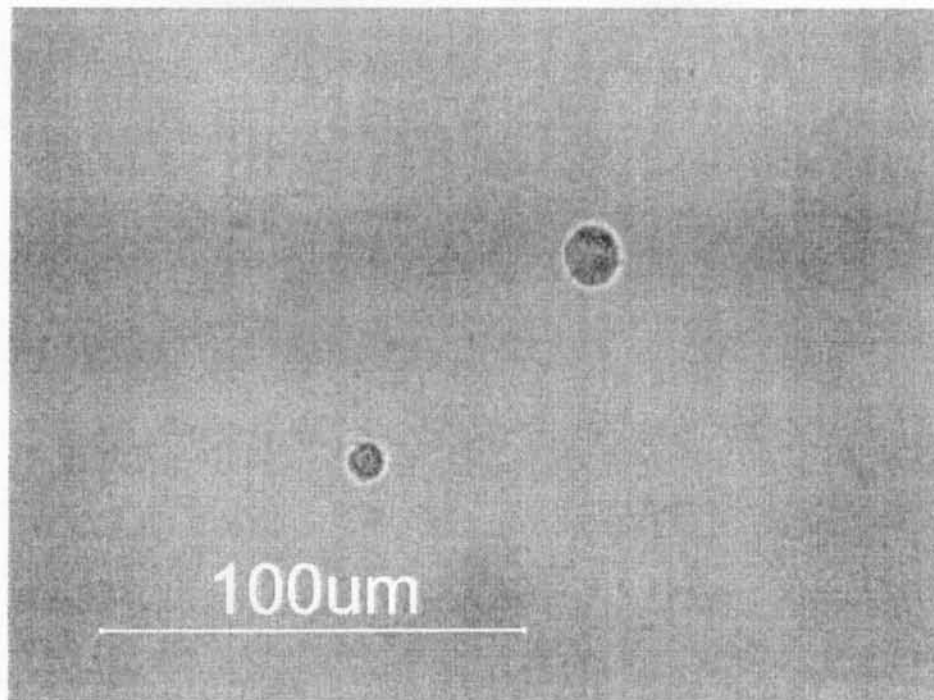
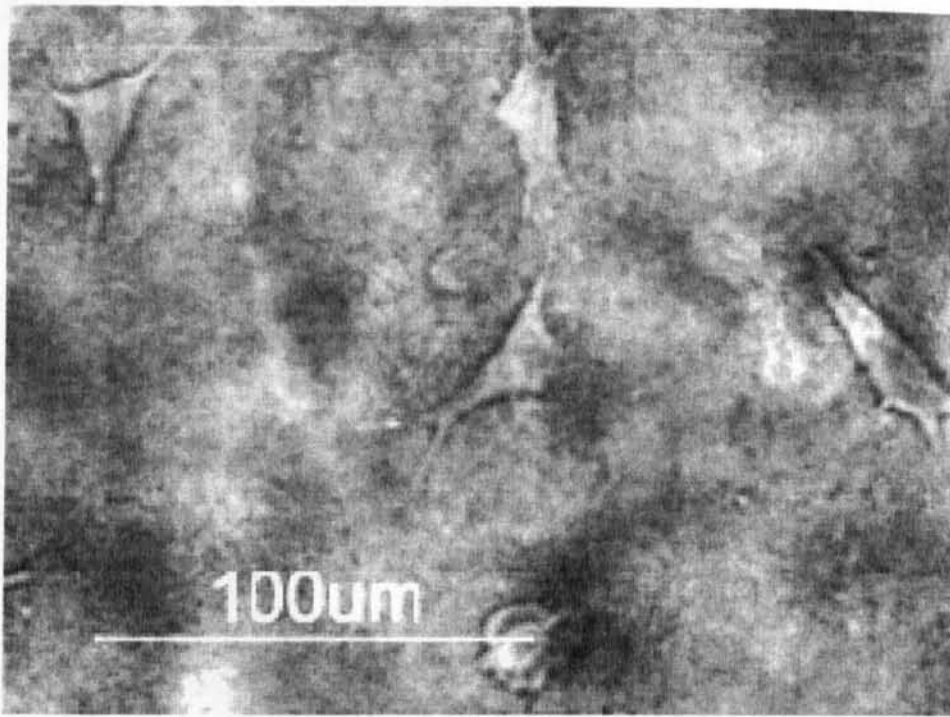


**Fig. 4.54: Cultured cells as observed on a GaN surface, before (top) and after (bottom) introducing trypsin in the medium.**

### 4.3.11 Effect of Drug H-7 on Cultured Cells

The cell response to the drug H-7, a protein kinase inhibitor, was first studied in culture dishes by optical observations. To visualize stress fibers of the cytoskeletal structure, the cells were fixed and labeled, and the stained cells were visualized using epifluorescence microscopy. In the absence of H-7, typical cell spreading and cytoskeletal organization were observed, shown in Fig. 4.55 (left). H-7 treatment reduced the abundance of large fibers (bright lines in the image) over the course of an hour, as shown in Fig. 4.55 (right). The loss of the fibers resulted in less cell-substrate contacts without dramatic change of cell morphology. Effect of trypsin is also shown in Fig. 4.56, as observed by epifluorescence microscopy

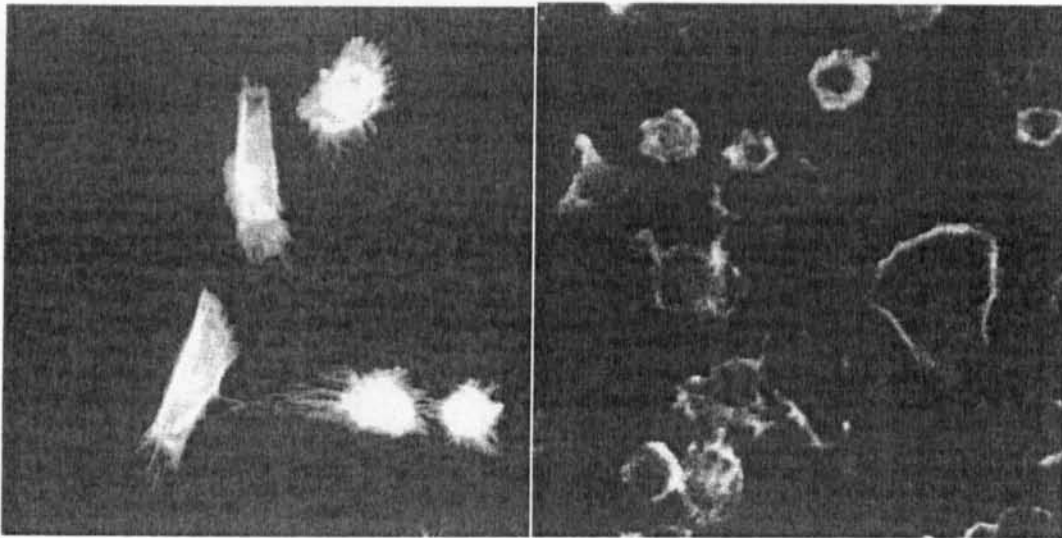


**Fig. 4.55: Epifluorescence microscopy images of cultured cells as observed on a GaN surface, before (left) and after an hour of introducing H7 (right) in the medium.**

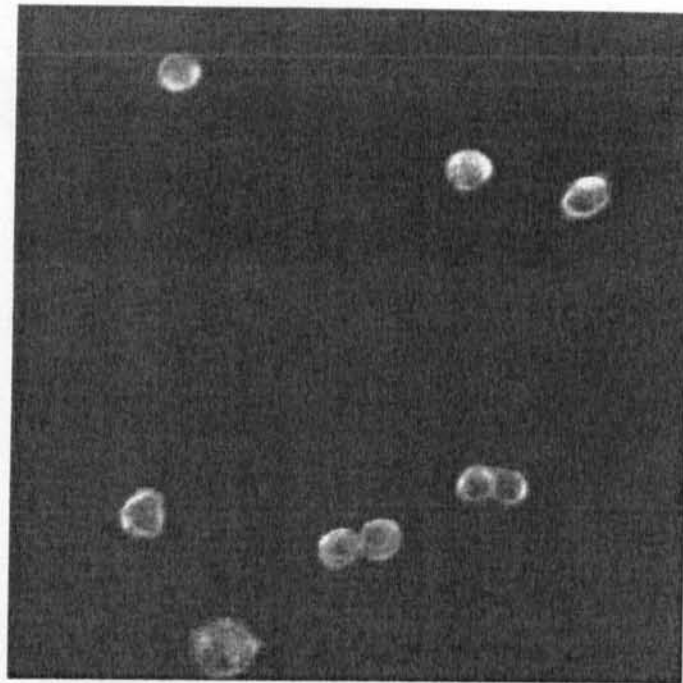


**Fig. 4.56: Epifluorescence microscopy images of cultured cells as observed on a GaN surface, 5 minutes after introducing trypsin in the medium.**

#### **4.3.12 Estimation of Cell Density and Growth Rate**

It was extremely difficult to optically observe the semiconductor attached cell density; hence the following method was used for estimation of the cell density at a particular time of growth. Though, cultured cells are not directly visible when attached to the surface, they can be efficiently observed as spherical objects seen in abundance after introducing trypsin. To determine the growth rate with time, Cell growth in a batch was performed on a number of samples. Then at different time intervals, a particular sample was taken out and exposed to trypsin. Due to the effects of trypsin, now the detached cells can easily be observed under the microscope. A fixed volume of 100  $\mu\text{l}$  was used to count the detached cells, and

was averaged for three different arbitrary regions chosen over the entire surface. Based on this data, rate of cell culture growth was determined, as shown in Fig. 4.57. The results suggest that a high density of cells can be achieved in a reasonable time to obtain a confluent monolayer of cells over the gate area.

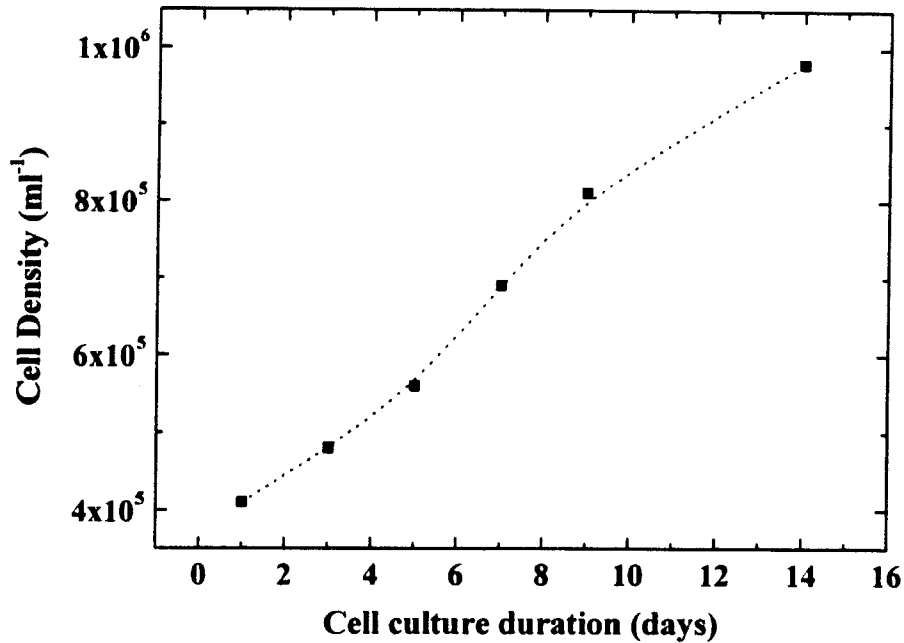


**Fig. 4.57: Growth profile of cell density with cell culture duration.**

### **4.3.13 Estimation of Detection Time**

It is necessary to understand the time evaluation of trypsin induced cell detachment effects. This is because; the electrical detection experiment will be carried out on the same time scale. A series of five graphs is presented here, which reflect the device density observed before introducing trypsin, and then every minute after that.

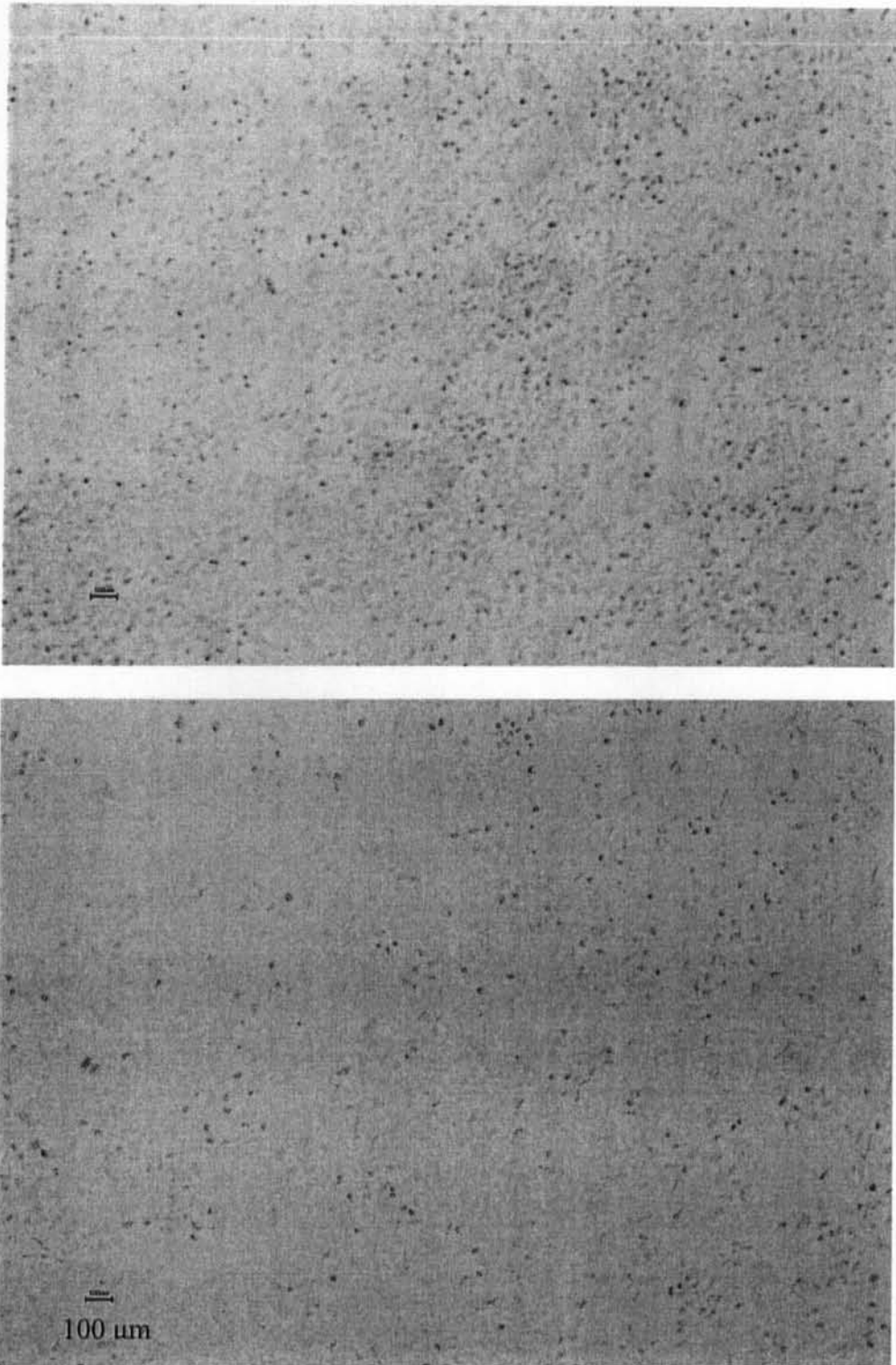


**Fig. 4.58: Cell density as observed before (up) and 1 minute after (down) introducing trypsin.**

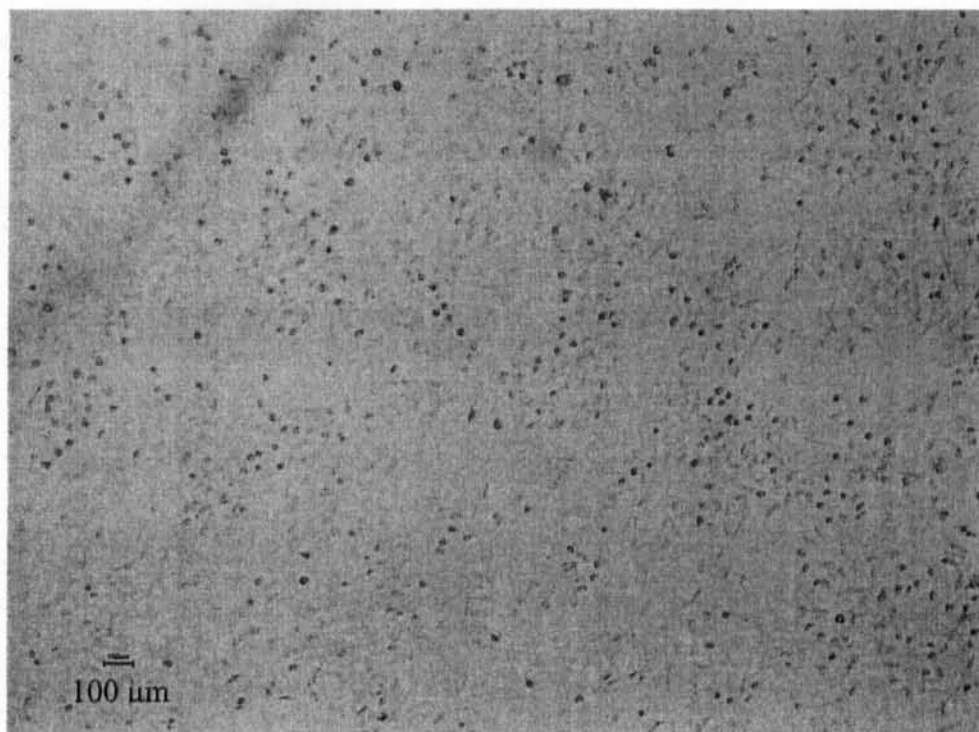
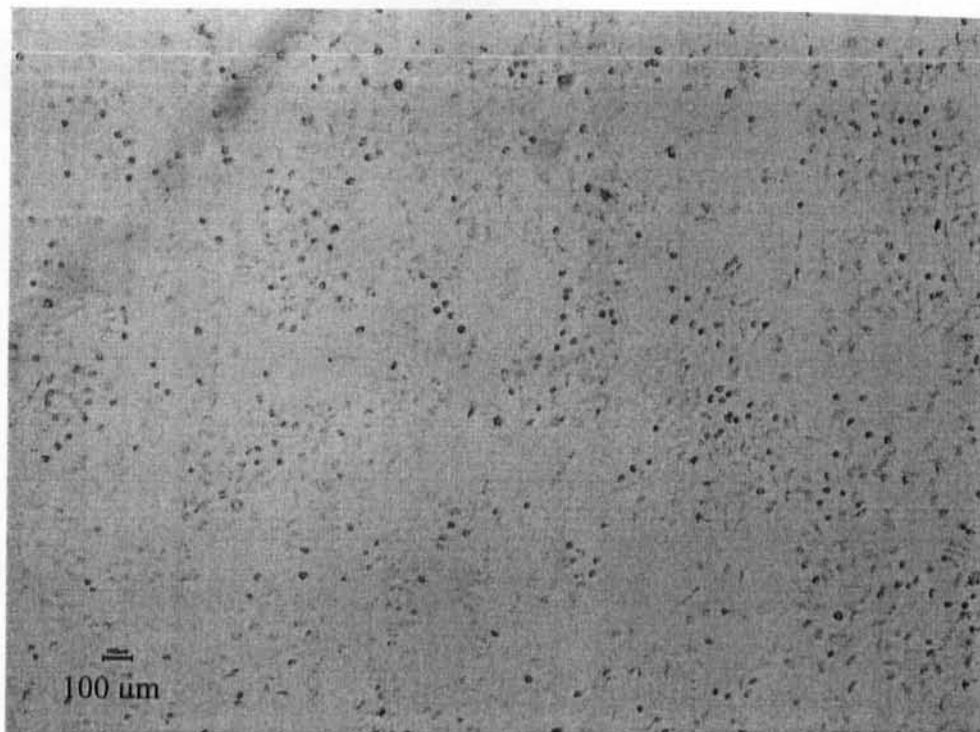


**Fig. 4.59 : Cell density as observed after 2 minute (up); and after 3 minute (down) of introducing trypsin.**

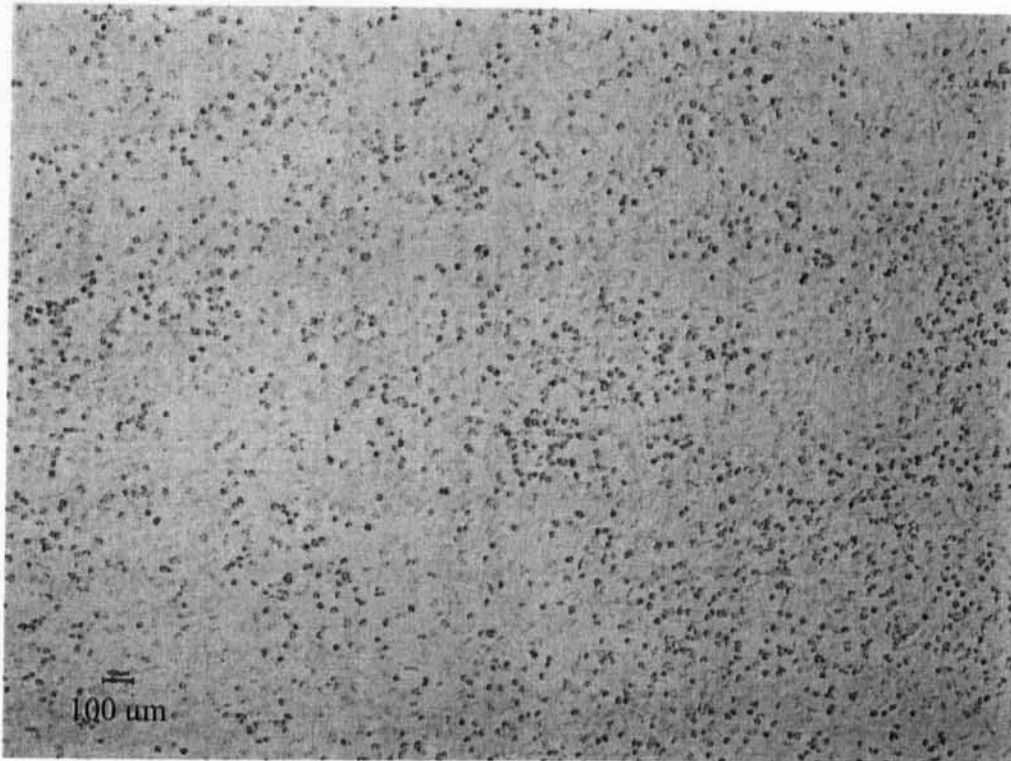


**Fig. 4.60: Cell density as observed after 4 minute of introducing trypsin.**

We find that gradually the number of dark spherical dots increase, reflecting the increasing number of detached cells from the device surface. After four minutes, not much observable change was seen, implying the saturation of the process that ends up with almost all the cells detached from the surface. A hint from this visual experiment was taken to decide the time span of electrical measurements and the frequency of a measurement during the detachment process of  $\sim 4$  minute duration. Hence, at least six to eight minutes of electrical monitoring was inferred.

### 4.3.14 Electrical Detection of the Influence of Trypsin

In the final stage of the work, electrical monitoring was used for the desired electrical detection of the influence of trypsin. For this,  $I$ - $V$  measurements were performed at different steps, to evaluate the cell response to trypsin. In the experiment, cells were cultured on the gate area for 24 hours to reach an essentially confluent monolayer. Two hours later, the H-7 was added into the medium to attain a final concentration of 120 mM. Then cells were cultured in the medium with H-7 for one more hour. Later, H-7 was removed by replacing the medium and the host device was subjected to  $I$ - $V$  measurements. Device current,  $I$ , was measured at a bias voltage,  $V_{DS}$ , and at a time,  $t$ .

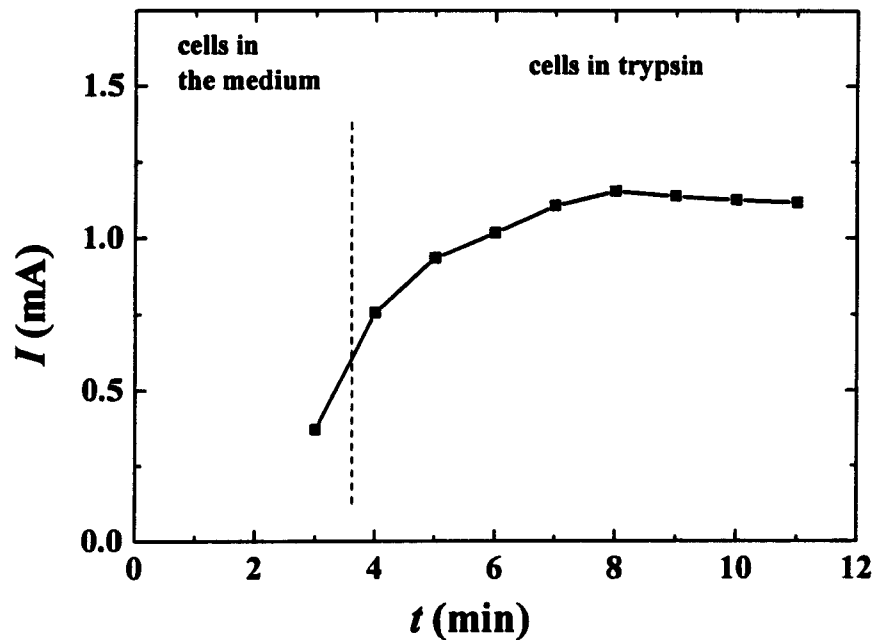


Fig. 4.61: Influence of trypsin on the device current observed at  $V_{DS} = 4$  V.

Experimental results are plotted as  $I$  vs.  $t$  plot for a fixed bias voltage of  $V_{DS} = 4$  V, as shown in Fig. 4.61. The plot clearly indicates increase of device current when subjected to trypsin. Presence of cells, lying in the cell medium and attached to the detector surface, results in an initial device current of 0.37 mA. When trypsin is introduced, the device current starts increasing with time and reaches a saturation value of  $\sim 1.1$  mA in four to five minutes. After reaching saturation, no significant change in the device current is observed until the cells are removed from the device surface. Observed variation in device current can be explained as follows. Initially, cells lie on the device surface in the culture medium. As explained in section 4.3.2, presence of abundance of cells attached over the gate area of the device has an electrical influence that is similar to applying a negative gate bias to the device. When trypsin is introduced in the medium at  $t = 3$  min., the process of detachment of cells, from the gate area, starts. As every gate-attached cell contributes a finite negative potential to the gate potential of the device, detachment of any cell from the gate area will result in a finite decrease of the negative gate bias. At a constant drain-to-source voltage, a finite decrease in negative gate bias will result in a finite increase in the drain current (the magnitude of decrease will be transconductance multiplied by change in the gate potential). Hence, introduction of trypsin causes an increment in recorded drain current with time, which is observed in the data range corresponding to  $t = 3$  to  $t = 7$  minutes. In this range cells continue to detach from the gate area until all the cells are detached at  $t \sim 7$  minute. As there are no more cells available to detach from the gate surface after  $t = 7$  min., no further increment in the drain current is observed for  $t > 7$  min., and a current saturation is observed.

The time scale over which the current decreased after exposure to trypsin (about four minutes) is consistent with the time scale that trypsin was optically observed to alter the abundance of cells, as shown in the previous section. A similar event scale observed from the optical inspection and the electrical detection confirms the validity of proposed sensing mechanism. This preliminary success also indicates the feasibility of more serious biosensing applications which can be further developed utilizing the potential of the presented AlGa<sub>N</sub>/Ga<sub>N</sub> HEMT based sensor structure. A summary of the outcomes of this feasibility study is listed as follows:

- It is feasible to immobilize osteoblast-like saos-2 cells on as grown Ga<sub>N</sub> surface,
- Surface modification can further improve the cell adhesion and likely, a variety of other cells can also be immobilized over the Ga<sub>N</sub> surface,
- Optical inspection of cell adhesion or detachment is easily accomplished using epifluorescence microscopy,
- Electrical detection of cell detachment is well demonstrated.

## REFERENCES (CHAPTER 4)

---

- <sup>1</sup> D. Sahoo, R. Lal, H. Kim, V. Tilak, and L. Eastman, "High-field effects in silicon nitride passivated GaN MODFETs," *IEEE Trans. Electron Devices*, Vol. 50, p. 1163, 2003.
- <sup>2</sup> G. Simin, A. Koudymov, A. Tarakji, X. Hu, J. Yang, M. A. Khan, M. S. Shur, and R. Gaska, "Induced strain mechanism of current collapse in AlGa<sub>N</sub>/Ga<sub>N</sub> heterostructure field-effect transistors," *Appl. Phys. Lett.*, Vol. 79, p. 2651, 2001.
- <sup>3</sup> B. Green, K. Chu, E. Chumbes, J. Smart, J. Shealy, and L. Eastman, "The effect of surface passivation on the microwave characteristics of undoped AlGa<sub>N</sub>/Ga<sub>N</sub> HEMT's," *IEEE Electron Device Lett.*, Vol. 21, p. 268, 2000.
- <sup>4</sup> L. K. J. Vandamme, "Noise as a diagnostic-tool for quality and reliability of electronic devices," *IEEE Trans. Electron Devices*, Vol. 41, p. 2176, 1993.
- <sup>5</sup> S. Ng and C. Surya, "Theory and experiments on flicker noise in In Ga As/AlAs/InAs resonant-tunneling diodes," *Journal of. Appl. Phys.*, Vol. 73, p. 7504, 1993.
- <sup>6</sup> Rashmi, S. Halder, and R. Gupta, "2-D analytical model for current-voltage characteristics and output conductance of AlGa<sub>N</sub>/Ga<sub>N</sub> MODFET", *Microwave and Optical Technology Letters*, Vol. 29, p. 117, 2001.
- <sup>7</sup> R F Voss, "1/f noise and percolation in impurity bands in inversion layers," *J Phys. C: Solid State Phys.*, Vol. 11, p. L923, 1978.
- <sup>8</sup> J. Neubauer and C. Van de Walle, "Hydrogen in GaN: Novel aspects of a common impurity," *Phys. Rev. Lett.*, Vol. 75, p. 4452, 1995.
- <sup>9</sup> S. Myers and A. Wright, "Theoretical description of H behavior in Ga<sub>N</sub> p-n junctions," *J. Appl. Phys.*, Vol. 90, p. 5612, 2001.
- <sup>10</sup> W. Ho and C. Surya, "Study of 1/f Noise in Hydrogenated Amorphous Silicon Thin Films," *Solid State Electronics*, Vol. 41, p. 1247, 1997.

- 
- <sup>11</sup> S. Limpijumnong and C. Van de Walle, "Stability, diffusivity, and vibrational properties of monatomic and molecular hydrogen in wurtzite GaN," *Phys. Rev. B*, Vol. 68, p. 203, 2003.
- <sup>12</sup> S. Pearton, C. Abernathy, C. Vartuli, J. Lee, J. MacKenzie, R. Wilson, R. Shul, F. Ren, and J. M. Zavada, "Unintentional hydrogenation of GaN and related alloys during processing," *J. Vac. Sci. Technol. A*, Vol. 14, p. 831, 1996.
- <sup>13</sup> R. Allam, C. Kolanowski, D. Theron, and Y. Crosnier, "Subharmonic gate mixer on a multichannel HEMT," *IEEE Microwave and Guided Wave Lett.*, Vol. 5, p. 122, 1995.
- <sup>14</sup> N. Sheng, C. Lee, R. Chen, D. Miller, and S. Lee, "Multiplechannel GaAs/AlGaAs high electron mobility transistors," *IEEE Electron Device Lett.*, Vol. 6, p. 307, 1985.
- <sup>15</sup> D. C. Dumka, G. Cueva, H. Hier, O. Aina, and I. Adesida, "DC and RF characteristics of doped multichannel AlAsSb/InGaAs field effect transistors with variable gate-lengths," *IEEE Electron Device Lett.*, Vol. 22, p. 11, 2001.
- <sup>16</sup> R. Chu, Y. Zhou, J. Liu, D. Wang, K. Chen, and K. Lau, "AlGaIn-GaN double-channel HEMTs," *IEEE Trans. Electron Devices*, Vol. 52, p. 438, 2005.
- <sup>17</sup> D. Thron, B. Bonte, C. Gaquiere, E. Playez, and Y. Crosnier, "Characterization of GaAs and InGaAs Double-Quantum Well Heterostructure FET's," *IEEE Trans. Electron Devices*, Vol. 40, p. 1935, 1993.
- <sup>18</sup> C. Eugster, T. Broekaert, A. Jesh, C. Fonstad, "An InAlAs/InAs MODFET," *IEEE Electron Device Lett.*, Vol. 12, p. 707, 1991.
- <sup>19</sup> D. Sodini, A. Touboul, G. Lecoy, and M. Savelli, *Electron. Lett.*, Vol. 12, p. 42, 1976.
- <sup>20</sup> M. Levinshtein and S. Rumyantsev, *Semicond. Sci. Technol.*, Vol. 9, p. 1183, 1994.
- <sup>21</sup> T. Wojtowicz, V. Matias, P. Marie, M. Mamos, B. Pipeleers, P. Ruterana and A. Vantomme, *Mater. Sci. Eng. B*, Vol. 105, p. 122, 2003.

- 
- <sup>22</sup> P. Hacke, T. Detchprohm, K. Hiramatsu, N. Sawaki, K. Tadatomo, and K. Miyake, *J. Appl. Phys.*, Vol. 76, p. 304.
- <sup>23</sup> W. Lee, T. Huang, J. Go, and M. Fueng, *Appl. Phys. Lett.*, Vol. 67, p. 1721, 1995.
- <sup>24</sup> S. Strite and H. Morkoc, *J. Vac. Sci. Technol. B*, Vol. 10, p. 1237, 1992.
- <sup>25</sup> Rumyantsev et al., "Low frequency noise in GaN metal semiconductor and metal oxide semiconductor field effect transistors," *Journal of Appl. Phys.*, Vol. 90, p. 310, 2001.
- <sup>26</sup> F. Hooge and A. Hoppenbrouwers, "1/f Noise in Continuous Thin Gold Films," *Physica*, Vol. 45, p. 386, 1969.
- <sup>27</sup> Balandin A, Wang KL, Cai S, Li R, Viswanathan CR, Wang EN et. al. Investigation of flicker noise and deep-levels in GaN/AlGaIn transistors. *J. Electron. Mat.* 2000; 29:297–301.
- <sup>28</sup> [17] Feyaerts R, Vandame LKJ, Kramer MCJC, Trefan G, and Zellwger C. Bulk and Contact 1/f noise in GaN TLM structures. *Proceedings of the 31<sup>st</sup> European Solid-State Device Research Conference (ESSDERC) 2001*; 355-358.
- <sup>29</sup> [18] Pala N, Rumyantsev S, Shur M, Gaska R, Hu X, Yang J et. al. Low frequency noise in AlGaIn/InGaIn/GaN double heterostructure field effect transistors. *Solid-State Electronics* 2003; 47:1099-1104.
- <sup>30</sup> [19] Danylyuk SV, Vitusevich SA, Kaper V, Tilak V, Klein N, Eastman LF, et al. Phase Noise Study of AlGaIn/GaN HEMT X-band Oscillator. *phys. stat. sol. (c)* 2005; 2:2615–18.
- <sup>31</sup> N. Carlson, *Foundations of Physiological Psychology*. Needham Heights, Massachusetts: Simon & Schuster, 1969, p. 48.
- <sup>32</sup> E. Wilkins, P. Atanasov, *Med. Eng. Phys.* 18 (4), 273–288, 1996.
- <sup>33</sup> K. Rogers, *Biosens. Bioelectron.* 10, 533–541, 1995.
- <sup>34</sup> M. Denyer, M. Riehle, S. Britland, A. Offenhausser, *Med. Biol. Eng. Comput.* 36, 638–644, 1998.

- 
- <sup>35</sup> S. Pogorelova, M. Zayats, A. Kharitonov, E. Katz, I. Willner, *Sens. Actuators B* 89, 40–47, 2003.
- <sup>36</sup> M. Schmidtner, P. Fromherz, *Biophys. J.* 90, 183–189, 2006.
- <sup>37</sup> J. Wiest, T. Stadthagen, M. Schmidhuber, M. Brischwein, J. Ressler, U. Raeder, H. Grothe, *Anal. Lett.* 39, 1759–1771, 2006.
- <sup>38</sup> M. Eickhoff, J. Schalwig, G. Steinhoff, O. Weidemann et. al. *Phys. Status Solidi C* 0, 1908–1918, 2003.
- <sup>39</sup> J. Schalwig, G. Muller, M. Eickhoff, O. Ambacher, M. Stutzmann, *Sens. Actuators B* 87, 425, 2002.
- <sup>40</sup> L. Spetz, A. Baranzahi, I. Lundstrom, *Phys. Status Solidi A* 162, 493, 1997.
- <sup>41</sup> B. Kang, F. Ren, L. Wang, C. Lofton, W. Tan et. al., *Appl. Phys. Lett.* 87, 023508-1–123508-3, 2005.
- <sup>42</sup> Donald Neaman, *Semiconductor Physics and Devices, Third Edition* 2003, McGraw Hill Publications, pages 498 and 608.

## CHAPTER 5

### CONCLUSIONS

---

Role and scope of semiconductor electronics is continuously increasing. Conventional Si based technologies are incapable of addressing the emerging technological demands arising from the consumer electronics, as well as military applications. New materials and technologies are required for high-speed communication, high-power applications, optoelectronics, and their integrated application.

GaN has emerged as a key material for such applications. GaN based heterostructures have been extensively explored to address the new technological need. Unique properties of GaN-based heterostructures allow raising standards of efficiency, power handling and sensitivity. There are limitations and a number of technological problems are yet to be solved for their commercialization. Quality and reliability concerns of the GaN heterostructure based technologies require intensive investigations. Non-destructive characterization techniques like, LFN, is one of the best suitable methods for characterizing a defect sensitive system, like AlGaIn/GaN heterostructure. Even though state-of-the-art GaN technology is not developed enough for a potential electronics market; it can be applied to other applications like in bioelectronics.

In this thesis, a few aspects of the key issues such as reliability, degradation and device performance are investigated in reference to AlGaIn/GaN heterostructure

based HEMT technology. In addition, potential application of the GaN heterostructure in bioelectronics is demonstrated. AlGaN/GaN heterostructure based devices, which incorporate (i) a *gate recessed* HEMT structure, (ii) a *double channel* HEMT structure, and (iii) a *gate-less* HEMT structure have been used for the investigations.

## 5.1 Summary of the Findings

Detailed experimental studies were conducted on the degradation of the low-frequency noise in GaN-based HEMTs due to voltage stressing. LFN was demonstrated to be successful non-destructive characterization tool for monitoring the device quality and reliability. The experimental results suggest that the initial degradation of the flicker noise occurs due to the generation of some positively charged ions at the AlGaN/GaN interface. Subsequent motion of the ions may be responsible for observed fluctuations in the low-frequency excess noise with stress time. Upon subjecting the devices to extended stressing, the transistors experienced irreversible degradations in the low-frequency noise. Experimental results on the flicker noise measured over a wide range of temperatures suggest that this final stage of degradation arises from the generation of interface states at the AlGaN/GaN hetero-interface.

Studies on the gate-recessed devices and unrecessed devices showed similar trends in the early stages of degradation. A two-phase degradation was observed in case of all devices. It was observed that recessed devices show distinct degradation behaviour that is characterised by a faster and earlier onset of second phase. Even at

room temperature, distinct noise characteristics of recessed and unrecessed devices are identified. Analysis show that subjecting the studied heterostructures to dry-etch process for even shortest durations will result in significant degradation of heterostructure quality. Thus, either an alternative recess-etch technology or alternative device designs should be chosen for any useful applications in conventional electronics of these heterostructures.

HEMT Devices, incorporating double-heterostructures, were extensively characterized. The dc performance of these devices was expectedly found promising. High current density and good transconductance are favorable for their application in conventional electronics. Clear signature of the existence of two parallel 2DEG layers, having high charge density, was observed both in transconductance and  $C$ - $V$  measurements. An efficient access to the buried channels was observed in the almost kink free  $I$ - $V$  characteristics. A hard pinch off was observed in transfer characteristics that reflects a good gate control over both of the conduction channels. All these observations are inline with the intended design of the double-heterostructure incorporating HEMT device and reflect their competence.

In addition to good dc characteristics, the double-heterostructure HEMT devices also show good noise properties, as reflected by the Hooge parameter of these devices that is comparable to those of baseline HEMTs. From the estimation approach, it was inferred that designing such device for a high current density is favorable. However, the design must also consider minimizing the contact resistances. This is because; a significant voltage drop across the ohmic-contacts occurs due to high currents. At low bias voltages, drop across the contacts is

significant. Also, a high contact resistance and a high current density will result in significant power-loss across the ohmic-contacts. Noise measurements were also performed on the TLM patterns fabricated on a similar double-heterostructure. The results revealed that contact-resistances does not contribute significantly to the device noise in the studied structures. Both,  $1/f$  noise and g-r noise were observed in the devices. At room temperature  $1/f$  noise was dominant while g-r bumps were observed at cryogenic temperatures. From the noise data, three trap-levels were identified and their activation energies were obtained from the Arrhenius-plots. Two of the traps were found to be very close in activation energy. From the low temperature noise data it is concluded that the sources of noise in the studied system are thermal activated.

In addition to the study of single and double heterostructure based HEMTs, feasibility of heterostructures for bio-sensing application was investigated. Results of a set of experiments were positive. Good quality heterostructures with high sheet charge density were grown and gate-less HEMT like device structures were fabricated. In the initial phase of these experiments, Saos-2 cells were successfully cultured over the heterostructure surface. In the second phase, a high density of the living cells was achieved by functionalizing the heterostructure surface which improved the cell-semiconductor interface. This success finally led to achievement of a confluent mono-layer over the gate-less area of the devices. In third phase, effect of drug-H7, and trypsin was visually inspected. In the final phase, influence of trypsin on the cells adherent to the device surface was electrically monitored. The time scales of optical and electrical observations were same and reflected the success

of the experiments. This preliminary success clearly demonstrated the potential of the existing state-of-the-art of GaN technology for sophisticated applications in other important disciplines, like bioelectronics.

## **5.2 Suggested Future Work**

During the investigations, following topics were noted for the future investigations:

1. Modeling of the bias stress induced noise degradation in a conventional heterostructure device.
2. Identification of the mechanism that assists and accelerates the degradation process and reduces the life-time significantly.
3. Investigation of the possible co-relation between the noise sources located in two 2DEG-channels and separated by a thin layer.
4. Development of a GaN based robust biosensor for drug detection.
5. Identification of the electrical signatures of drug delivery to the biological species.